Probing electron dynamics in strong-field-driven solids with ultrafast x-ray absorption spectroscopy

Dissertation
zur Erlangung des Doktorgrades
an der Fakultät für Mathematik, Informatik und Naturwissenschaften
Fachbereich Physik
der Universität Hamburg

vorgelegt von

Tatiana Bezriadina

Hamburg

2025

Gutachter/innen der Dissertation:	Prof. Dr. Daria Gorelova
	Prof. Dr. Martin Eckstein
	Prof. Dr. Jan Marcus Dahlström
Zusammensetzung der Prüfungskommission:	Prof. Dr. Daria Gorelova
	Prof. Dr. Martin Eckstein
	Dr. Frank Schlawin
	Prof. Dr. Franz X. Kärtner
	Prof. Dr. Daniela Pfannkuche
Vorsitzende/r der Prüfungskommission:	Prof. Dr. Daniela Pfannkuche
Datum der Disputation:	16.03.2026
Vorsitzender des Fach-Promotionsausschusses PHYSIK:	Prof. Dr. Wolfgang J. Parak
Leiter des Fachbereichs PHYSIK:	Prof. Dr. Markus Drescher
Dekan der Fakultät MIN:	Prof. Dr -Ing. Norbert Ritter

Contents

Declaration on Oath

I hereby declare and affirm that this doctoral dissertation is my own work and that I have not used any aids and sources other than those indicated.

If electronic resources based on generative artificial intelligence (gAI) were used in the course of writing this dissertation, I confirm that my own work was the main and value-adding contribution and that complete documentation of all resources used is available in accordance with good scientific practice. I am responsible for any erroneous or distorted content, incorrect references, violations of data protection and copyright law or plagiarism that may have been generated by the gAI.

20/10/2025

Date

Signature of the doctoral candidate

Abstract

Time-resolved x-ray techniques have made it possible to track laser-dressed electron dynamics in solids on a subfemtosecond timescale and with sub-nanometer spatial resolution. Further development of these techniques requires advances in theoretical methods for describing such experiments and interpreting the data. In this thesis, we consider two complementary x-ray techniques for investigating laser-dressed electron dynamics in solids, i.e. x-ray diffraction and ultrafast x-ray absorption spectroscopy (XAS).

We begin with the description of an x-ray diffraction experiment on a laser-dressed material, where an x-ray and an optical field interact with a crystal simultaneously. We model the x-ray diffraction measurement for a laser-dressed silicon crystal using the previously established formalism. The results of our modeling show excellent agreement with recent measurements. In particular, in collaboration with an experimental research team, we demonstrate a non-zero second-order response in a centrosymmetric crystal such as silicon. We show that this response originates from a laser-driven charge redistribution that breaks local inversion symmetry and gives rise to a finite microscopic second-order susceptibility.

While x-ray diffraction requires pulses with very high photon energy and intensity, which are only accessible at a free-electron laser, ultrafast XAS can be performed with table-top sources. Its *ab initio* description is, however, more challenging because it involves core-electron excitation, which requires the treatment of core and valence electrons on an equal footing. In this thesis, we develop a theoretical framework and an *ab initio* computational scheme for describing the experiments in which ultrafast XAS is applied to study laser-dressed electron dynamics. This scheme combines the Floquet–Bloch formalism and density functional theory (DFT) with the linearized augmented plane wave plus localized orbitals (LAPW+lo) method. The Floquet–Bloch formalism provides a non-perturbative description of laser-dressed solids and allows the study of higher orders of the microscopic optical response. The LAPW+lo method provides a full-potential treatment of the electronic structure of crystals and allows for an accurate description of core electrons. We consider two approaches for calculating the absorption cross section: one applicable only to a quasi-monochromatic probe pulse, and the other suitable for the general case of ultrashort pulses. Using the latter approach together with our computational scheme, we model ultrafast XAS of a laser-dressed zinc oxide crystal at several absorption edges over a wide energy range.

In XAS, the absorption profile reflects the unoccupied partial density of states (PDOS), which allows information about the crystal's electronic structure to be extracted from the data. In this thesis, we additionally develop a computational framework for calculating

the PDOS of a laser-dressed material, which we then use to interpret the results of our ultrafast XAS modeling. We also show that the laser-dressed PDOS provides a valuable computational tool on its own. It captures laser-driven changes in the electronic population in a site- and orbital-resolved way. We illustrate the developed approach using calculations for a laser-dressed zinc oxide crystal. We connect the evolution of the laser-dressed PDOS with the corresponding laser-dressed electron density. We show that the laser-dressed PDOS provides information about the structure of the bonds forming the laser-dressed electron density, in a manner analogous to the field-free case.

We calculate the ultrafast x-ray absorption spectra at the zinc and oxygen absorption edges over an energy range covering both valence and conduction bands. In the conduction-band region, we observed a reduction in signal intensity due to carrier excitation. Around the valence band, a pre-edge feature emerges due to a vacancy left behind after carrier excitation in the conduction band. We compare the results for the ultrafast absorption cross section with the corresponding laser-dressed PDOS to illustrate how the signal is connected to the laser-dressed electron dynamics. In particular, we show that the Fourier amplitudes of the time-dependent absorption cross section follow the amplitudes of the corresponding laser-dressed PDOS. Furthermore, we find that, for ultrashort probe pulses, the absorption of a spectral component also depends on its initial intensity within the probe pulse.

In summary, this thesis presents a theoretical framework and an *ab initio* computational scheme for describing ultrafast XAS in laser-dressed materials. It additionally draws a connection between the ultrafast XAS signal and the underlying laser-dressed electron dynamics. The results provide analytical tools for interpreting ultrafast XAS experiments on laser-dressed materials and for developing strategies for the optical manipulation of material properties.

Zusammenfassung

Zeitaufgelöste Röntgentechniken ermöglichen es, die Dynamik von Elektronen in laserangeregten Festkörpern im Subfemtosekundenbereich und mit einer Auflösung im Subnanometerbereich zu beobachten. Für die Weiterentwicklung dieser Techniken sind Fortschritte bei den theoretischen Methoden zur Beschreibung solcher Experimente und zur Interpretation der Daten erforderlich. In dieser Arbeit betrachten wir zwei komplementäre Röntgentechniken zur Untersuchung der Dynamik von Elektronen in laserangeregten Festkörpern: die Röntgenbeugung und die ultraschnelle Röntgenabsorptionsspektroskopie (XAS).

Wir beginnen mit der Beschreibung eines Röntgenbeugungsexperiments an einem laserangeregten Festkörper, bei dem ein Röntgenstrahl und ein optisches Feld gleichzeitig mit einem Kristall wechselwirken. Wir modellieren die Röntgenbeugungsmessung eines laserangeregten Siliziumkristalls und verwenden dabei den zuvor erstellten Formalismus. Die Ergebnisse unserer Modellierung stimmen ausgezeichnet mit aktuellen Messungen überein. Insbesondere zeigen wir in Zusammenarbeit mit einem experimentellen Forschungsteam eine von Null verschiedene Response zweiter Ordnung in einem zentrosymmetrischen Kristall wie Silizium. Wir weisen nach, dass diese aus einer durch den Laser angeregten Änderung der Ladungsverteilung entsteht, welche die lokale Inversionssymmetrie bricht und zu einer endlichen mikroskopischen Suszeptibilität zweiter Ordnung führt.

Während für die Röntgenbeugung Impulse mit sehr hoher Photonenenergie und -intensität erforderlich sind, die nur durch Freie-Elektronen-Laser erzeugt werden können, kann die ultraschnelle XAS auch mit kleineren Labor-Röntgenquellen durchgeführt werden. Seine *ab initio* Beschreibung gestaltet sich jedoch schwieriger, da sie die Anregung der inneren Elektronen beinhaltet und somit eine gleichwertige Behandlung von inneren Elektronen und Valenzelektronen erfordert. In dieser Arbeit erstellen wir ein theoretisches Modell und ein *ab initio* Berechnungsschema für die ultraschnelle XAS zur Analyse der Elektronendynamik in laserangeregten Festkörpern. Das Modell kombiniert den Floquet–Bloch-Formalismus und die Dichtefunktionaltheorie mit der LAPW+lo-Methode. Der Floquet-Bloch-Formalismus ermöglicht eine, von der Störungstheorie unabhängige, Beschreibung sowie die Analyse von Response höherer Ordnung. Mit der LAPW+lo-Methode kann die gesamte elektronische Struktur durch die Berücksichtigung des vollen Potentials widergespiegelt werden. Somit werden die inneren Elektronen genau beschrieben. Wir betrachten zwei Ansätze zur Berechnung des Absorptionsquerschnitts: einen, der nur für quasi-monochromatische Röntgenpulse gilt, und einen, der für den allgemeinen Fall ultrakurzer Röntgenpulse geeignet ist. Mithilfe des letztgenannten Ansatzes und un-

seres Berechnungsschemas modellieren wir die ultraschnelle XAS eines laserangeregten Zinkoxidkristalls an mehreren Absorptionskanten über einen weiten Energiebereich.

Bei der XAS wird das Absorptionsprofil zur Bestimmung der unbesetzten partiellen Zustandsdichte verwendet, um aus den Messdaten Informationen über die elektronische Struktur des Kristalls zu gewinnen. In dieser Dissertation erstellen wir ein Modell zur Berechnung der partiellen Zustandsdichte laserangeregter Materialien. Anschließend verwenden wir es zur Interpretation der Ergebnisse unserer Modellierung der ultraschnellen XAS. Wir zeigen auch, dass die laserangeregte partielle Zustandsdichte selbst ein wertvolles Berechnungswerkzeug darstellt. Es erfasst lasergesteuerte Änderungen in der atomar- und orbitalaufgelösten elektronischen Population. Zur Veranschaulichung des entwickelten Ansatzes führen wir Berechnungen für einen laserangeregten Zinkoxidkristall durch. Dabei wird die partielle Zustandsdichte mit der entsprechenden Elektronendichte verglichen, was zeigt, dass die partielle Zustandsdichte – analog zum feldfreien Fall – Informationen über die chemische Bindung enthält.

Wir berechnen die ultrakurzen Röntgenabsorptionsspektren an den Absorptionskanten von Zink und Sauerstoff über einen Energiebereich, der sowohl Valenz- als auch Leitungsbänder umfasst. Im Leitungsband beobachten wir eine Verringerung der Signalintensität infolge der Ladungsträgeranregung. Im Valenzband entsteht aufgrund eines Elektronenlochs, das nach der Anregung eines Elektrons in das Leitungsband zurückbleibt, ein Vorkantenmerkmal. Wir vergleichen die Ergebnisse für den ultrakurzen Absorptionsquerschnitt mit der entsprechenden laserangeregten partiellen Zustandsdichte, um zu veranschaulichen, wie das Signal mit der Dynamik der laserangeregten Elektronen zusammenhängt. Insbesondere zeigen wir, dass die Fourieramplituden des zeitabhängigen Absorptionsquerschnitts den Amplituden der entsprechenden laserangeregten partiellen Zustandsdichte folgen. Darüber hinaus stellen wir fest, dass bei ultrakurzen Pulsen die Absorption einer spektralen Komponente auch von ihrer anfänglichen Intensität abhängt.

Diese Arbeit entwickelt ein theoretisches Modell und ein *ab initio* Berechnungsschema zur Beschreibung der ultraschnellen XAS in laserangeregten Materialien. Sie stellt eine Verbindung zwischen den Observablen der ultraschnellen XAS und der zugrunde liegenden Elektronendynamik her. Die gewonnenen Ergebnisse bieten analytische Werkzeuge zur Interpretation entsprechender Experimente und zur Entwicklung von Strategien für die optische Kontrolle von Materialeigenschaften.

Acknowledgements

I would like to express my gratitude to my supervisor, Prof. Dr. Daria Gorelova, for giving me the opportunity to contribute to this project. Thank you for your support, encouragement, and guidance throughout my PhD. I am grateful for the physical insights and scientific expertise you shared with me. I also thank Prof. Dr. Tim Wehling for his advisement and assistance in navigating the challenges during my PhD.

I appreciate our postdoctoral researchers, Dr. Dmitry Tumakov and Dr. Kalyani Chordiya, for sharing their expertise in physics and for providing an environment of collaboration and learning during the time of their postdoc research. Special thanks go to Dr. Dmitry Tumakov for his careful reading of this thesis and his valuable suggestions for corrections. Without your efforts, this manuscript would not be nearly as readable.

I would also like to thank the experimental research team for our many productive meetings and discussions. In particular, I would like to express my deepest gratitude to Prof. David A. Reis and Chance Ornelas-Skarin for their clear and engaging communication of physical science.

I am very grateful to be part of the CUI: Advanced Imaging of Matter. I would like to thank all the professors who took the time to listen to my project presentation and provide valuable feedback. This includes Prof. Dr. Martin Eckstein, Dr. Ch. Bömer, Prof. D. Pfannkuche, Prof. A. Lichtenstein, and many others. Thank you to everyone in the cluster office, especially Prof. Dr. Henry Chapman, Dr. Hans Behringer, Sarah-Christin Stöwer, and Cindy Hirsch. Special thanks go to Jutta Voigtmann, who was always there to support young researchers at CUI. I would also like to thank Eileen Schwanold for her seminars on diversity.

These past four years have been a long and transformative journey, and they will hold great significance for me. I am grateful to everyone I have learned from during meetings, conferences, and the many diverse events held on the DESY campus.

This thesis would not exist without some of the most important people in my life. I thank my mother, who has always given me the freedom to be who I am and who I want to become. Deep thanks go to my best friend, Vasilisa Anikeeva, a physicist herself, who has supported me through this difficult journey in a field still male-dominated. Thank you for many years of friendship—and for many more to come. Finally, my greatest thanks go to my partner, whose love and support have been the foundation of my journey.

List of Publications

1. T. Bezriadina and D. Popova-Gorelova, "Laser-dressed partial density of states," *arXiv preprint arXiv:2505.19894* (2025). Available at: https://arxiv.org/abs/2505.19894
2. C. Ornelas-Skarin, T. Bezriadina, M. Fuchs, S. Ghimire, J. B. Hastings, Q. L. Nguyen, G. de la Peña, T. Sato, S. Shwartz, *et al.*, "Second-order microscopic nonlinear susceptibility in a centrosymmetric material: application to imaging valence electron motion," *Phys. Rev. X* **16**, 011006 (2026). Available at: https://doi.org/10.1103/7vqw-jbs7
3. T. Hansen, T. Bezriadina, and D. Popova-Gorelova, "Theoretical Description of Attosecond X-ray Absorption Spectroscopy of Frenkel Exciton Dynamics," *Molecules* **28**(11), 4502 (2023). Available at: https://doi.org/10.3390/molecules28114502

List of Abbreviations

APW augmented plane waves

APW+lo augmented plane wave plus local orbitals

BZ Brillouin zone

DFT density functional theory

DOS density of states

EXAFS extended x-ray absorption fine structure

FWHM full width at half maximum

GGA-PBE generalized gradient approximation functional of Perdew, Burke, and Ernzerhof

LAPW linearized augmented plane waves

LAPW+lo linearized augmented plane wave plus localized orbitals

lo,LO local orbital

MT muffin-tin

NEXAFS near-edge x-ray absorption fine structure

PDOS partial density of states

RT-TDDFT real-time time-dependent density functional theory

RWA rotating wave approximation

TrARPES time- and angle-resolved photoemission spectroscopy

TrXAS time-resolved x-ray absorption spectroscopy

XAFS x-ray absorption fine structure

XAS x-ray absorption spectroscopy

XUV extreme ultraviolet

1. Introduction

The generation of subfemtosecond pulses of high intensity has made it possible to control the collective motion of electrons in solids on an ultrafast timescale [1–4]. Following the observation of the subfemtosecond response of solids to the driving field [5–8], laser-driven electron dynamics in solids has attracted significant scientific and practical interest. Subfemtosecond control of carriers and photoexcited currents has been demonstrated in solid-state systems, including semiconductors [9, 10] and dielectrics [11–13]. Such optical control is of significant interest for the development of optoelectronic devices. It is particularly important for the design of new devices capable of ultrafast modulation and switching of optical signals on a petahertz timescale [14–17].

The petahertz, or light-wave electronics, utilize systems where emitted electrons are directly sensitive to the amplitude of the electromagnetic field of the driving light rather than its time-averaged intensity [17–19]. For a measurable residual electronic current sensitive to the amplitude of the electric field, the carriers need to be injected within a timescale below the cycle duration of the driving optical field. The main parameter defining the speed of the carrier's injection within a solid is the time it takes for electronic band transitions [20]. According to Keldysh theory [21, 22], the cycle-averaged rate of interband transitions in a monochromatic field can be approximated as $\omega_t = eE_0/\sqrt{m_e^*\Delta}$ for the linearly polarized light. Here e is an elementary charge and E_0 is the applied electric field strength. The material parameters are an effective electron mass m_e^* and the bandgap Δ. Building petahertz electronics using semiconductors with a bandgap of ~ 1 eV requires an electric field strength on the order of ~ 1 V/nm [17]. Therefore, to increase the transition frequency and obtain a system response that is sensitive to the amplitude of the driving field, the strength of the field needs to be increased towards the so-called field-driven regime [22–25]. This is the regime where the electric field strength matches the value of the interatomic forces within a solid.

The emerging properties of the light-driven matter depend strongly on the driving field parameters, opening the way for optical manipulation of the material properties through Floquet engineering [26–29]. This approach has been used for the experimental realization of new band structures [30–32], laser control over topological properties [33–35], and photo-induced phase transitions, including photo-induced metallic [36–38] and superconducting states [39–42]. The experimental realisation of the Floquet states requires extremely high electric field strengths and low photon energies [43], which can only be met using femtosecond laser pulses. Given the ultrafast timescale and the inherently short lifetime, Floquet states survive no longer than a few picoseconds. In solids, the intrinsic timescale of scattering and dephasing further limits their lifetime [44]. For this reason, the observation

of Floquet physics has been limited to materials with exceptionally long scattering times, such as topological insulators [30, 31] and graphene at low temperatures [34, 45].

Recently, the concept of Floquet engineering has been extended from controlling the properties of quasi-equilibrium steady states to manipulating electron dynamics in real time on subfemtosecond timescales [9–13]. Meanwhile, developments in time-resolved spectroscopy instrumentation have provided an unprecedented opportunity to observe emergent steady states and transport properties in non-equilibrium systems. A prominent example of such a technique is time- and angle-resolved photoemission spectroscopy (trARPES), which has been applied to probe Floquet dynamics in quantum materials [30–32, 35, 46]. In laser-driven solids, photon-dressed bands form a periodic structure in both energy and momentum space, and the interaction between different orders of these Floquet–Bloch bands results in dynamic band gaps. TrARPES is a powerful technique capable of resolving such photo-induced band gaps. Using this technique, the first direct experimental evidence of Floquet states was demonstrated in the topological insulator Be_2Se_3, driven by an intense ultrashort pulse with energy below the bulk band gap [30]. It has also been used to explore the dynamic transitions between Floquet–Bloch and Volkov states on the surface of the topological insulator Be_2Se_3 [31]. In graphene, the formation of Floquet states has been demonstrated through the light-induced anomalous Hall effect or photovoltaic Hall effect [34]. A further study in Ref. [45] reported the experimental realization of steady Floquet–Andreev states in graphene Josephson junctions.

Time-resolved spectroscopic techniques were initially limited to measurements of transient absorption and reflectivity [47], and later developed into a wide range of techniques where the particular details of experiments depend on the targeted system and dynamics [29, 48]. Novel light sources are now capable of generating intense pulses with wavelengths ranging from terahertz to extreme ultraviolet (XUV), offering various pulse durations and repetition rates and enabling precise control in pump-probe experiments. It allows for selectively exciting electronic transitions, coupling directly to collective modes, or avoiding resonances entirely. The application of the probe across the XUV to hard x-ray energy range in particular allows the study of laser-driven transient modifications with subnanometer spatial resolution at the subfemtosecond timescale. Ultrafast x-ray probing techniques provide useful instruments for the detection of photo-excited dynamics within molecular systems and solid materials [49–54].

A beneficial x-ray imaging technique for probing laser-dressed electron dynamics is x-ray diffraction. This technique uses photon wavelengths comparable to atomic spacing to study structural dynamics [55–58] or the evolution of spin and charge electronic orders [59–64]. In standard x-ray diffraction, the intensity of diffraction peaks at Bragg reflections $\mathbf{G}$ is proportional to the square of the $\mathbf{G}$th Fourier component of the electron density. In the presence of a driving field, side peaks appear at Bragg reflections $\mathbf{G}$ [65, 66], located at momentum $\mathbf{G} + \mathbf{q}$ and separated in energy by ω, where $\mathbf{q}$ and ω are the momentum and

energy of the driving-field photons. The intensity of the side peaks encodes information about the laser-dressed electron density based on the material's microscopic optical response. It is proportional to the squared $\mathbf{G}$th Fourier component of laser-dressed charge distribution, similar to the stationary case. The first x-ray diffraction measurement in the presence of a driving field was carried out at the Free-Electron Laser LCLS to probe the linear optical response of diamond [66]. Later, it was shown that the concept remains valid for a high-order optical response [67–69]. The side peaks at $\mathbf{G} + n\mathbf{q}$ represent the $\mathbf{G}$th Fourier components of laser-dressed charge distributions resulting from nth-order optical response. The main advantage of such a measurement is that it provides a way to probe the valence charge density in a material, which is not accessible in standard x-ray diffraction experiments [66]. It can also selectively probe certain parts of the valence charge because a material's optical polarizability is not uniformly distributed across them.

In x-ray diffraction measurements, the probe pulse is usually chosen to have a high photon energy to avoid resonance with core-electron excitations. These measurements typically require large-scale facilities, such as free-electron lasers. In contrast, resonant x-ray probe techniques use photon energies that are carefully tuned to the binding energies of localized core electrons of specific atoms. As a result, they are atomic and orbital selective, and therefore sensitive to specific orbital contributions to the laser-driven dynamics of delocalized valence states [70–72]. Importantly, resonant x-ray techniques can often be carried out using tabletop x-ray sources. A prominent example is time-resolved x-ray absorption spectroscopy (trXAS), which is an extension of x-ray absorption spectroscopy (XAS) to the time domain.

In XAS, an incident photon excites a core electron into an unoccupied state, as shown in Fig. 1.1. Since the binding energies of core electrons differ significantly between elements and even between core shells of the same atom, XAS provides both elemental and orbital selectivity. By tuning the incident photon energy, one can choose the absorbing atom and the specific core level from which the electron is excited. In experiments, XAS spectra are recorded in transmission mode, where the ratio of incident and transmitted beam intensities is measured while the photon energy of the x-ray pulse is scanned through the binding energy of a chosen core shell. At the absorption edge, a sharp increase in absorption occurs, corresponding to transitions into the lowest unoccupied states, for example, into bound core excitons in insulators. The absorption edges are labeled according to the initial core level: excitations from the $1s$ state correspond to the K-edge; from the $2s$ state, to the L_1-edge; from the $2p$ states, to the $L_{2,3}$-edges; from the $3s$, $3p$, and $3d$ states, to the M_1-, $M_{2,3}$-, and $M_{4,5}$-edges, respectively; and higher shells are labeled analogously.

The absorption edge region is followed by the x-ray absorption fine structure (XAFS). The latter includes the near-edge x-ray absorption fine structure (NEXAFS) region and the extended x-ray absorption fine structure (EXAFS) region. In XAFS spectroscopy, the core

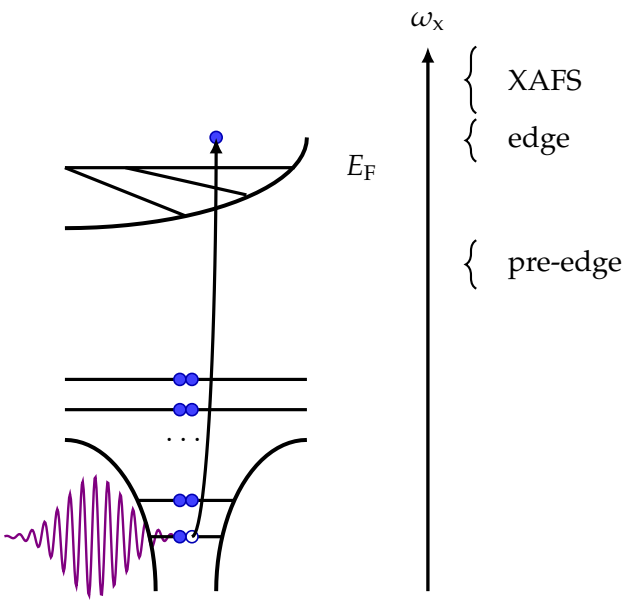

Figure 1.1.: Schematic representation of x-ray absorption spectroscopy.

electron is excited from the bound core-level state into the unoccupied valence state or continuum [70, 73, 74]. NEXAFS corresponds to the transition to unoccupied valence states. As it involves the promotion of core-level electrons into unoccupied valence states, NEXAFS probes the unoccupied density of states [75, 76]. EXAFS corresponds to bound-free transitions of core-level electrons. In this region, photo-excited electrons undergo multiple scattering from neighboring atoms, leading to oscillations in the absorption profile. EXAFS therefore contains information about the atomic configurations or lattice spacings of solids [77, 78]. Taken together, NEXAFS and EXAFS allow for the measurement of both the electronic and lattice structure of a material. The extension of XAFS spectroscopy to time-resolved measurement schemes has enabled the observation of electronic and structural dynamics in real time on a subfemtosecond timescale [79–82].

In trXAS, an ultrashort XUV or x-ray probe pulse records the electronic and structural dynamics in the absorption spectrum [79, 83, 84]. In solids, trXAS enables measurements of laser-driven changes in both the electronic structure and the atomic arrangement [49, 85–87]. In a typical experimental setup, dynamic changes in the x-ray absorption profile are followed by varying the time delay between the pump and probe pulses, which can be translated into the evolution of the carrier population and coupled electron–phonon dynamics during the action of the driving field. In the case of time-resolved NEXAFS spectroscopy [49], the high photon energy of the broadband XUV pulse, which typically lies above the energy range of interband transitions, offers an additional advantage. It enables simultaneous observation of laser-dressed carrier dynamics in both the valence and conduction bands, thus avoiding the ambiguities often found in optical pump-probe spectroscopy due to overlapping spectral features. This technique has been used to resolve electron, hole and phonon dynamics in materials with a subfemtosecond resolution

including times during the interaction with a driving pulse [7, 8, 86, 88, 89].

These novel experiments, capable of resolving electron dynamics during laser driving, motivate theoretical developments and advances in *ab initio* computational tools for interpreting the experimental data. Real-time time-dependent density functional theory (RT-TDDFT) is widely used to describe electron dynamics in molecules and solids under both weak and strong external driving fields [90, 91]. It replaces the full time-dependent Schrödinger equation for the many-electron wavefunction with a set of time-dependent Kohn–Sham equations which, in principle, gives the exact time-dependent electron density. Interelectronic interactions are included through exchange–correlation potentials, although their exact forms remain unknown.

Theoretical modeling of ultrafast x-ray absorption spectroscopy within the RT-TDDFT framework involves propagating the electronic system under the full time-dependent Hamiltonian, including both the driving field and probe x-ray field. The transient absorption spectrum is extracted by subtracting the pump-only dynamics from the pump-probe simulation to obtain the probe-induced response. Different implementations rely on different exchange-correlation functionals and basis sets. Plane-wave pseudopotentials are efficient for extended states, while atomic functions are often used to describe core excitations. RT-TDDFT with the Gaussian basis sets was applied to simulate attosecond transient absorption at the oxygen and nitrogen K-edges in aminophenol and the silicon $L_{2,3}$-edge in bulk-like α-quartz clusters in Ref. [92]. Relativistic RT-TDDFT was implemented in Ref. [93] to describe ultrafast XAS across the periodic table, including the sulfur $L_{2,3}$-edge and transition-metal edges. In Ref. [94], attosecond transient absorption of SiO_2 and diamond was simulated based on bulk-mimicking clusters and RT-TDDFT with Gaussian basis sets. A broader review of RT-TDDFT applications to ultrafast materials science was given by Sato *et al.* [91], who summarized simulations of attosecond transient absorption in magnetic solids, including the Co $M_{2,3}$-edge. RT-TDDFT implementation has been developed using the all-electron, full-potential LAPW+lo basis in the `exciting` in Ref. [95]. However, it is not currently possible to model ultrafast x-ray absorption spectroscopy with this implementation.

The description of resonant x-ray techniques within RT-TDDFT remains challenging since conducting an accurate analysis of core-excited states in materials is a difficult task. A significant numerical challenge arises from using a uniform basis to simultaneously describe both localized core electrons and delocalized valence electrons. Many basis functions are required to accurately represent the wavefunction of a core electron in the plane-wave basis [96] or the wavefunction of a valence electron in the basis of atomic functions [97]. Additionally, capturing nontrivial electronic correlation effects remains a significant challenge for density functional theory (DFT)-based methods. Non-equilibrium Green's functions and diagrammatic techniques provide a framework for computing few-body correlation functions in time-dependent problems without solving the full many-

body wavefunction [98, 99]. However, the application of these methods to non-equilibrium systems is more challenging, as time-translational invariance no longer holds. As a result, physical quantities must be described as functions of two distinct time variables rather than a single energy variable, which significantly increases computational complexity. A prominent example of the application of non-equilibrium Green's functions methods to XAS is the use of the Bethe–Salpeter equation formalism to compute bound two-particle states [100–102]. Several works have extended the Bethe–Salpeter equation to the time domain [103–106]. However, these have not been applied to ultrafast XAS in real solids.

In practice, the theoretical description of XAS in the presence of a strong driving field involves a combination of computational time propagation and linear-response theory. The system is propagated nonperturbatively under the strong pump field, while the probe is introduced as a perturbation to extract the transient response. As the probe pulse can be treated as a perturbation, the absorption spectrum can be expressed as the linear response of the pump-driven medium. For example, the equations of motion for the single-particle density matrix can be solved in a Bloch basis. This results in the semiconductor Bloch equations, in which the pump field is included non-perturbatively and phenomenological dephasing and relaxation can be introduced. The x-ray probe is then treated perturbatively, and transient absorption is derived from probe-induced polarization or current in the pump-driven medium. The density-matrix formalism is particularly useful when the system is in a mixed state or when relaxation processes are significant. In Ref. [107], a four-band density matrix was used to simulate pump-driven dynamics with a finite core-hole lifetime in graphene, and the resulting time-dependent polarization was analyzed to extract the absorption spectrum. In Ref. [108], trXAS was formulated for a periodic crystal by propagating density-matrix equations in a Houston-state basis and computing the probe-induced conductivity. This captures the dynamical Franz–Keldysh effect around the band edge, demonstrating that the absorption spectrum encodes full information on the momentum-dependent band gap across the entire Brillouin zone. In Refs. [109, 110], the authors developed a framework for describing XAS of laser-driven materials using a similar approach based on time propagation of the system's density matrix in reciprocal space. The implementations include tight-binding model and the Kohn–Sham DFT scheme, with localized orbitals or Wannier basis, including the description of excitonic effects. The framework was demonstrated by modeling an attosecond ultrafast spectroscopy experiment in a few-layer graphite interacting with a mid-IR ultrashort pulse.

In this thesis, we present an *ab initio* computational scheme for describing ultrafast XAS. The scheme combines the Floquet–Bloch formalism with DFT using the LAPW+lo method. The Floquet–Bloch formalism enables the study of non-perturbative electron dynamics in solids driven by intense laser fields without explicit time propagation of the electronic states [111, 112]. This makes it computationally more efficient than RT-TDDFT or Green's function approaches [44, 113–115]. Although Floquet theory assumes a continuous periodic driving field, it has recently been demonstrated that the Floquet picture remains a valid

approximation even for strong optical pulses comprising only 10–15 cycles [32, 116, 117]. Within our scheme, the use of the Floquet–Bloch formalism both facilitates the interpretation of the physical processes and provides computational feasibility. The LAPW+lo method provides a full-potential treatment of the crystal electronic structure, accurately capturing the effects of both valence and core electrons.

In the next Chapter 2, we introduce the theoretical background for calculating the ground and laser-dressed state of solids and computational methods that are the basis of the results presented in this thesis. It begins with an overview of Floquet theory as a formalism for describing systems under periodic external fields, followed by a discussion of its numerical implementation using the extended Hilbert space approach. We then introduce Floquet–Bloch theory as a tool to treat periodicity in both time and space. Finally, we outline the main features of the DFT method in use, which is the plane wave basis set and pseudopotentials in the case of x-ray diffraction and the family of augmented plane wave (APW) methods in the case of trXAS. We additionally explain the treatment of semicore and core electronic states as it is implemented in `exciting`.

In Chapter 3 we begin with a description of the x-ray diffraction experiment on the laser-dressed material. We first introduce the general formalism developed in the Ref. [67]. We then focus on the angular dependence of the side peaks to the elastic Bragg peak. We model the x-ray diffraction signal from a laser-dressed silicon crystal using a previously developed *ab initio* computational scheme combining Floquet–Bloch formalism with DFT [67]. We compare our results of computational modeling for a silicon crystal with the recent experimental measurement of the angular dependence of the first- and second-order side peaks to the (220) elastic Bragg peak. Together with the experimental research team, we show how the measurement of the higher-order side peaks provides atomic-scale information on the local symmetry of the laser-dressed electron density.

This motivates us to consider another technique for probing electron dynamics in laser-dressed solids, namely ultrafast XAS. In XAS, the absorption profile reflects the unoccupied PDOS, which allows information about the crystal's electronic structure to be extracted from the data. To interpret the results of our ultrafast XAS modeling we develop a framework for calculating the PDOS of laser-dressed materials in Chapter 4. We also show that laser-dressed PDOS provides a valuable computational tool on its own as it captures laser-driven changes in the electronic population in a site- and orbital-resolved way. The developed an *ab initio* computational scheme combines the Floquet–Bloch formalism with DFT using the LAPW+lo basis. We use the LAPW+lo method since it provides full-potential treatment of the electronic structure and provides a convenient way to distinguish the contributions of different orbital types to the density of states. Using wurtzite zinc oxide crystal as a case study, we connect the evolution of the laser-dressed PDOS with the corresponding laser-dressed electron density. We show that the laser-dressed PDOS provides information about the structure of the bonds that form

the laser-dressed electron density, analogous to the field-free case. We also show that analyzing the time dependence of the laser-dressed PDOS reveals the contributions of different orbital types to laser-dressed electron dynamics. We additionally introduce the laser-dressed electron density for a selected energy window to draw a connection between the hybridized orbitals and the bonding or antibonding character of their interaction. We further use the introduced electron density for a selected energy window to interpret laser-driven bond weakening.

Chapter 5 presents theoretical description and developed *ab initio* computational scheme to describe a process in which trXAS is applied to study laser-dressed electron dynamics in solids. The computational scheme is based on the Floquet–Bloch formalism and DFT with LAPW+lo basis. The Floquet–Bloch formalism provides a non-perturbative description of laser-dressed solids and allows the study of higher orders of the microscopic optical responses. The LAPW+lo method provides a full-potential treatment of the crystal electronic structure, accurately capturing the effects of both valence and core electrons. We introduce two different methods to calculate absorption cross section, one based on the so-called projection treatment of x-ray absorption and the other based on the so-called time- and frequency-domain treatment of x-ray absorption. We compare the results of the two methods for calculating the x-ray absorption cross section with the corresponding time-dependent PDOS. Using a wurtzite zinc oxide crystal as a case study, we show how trXAS measurements can reveal information about laser-dressed electron dynamics in the conduction band and hole dynamics in the valence band in a site- and orbital-resolved manner.

Appendix A contains the details of the derivations of the x-ray absorption cross section in Chapter 5, including the description of the core hole decay.

2. Theoretical background

2.1. Floquet theory

Floquet theory, the central method of this thesis, describes periodically driven systems [27, 118, 119]. It applies to the systems with a time-periodic Hamiltonian $\hat{H}(t) = \hat{H}(t+T)$, where T is the period. System dynamics is governed by the time-dependent Schrodinger equation

$$i\frac{d}{dt}\left|\Psi(t)\right\rangle = \hat{H}(t)\left|\Psi(t)\right\rangle. \tag{2.1}$$

According to Floquet theory [120, 121], there exists a time-periodic unitary operator $\hat{U}_{\mathrm{F}}(t) = \hat{U}_{\mathrm{F}}(t+T)$ that defines a transition to a rotating frame. In this frame, the transformed state $\left|\Psi_{\mathrm{F}}(t)\right\rangle = \hat{U}_{\mathrm{F}}^{\dagger}(t)\left|\Psi(t)\right\rangle$ evolves under an effective time-independent Hamiltonian:

$$\hat{H}_{\mathrm{F}} = \hat{U}_{\mathrm{F}}^{\dagger}(t)\hat{H}(t)\hat{U}_{\mathrm{F}}(t) - i\hat{U}_{\mathrm{F}}^{\dagger}(t)\frac{d}{dt}\hat{U}_{\mathrm{F}}(t). \tag{2.2}$$

The effective time-independent Hamiltonian $\hat{H}_{\mathrm{F}}$ allows to describe the evolution of the system in a way similar to that of a stationary system. The eigenvalue problem of the effective Hamiltonian

$$\hat{H}_{\mathrm{F}}\left|\tilde{\Phi}_K\right\rangle = \mathcal{E}_K\left|\tilde{\Phi}_K\right\rangle \tag{2.3}$$

gives a set of stationary states $\left|\Psi_K(t)\right\rangle$ of the time-dependent Schrödinger equation, called Floquet states. They have the following form [119–121]

$$\left|\Psi_K(t)\right\rangle = e^{-i\mathcal{E}_K t}\left|\Phi_K(t)\right\rangle, \quad \left|\Phi_K(t)\right\rangle = \left|\Phi_K(t+T)\right\rangle, \tag{2.4}$$

where $\left|\Phi_K(t)\right\rangle = \hat{U}_{\mathrm{F}}(t)\left|\tilde{\Phi}_K\right\rangle$ is the Floquet mode with periodic time dependence, and $\mathcal{E}_K$ is the quasienergy.

The Floquet states are eigenstates of the time evolution operator over one driving period,

$$\left|\Psi_K(t+T)\right\rangle = \hat{U}(t+T,t)\left|\Psi_K(t)\right\rangle = e^{-i\mathcal{E}_K T}\left|\Psi_K(t)\right\rangle. \tag{2.5}$$

For each time point t, the Floquet states form a complete and orthogonal basis. In the cases where the system was prepared in a single Floquet state, its time evolution is periodic, defined by the Floquet mode $\left|\Phi_K(t)\right\rangle$, and by this means quasistationary [119–121]. If the system was prepared in a coherent superposition of several Floquet states,

$$\left|\Psi(t)\right\rangle = \sum_K C_K e^{-i\mathcal{E}_K t}\left|\Phi_K(t)\right\rangle, \quad C_K = e^{i\mathcal{E}_K t_0}\left\langle\Phi_K(t_0)|\Psi(t_0)\right\rangle, \tag{2.6}$$

deviations from a periodic evolution are defined by the quasienergies $\mathcal{E}_K$ and initial condition for $|\Psi(t_0)\rangle$.

Example: A two-level system in a circularly polarized field

As a simple example, we apply Floquet theory to solve the time-dependent Schrödinger equation in the case of a two-level system in a circularly polarized field [122]. The Hamiltonian of a two-level system in a classical, spatially uniform, circularly polarized electric field has the form

$$\hat{H}(t) = \frac{\omega_0}{2}\hat{\sigma}_z + F\cos(\omega t)\hat{\sigma}_x + F\sin(\omega t)\hat{\sigma}_y. \tag{2.7}$$

Here, $\hat{\sigma}_{x,y,z}$ are the Pauli matrices, ω_0 denotes the transition frequency between the two states of the undriven system, and F and ω refer to the amplitude and the frequency of the driving force.

The transformation to a reference frame co-rotating with the field is implemented by a unitary operator:

$$\hat{U}_{\mathrm{F}}(t) = \exp\left(-i\frac{\omega t}{2}\left(\hat{\mathbb{1}} - \hat{\sigma}_z\right)\right), \tag{2.8}$$

In the rotating frame, the transformed Hamiltonian, given by Eq. (2.2), takes the form:

$$\hat{H}_{\mathrm{F}}^{\mathrm{c}} = \frac{\omega}{2}\hat{\mathbb{1}} + \frac{\Delta}{2}\hat{\sigma}_z + F\hat{\sigma}_x, \tag{2.9}$$

where $\Delta = \omega_0 - \omega$ is the detuning from resonance and the superscript c indicates that we are considering a circularly polarized driving field. After diagonalization, this Hamiltonian gives the quasienergies

$$\mathcal{E}_\pm = \frac{1}{2}(\omega \pm \Omega_{\mathrm{R}}), \tag{2.10}$$

with the generalized Rabi frequency

$$\Omega_{\mathrm{R}} = \sqrt{\Delta^2 + F^2}. \tag{2.11}$$

The eigenvectors of the Hamiltonian $\hat{H}_{\mathrm{F}}^{\mathrm{c}}$ give rise to the Floquet states, which can be evaluated according to Eqs. (2.3),(2.4).

The time-periodic operator $\hat{U}_{\mathrm{F}}(t)$ in Eq. (2.2) is not uniquely defined, leading to multiple choices for the effective time-independent Hamiltonian $\hat{H}_{\mathrm{F}}$. Given one operator $\hat{U}_{\mathrm{F}}(t)$, a new operator $\hat{U}'_{\mathrm{F}}(t)$ can be obtained by applying a unitary transformation. However, since Floquet states $|\Psi_K(t)\rangle$ are eigenstates of the time evolution operator over one driving period (Eq. (2.5)), they will not be altered by such operations. For example, we can multiply the operator with an arbitrary time-independent unitary operator $\hat{U}$ from the

right, $\hat{U}'_{\mathrm{F}}(t) = \hat{U}_{\mathrm{F}}(t)\hat{U}$, so that $\hat{H}'_{\mathrm{F}} = \hat{U}^{\dagger}\hat{H}_{\mathrm{F}}\hat{U}$. If we choose $\hat{U}'_{\mathrm{F}}(t) = \hat{U}_{\mathrm{F}}(t)\hat{U}^{\dagger}_{\mathrm{F}}(t_0) \equiv \hat{U}_{\mathrm{F}}(t;t_0)$, we obtain an operator that is equal to the identity once during each period T, $\hat{U}'_{\mathrm{F}}(t_0) = \hat{U}_{\mathrm{F}}(t_0;t_0) = 1$. Thus, we can write the time evolution operator as follows [119, 123]:

$$\hat{U}(t,t_0) = \hat{U}_{\mathrm{F}}(t;t_0)\exp\left(-i(t-t_0)\hat{H}^{t_0}_{\mathrm{F}}\right), \tag{2.12}$$

with the Floquet Hamiltonian

$$\hat{H}^{t_0}_{\mathrm{F}} = \hat{U}_{\mathrm{F}}(t_0)\hat{H}_{\mathrm{F}}\hat{U}^{\dagger}_{\mathrm{F}}(t_0). \tag{2.13}$$

In particular, for $t = t_0 + T$, Eq. (2.12) becomes

$$\hat{U}(t_0+T,t_0) = \exp\left(-iT\hat{H}^{t_0}_{\mathrm{F}}\right). \tag{2.14}$$

Therefore, the Floquet Hamiltonian corresponds to the time evolution in steps of the driving field period T. $\hat{H}^{t_0}_{\mathrm{F}}$ depends on the initial time t_0 as a parameter and thus also on the driving field phase. However, according to Eq. (2.13), this dependence sits in a unitary transformation, so that the eigenvalues of the Floquet Hamiltonian are independent of t_0 and the driving field phase [119].

Another way to obtain a new operator $\hat{U}'_{\mathrm{F}}(t)$ and the effective Hamiltonian $\hat{H}'_{\mathrm{F}}$ is the following $\hat{U}'_{\mathrm{F}}(t) = \hat{U}_{\mathrm{F}}(t)e^{i\mu\omega t|\tilde{\Phi}_K\rangle\langle\tilde{\Phi}_K|}$, where $\omega = 2\pi/T$ is the angular frequency and μ is an integer [119], which gives

$$\hat{H}'_{\mathrm{F}} = \hat{H}_{\mathrm{F}} + \mu\omega\,|\tilde{\Phi}_K\rangle\,\langle\tilde{\Phi}_K|\,. \tag{2.15}$$

The introduced transformation results in the new quasienergy and the corresponding Floquet modes labeled by μ as follows:

$$\mathcal{E}^{\mu}_K = \mathcal{E}_K + \mu\omega, \quad |\Phi^{\mu}_K(t)\rangle = e^{i\mu\omega t}\,|\Phi_K(t)\rangle\,, \tag{2.16}$$

the Floquet state remains unchanged by this transformation,

$$|\Psi_K(t)\rangle = e^{-i\mathcal{E}_K t}\,|\Phi_K(t)\rangle = e^{-i\mathcal{E}^{\mu}_K t}\,|\Phi^{\mu}_K(t)\rangle\,. \tag{2.17}$$

From the Eq. (2.16) it follows that quasienergies are defined up to integer multiples of the driving field frequency ω, in agreement with the earlier observation that Eq. (2.2) does not define the Floquet Hamiltonian uniquely. Therefore, we can choose the index μ independently for each Floquet state K, and in this way map all quasienergies into a single energy range of width ω. This range is usually referred to as the Floquet–Brillouin zone [27, 118, 119, 124], similar to the definition of the Brillouin zone followed from Bloch's theory for spatially periodic systems [125]. If a certain harmonic $\mu' = \mu_0$ dominates the Floquet mode $|\Phi_K(t)\rangle \equiv \sum_{\mu'}|\Phi^{(\mu')}_K\rangle\,e^{-i\mu'\omega t}$ in a certain reference frame, then $\mathcal{E}^{\mu_0}_K$ is a natural choice for

quasienergy, which in the limit of a vanishing field gives a stationary energy spectrum.

2.1.1. Numerical methods to solve the Floquet problem

Only a few Floquet Hamiltonians can be found in a closed form, as in the case of the circularly driven two-level system discussed earlier. As a simple example, we consider instead a linearly driven two-level system, described by the Hamiltonian [126]:

$$\hat{H}(t) = \frac{\omega_0}{2}\hat{\sigma}_z + 2F\hat{\sigma}_x \cos(\omega t), \tag{2.18}$$

which can be interpreted as a superposition of left- and right-hand circularly polarized driving fields. The Hamiltonian will retain some time dependence after applying the transformation into the rotating frame. One of the two circular components is effectively "rotated away," while the "counter-rotating" term will oscillate at twice the driving frequency

$$\hat{H}_{\text{rot}}(t) = \hat{H}_{\text{F}}^{\text{c}} + F\cos(2\omega t)\hat{\sigma}_x - F\sin(2\omega t)\hat{\sigma}_y. \tag{2.19}$$

For a very high driving frequency $\omega \gg F$, one can neglect the 2ω terms, and the Hamiltonian in Eq. (2.19) reduces to $\hat{H}_{\text{F}}^{\text{c}}$. This is the famous rotating wave approximation (RWA), the prominent example of high-frequency expansion [119, 127, 128]. A high-frequency expansion can be used to get a good approximation of the effective Hamiltonian $\hat{H}_{\text{F}}$ and the corresponding unitary transformation operator $\hat{U}_{\text{F}}$ when the driving frequency ω is large compared to the characteristic matrix elements of the Hamiltonian. However, to overcome the limitations of this approximation, particularly in regimes where ω is of comparable magnitude with the coupling to the driving field, a more general approach is required. This involves working within the extended Floquet Hilbert space of time-periodic states, which is one of the main numerical methods used to solve the Floquet problem.

Extended Hilbert space

Substituting the Floquet state $|\Psi_K(t)\rangle$, as defined in Eq. (2.3),(2.4), into the time-dependent Schrödinger equation yields the following equation for the Floquet modes $|\Phi_K^\mu(t)\rangle$:

$$[\hat{H}(t) - i\frac{d}{dt}]\,|\Phi_K^\mu(t)\rangle = \mathcal{E}_K^\mu\,|\Phi_K^\mu(t)\rangle\,. \tag{2.20}$$

Equation (2.20) is the eigenvalue problem of the Hermitian quasienergy operator [121], which can be identified with the Floquet Hamiltonian $\hat{H}_{\text{F}}$:

$$\hat{Q}(t) = \hat{H}(t) - i\frac{d}{dt}, \tag{2.21}$$

acting on the extended Hilbert space $\mathcal{F} = \mathcal{H} \otimes \mathcal{T}$. This space is the tensor product of the Hilbert space $\mathcal{H}$ and the space of time-periodic functions $\mathcal{T}$. The inner product in $\mathcal{F}$

combines the scalar product of $\mathcal{H}$ with time averaging and reads:

$$\langle\langle f|g\rangle\rangle = \frac{1}{T}\int_0^T dt\,\langle f(t)|g(t)\rangle\,, \tag{2.22}$$

where a double ket $|f\rangle\rangle$ denotes the elements of $\mathcal{F}$ and $|f(t)\rangle$ denotes the corresponding state at time t in $\mathcal{H}$. A state $|f(t)\rangle = |f(t+T)\rangle$, including its full periodic time dependence, is written as $|f\rangle\rangle$ when considered as an element of $\mathcal{F}$. An operator acting in $\mathcal{F}$ is indicated by an overbar to distinguish it from operators acting in $\mathcal{H}$, which are marked by a caret [119–121]. The eigenvalue problem of the quasienergy operator $\bar{Q}$ is now written as follows:

$$\bar{Q}\,|\Phi_K^\mu\rangle\rangle = \mathcal{E}_K^\mu\,|\Phi_K^\mu\rangle\rangle. \tag{2.23}$$

In Floquet space, the states $|\Phi_K^\mu\rangle\rangle$ and $|\Phi_K^{\mu'}\rangle\rangle$, defined by Eq. (2.16), are orthogonal if $\mu' \neq \mu$, so that the quasienergy spectrum is periodic with period ω. Despite this redundancy, working in $\mathcal{F}$ has the advantage that one can use intuition developed for the stationary systems.

From a complete basis of orthogonal states $|\varphi_n\rangle$ of $\mathcal{H}$, one can construct a complete basis of orthogonal states $|\varphi_n, \mu\rangle\rangle$ of $\mathcal{F}$, given by $|\varphi_n, \mu(t)\rangle = |\varphi_n\rangle\, e^{i\mu\omega t}$ with integer μ. In terms of these basis states, the quasienergy operator has the matrix elements [120, 121, 129–131]:

$$\langle\langle\varphi_m, \mu'|\,\bar{Q}\,|\varphi_n, \mu\rangle\rangle = \langle\varphi_m|\,\hat{H}_{\mu'-\mu}\,|\varphi_n\rangle + \mu\omega\delta_{\mu'\mu}\delta_{nm}, \tag{2.24}$$

where $\hat{H}_{\mu'-\mu}$ is the $(\mu'-\mu)^{th}$ Fourier component of the time-dependent Hamiltonian

$$\hat{H}_\mu = \frac{1}{T}\int_0^T dt e^{-i\mu\omega t}\hat{H}(t) = \hat{H}_{-\mu}^\dagger. \tag{2.25}$$

The matrix defined by Eq. (2.24) has a block structure with respect to μ. The diagonal blocks are defined by the time-averaged Hamiltonian $\hat{H}_0$ and shifted with respect to each other by integer multiples of ω in quasienergy. As an example, we consider a common time-dependent Hamiltonian that is of the following form:

$$\hat{H}(t) = \hat{H}_0 + \hat{V}e^{i\omega t} + \hat{V}^\dagger e^{-i\omega t}. \tag{2.26}$$

Here, $\hat{H}_0$ is the unperturbed Hamiltonian of the system and $\hat{V}$ is a perturbation oscillating at frequency ω. In this case, the matrix elements of the quasienergy operator in Eq. (2.24)

take the simple form

$$\begin{pmatrix} \ddots & \ddots & \ddots & \ddots & \ddots \\ \ddots & \hat{E}+\omega\hat{\mathbb{1}} & \hat{V} & 0 & \ddots \\ \ddots & \hat{V}^{\dagger} & \hat{E} & \hat{V} & \ddots \\ \ddots & 0 & \hat{V}^{\dagger} & \hat{E}-\omega\hat{\mathbb{1}} & \ddots \\ \ddots & \ddots & \ddots & \ddots & \ddots \end{pmatrix}, \tag{2.27}$$

where $\hat{E}$ is a diagonal matrix containing the eigenvalues of the unperturbed Hamiltonian $\hat{H}_0$, $\hat{E} = \mathrm{diag}(E_{\varphi_1}, E_{\varphi_2}, ...)$, $\hat{V}$ is a matrix with elements $V_{n',n} = \langle \varphi_{n'} | \hat{V} | \varphi_n \rangle$ and $\hat{\mathbb{1}}$ is a unit matrix. Numerical evaluation of the eigenvalues and eigenvectors of the block-tridiagonal matrix in Eq. (2.27) can be very efficient due to the number of algorithms developed, but since it is infinite-dimensional, a convergence study over the number of blocks is required.

2.2. Floquet theory in quantum electrodynamics

The structure of the Floquet Hamiltonian matrix in Eq. (2.27) is similar to that of a Hamiltonian matrix for a system interacting with a quantized field in the large photon number limit, i.e., coherent light [120]. In this model, μ is referred to as the photon number, and the corresponding matrix elements, $\hat{H}_\mu$, describe μ-photon processes [69]. The interpretation of the results in terms of states for a quantized field becomes clearer when we consider the periodic term in the Hamiltonian $\hat{H}$ as arising from the interaction of a system with a quantized field. We introduce the total Hamiltonian:

$$\hat{H}_{\mathrm{el-em}} = \hat{H}_{\mathrm{el}} + \hat{H}_{\mathrm{em}} + \hat{H}_{\mathrm{int}}, \tag{2.28}$$

where $\hat{H}_{\mathrm{el}}$ is the electronic Hamiltonian, $\hat{H}_{\mathrm{em}}$ is the electromagnetic field Hamiltonian, and $\hat{H}_{\mathrm{int}}$ describes the interaction between the electrons and the external field.

The electromagnetic field is described by a single mode Hamiltonian

$$\hat{H}_{\mathrm{em}} = \omega\, \hat{a}^{\dagger}_{\boldsymbol{\kappa}_0,s_0} \hat{a}_{\boldsymbol{\kappa}_0,s_0}, \tag{2.29}$$

where $\hat{a}^{\dagger}_{\boldsymbol{\kappa}_0,s_0}$ and $\hat{a}_{\boldsymbol{\kappa}_0,s_0}$ are the photon creation and annihilation operators for the mode with wave vector $\boldsymbol{\kappa}_0$ and polarization s_0, and $\omega = |\boldsymbol{\kappa}_0| c$ is the mode frequency. The electromagnetic field is assumed to occupy a single coherent mode with polarization vector $\boldsymbol{\epsilon}_0$ and is described by a coherent state $|\alpha(t)\rangle$, since it is the state of a quantum oscillator that most closely approximates the classical description.

In the Coulomb gauge, the interaction Hamiltonian has the form:

$$\hat{H}_{\text{int}} = \frac{1}{c}\int d^3r\hat{\psi}^\dagger(\mathbf{r})\left(\hat{\mathbf{A}}_{\text{em}}(\mathbf{r})\cdot\mathbf{p}\right)\hat{\psi}(\mathbf{r}), \tag{2.30}$$

where $\hat{\mathbf{A}}_{\text{em}}(\mathbf{r})$ is the vector potential operator of the electromagnetic field, which is usually expanded into plane waves as

$$\hat{\mathbf{A}}_{\text{em}}(\mathbf{r}) = \sum_{\boldsymbol{\kappa},s}\sqrt{\frac{2\pi c^2}{V\omega_{\boldsymbol{\kappa}}}}\left(\hat{a}_{\boldsymbol{\kappa},s}\boldsymbol{\epsilon}_{\boldsymbol{\kappa},s}e^{i\boldsymbol{\kappa}\mathbf{r}} + \hat{a}^\dagger_{\boldsymbol{\kappa},s}\boldsymbol{\epsilon}^*_{\boldsymbol{\kappa},s}e^{-i\boldsymbol{\kappa}\mathbf{r}}\right). \tag{2.31}$$

The Hamiltonian $\hat{H}_{\text{el}-\text{em}}$ can be represented as a matrix in the basis of product states formed by many-body eigenstates $|\Phi_n\rangle$ of electronic Hamiltonian $\hat{H}_{\text{el}}$ and Fock states of the mode $(\boldsymbol{\kappa}_0, s_0)$, $|\Phi_n\rangle\,|N-\mu\rangle$. Here μ is an integer and N approximates the average number of photons in the mode $(\boldsymbol{\kappa}_0, s_0)$: $\langle\alpha(t)|\,\hat{a}^\dagger_{\boldsymbol{\kappa}_0,s_0}\hat{a}_{\boldsymbol{\kappa}_0,s_0}\,|\alpha(t)\rangle$; μ is related to the number of photons involved in the interaction between the electronic system and electromagnetic field with $-\mu_{\max} \leq \mu \leq \mu_{\max}$.

In the basis of states $|\Phi_n\rangle\,|N-\mu\rangle$, both $\hat{H}_{\text{el}}$ and $\hat{H}_{\text{em}}$ are diagonal. In the matrix representation of $\hat{H}_{\text{el}-\text{em}}$ the similarities with the Floquet Hamiltonian defined with its matrix elements in Eq. (2.24) become apparent

$$\begin{aligned}\langle\Phi_m|\,\langle N-\mu'|\,\hat{H}_{\text{el}-\text{em}}\,|\Phi_n\rangle\,|N-\mu\rangle = (E_{\Phi_n} + (N-\mu)\omega)\delta_{\mu'\mu}\delta_{nm} \\ + \langle\Phi_m|\,\langle N-\mu'|\,\hat{H}_{\text{int}}\,|\Phi_n\rangle\,|N-\mu\rangle\,.\end{aligned} \tag{2.32}$$

The difference between the Hamiltonian $\hat{H}_{\text{F}}$ and $\hat{H}_{\text{el}-\text{em}}$ is that the off-diagonal elements of $\hat{H}_{\text{el}-\text{em}}$ depend on μ; they are proportional to the $\sqrt{\mu}$ since $\hat{H}_{\text{int}}$ is proportional to the annihilation operator, whereas those of $\hat{H}_{\text{F}}$ do not. However, when considering $\hat{H}_{\text{el}-\text{em}}$ in the vicinity of a large photon number N, the variation of the matrix elements of $\hat{H}_{\text{int}}$ with μ becomes only of order $1/N$. Thus, one can approximate:

$$\hat{H}_{\text{el}-\text{em}} \approx \hat{H}_{\text{F}} + N\omega\hat{\mathbb{1}}, \tag{2.33}$$

this holds for photon numbers close to N. In this limit of a large photon number N, one can associate the quantum problem with its semiclassical limit.

The eigenstates of the Hamiltonian $\hat{H}_{\text{el}-\text{em}}$ can be represented as a superposition

$$|\Psi_K\rangle = \sum_{n,\mu} C^K_{n\mu}\,|\Phi_n\rangle\,|N-\mu\rangle\,, \tag{2.34}$$

which gives rise to the generalized stationary states of the time-dependent Schrodinger equation with the Hamiltonian $\hat{H}_{\text{el}-\text{em}}$, similar to the Floquet modes defined by Eq. (2.4).

Under the assumption that the electromagnetic field's state is not changed by its interaction with the electronic system, the solution can be represented as the product $|\Psi(t)\rangle = |\Psi_{\mathrm{el}}(t)\rangle\,|\alpha(t)\rangle$, precisely [67]:

$$|\Psi(t)\rangle = \sum_K C_K e^{-i\mathcal{E}_K t}\,|\Theta_K(t)\rangle\,, \tag{2.35}$$

where superposition

$$|\Theta_K(t)\rangle = \sum_{n,\mu} C^K_{n\mu} e^{-i\mu\omega t}\,|\Phi_n\rangle\,|\alpha(t)\rangle\,, \tag{2.36}$$

involves physically equivalent Floquet states with energies $\mathcal{E}_{K_{\Delta\mu}} = \mathcal{E}_K + \Delta\mu\omega$.

2.2.1. Jaynes–Cummings model

We use a two-level atom interacting with a quantized mode of an optical cavity as an example of a physical system described by the Hamiltonian in Eq. (2.28). This system is particularly studied within the framework of the Jaynes–Cummings model [132]. The model was originally developed to investigate the interaction between atoms and the quantized electromagnetic field, especially spontaneous emission and photon absorption processes in a cavity. In this model, RWA is applied to eliminate counter-rotating terms, simplifying the system into an exactly solvable form with dressed-state eigenstates. Importantly, we will demonstrate that the energy spectrum obtained in the Jaynes–Cummings model under RWA and near-resonance conditions is equivalent to the quasienergy spectrum of a two-level system driven by a circularly polarized classical field, as in Eq. (2.10). The Hamiltonian for the atom–field system has the form:

$$\hat{H} = \hat{H}_{\mathrm{A}} + \hat{H}_{\mathrm{F}} + \hat{H}_{\mathrm{AF}}, \tag{2.37}$$

where the Hamiltonian of the atom $\hat{H}_{\mathrm{A}}$ is

$$\hat{H}_{\mathrm{A}} = E_g\,|g\rangle\,\langle g| + E_e\,|e\rangle\,\langle e| \tag{2.38}$$

and includes the ground state $|g\rangle$ and the excited state $|e\rangle$. Setting the energy of the ground state to zero simplifies this to

$$\hat{H}_{\mathrm{A}} = E_e\,|e\rangle\,\langle e| = \omega_{eg}\,|e\rangle\,\langle e|\,, \tag{2.39}$$

where ω_{eg} is the resonance frequency of transitions between the sublevels of the atom.

The Hamiltonian of the quantized electromagnetic field $\hat{H}_{\mathrm{F}}$ is

$$\hat{H}_{\mathrm{F}} = \omega_{\mathrm{c}}\left(\hat{a}^\dagger_{\mathrm{c}}\hat{a}_{\mathrm{c}} + \frac{1}{2}\right), \tag{2.40}$$

where the operators $\hat{a}_c^\dagger$ and $\hat{a}_c$ are the photon creation and annihilation operators, and the subscript c indicates that we are considering only the resonant mode of the cavity.

In the Jaynes–Cummings model, the interaction Hamiltonian $\hat{H}_{AF}$ represents the coupling between the atomic dipole and a single mode of the electromagnetic field within a cavity. The interaction Hamiltonian is thus given by

$$\hat{H}_{AF} = -\hat{\mathbf{d}} \cdot \hat{\mathbf{E}}(\mathbf{R}), \tag{2.41}$$

where $\mathbf{R}$ denotes the atomic position. We simplify the expression for the electric field operator at the position of the atom as follows:

$$\hat{\mathbf{E}}(\mathbf{R}) = i\sqrt{\frac{2\pi\omega_c}{V}}\left(\hat{a}_c e^{i\mathbf{k}_c\cdot\mathbf{R}} - \hat{a}_c^\dagger e^{-i\mathbf{k}_c\cdot\mathbf{R}}\right), \tag{2.42}$$

with $\mathbf{k}_c$ and ω_c being the wavevector and frequency of the cavity mode, respectively. Further, we assume that the atomic position is to be at the origin. The dipole operator is expressed as

$$\hat{\mathbf{d}} = \hat{\sigma}_+ \langle e|\,\hat{\mathbf{d}}\,|g\rangle + \hat{\sigma}_- \langle g|\,\hat{\mathbf{d}}\,|e\rangle, \tag{2.43}$$

where $\hat{\sigma}_+ = |e\rangle\langle g|$ and $\hat{\sigma}_- = |g\rangle\langle e|$ are the raising and lowering operators acting in the $\{|e\rangle, |g\rangle\}$ subspace of the atom. We define the coupling constant for the cavity mode as follows:

$$g_c = i\sqrt{\frac{2\pi\omega_c}{V}}\langle e|\hat{\mathbf{d}}|g\rangle. \tag{2.44}$$

This results in an interaction Hamiltonian of the following form:

$$\hat{H}_{AF} = g_c\hat{\sigma}_+\hat{a}_c - g_c^*\hat{\sigma}_-\hat{a}_c^\dagger - g_c\hat{\sigma}_+\hat{a}_c^\dagger + g_c^*\hat{\sigma}_-\hat{a}_c. \tag{2.45}$$

Transitioning to the co-rotating frame simplifies the analysis by allowing the introduction of some assumptions about the interaction Hamiltonian $\hat{H}_{AF}$. This is achieved by using the interaction picture, where the Hamiltonian for noninteracting parts is $\hat{H}_0 = \hat{H}_A + \hat{H}_F$. The interaction Hamiltonian in the interaction picture is computed as

$$\hat{H}_{AF}(t) = e^{i\hat{H}_0 t}\hat{H}_{AF}e^{-i\hat{H}_0 t} \tag{2.46}$$

and becomes

$$\begin{aligned}\hat{H}_{AF}(t) = {} & g_c\hat{\sigma}_+\hat{a}_c^\dagger e^{i(\omega_c+\omega_{eg})t} + g_c^*\hat{\sigma}_-\hat{a}_c e^{-i(\omega_c+\omega_{eg})t} \\ & - g_c^*\hat{\sigma}_-\hat{a}_c^\dagger e^{-i(\omega_{eg}-\omega_c)t} - g_c\hat{\sigma}_+\hat{a}_c e^{i(\omega_{eg}-\omega_c)t}.\end{aligned} \tag{2.47}$$

We now assume that the resonance frequency of the cavity is near the transition frequency of the atom. Under this condition, the exponential terms oscillating at $\omega_{eg} - \omega_c \simeq 0$ are nearly resonant, while the other exponential terms oscillating at $\omega_{eg} + \omega_c \simeq 2\omega_c$ are nearly

antiresonant. The net effect of the quickly oscillating antiresonant terms tends to average to zero for the timescales of the resonant behavior. We may thus neglect the antiresonant terms altogether, since their value is negligible compared to that of the nearly resonant terms. This approximation is known as the RWA. The interaction Hamiltonian, assuming g_c is real for simplicity, becomes

$$\hat{H}_{\mathrm{AF}}(t) = -g_c \left(\hat{\sigma}_+ \hat{a}_c e^{i(\omega_{eg}-\omega_c)t} + \hat{\sigma}_- \hat{a}_c^\dagger e^{-i(\omega_{eg}-\omega_c)t} \right). \tag{2.48}$$

In the Schrödinger picture, the interaction Hamiltonian reads

$$\hat{H}_{\mathrm{AF}} = e^{-i\hat{H}_0 t} \hat{H}_{\mathrm{AF}}(t) e^{i\hat{H}_0 t} = g_c \left(\hat{\sigma}_+ \hat{a}_c + \hat{\sigma}_- \hat{a}_c^\dagger \right). \tag{2.49}$$

Using the results above, the full Jaynes–Cummings Hamiltonian is given by

$$\hat{H}_{\mathrm{JC}} = \omega_c \hat{a}_c^\dagger \hat{a}_c + \omega_{eg} |e\rangle\langle e| + g_c \left(\hat{\sigma}_+ \hat{a}_c + \hat{\sigma}_- \hat{a}_c^\dagger \right), \tag{2.50}$$

omitting the constant term $\frac{1}{2}\omega_c$, which represents the zero-point energy of the field. We define the basis of tensor product states $\{|g,0\rangle; |e,0\rangle, |g,1\rangle; \cdots; |e,n-1\rangle, |g,n\rangle\}$, where the states $\{|n\rangle\}$ of the field are those with a definite number n of photons. In this basis, the Hamiltonian takes on a block-diagonal structure

$$\hat{H}_{\mathrm{JC}} = \begin{bmatrix} H_0 & 0 & 0 & 0 & \cdots & \cdots & \cdots \\ 0 & \hat{H}_1 & 0 & 0 & \ddots & \ddots & \ddots \\ 0 & 0 & \hat{H}_2 & 0 & \ddots & \ddots & \ddots \\ \vdots & \ddots & \ddots & \ddots & \ddots & \ddots & \ddots \\ \vdots & \ddots & \ddots & 0 & \hat{H}_n & 0 & \ddots \\ \vdots & \ddots & \ddots & \ddots & \ddots & \ddots & \ddots \end{bmatrix}. \tag{2.51}$$

Each block $\hat{H}_n$ on the diagonal is itself a 2×2 matrix of the form

$$\hat{H}_n = \begin{bmatrix} \omega_c(n-1) + \omega_{eg} & \langle e, n-1 | \hat{H}_{\mathrm{JC}} | g, n \rangle \\ \langle g, n | \hat{H}_{\mathrm{JC}} | e, n-1 \rangle & n\omega_c \end{bmatrix}. \tag{2.52}$$

The matrix elements of the interaction Hamiltonian in Eq. (2.49) are

$$\langle g, n | \hat{H}_{\mathrm{JC}} | e, n-1 \rangle = g_c \langle g, n | \hat{a}_c^\dagger \hat{\sigma}_- | e, n-1 \rangle + g_c \langle g, n | \hat{a}_c \hat{\sigma}_+ | e, n-1 \rangle = \sqrt{n} g_c. \tag{2.53}$$

Thus, we obtain the part of the Hamiltonian that acts in the nth subspace as

$$\hat{H}_n = \begin{bmatrix} n\omega_c - \frac{1}{2}\Delta & \frac{\sqrt{n}\Omega}{2} \\ \frac{\sqrt{n}\Omega}{2} & n\omega_c + \frac{1}{2}\Delta \end{bmatrix}, \tag{2.54}$$

where we have identified $2g_c = \Omega$ as the Rabi frequency of the system, and $\Delta = \omega_c - \omega_{eg}$ is the so-called "detuning" between the frequencies of the cavity and atomic transition.

This simple 2×2 Hamiltonian is of the same form as that found in the Rabi problem for the Hamiltonian in Eq. (2.9). Diagonalization gives the energy eigenvalues

$$\mathcal{E}_{n,\pm} = \left(n\omega_c - \frac{1}{2}\Delta\right) \pm \frac{1}{2}\sqrt{\Delta^2 + n\Omega^2} \tag{2.55}$$

which correspond to the eigenstates

$$|n,+\rangle = \cos\left(\frac{\theta_n}{2}\right)|e,n-1\rangle + \sin\left(\frac{\theta_n}{2}\right)|g,n\rangle \tag{2.56}$$

$$|n,-\rangle = \cos\left(\frac{\theta_n}{2}\right)|g,n\rangle - \sin\left(\frac{\theta_n}{2}\right)|e,n-1\rangle \tag{2.57}$$

where the angle θ_n is defined by the relation $\tan\theta_n = -\frac{\sqrt{n}\Omega}{\Delta}$.

2.3. Floquet–Bloch theory

Throughout this thesis, we consider a spatially periodic material as an example of a quantum system under study. The extension of the Floquet theory to the case of a spatially periodic system is called the Floquet–Bloch theory. Before introducing it, let us briefly review Bloch's theorem.

2.3.1. Bloch states and band structure

In the ground state of the material, without external perturbation, the crystal is described by the field-free Hamiltonian $\hat{H}_0$:

$$\hat{H}_0 = -\frac{\nabla^2}{2} + \hat{V}_c(\mathbf{r}), \tag{2.58}$$

where $\hat{V}_c(\mathbf{r})$ is a space-periodic crystal potential satisfying $\hat{V}_c(\mathbf{r}+\mathbf{R}) = \hat{V}_c(\mathbf{r})$, and $\mathbf{R}$ is the lattice vector. The Bloch theorem [125] states that solutions to the Schrödinger equation with the Hamiltonian in Eq. (2.58) can be expressed as plane waves modulated by periodic functions as follows:

$$\varphi_{n\mathbf{k}}(\mathbf{r}) = e^{i\mathbf{k}\cdot\mathbf{r}} u_{n\mathbf{k}}(\mathbf{r}). \tag{2.59}$$

Here, $u_{n\mathbf{k}}(\mathbf{r}) = u_{n\mathbf{k}}(\mathbf{r}+\mathbf{R})$ are the Bloch modes with the band index n and the Bloch wave vector $\mathbf{k}$. The corresponding stationary Schrödinger equation

$$\hat{H}_0\varphi_{n\mathbf{k}}(\mathbf{r}) = E_{n\mathbf{k}}\varphi_{n\mathbf{k}}(\mathbf{r}), \tag{2.60}$$

gives the energy $E_{n\mathbf{k}}$ of the Bloch state $\varphi_{n\mathbf{k}}(\mathbf{r})$, representing the energy dispersion relation for the nth electronic band.

2.3.2. Floquet–Bloch states and quasienergy band structure

Consider the problem of a solid interacting with an electromagnetic field. Since the wavelengths for an optical field are much larger than the lattice parameter, the field can be considered as spatially uniform on the lattice size. The time-dependent Hamiltonian $\hat{\mathcal{H}}(t)$, for a crystal in the presence of a spatially uniform and temporally periodic electric field $\mathbf{E}(t) = \mathbf{F}_0 \sin(\omega t)$, is then given by

$$\hat{\mathcal{H}}(t) = \frac{1}{2}\left(\hat{\mathbf{p}} + \frac{1}{c}\mathbf{A}(t)\right)^2 + V_c(\mathbf{r}), \tag{2.61}$$

where the vector potential $\mathbf{A}(t)$ is defined as

$$\mathbf{A}(t) = \frac{c\mathbf{F}_0}{\omega}\cos(\omega t). \tag{2.62}$$

A unitary transformation is used to eliminate the $\mathbf{A}^2(t)$ term in $\mathcal{H}(t)$. Upon this unitary transformation, the time-dependent Hamiltonian $\hat{H}(t)$ that we have to consider now becomes

$$\hat{H}(t) = \hat{H}_0 + \frac{1}{c}\mathbf{A}(t)\cdot\hat{\mathbf{p}}, \tag{2.63}$$

where $\hat{H}_0$ is the field-free Hamiltonian defined in Eq. (2.58).

The Hamiltonian in Eq. (2.63) is periodic in both space and time. Based on the Floquet–Bloch theorem, the steady-state solution of the time-dependent Schrodinger equation

$$i\frac{d}{dt}\Psi(\mathbf{r},t) = \hat{H}(t)\Psi(\mathbf{r},t) \tag{2.64}$$

can be written as [67, 120, 133–136]

$$\Psi_{i\mathbf{k}}(\mathbf{r},t) = \frac{1}{\sqrt{V}}e^{-i\mathcal{E}_{i\mathbf{k}}t}e^{i\mathbf{k}\mathbf{r}}\Phi_{i\mathbf{k}}(\mathbf{r},t). \tag{2.65}$$

Here, $\Phi_{i\mathbf{k}}(\mathbf{r},t)$ is the Floquet–Bloch mode with band index i, quasimomentum $\mathbf{k}$, and quasienergy $\mathcal{E}_{i\mathbf{k}}$. These modes are periodic in both time and space, satisfying $\Phi_{i\mathbf{k}}(\mathbf{r},t+T) = \Phi_{i\mathbf{k}}(\mathbf{r}+\mathbf{R},t) = \Phi_{i\mathbf{k}}(\mathbf{r},t)$. They are the eigenstates of the effective Floquet–Bloch Hamiltonian $\hat{H}_\mathrm{F}(\mathbf{k})$

$$\hat{H}_\mathrm{F}(\mathbf{k})\Phi_{i\mathbf{k}}(\mathbf{r},t) = \mathcal{E}_{i\mathbf{k}}\Phi_{i\mathbf{k}}(\mathbf{r},t), \tag{2.66}$$

where $H_\mathrm{F}(\mathbf{k})$ is given by [133–135]

$$\hat{H}_\mathrm{F}(\mathbf{k}) = \hat{H}_0(\mathbf{k}) + \mathbf{F}_0\cdot(\mathbf{k}+\hat{\mathbf{p}})\cos(\omega t) - i\frac{\partial}{\partial t}. \tag{2.67}$$

Solving the eigenvalue problem in Eq. (2.66) requires an appropriate basis set that contains both space and time. The Floquet–Bloch modes can be expanded in terms of their time Fourier components and the whole set of Bloch states due to their time and space periodicity as follows:

$$\Phi_{i\mathbf{k}}(\mathbf{r},t) = \sum_{\mu=-\infty}^{+\infty} \sum_{n} C^{i}_{n\mathbf{k}\mu} e^{-i\mu\omega t} u_{n\mathbf{k}}(\mathbf{r}), \tag{2.68}$$

where $u_{n\mathbf{k}}(\mathbf{r})$ represents the periodic part of the Bloch wavefunction and $C^{i}_{n\mathbf{k}\mu}$ are coefficients to be determined.

We introduce the basis states in the extended Hilbert space $|\mathbf{k}, n, \mu\rangle\rangle$ such that

$$\langle \mathbf{r}, t|\mathbf{k}, n, \mu\rangle = e^{i\mu\omega t} u_{n\mathbf{k}}(\mathbf{r}), \tag{2.69}$$

and the inner product

$$\langle\langle \mathbf{k}, n, \mu|\mathbf{k}, n', \mu'\rangle\rangle = \int_0^{2\pi/\omega} dt \int d\mathbf{r}\, e^{-i\mu\omega t} u^{*}_{n\mathbf{k}}(\mathbf{r}) e^{i\mu'\omega t} u_{n'\mathbf{k}}(\mathbf{r}). \tag{2.70}$$

Using the definition of the basis $|\mathbf{k}, n, \mu\rangle\rangle$, we can convert a time-dependent differential equation Eq. (2.66) into a time-independent eigenvalue equation

$$\sum_{n',\mu'} \langle\langle \mathbf{k}, n, \mu|\, H_{\mathrm{F}}(\mathbf{k})\, |\mathbf{k}, n', \mu'\rangle\rangle C_{n'\mathbf{k}\mu'} = \mathcal{E}_{\mathbf{k}} C_{n\mathbf{k}\mu}. \tag{2.71}$$

In this basis the matrix elements of $H_{\mathrm{F}}(\mathbf{k})$ can be written as [133–135]

$$\begin{aligned} \langle\langle \mathbf{k}, n, \mu|\, H_{\mathrm{F}}(\mathbf{k})\, |\mathbf{k}, n', \mu'\rangle\rangle = {} & (E_{n\mathbf{k}} + \mu\omega)\, \delta_{n,n'}\delta_{\mu,\mu'} \\ & + \frac{\mathbf{F}_0}{2\omega} \cdot (\mathbf{k}\delta_{n,n'} + \mathbf{D}_{n,n'}(\mathbf{k}))\, (\delta_{\mu,\mu'+1} + \delta_{\mu,\mu'-1}), \end{aligned} \tag{2.72}$$

where the matrix $\mathbf{D}_{n,n'}(\mathbf{k})$ is defined as

$$\mathbf{D}_{n,n'}(\mathbf{k}) = -i \int d\mathbf{r}\, u^{*}_{n\mathbf{k}}(\mathbf{r}) \boldsymbol{\nabla} u_{n'\mathbf{k}}(\mathbf{r}). \tag{2.73}$$

The solution of the matrix equation (2.71) gives the coefficients $C_{n\mathbf{k}\mu}$ of $\Phi_{i\mathbf{k}}(\mathbf{r},t)$; the Floquet–Bloch states $\Phi_{i\mathbf{k}}(\mathbf{r},t)$ can then be found by using Eq. (2.65),(2.68). Similar to the Floquet states in Eq. (2.17), two Floquet–Bloch states at a given $\mathbf{k}$-point with quasienergies differing by ω are physically equivalent. Therefore, physically different Floquet–Bloch states can be chosen all in the energy range of $-\frac{\omega}{2} \leq \mathcal{E}_{i\mathbf{k}} < \frac{\omega}{2}$, which is usually referred to as the Floquet–Brillouin zone [133–135].

When the external field vanishes, the Floquet matrix in the Eq. (2.72) is diagonal, and the quasienergy is equal to $\mathcal{E}_{i\mathbf{k}} = E_{i\mathbf{k}} + \mu\omega$ for all $\mathbf{k}$-points. Thus, the quasienergies $\mathcal{E}_{i\mathbf{k}}$ correspond to the field-free energies of $E_{i\mathbf{k}}$ folded onto the Floquet–Brillouin zone in the

vanishing field limit. In this limit, the time-dependent Floquet–Bloch states are equal to the time-independent Bloch states multiplied by a phase factor, namely, $\Psi_{i\mathbf{k}}(\mathbf{r},t) = \frac{1}{\sqrt{V}} e^{-i\mathcal{E}_{i\mathbf{k}}t} e^{-\mathbf{k}\mathbf{r}} u_{i\mathbf{k}}(\mathbf{r})$, with $\mathcal{E}_{i\mathbf{k}} = E_{i\mathbf{k}} + \mu\omega$, and the mean quasienergy $\langle \mathcal{E}_{i\mathbf{k}} \rangle$ given by the field-free eigenenergy $E_{i\mathbf{k}}$. When an external field is applied, the quasienergy and mean energy band structure deviate from the field-free band structure[133–135].

2.3.3. Floquet–Bloch theory in quantum electrodynamics

We briefly review the Floquet–Bloch formalism in the second quantization, which is used to describe the interaction of a strong driving field with a crystal [67, 120, 136]. We introduce this representation in order to describe the interaction between a laser-dressed crystal and an ultrashort x-ray pulse within the quantum electrodynamics in the next chapters. The total Hamiltonian describing the interaction between electrons in a crystalline solid and an electromagnetic field is given by

$$\hat{H}_{\text{el-em}} = \hat{H}_{\text{el}} + \hat{H}_{\text{int}} + \hat{H}_{\text{em}}. \tag{2.74}$$

Here, $\hat{H}_{\text{el}}$ is the electronic Hamiltonian of the unperturbed crystal, $\hat{H}_{\text{em}}$ is the electromagnetic field Hamiltonian, and $\hat{H}_{\text{int}}$ describes the interaction between the electrons and the external field.

The electronic Hamiltonian in second quantization reads

$$\hat{H}_{\text{el}} = \int d^3\mathbf{r}\, \hat{\psi}^\dagger(\mathbf{r}) \left[\frac{\hat{\mathbf{p}}^2}{2} + \hat{V}_c(\mathbf{r}) \right] \hat{\psi}(\mathbf{r}), \tag{2.75}$$

where $\hat{\psi}^\dagger(\mathbf{r})$ and $\hat{\psi}(\mathbf{r})$ are the fermionic field creation and annihilation operators, respectively, and $\hat{\mathbf{p}}$ is the canonical momentum operator. The potential $\hat{V}_{\text{c}}(\mathbf{r}) = \hat{V}_{\text{c}}(\mathbf{r}+\mathbf{R})$ represents the periodic mean-field crystal potential, with $\mathbf{R}$ a lattice vector. According to Bloch's theorem, the single-particle eigenstates $|\varphi_{n\mathbf{k}}\rangle$ take the form

$$\varphi_{n\mathbf{k}}(\mathbf{r}) = e^{i\mathbf{k}\cdot\mathbf{r}} u_{n\mathbf{k}}(\mathbf{r}), \tag{2.76}$$

where $u_{n\mathbf{k}}(\mathbf{r}) = u_{n\mathbf{k}}(\mathbf{r}+\mathbf{R})$ is a lattice-periodic function with the Bloch wave vector $\mathbf{k}$ and the band and spin index n.

The electromagnetic field is described by a single mode Hamiltonian

$$\hat{H}_{\text{em}} = \omega\, \hat{a}^\dagger_{\boldsymbol{\kappa}_0,s_0} \hat{a}_{\boldsymbol{\kappa}_0,s_0}, \tag{2.77}$$

where $\hat{a}^\dagger_{\boldsymbol{\kappa}_0,s_0}$ and $\hat{a}_{\boldsymbol{\kappa}_0,s_0}$ are the photon creation and annihilation operators for the mode with wave vector $\boldsymbol{\kappa}_0$ and polarization s_0, and $\omega = |\boldsymbol{\kappa}_0|c$ is the mode frequency. The electromagnetic field is assumed to occupy a single coherent mode with polarization vector $\boldsymbol{\epsilon}_0$ and is described by a coherent state $|\alpha(t)\rangle$.

In the minimal coupling, the interaction between the electrons and the electromagnetic field is given by

$$\hat{H}_{\text{int}} = \frac{1}{c} \int d^3\mathbf{r}\, \hat{\psi}^\dagger(\mathbf{r}) \left(\hat{\mathbf{A}}_{\text{em}}(\mathbf{r}) \cdot \hat{\mathbf{p}}\right) \hat{\psi}(\mathbf{r}), \tag{2.78}$$

where $\hat{\mathbf{A}}_{\text{em}}(\mathbf{r})$ is the quantized vector potential operator of the electromagnetic field. In the following, the $\hat{\mathbf{A}}^2_{\text{em}}(\mathbf{r})$ term is neglected, which is valid for moderate optical field strengths.

We assume that the state of the electromagnetic field $|\alpha(t)\rangle$ remains unchanged by the interaction with the electronic system. Under this assumption, the one-body solution of the time-dependent Schrödinger equation $\mathrm{i}\frac{d}{dt}|\psi_{i\mathbf{k}}(t)\rangle = \hat{H}_{\text{el-em}}|\psi_{i\mathbf{k}}(t)\rangle$ can be represented as the product $|\psi_{i\mathbf{k}}(t)\rangle = |\phi^{\text{el}}_{i\mathbf{k}}(t)\rangle\,|\alpha(t)\rangle$. The corresponding electronic one-body Floquet–Bloch wavefunction is defined as follows:

$$\phi^{\text{el}}_{i\mathbf{k}}(\mathbf{r}, t) = \sum_{n,\mu} c^i_{n\mathbf{k}\mu} e^{-\mathrm{i}\mu\omega t} \varphi_{n\mathbf{k}}(\mathbf{r}), \tag{2.79}$$

where $c^i_{\mathbf{k}m\mu}$ are expansion coefficients with the integer μ.

The electron density of the laser-dressed system evolves in time as

$$\rho(\mathbf{r}, t) = \sum_{\mu} e^{\mathrm{i}\mu\omega t} \tilde{\rho}_\mu(\mathbf{r}) \tag{2.80}$$

with μth-order density amplitudes

$$\tilde{\rho}_\mu(r) = \int_{\text{BZ}} d^3k \frac{V_{\text{cell}}}{(2\pi)^3} \sum_i \sum_{n,n',\mu'} c^{i*}_{n'\mathbf{k}\mu'+\mu} c^i_{n\mathbf{k}\mu'} u^\dagger_{n'\mathbf{k}}(\mathbf{r}) u_{n\mathbf{k}}(\mathbf{r}), \tag{2.81}$$

where V_{cell} is the volume of a unit cell, i denotes the index of occupied one-body Floquet–Bloch states, and the integration is over the Brillouin zone (BZ). The μth-order density amplitude describes the μth-order macroscopic optical response of a material. For example, the polarization can be calculated from the time-dependent electron density, and thus the μth-order amplitude of the polarization is connected to the μth-order density amplitude. Further, the amplitudes $\tilde{\rho}_\mu(\mathbf{r})$ are referred to as optically induced charge distributions.

2.4. Numerical implementation

The calculations presented throughout this thesis are based on an *ab initio* computational framework that combines the Floquet–Bloch formalism with DFT. The DFT is used to obtain the one-body wavefunctions $\varphi_{n\mathbf{k}}(\mathbf{r})$ of the field-free Hamiltonian $H^{(0)}$, which describe the ground state of the material. The following section outlines the key elements of the DFT approach used to calculate the ground state, including the choice of basis set and the treatment of core states as it is implemented in the `exciting` [137].

In DFT, the complex problem of many interacting electrons is simplified by reducing it to a calculation of electron density. This density depends on three spatial coordinates and the spin of the electron. The many-body problem is transformed into an equivalent problem for noninteracting quasiparticles within an effective potential satisfying the Kohn–Sham equation, which is the central equation of DFT

$$\left(-1/2\boldsymbol{\nabla}^2 + V_{\text{eff}}(\mathbf{r})\right) \varphi_{n\mathbf{k}}(\mathbf{r}) = E_{n\mathbf{k}}\varphi_{n\mathbf{k}}(\mathbf{r}), \tag{2.82}$$

where $\varphi_{n\mathbf{k}}(\mathbf{r})$, $E_{n\mathbf{k}}$, and $V_{\text{eff}}(\mathbf{r})$ are the wavefunctions, eigenenergies, and effective potential of the Kohn–Sham system.

A major challenge in applying DFT to solids is finding an efficient way to represent electron wavefunctions. These functions are smooth between atoms but vary strongly near nuclei. Core states localize near nuclei, whereas valence wavefunctions oscillate rapidly to maintain orthogonality. The most common approach for addressing numerical challenges in the core region is the use of pseudopotentials or projectors [96]. These methods typically replace the effect of core electrons and their nucleus with an effective potential, or pseudopotential, and formulate the Kohn–Sham equation for smooth pseudo-wavefunctions of valence electrons. Iterative diagonalization algorithms are highly efficient, even with a large number of plane waves or grid points. However, the approximations employed in the formulation of pseudopotentials or projectors result in an oversimplified representation of the effect of core states in these methods.

2.4.1. Pseudopotential treatment

The pseudopotential approach is based on the idea of replacing the effect of the atomic core, which consists of the nucleus and tightly bound core electrons, with a smoother, effective potential that acts only on the valence electrons. This means that the chemically active valence electrons are treated explicitly, while the core electrons are 'frozen' and considered together with the nuclei as rigid, non-polarizable ion cores. The resulting valence pseudo-wavefunctions are smoother than all-electron counterparts because they contain significantly fewer radial nodes in the core region. It makes plane-wave basis sets feasible in practice and reduces computational cost. Among the various forms of pseudopotentials, the most widely used are the norm-conserving [96] and ultrasoft pseudopotentials [138]. In this thesis, the pseudopotentials were generated following the Troullier–Martins scheme as it is implemented in the ABINIT software package [139–142].

2.4.2. Full-potential treatment

An alternative approach is to augment the plane-wave basis with localized, atomic-like functions around the nuclei, as done in the family of APW methods, which corresponds to

a full-potential treatment.

Augmented plane wave methods

An alternative approach is the family of APW methods, originally introduced by Slater [143]. APW retains a full representation of the core states, unlike pseudopotential methods. It divides space into two regions: atomic spheres and the interstitial space. Within the atomic spheres, wavefunctions are expanded in terms of atomic-like basis functions, while in the interstitial region, plane waves describe the wavefunctions. This dual representation improves accuracy and avoids the limitations of pseudopotentials [137]. In general, the Bloch state is given by

$$\varphi_{n\mathbf{k}}(\mathbf{r}) = \sum_{\mathbf{G}} C_{i\mathbf{G}}^{\mathbf{k}} e^{i(\mathbf{G}+\mathbf{k})\mathbf{r}} \equiv \sum_{\mathbf{G}} C_{i\mathbf{G}}^{\mathbf{k}} \phi_{\mathbf{G}+\mathbf{k}}(\mathbf{r}). \tag{2.83}$$

In the APW basis, basis functions $\phi_{\mathbf{G}+\mathbf{k}}(\mathbf{r})$ has different forms inside atomic spheres, muffin-tins (MTs), and in the space in between, the interstitial region, denoted as I

$$\phi_{\mathbf{G}+\mathbf{k}}(\mathbf{r}) = \begin{cases} \sum_{lm} A_{lm\alpha}^{\mathbf{G}+\mathbf{k}} u_{l\alpha}(r_\alpha) Y_{lm}(\hat{\mathbf{r}}_\alpha), r_\alpha \leq R_{\mathrm{MT}} \\ \frac{1}{\sqrt{\Omega}} e^{i(\mathbf{G}+\mathbf{k})\mathbf{r}}, \mathbf{r} \in \mathrm{I}. \end{cases} \tag{2.84}$$

Each plane wave in the second line of Eq. (2.84) is augmented in each MT by a function defined in the first line. The MTs are spheres of radii R_{MT} centered on atoms labeled α at positions $\mathbf{R}_\alpha$. The MT part of $\phi_{\mathbf{G}+\mathbf{k}}(\mathbf{r})$ is expanded in terms of spherical harmonics $Y_{lm}(\hat{\mathbf{r}}_\alpha)$ and radial functions $u_{l\alpha}(r_\alpha)$, with $\mathbf{r}_\alpha = \mathbf{r} - \mathbf{R}_\alpha$. Matching coefficients $A_{lm\alpha}^{\mathbf{G}+\mathbf{k}}$ ensure the continuity of the wavefunction at the sphere boundary. The resulting radial Schrödinger equation on function $u_{l\alpha}(r_\alpha)$ has the form

$$\left(-\frac{1}{2}\frac{d^2}{dr^2} + \frac{l(l+1)}{2r^2} + v_0(r) - E_{n\mathbf{k}}\right)(r u_{l\alpha}(r)) = 0. \tag{2.85}$$

In Eq. (2.85), the effective potential $V_{\mathrm{eff}}(\mathbf{r})$ is replaced by its spherical average $v_0(r)$. This assumes that proximity to the nucleus dominates the potential. We can use the introduced basis to solve the Kohn–Sham equation, which we can write in the matrix form as a generalized eigenvalue problem.

$$H^{\mathbf{k}} C^{\mathbf{k}} = E^{\mathbf{k}} S^{\mathbf{k}} C^{\mathbf{k}}, \tag{2.86}$$

where $H^{\mathbf{k}}$ and $S^{\mathbf{k}}$ are the Hamiltonian matrices and the overlap matrices with their elements being

$$H_{\mathbf{G}\mathbf{G}'}^{\mathbf{k}} = \langle \phi_{\mathbf{G}+\mathbf{k}} | -\frac{1}{2}\nabla^2 + v_0(r) | \phi_{\mathbf{G}'+\mathbf{k}} \rangle \tag{2.87}$$

and

$$S^{\mathbf{k}}_{\mathbf{G}\mathbf{G}'} = \langle \phi_{\mathbf{G}+\mathbf{k}} | \phi_{\mathbf{G}'+\mathbf{k}} \rangle \,. \tag{2.88}$$

The infinite sum over $\mathbf{G}$ in Eq. (2.83) is made finite by introducing a plane wave cutoff $G_{\max}$ such that $|\mathbf{G}+\mathbf{k}| < G_{\max}$ or dimensionless cutoff parameter $R_{\mathrm{MT}}G_{\max}$, where R_{MT} is the smallest MT radius. This is necessary because if the MT radius R_{MT} is reduced for a specific atom, the interstitial region now contains space where wavefunctions vary more rapidly. Thus, maintaining a consistent level of accuracy requires an increase in plane wave cutoff $G_{\max}$.

Linearized augmented plane wave method

The Kohn–Sham equation in the APW basis, as defined in Eq. (2.86), is nonlinear in energy. This nonlinearity arises because the Hamiltonian matrix $H^{\mathbf{k}}$ and the overlap matrix $S^{\mathbf{k}}$ depend on energy. This dependence occurs since basis functions $\phi_{\mathbf{G}+\mathbf{k}}(\mathbf{r})$ depend on the picked energy eigenvalue $E_{n\mathbf{k}}$, which is apparent from the definition of the radial function in Eq. (2.85).

Different approaches for linearization exist. One method assumes selecting a fixed energy value $E_{l\alpha}$ for each angular momentum l in Eq. (2.85) and keeping it the same during the calculation $u_{l\alpha}(r_\alpha; E) \approx u_{l\alpha}(r_\alpha; E_{l\alpha})$. However, this approach introduces two challenges. The first issue is that it cannot describe states with the same l but different principal quantum numbers. This limitation is significant when dealing with elements containing both valence and core electrons. A solution is to treat core and valence electrons separately. Core electrons are highly localized and generally do not interact with valence electrons. Therefore, their wavefunctions can be computed independently by solving Eq. (2.85), or more generally, the Dirac equation, with the reasonable boundary condition. This approach is suitable for deep core states. However, it is not a suitable method for semicore states, which have significant overlap with valence electron states or can not be considered as localized within MTs. The second limitation is the difference between the energy parameter $E_{l\alpha}$ and the eigenenergy E corresponding to a state of the l character. This mismatch introduces an error in the calculated wavefunctions of order $O(E_{l\alpha} - E)$ and in the band and total energies of order $O(E_{l\alpha} - E)^2$. Ideally, the energy parameters should closely match the corresponding eigenenergies. However, in practice, this is often impossible. Band dispersion and the splitting into bonding and antibonding states make it unlikely that $E_{l\alpha}$ will match all states with the l character at the same time.

This method for linearization, expressed as $u_{l\alpha}(r_\alpha; E) \approx u_{l\alpha}(r_\alpha; E_{l\alpha})$, can be improved by using the Taylor expansion of the function.

$$u_{l\alpha}(r_\alpha; E) \approx u_{l\alpha}(r_\alpha; E_{l\alpha}) + (E_{l\alpha} - E)u'_{l\alpha}(r_\alpha; E_{l\alpha}), \tag{2.89}$$

where $u'_{l\alpha}(r_\alpha; E_{l\alpha}) = \partial u_{l\alpha}(r_\alpha; E)/\partial E$. The leading correction to $u_{l\alpha}(r_\alpha; E_{l\alpha})$ has to be searched in the energy derivative $u'_{l\alpha}(r_\alpha; E_{l\alpha})$ if the radial functions are considered vectors in some linear space. This gives rise to the LAPW method introduced independently by Andersen [144], Koeling, and Arbman [145]. In the LAPW basis, the MT part is defined as

$$\phi_{\mathbf{G}+\mathbf{k}}(\mathbf{r}) = \sum_{lm} \left[A^{\mathbf{G}+\mathbf{k}}_{lm\alpha} u_{l\alpha}(r_\alpha; E_{l\alpha}) + B^{\mathbf{G}+\mathbf{k}}_{lm\alpha} u'_{l\alpha}(r_\alpha; E_{l\alpha}) \right] Y_{lm}(\hat{\mathbf{r}}_\alpha) \tag{2.90}$$

$A^{\mathbf{G}+\mathbf{k}}_{lm\alpha}$ and $B^{\mathbf{G}+\mathbf{k}}_{lm\alpha}$ are the matching coefficients that ensure continuity of the basis functions $\phi_{\mathbf{G}+\mathbf{k}}(\mathbf{r})$ and its spatial derivative at the MT boundary. Even though such an approach improves the error in the band and total energies, it remains unclear how to treat semicore states.

Description of the semicore states

Alternatively, in addition to the APW basis functions with fixed energy parameters, one can introduce a set of local orbitals (LOs). This approach leads to the APW+lo method, first introduced by Singh [146, 147]. In this method, the linearization of $u_{l\alpha}(r_\alpha; E)$ is achieved by augmenting APWs with additional basis functions [147]. These additional functions improve flexibility in representing wavefunctions, particularly for semicore and valence states

$$\phi_\mu(\mathbf{r}) = \begin{cases} \delta_{\alpha\mu}\delta_{ll_\mu}\delta_{mm_\mu} \left[a_\mu u_{l_\alpha}(r_\alpha; E_{l\alpha}) + b_\mu u'_{l_\alpha}(r_\alpha; E_{l\alpha}) \right] Y_{lm}(\hat{\mathbf{r}}_\alpha), & r \le R_{\mathrm{MT}} \\ 0, & r \in I. \end{cases} \tag{2.91}$$

The coefficients a_μ and b_μ ensure that the function is localized inside the MT, with the boundary condition $\phi_\mu(\mathbf{r}) = 0$ at the MT sphere, and is normalized as $\int_\Omega |\phi_\mu(\mathbf{r})|^2 d\mathbf{r} = 1$. The set of functions defined by Eq. (2.91) are non-zero strictly within one considered MT. In the APW+lo basis, the wavefunction is represented as

$$\varphi_{n\mathbf{k}}(\mathbf{r}) = \sum_{\mathbf{G}} C^{\mathbf{k}}_{i\mathbf{G}} \phi_{\mathbf{G}+\mathbf{k}}(\mathbf{r}) + \sum_\mu C^{\mathbf{k}}_{i\mu} \phi_\mu(\mathbf{r}). \tag{2.92}$$

The wavefunction within the MT enclosing atom α is given by

$$\begin{aligned} \varphi_{n\mathbf{k}}(\mathbf{r}) = &\sum_{\mathbf{G}} \sum_{lm} C^{\mathbf{k}}_{n\mathbf{G}} A^{\mathbf{G}+\mathbf{k}}_{lm\alpha} u_{l\alpha}(r_\alpha; E_{l\alpha}) Y_{lm}(\hat{\mathbf{r}}_\alpha) \\ &+ \sum_\mu \sum_{lm} C^{\mathbf{k}}_{n\mu} \left[a_\mu u_{l\alpha}(r_\alpha; E_{l\alpha}) + b_\mu u'_{l\alpha}(r_\alpha; E_{l\alpha}) \right] Y_{lm}(\hat{\mathbf{r}}_\alpha) \delta_{\alpha\mu}\delta_{ll_\mu}\delta_{mm_\mu}. \end{aligned} \tag{2.93}$$

A more compact form is

$$\varphi_{n\mathbf{k}}(\mathbf{r}) = \sum_{lm} \left[c^{n\mathbf{k}}_{lm} u_{l\alpha}(r_\alpha; E_{l\alpha}) + d^{n\mathbf{k}}_{lm} u'_{l\alpha}(r_\alpha; E_{l\alpha}) \right] Y_{lm}(\hat{\mathbf{r}}_\alpha), \tag{2.94}$$

where $c_{lm}^{n\mathbf{k}}$ and $d_{lm}^{n\mathbf{k}}$ incorporate the corresponding coefficients from Eq.(2.93). In the LAPW basis, $\varphi_{n\mathbf{k}}(\mathbf{r})$ also follows Eq.(2.94), but the coefficients are further constrained by the smoothness condition for the basis functions. The APW+lo method provides greater flexibility, leading to a smaller linearization error compared to LAPW, though both methods have the same error order for total energy. The error can be further reduced if we consider the Taylor expansion of $u_{l\alpha}(r_\alpha; E)$, truncated after the higher-order terms.

LOs are particularly useful for describing semicore states and were originally introduced for this purpose, [146]. Consider LOs defined as

$$\phi_\mu(r) = \delta_{\alpha\mu}\delta_{ll_\mu}\delta_{mm_\mu}\left[a_\mu u_{l\alpha}(r_\alpha; E_{l\alpha}) + b_\mu u_{l\alpha}(r_\alpha; E_{l\alpha}^{\mathrm{sc}})\right] Y_{lm}(\hat{\mathbf{r}}_\alpha), \tag{2.95}$$

where the energy parameters E_l and E_l^{sc} correspond to valence and semicore state energies, respectively. Similar to Eq. (2.94), a wavefunction can be expressed as

$$\varphi_{n\mathbf{k}}(r) = \sum_{lm}\left[c_{lm}^{n\mathbf{k}} u_{l\alpha}(r_\alpha; E_{l\alpha}) + d_{lm}^{n\mathbf{k}} u_{l\alpha}(r_\alpha; E_{l\alpha}^{\mathrm{sc}})\right] Y_{lm}(\hat{\mathbf{r}}_\alpha). \tag{2.96}$$

Since $u_{l\alpha}(r_\alpha; E_{l\alpha})$ is also used in APW functions, the coefficients $c_{lm}^{n\mathbf{k}}$ and $d_{lm}^{n\mathbf{k}}$ are variational and linearly independent. This ensures that either $c_{lm}^{n\mathbf{k}}$ or $d_{lm}^{n\mathbf{k}}$ becomes zero when $\varphi_{n\mathbf{k}}(\mathbf{r})$ corresponds to a semicore or valence state with the same angular momentum, respectively. In practice, E_l and E_l^{sc} are not exactly equal to eigenenergies. In theory the exact energy can be found by adding more LOs that include the energy derivatives of $u_{l\alpha}(r_\alpha; E_{l\alpha})$ and $u_{l\alpha}(r_\alpha; E_{l\alpha}^{\mathrm{sc}})$.

Description of the core states

The highly localized core states require a different treatment compared to the extended valence and conduction states. Unlike the pseudopotential methods, the self-consistent calculations in `exciting` [137] explicitly include the core electrons.

In the description of the x-ray absorption process in Chapter 5, the initial core state is obtained as a solution of the Dirac equation in a spherically symmetric atomic potential. This is because such states are highly localized and dominated by relativistic effects. The solution is the four-component Dirac wavefunction $\Psi_{\kappa,m}(\mathbf{r})$, which can be written as

$$\Psi_{\kappa,m}(\mathbf{r}) = \frac{1}{r}\begin{pmatrix} u_\kappa(r)\Omega_{\kappa,m}(\hat{\mathbf{r}}) \\ -iv_\kappa(r)\Omega_{-\kappa,m}(\hat{\mathbf{r}}) \end{pmatrix}, \tag{2.97}$$

where we have introduced a unique index κ for a core state

$$\kappa = \begin{cases} -l-1, & \text{for } j = l + \frac{1}{2}, \\ l, & \text{for } j = l - \frac{1}{2}. \end{cases} \tag{2.98}$$

The spherical part of the core wavefunctions $\Psi_{\kappa,m}(\mathbf{r})$ is given by the spin spherical harmonics $\Omega_{l,s,j,m}(\hat{\mathbf{r}})$. The coupled Dirac equations give the radial functions $u_\kappa(r)$ for the "large" component and $-iv_\kappa(r)$ for the "small" component

$$\frac{\partial u_\kappa(r)}{\partial r} = \frac{1}{c}(v^{\mathrm{s}}_{\mathrm{eff}}(r) - E_\kappa)v_\kappa(r) + \left(\frac{\kappa-1}{r}\right)u_\kappa(r), \tag{2.99}$$

$$\frac{\partial v_\kappa(r)}{\partial r} = -\frac{\kappa+1}{r}v_\kappa(r) + (2c + \frac{1}{c}(E_\kappa - v^{\mathrm{s}}_{\mathrm{eff}}(r)))u_\kappa(r), \tag{2.100}$$

where $v^{\mathrm{s}}_{\mathrm{eff}}(r)$ is the spherically averaged effective Kohn–Sham potential. The spin-spherical harmonics $\Omega_{l,s,j,m}(\hat{\mathbf{r}})$ are given by

$$\Omega_{l+\frac{1}{2},m}(\hat{\mathbf{r}}) = \begin{pmatrix} \sqrt{\frac{l+m+\frac{1}{2}}{2l+1}}Y_{l,m-\frac{1}{2}}(\hat{\mathbf{r}}) \\ \sqrt{\frac{l-m+\frac{1}{2}}{2l+1}}Y_{l,m+\frac{1}{2}}(\hat{\mathbf{r}}) \end{pmatrix}, \quad \Omega_{l-\frac{1}{2},m}(\hat{\mathbf{r}}) = \begin{pmatrix} -\sqrt{\frac{l-m+\frac{1}{2}}{2l+1}}Y_{l,m-\frac{1}{2}}(\hat{\mathbf{r}}) \\ \sqrt{\frac{l+m+\frac{1}{2}}{2l+1}}Y_{l,m+\frac{1}{2}}(\hat{\mathbf{r}}) \end{pmatrix}. \tag{2.101}$$

In order to calculate matrix elements with the scalar-relativistic states in the conduction band, the small component of the core states is neglected, thereby producing spinor solutions at an atomic site α:

$$\Psi^{\alpha}_{\kappa,m}(\mathbf{r}) = \begin{cases} u_{\kappa\alpha}(r_\alpha)\Omega_{\kappa,m}(\hat{\mathbf{r}}_\alpha), & \text{for } r_\alpha \leq R_{\mathrm{MT}}, \\ 0, & \text{else.} \end{cases} \tag{2.102}$$

This approximation is required since the conduction states are solutions of the scalar-relativistic Hamiltonian, and therefore the small component of these states is not accessible. In `exciting`, the Dirac equation is solved for the core electrons, and the Bloch state is found by taking the localized core states

$$\Psi^{\mathbf{k}}_{\kappa,M\alpha} = \sum_{\mathbf{R}} \phi_{\kappa,M\alpha}(\mathbf{r}_\alpha - \mathbf{R})e^{i\mathbf{k}\mathbf{R}}. \tag{2.103}$$

3. Microscopic optical response with x-ray diffraction

In this chapter, we theoretically describe an x-ray diffraction experiment on a laser-dressed material. In such an experiment, the driving field and x-ray probe field interact with a material simultaneously. We apply a previously developed *ab initio* computational scheme based on the Floquet–Bloch formalism to analyze the angular dependence of the first- and second-order side peaks to the elastic Bragg peak. Theoretical results are compared with experimental data obtained by collaborators. The results demonstrate how the measurement of higher-order side peaks provides atomic-scale information on the local symmetry of the laser-dressed electron density. The results of the chapter are published in Ref. [148].

3.1. Introduction

X-ray diffraction is a powerful technique that can serve as an atomic-scale probe of the microscopic details of light-matter interactions within materials. Light-matter interactions are intensively studied, particularly within the optical range. However, the microscopic details are often overlooked because they cannot be accessed directly in measurements. At the same time, the optical response is a complex process defined by the details of many-body electron interactions. These vary on an atomic length scale, rather than on the scale of the long-wavelength applied field.

In x-ray diffraction from a laser-dressed material, x-rays inelastically scatter from laser-dressed electron density, in analogy to standard x-ray diffraction. This approach to measuring valence charge density was originally proposed by Freund and Levine [149] and Eisenberger and McCall [65] and first demonstrated on single-crystal diamond by Glover *et al*. [66]. Standard x-ray diffraction experiments provide the information about material structure by probing the total electron density, valence, and core. In such experiments, it is difficult to separate the information about the valence electron density, since valence electrons are delocalized and contribute only a small amount to the total electron density.

The presence of the driving field in x-ray diffraction measurement results in side peaks to elastic Bragg peaks. These side peaks only emerge when two fields drive a coherent electronic response simultaneously. In this case, the simultaneously polarized charge is equal to the optically polarized valence charge. This is because only this charge has significant polarizability for both fields; tightly bound core electrons can only be polarized by x-ray radiation [66]. In general, if the wavelength of the driving field is varied, the

polarized charge corresponds to different charge components in a material. For example, the technique can be extended to probe the full valence charge distribution by mixing x-rays with XUV radiation of a frequency high enough for a uniform response of all valence electrons but low enough that the polarizability of tightly bound core charge can be neglected.

The amplitude and phase of side peaks contain information about laser-dressed charge density and associated microscopic field in reciprocal space. When side peaks can be separated from the elastic background, the measurement of their amplitude and phases can be used to reconstruct the laser-dressed electron density and associated microscopic field within the unit cell [148]. The measurement of the first-order side peaks allows us to probe the linear optical susceptibility of a material on a microscopic length scale. Higher-order side peaks provide a way to probe nonlinear optical susceptibilities; see Fig. 3.1. For example, x-rays could scatter from a laser-dressed electron density oscillating at twice the optical frequency.

The positions of side peaks in energy and momentum space are determined by energy and momentum conservation [66, 148]. In the experiment [148], the setup is first aligned to a chosen elastic Bragg peak, at a certain Bragg angle, θ_B, depending on the x-ray energy. After reaching the Bragg peak, the crystal is detuned according to the phase-matching condition for the side peak of interest. In general the phase-matching condition is given by energy and momentum conservation

$$\begin{aligned} \omega_n' &= \omega_x + n\omega_o \\ \mathbf{k}_n' - \mathbf{k}_x &= n\mathbf{k}_o + \mathbf{G} \equiv \mathbf{Q}_n. \end{aligned} \tag{3.1}$$

Here, $\mathbf{k}_o, \mathbf{k}_x, \mathbf{k}_n'$ are the optical, incident x-ray, and nonlinear diffracted x-ray wave vectors inside the material. Diffracted x-ray photons probe a certain Fourier component of the

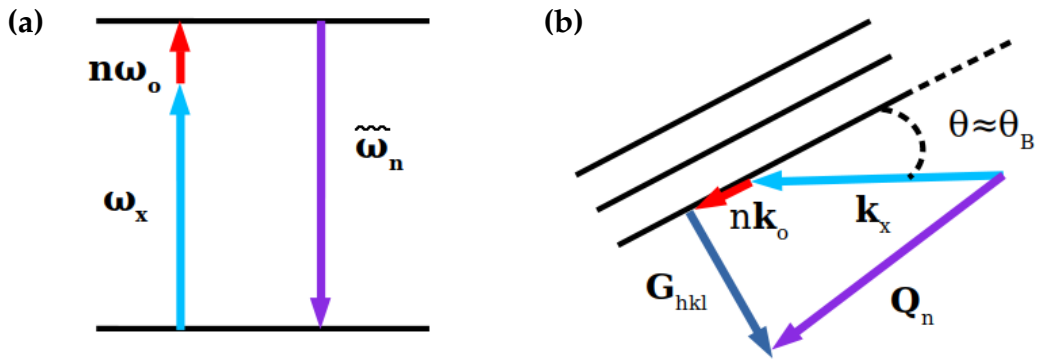

Figure 3.1.: Phase matching condition for the energy and wave vectors in x-ray diffraction from a laser-dressed material.

charge density similar to the x-ray diffraction in the stationary case. In particular, for the elastic Bragg peak at the reciprocal lattice vector $\mathbf{G}$, the first-order side peak contains

information about the ($\mathbf{Q} = \mathbf{k}_o + \mathbf{G}$)th Fourier component of the laser-driven charge change to the valence electron density $\delta\rho_o(\mathbf{Q})$.

Next, we first briefly introduce the theoretical framework for x-ray diffraction in a laser-driven material, as developed in Refs. [67, 150]. We then analyze the angular dependence of the Floquet side peaks using a simple model based on the concept of optical polarizability density. We then used a previously developed *ab initio* computational scheme to calculate the x-ray diffraction signal and the corresponding laser-dressed electron density in a silicon crystal. The results of the computational modeling are compared with measurements of the intensity and polarization dependence of the diffraction side peaks at the LCLS free-electron laser [148].

3.2. Theory of x-ray diffraction from a laser-driven material

We begin by briefly reviewing the theoretical framework for x-ray scattering in a laser-driven material, as developed in Refs. [67, 150]. The interaction between a nonresonant hard x-ray pulse and the laser-dressed electronic system is described within the framework of the quantum electrodynamics and the density matrix formalism. The total Hamiltonian takes on the following form:

$$\hat{H} = \hat{H}_{\mathrm{el-em}} + \hat{H}_{\mathrm{x}} + \hat{H}^{\mathrm{x}}_{\mathrm{int}}, \tag{3.2}$$

where $\hat{H}_{\mathrm{el-em}}$ describes the laser-driven electronic system, discussed in Chapter 2, and $\hat{H}_{\mathrm{x}}$ is the Hamiltonian of the x-ray field

$$\hat{H}_{\mathrm{x}} = \sum_{\boldsymbol{\kappa}_{\mathrm{x}}, s_{\mathrm{x}}} \omega_{\boldsymbol{\kappa}_{\mathrm{x}}} \hat{a}^{\dagger}_{\boldsymbol{\kappa}_{\mathrm{x}}, s_{\mathrm{x}}} \hat{a}_{\boldsymbol{\kappa}_{\mathrm{x}}, s_{\mathrm{x}}}, \tag{3.3}$$

operators $\hat{a}^{\dagger}_{\boldsymbol{\kappa}_{\mathrm{x}}, s_{\mathrm{x}}}$ and $\hat{a}_{\boldsymbol{\kappa}_{\mathrm{x}}, s_{\mathrm{x}}}$ are the creation and annihilation operators of the x-ray photon with wave vector $\boldsymbol{\kappa}_{\mathrm{x}}$ and polarization s_{x}. $\hat{H}^{\mathrm{x}}_{\mathrm{int}}$ denotes the interaction between the x-ray probe pulse and the laser-driven system within the minimal coupling scheme, where the interaction Hamiltonian is defined up to second order as follows:

$$\hat{H}^{\mathrm{x}}_{\mathrm{int}} = \frac{1}{c} \int d^3r\, \hat{\psi}^{\dagger}(\mathbf{r}) \left(\hat{\mathbf{A}}_{\mathrm{x}}(\mathbf{r}) \cdot \hat{\mathbf{p}}\right) \hat{\psi}(\mathbf{r}) + \frac{1}{2c^2} \int d^3r\, \hat{\psi}^{\dagger}(\mathbf{r}) \hat{\mathbf{A}}^2_{\mathrm{x}}(\mathbf{r}) \hat{\psi}(\mathbf{r}). \tag{3.4}$$

Here, the first term corresponds to resonant x-ray scattering, while the second term describes nonresonant, Thomson-like, scattering. In the following, we assume that the x-ray photon energy is far from any core-level resonances, allowing the first term to be neglected.

The driving field brings the electronic system to a state $|\Psi(t)\rangle$ given by Eq. (2.35). It has been shown that the probability of x-ray scattering, in the general case contains quasielastic and inelastic contributions. The quasielastic contribution corresponds to transitions into

Floquet eigenstates $\overline{F}$ that are already present in the initial state of the laser-dressed crystal $|\Psi(t)\rangle$, such that $C_{\overline{F}} \neq 0$. The inelastic contribution corresponds to transitions into final Floquet states F that are absent from the initial state of the laser-driven crystal, such that $C_F = 0$. When the laser-dressed system can be described by a single series of Floquet states and the probe x-ray pulse has a bandwidth sufficiently narrow to isolate the quasielastic contribution, the probability of quasielastic scattering does depend on the time-dependent electron density $\rho(\mathbf{r}, t)$. A probe is sufficiently narrow if its bandwidth is smaller than the driving frequency Ω, the energy differences between the Floquet states I_μ and $K_{\Delta\mu'}$ that form the wave packet $|\Psi(t)\rangle$, and the energy differences between these states and the other Floquet states $F_{\Delta\mu''}$ for any $\Delta\mu$, $\Delta\mu'$, and $\Delta\mu''$. Under these conditions, scattering events leading to different final states can be spectroscopically distinguished.

In the stationary case, in x-ray diffraction measurement, the inelastic contributions are usually negligible in comparison to the elastic ones. However, in the case of the laser-driven system, the inelastic contributions can be comparable to or larger than the quasielastic contribution related to the density component $\tilde{\rho}_{\mu\neq 0}(\mathbf{r})$ and thus can not be neglected. In the particular case of an ultrashort probe x-ray pulse, it may not be possible to spectroscopically distinguish between inelastic and quasielastic contributions to the scattering probability. That is why conducting the time-resolved x-ray diffraction measurement is such a difficult task. If there is no way to separate the quasielastic contribution in such a measurement, there is no way to connect the resulting signal to the time-dependent electron density.

In principle, the process of quasielastic scattering is optically modulated x-ray diffraction, which encodes information about the distributions of laser-driven electron density and currents. The probability of quasielastic scattering for a Gaussian-shaped x-ray pulse with a duration τ_p, as derived in Ref. [67], is given by

$$P_{\text{q.e.}}(\omega_s, \mathbf{G}) = P_0 \sum_\mu \mathcal{E}_\mu^2 \left| \int d^3r e^{i\mathbf{G}\mathbf{r}} \tilde{\rho}_\mu(\mathbf{r}) \right|^2 + (-1)^{\Delta\mu} P_0 \sum_{\mu,\Delta\mu} 2\,\text{Re}\left(\mathcal{E}_\mu \mathcal{E}_{\mu+\Delta\mu} e^{\Delta\mu\Omega t_p} \int d^3r e^{i\mathbf{G}\mathbf{r}} \tilde{\rho}_\mu(\mathbf{r}) \int d^3r e^{-i\mathbf{G}\mathbf{r}} \tilde{\rho}^*_{\mu+\Delta\mu}(\mathbf{r}) \right). \tag{3.5}$$

Here, the prefactor is defined as $P_0 = \sum_{s_s} |(\boldsymbol{\epsilon}_{\text{in}} \cdot \boldsymbol{\epsilon}^*_{\text{x},\kappa_s,s_s})|^2 \omega_s^2 / (4\pi^2 \omega_{\text{in}}^2 c^3)$, where ω_{in} and $\boldsymbol{\epsilon}_{\text{in}}$ are the central photon energy and polarization vector of the incident x-ray beam, respectively, ω_s is the energy of the scattered photon with momentum $\boldsymbol{\kappa}_s$, and the sum over s_s accounts for the two orthogonal polarization vectors of the scattered photon, $\boldsymbol{\epsilon}^*_{\text{x},\kappa_s,s_s}$. Note that Eq. (3.5) does not describe the shift of a scattering vector by $\mathbf{k}_0$ relative to the reciprocal lattice vector $\mathbf{G}$. This is due to the dipole approximation to the interaction between the crystal and the driving electromagnetic field. This assumption results in the approximated time-dependent electron density with the same spatial periodicity as the stationary electron density of the crystal. This is not connected to the description of the

interaction with the nonresonant probe x-ray pulse.

In Eq. (3.5), $\mathcal{E}_\mu$ is the μth spectral component of the Fourier transform of the x-ray pulse envelope, given by $\mathcal{E}_\mu = \sqrt{\frac{\tau_p^2 \pi}{2 \ln 2}} e^{-(\omega_s - \omega_{in} - \mu\Omega)^2 \tau_p^2 / 8 \ln 2}$. If the duration of the probe pulse τ_p is much longer than the optical cycle, the spectral components $\mathcal{E}_\mu$ and $\mathcal{E}_{\mu+\Delta\mu}$ are narrow and don't overlap. In this case, the second term in Eq. (3.5) can be neglected, and the resulting signal becomes independent of the arrival time t_p of the x-ray pulse. As the duration τ_p decreases, the functions $\mathcal{E}_\mu$ and $\mathcal{E}_{\mu+\Delta\mu}$ broaden spectrally and begin to overlap. In this case, interference between the μ and $\mu + \Delta\mu$ components becomes significant, and the second term in Eq.(3.5) can no longer be neglected. The resulting signal therefore becomes sensitive to the time arrival t_p.

The main advantage of a time-resolved measurement over a time-unresolved one is that, in principle, it can be used to reconstruct both the amplitude and phase of the Fourier components of the laser-driven charge density, $\int d^3 r e^{i\mathbf{G}\cdot\mathbf{r}} \tilde{\rho}_\mu(\mathbf{r})$. In contrast, a time-unresolved measurement produces separate side peaks for each μ, with intensities that depend only on the amplitude of the corresponding Fourier component and contain no information about its phase. In the following sections, we will consider only the case of a time-unresolved measurement. For a more detailed discussion of the time-resolved case and how it can, in principle, be used to reconstruct the phase, we refer the reader to Ref. [69].

3.3. Results

In this section, we demonstrate how a time-unresolved measurement of the angular dependence of the diffraction side peaks can provide additional information about laser-driven electron dynamics in a material.

3.3.1. Polarization dependence of the Floquet side peaks

We begin by presenting the expressions for the laser-dressed charge and current densities, as the intensity of the μth-order side peak is proportional to the squared amplitude of the corresponding Fourier component of the laser-dressed electron density; see Eq. (3.5). Thus the measurement of the side peaks' intensities as a function of varying polarization of the driving optical field contains information about the spatial distribution of the laser-dressed electron density and current density.

If the electron system has a time-reversal symmetry and the vector potential of the driving field evolve in time periodically as $\cos(\Omega t)$, then its electron density evolves in time as

[69]

$$\rho(\mathbf{r},t) = \widetilde{\rho}_0(\mathbf{r}) - \sum_{\mu_{\text{odd}}\geq 1} \rho_{\mu_{\text{odd}}}(\mathbf{r}) \sin(\mu_{\text{odd}}\Omega t) + \sum_{\mu_{\text{even}}\geq 2} \rho_{\mu_{\text{even}}}(\mathbf{r}) \cos(\mu_{\text{even}}\Omega t), \tag{3.6}$$

where $\rho_\mu(\mathbf{r})$ are laser-dressed charge distributions. The electron-current density amplitudes vary in time as follows:

$$\mathbf{j}(\mathbf{r},t) = -\sum_{\mu_{\text{odd}}\geq 1} \mathbf{j}_{\mu_{\text{odd}}}(\mathbf{r}) \cos(\mu_{\text{odd}}\Omega t) - \sum_{\mu_{\text{even}}\geq 2} \mathbf{j}_{\mu_{\text{even}}}(\mathbf{r}) \sin(\mu_{\text{even}}\Omega t), \tag{3.7}$$

$\rho_\mu(\mathbf{r})$ and $\mathbf{j}_\mu(\mathbf{r})$ are the real-valued charge and current density amplitudes.

The electron density and the electron current density are related via the continuity equation as $\partial\rho(\mathbf{r})/\partial t + \nabla\cdot\mathbf{j}(\mathbf{r}) = 0$, which leads to the relation between μth-order laser-dressed charge distributions $\rho_\mu(\mathbf{r})$ and μth-order electron-current density amplitudes $\mathbf{j}_\mu(\mathbf{r})$ as $\mu\Omega\rho_\mu(\mathbf{r}) = -\nabla\cdot\mathbf{j}_\mu(\mathbf{r})$. This, together with the vector algebra relations, provides the following connection between their Fourier transforms

$$\mu\Omega \int d^3r e^{i\mathbf{G}\mathbf{r}} \rho_\mu(\mathbf{r}) = \mathbf{G}\cdot\int d^3r e^{i\mathbf{G}\mathbf{r}} \mathbf{j}_\mu(\mathbf{r}), \tag{3.8}$$

where $\mathbf{G}$ is a reciprocal lattice vector in the case of the electron system being periodic.

First-order optical response

The first-order microscopic susceptibility tensor $\chi^{(1)}_{ij}(\mathbf{r})$ gives rise to the first-order electron-current amplitude and satisfies

$$(\mathbf{j}_1)_i(\mathbf{r}) = \chi^{(1)}_{ij}(\mathbf{r})\,\epsilon_j, \tag{3.9}$$

where $\boldsymbol{\epsilon}$ is the polarization vector of the driving electromagnetic field. If the system is isotropic, the first-order microscopic susceptibility tensor is proportional to the identity matrix, $\chi^{(1)}_{ij}(\mathbf{r}) = \chi(\mathbf{r})\delta_{ij}$, and the resulting first-order electron current density is parallel to the polarization vector,

$$(\mathbf{j}_1)_i(\mathbf{r}) = \chi(\mathbf{r})\,\epsilon_i. \tag{3.10}$$

The Fourier component of the first-order laser-dressed charge distribution then satisfies

$$\Omega\int d^3r\, e^{i\mathbf{G}\cdot\mathbf{r}} \rho_1(\mathbf{r}) = (\mathbf{G}\cdot\boldsymbol{\epsilon})\int d^3r\, e^{i\mathbf{G}\cdot\mathbf{r}}\chi(\mathbf{r}). \tag{3.11}$$

Thus, the intensity of the first-order side peak of a Bragg peak $\mathbf{G}$ varies as $\cos^2\varphi$ in the case of an isotropic system, where φ is the angle between the polarization vector $\boldsymbol{\epsilon}$ and a reciprocal lattice vector $\mathbf{G}$.

This conclusion is in line with Ref. [67], where the dependence of the first-order Bragg

peak intensity at $\mathbf{G} = (0, 0, 2)$ on the polarization of the pump pulse was computationally analyzed for a laser-dressed MgO crystal. It was found that the intensity of the first-order Bragg peak is proportional to $(\boldsymbol{\epsilon} \cdot \mathbf{G})^2$, leading to the conclusion that the spatial Fourier transform of the amplitude $\rho_1(\mathbf{r})$ of the time-dependent electron density of MgO has a linear dependence on $(\boldsymbol{\epsilon} \cdot \mathbf{G})$. These results are additionally supported by the experiment of Glover et al [66], who observed the same polarization dependence of the signal intensity on an optical pulse.

Second-order optical response

The second-order microscopic susceptibility tensor $\chi^{(2)}_{ijk}(\mathbf{r})$ gives rise to the second-order electron-current density amplitude and satisfies the relation

$$(\mathbf{j}_2(\mathbf{r}))_i = \chi^{(2)}_{ijk}(\mathbf{r})\epsilon_j\epsilon_k. \tag{3.12}$$

The second-order amplitudes $\rho_2(\mathbf{r})$ and $\mathbf{j}_2(\mathbf{r})$ are related via the continuity equation as $\rho_2(\mathbf{r}) = \nabla \cdot \mathbf{j}_2(\mathbf{r})/2\Omega$. Thus, we can also represent the second-order laser-dressed charge distribution using a tensor $\chi^{(2)}_{ijk}(\mathbf{r})$ as follows:

$$\rho_2(\mathbf{r}) = \Gamma^{(2)}_{jk}(\mathbf{r})\epsilon_j\epsilon_k. \tag{3.13}$$

The components of the tensor $\Gamma^{(2)}_{jk}(\mathbf{r})$ relate to the components of the second-order microscopic susceptibility tensor $\chi^{(2)}_{ijk}(\mathbf{r})$ as follows:

$$\Gamma^{(2)}_{jk}(\mathbf{r}) = \frac{1}{2\Omega}\sum_i \frac{\partial \chi^{(2)}_{ijk}(\mathbf{r})}{\partial r_i}. \tag{3.14}$$

In the experiment [148], the polarization of the driving pulse was rotated from the direction along $(1, 1, 0)$ to the direction along $(1, -1, 0)$ via the direction along $(1, 0, 0)$. Thus, the polarization can be expressed as $\boldsymbol{\epsilon} = (\sin(\frac{\pi}{4} + \varphi), \cos(\frac{\pi}{4} + \varphi), 0)$, where φ changes from 0 to $\frac{\pi}{2}$. Substituting the polarization $\boldsymbol{\epsilon}$ in Eq. (3.13) results in

$$\begin{aligned}\rho_2(\mathbf{r}) = \Gamma^{(2)}_{xx}(\mathbf{r})\sin^2\left(\frac{\pi}{4} + \varphi\right) + \Gamma^{(2)}_{yy}(\mathbf{r})\cos^2\left(\frac{\pi}{4} + \varphi\right) \\ + 2\Gamma^{(2)}_{xy}(\mathbf{r})\sin\left(\frac{\pi}{4} + \varphi\right)\cos\left(\frac{\pi}{4} + \varphi\right),\end{aligned} \tag{3.15}$$

where we took into account that $\Gamma^{(2)}_{xy} = \Gamma^{(2)}_{yx}$ as follows from crystal symmetry.

The intensity of the second-order side peak is proportional to the square of the module of the Fourier transform of the amplitude of the second-order laser-dressed charge

distribution, and depends on φ as follows:

$$I_2(\mathbf{G},\boldsymbol{\epsilon}) \propto \Big| \tilde{\Gamma}^{(2)}_{xx}(\mathbf{G}) \sin^2\left(\frac{\pi}{4}+\varphi\right) + \tilde{\Gamma}^{(2)}_{yy}(\mathbf{G}) \cos^2\left(\frac{\pi}{4}+\varphi\right) + 2\tilde{\Gamma}^{(2)}_{xy}(\mathbf{G}) \sin\left(\frac{\pi}{4}+\varphi\right) \cos\left(\frac{\pi}{4}+\varphi\right) \Big|^2, \tag{3.16}$$

where $\tilde{\Gamma}^{(2)}_{jk}(\mathbf{G}) = \int d^3r e^{i\mathbf{G}\mathbf{r}} \tilde{\Gamma}^{(2)}_{jk}(\mathbf{r})$ is the Fourier transform of the reduced second order microscopic susceptibility tensor.

It follows from the *ab initio* calculations for silicon that the tensor components $\Gamma^{(2)}_{jk}(\mathbf{r})$ are related by cyclic permutations of the Cartesian coordinates, such that

$$\Gamma^{(2)}_{yy}(\mathbf{r}) = \Gamma^{(2)}_{xx}(P[\mathbf{r}]), \quad \Gamma^{(2)}_{zz}(\mathbf{r}) = \Gamma^{(2)}_{yy}(P[\mathbf{r}]), \quad \Gamma^{(2)}_{yz}(\mathbf{r}) = \Gamma^{(2)}_{xy}(P[\mathbf{r}]), \quad \Gamma^{(2)}_{zx}(\mathbf{r}) = \Gamma^{(2)}_{yz}(P[\mathbf{r}]), \tag{3.17}$$

where $P[\mathbf{r}]$ denotes the position vector obtained by cyclically permuting the spatial coordinates, i.e., $P(x,y,z) = (y,z,x)$. This results for the Fourier components of the laser-dressed charge distributions that $\tilde{\Gamma}^{(2)}_{xx}(\mathbf{G}) = \tilde{\Gamma}^{(2)}_{yy}(\mathbf{G})$ for $\mathbf{G} = (2,2,0)$. Thus, the dependence of the intensity of the second order side peak of the Bragg peak $(2,2,0)$ on the angle between $\mathbf{G}$ and the polarization reduces to the relation

$$I_2(\mathbf{G}) \propto \left| \tilde{\Gamma}^{(2)}_{xx}(\mathbf{G}) + \tilde{\Gamma}^{(2)}_{xy}(\mathbf{G}) \cos(2\varphi) \right|^2. \tag{3.18}$$

3.3.2. *Ab initio* calculations

We perform *ab initio* calculations of the x-ray diffraction in the presence of a driving optical field for various laser pulse polarizations $\boldsymbol{\epsilon}$. We also compute the corresponding laser-dressed density $\rho(\mathbf{r},t)$ to understand what information about the spatial distribution of $\rho(\mathbf{r},t)$ can be obtained from the polarization dependence of the diffraction signal. The calculations are based on a theoretical framework derived from quantum electrodynamics [67] and described in Section 3.2. Within this framework, we apply the Floquet–Bloch formalism to compute the laser-dressed electronic states induced by the optical field and then evaluate the scattering probability of an x-ray pulse interacting with the driven system according to Eq. (3.5). As it was shown in the case of time-unresolved measurement, the intensity of a side peak is proportional to the Fourier transform of the corresponding component of the time-dependent electron density.

The calculations involve first computing the Kohn–Sham wavefunctions of the ground-state of a crystal with the ABINIT software package [139–142], using the generalized gradient approximation functional of Perdew, Burke, and Ernzerhof (GGA-PBE) [151, 152]. These Kohn–Sham states are then used to construct the Floquet–Bloch Hamiltonian as

described in Chapter 2.

In the calculations of laser-dressed states for a silicon crystal in Ref. [148], we consider a driving field with a photon energy of 0.95 eV and an intensity of 5×10^{11} W/cm^2. The calculations are performed using 4 valence bands and 76 conduction bands on a four-times shifted $12 \times 12 \times 12$ Monkhorst-Pack $\mathbf{k}$-point grid. The infinite Floquet–Bloch Hamiltonian is approximated by a matrix with 301 blocks, each containing 80 states. The $\mathbf{k}$-point grid, the number of bands and the blocks are selected based on a convergence study. We apply the scissors approximation [153] to correct the direct band gap from the calculated 2.5 eV to the experimental value of 3.5 eV [154, 155].

Silicon has a centrosymmetric crystal structure similar to that of diamond. This symmetry requires $\chi^{(2)}_{ijk}(\mathbf{r}) = -\chi^{(2)}_{ijk}(-\mathbf{r})$ and leads to the macroscopic second-order optical susceptibility to vanish when the microscopic response is averaged over space. However, local inversion symmetry breaking can result in a non-zero microscopic second-order susceptibility. The optically modulated x-ray diffraction is specifically sensitive to these microscopic details of the nonlinear optical response. Figure 3.2 shows *ab initio* calculations of the first- and second-order microscopic optical responses as the driving electric field is rotated within the (001) plane. Panels (a) and (b) show the first-order response in real and reciprocal space, respectively. Panels (c) and (d) show the corresponding second-order response. In the real-space plots (a) and (c), isosurfaces are plotted using VESTA [156], with the direction of the applied optical field indicated in red. In reciprocal space (b) and (d), red and blue spheres correspond to reciprocal lattice vectors from the $\{111\}$ and $\{220\}$ families, respectively, with the size of each sphere encoding the absolute value of the corresponding Fourier component of the laser-dressed electron density. The applied field breaks the cubic symmetry of the crystal, so Fourier components belonging to the same family are no longer equivalent. In real space, the density shown is restricted to the valence contribution and is concentrated mainly in the interstitial regions rather than on the atomic sites. The first-order density variation largely follows the direction of the applied field. In reciprocal space, the induced charge amplitude aligns with the polarization direction of the optical field, consistent with the Eq. (3.11). In contrast, the polarization dependence of the second-order side peak is more complex.

3.4. Comparison with the experimental data

The measurements in Ref. [148] were performed using the X-ray Pump-Probe instrument at the LCLS hard x-ray free-electron laser [157]. The silicon sample was oriented so that the (220) lattice vector lay in the scattering plane, allowing a symmetric Laue geometry. The incident hard x-ray beam, with a photon energy of 9.5 keV, was monochromatized and collimated to ensure sufficiently narrow energy bandwidth and angular divergence, allowing clear separation of diffraction side peaks from the elastic background. Simultane-

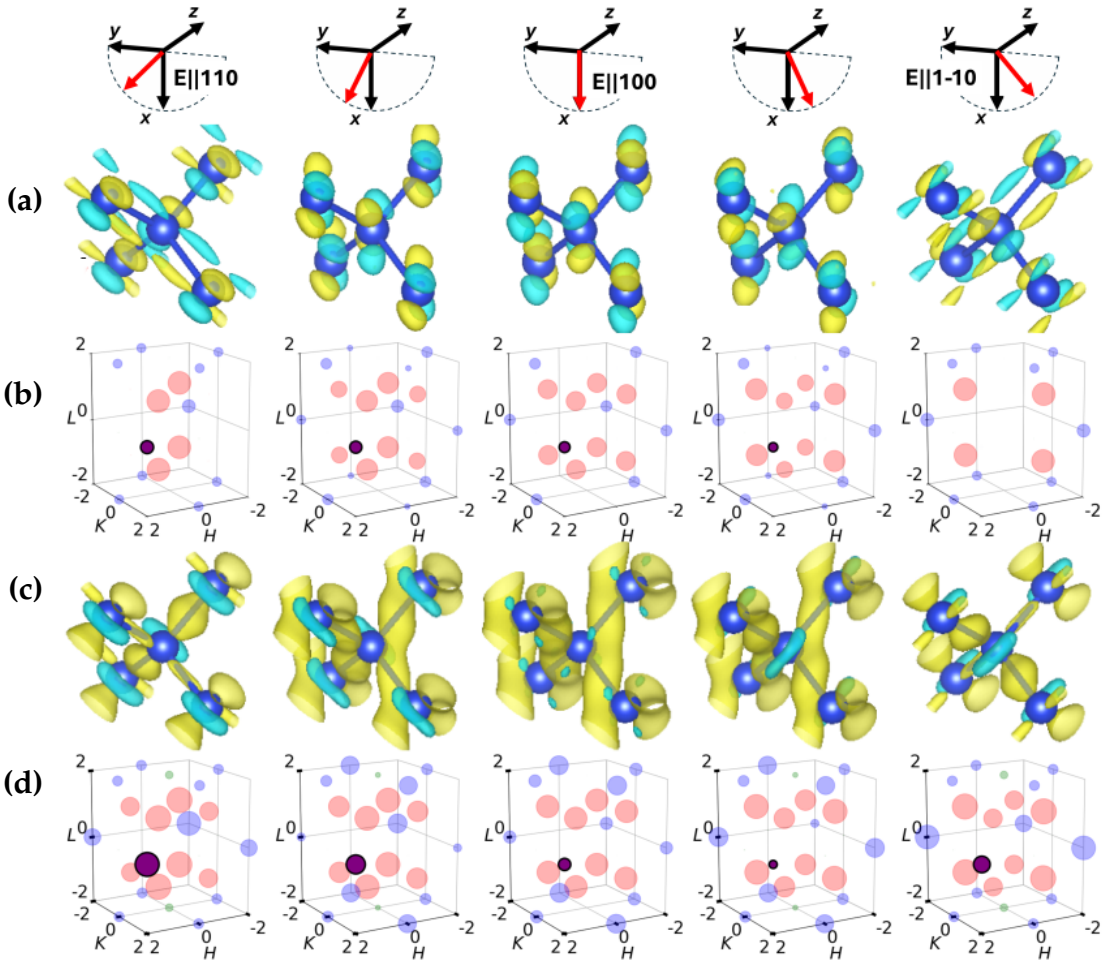

Figure 3.2.: *Ab initio* calculations of the first- and second-order microscopic optical responses as a function of varying electric field direction. Panels (a) and (b) show the first-order response in real and reciprocal space, respectively. Panels (c) and (d) show the second-order response in real and reciprocal space, respectively. In panels (b) and (d) the red, blue, green, and purple spheres correspond to points in the $\{111\}$, $\{220\}$, $\{200\}$, and (220) families, respectively. The size of the spheres encodes the absolute value of the corresponding Fourier component of the laser-dressed electron density. The isosurfaces in (a) and (c) are visualized using VESTA [156]. The yellow and blue colors represent negative and positive charges, respectively. Adapted from Ref. [148].

ously, the sample was pumped with sub-bandgap optical pulses at 0.95 eV. The pump was linearly polarized and had a peak intensity of approximately 10^{12} W/cm^2 at the sample position. The relative time delay between the optical and x-ray pulses was defined on a shot-by-shot basis. The difference between the experimental intensity and the intensity used in the *ab initio* calculations is because the pulse intensity on the sample surface differs from that inside the sample.

The experimental setup was first aligned to a selected elastic Bragg peak, corresponding to a specific Bragg angle θ_B determined by the x-ray photon energy ω_x. Once aligned, the crystal was detuned to satisfy the phase-matching condition for the side peak of interest,

as described by Eqs. (3.1). A crystal analyzer, positioned near the nominal scattering angle for the Si (220) reflection, was used to filter the scattered signal. By adjusting the energy and scattering angle, the analyzer selectively transmitted diffracted photons while filtering out elastic background outside its angular acceptance.

Clear signatures of first- and second-order side peaks were observed. The first-order side peak appeared approximately 1 eV above the elastic Bragg peak. The second-order side peak was detected near 2 eV above the elastic line, as expected from the nonlinear mixing of a single x-ray photon with two infrared photons.

In the experiment, under the assumption of negligible x-ray absorption and dispersion, the intensity of diffraction signal in the kinematic limit is proportional to the Fourier transform of the laser-dressed charge density. The measured relative efficiency of the μth-order side peak with respect to the elastic, zero-order, peak is given by

$$\eta_{\mathbf{G}}^{(\mu)} = \frac{|\rho_{\mathbf{G}}^{(\mu)}|^2}{|\rho_{\mathbf{G}}^{(0)}|^2}. \tag{3.19}$$

Since $\rho_{\mathbf{G}}^{(\mu)}$ is generally complex, the side peak intensity provides no direct phase information, resulting in a phase problem similar to that in standard x-ray crystallography. However, in contrast with conventional diffraction, the higher-order side peaks encode additional information about optically driven electron density. In the experiment, it was demonstrated that a single higher-order side peak around a single elastic Bragg peak can be used to get insights into the local symmetry of the laser-dressed charge distribution.

In the experiment the polarization dependence of the first- and second-order side peaks was studied. Figures 3.3(a) and (b) show the measured efficiencies of the first- and second-order side peaks, respectively, as a function of the driving laser polarization direction. The optical field was rotated within the plane perpendicular to the (001) axis.

The intensity of the first-order side peak, shown in Fig. 3.3(a), exhibits a clear dependence on the projection of the electric field along the (220) reciprocal lattice vector as follows from Eq. (3.11). This behavior is consistent with the linear driven current following the field direction, as expected in a centrosymmetric cubic crystal, see Eq. (3.10). The measured angular dependence agrees well with the results of *ab initio* calculations.

In contrast, the second-order side peak, shown in Fig. 3.3(b), displays a distinctly different angular dependence. The observed signal is not consistent with a simple picture in which the driven charges follow the field direction. Furthermore, the relatively high efficiency of the second-order side peak cannot be explained by the theory in Section 3.2, suggesting that its origin cannot be attributed only to weak multipole contributions. The data indicate that the second-order response arises from regions of the unit cell where local symmetry is broken—such as interstitial or bond-centered sites—which allow a nonzero microscopic second-order susceptibility despite the macroscopic centrosymmetry of the crystal [148].

The measured angular dependence shown in Fig. 3.3(b) agrees well with the results of *ab initio* calculations and follows Eq. (3.18).

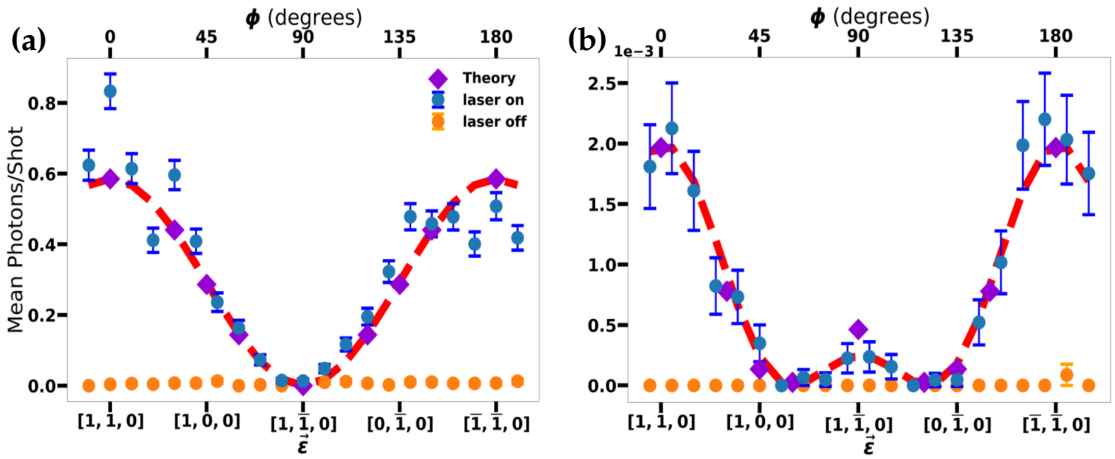

Figure 3.3.: The angular dependence of the side peaks to the elastic Bragg peak at $\mathbf{G} = (220)$ as polarization is rotated in (001) plane for the first-order response in (a) and the second-order response in (b). The solid red line shows the fit to the experimental data and the corresponding theoretical values are shown in purple. Adapted from Ref. [148].

For the interpretation of the measured side peak efficiencies and their polarization dependence, our collaborators developed a phenomenological model. This model treats the laser-dressed charge density $\rho(\mathbf{r}, t) = \rho(\mathbf{r} + \mathbf{R}, t + T_o)$ as a set of point dipoles. In this model, the Fourier components of the charge density are expanded in terms of small displacements from the equilibrium atomic positions. The small displacement from the site position $\mathbf{r}_s$ is then associated with the dipole density $\mathbf{p}(\mathbf{r}_s, t)$ and a nonlinear susceptibility $\chi^{(n)}(\mathbf{r}_s)$, similar to the theoretical model described in Section 3.2.

If the laser-induced polarization comes from the tetrahedral sites of the diamond structure, called the $(8a)$ Wyckoff positions and denoted by $\mathbf{r}_{8a}$, then the selection rules for the first-order side peak match those of the static charge density. In particular, for the first-order laser-driven charge originating from the tetrahedral sites [148]

$$\rho^{(1)}_{hkl}(\mathbf{r}_{8a}) = \frac{2Z_v}{\pi a^3}(\mathbf{E}\cdot\mathbf{G})\chi^{(1)}(\mathbf{r}_{8a})\cos\left(\frac{\pi}{4}(h+k+l)\right), \tag{3.20}$$

where Z_v is the number of valence electrons at the tetrahedral sites.

The model predicts that the second-order response from atomic sites does not contribute to the (220) Fourier component. The next relevant sites are the $3m$ (C_{3v}) symmetry positions, which lie between the atoms and the centers of the bonds. These positions support four independent second-order susceptibility components: χ_{11}, χ_{12}, χ_{14}, and χ_{15}. For the (220) component, the model is sensitive to three of them: χ_{11}, χ_{12}, and χ_{15}. The corresponding (220) Fourier component of the reduced second-order tensor, $\Gamma^{(2)}(\mathbf{r}_{32e})$,

takes the form [148]

$$\Gamma^{(2)}_{220} = 8 f_{32e} \sin 8\pi\epsilon \begin{pmatrix} \chi_{11}+\chi_{12} & \chi_{15} & 0 \\ \chi_{15} & \chi_{11}+\chi_{12} & 0 \\ 0 & 0 & 2\chi_{12} \end{pmatrix}. \tag{3.21}$$

In the experiment, the optical field is in the (001) plane and forms an angle ϕ with the (220) reciprocal lattice vector. For this geometry, and assuming the second-order response comes from the C_{3v} sites, the laser-driven charge density follows the polarization dependence [148]:

$$\rho^{(2)}_{220}(\mathbf{r}_{32e}, \phi) \propto |\mathbf{E}|^2 \left(\chi^{(2)}_{11} + \chi^{(2)}_{12} + 2\chi^{(2)}_{15} \cos(2\phi)\right). \tag{3.22}$$

This result matches the experimental and theoretical data shown in Fig. 3.3(b).

3.5. Summary

In this chapter, we theoretically describe an x-ray diffraction experiment on a laser-dressed silicon crystal. The results of the modeling show excellent agreement with recent experimental measurements, particularly for the polarization dependence of the first- and second-order diffraction side peaks. These side peaks arise from nonlinear interactions between a periodic electronic system and simultaneous optical and x-ray fields. They are directly sensitive to the spatial and temporal Fourier components of the laser-dressed charge density and current. The angular dependence of the first-order side peak is consistent with the laser-driven current following the field direction, while the second-order side peak exhibits a distinctly different angular dependence.

The study demonstrates that the measurement of higher-order side peaks can reveal atomic-scale information about the local symmetry of the driven valence-electron density-without direct phase information and even from a single Bragg reflection. Second-order microscopic nonlinear susceptibility in a centrosymmetric material is shown to originate from dipole-active sites within the unit cell that locally break inversion symmetry. Using a phenomenological point-dipole model, our collaborators identify C_{3v}-symmetric sites along sp^3 bonds as the dominant contributors to the observed signal. Within the constraints of the experimental geometry, three out of four independent components of the second-order microscopic susceptibility tensor are extracted [148]. These findings are further supported by our *ab initio* Floquet–Bloch calculations of the delocalized charge density.

As an outlook, it would be important to examine how the coupling between valence electrons and ionic motion appears in the x-ray diffraction signal. Similar to how x-ray diffraction has been used to study coherent phonons and phonon-polariton propagation, time-resolved measurements of valence electron motion could give direct access to

changes in bonding. This includes induced bond oscillations, bond delocalization, or even ultrafast bond breaking effects that could have clear signatures in the evolution of selected diffraction side peaks and are particularly relevant for photoactive materials.

4. Laser-dressed partial density of states

In this chapter, we present an *ab initio* computational scheme for calculating the time-dependent PDOS of a material during its interaction with a driving electromagnetic field. Using a laser-dressed wurtzite ZnO crystal as an example, we demonstrate how the analysis of the laser-dressed PDOS provides a site- and orbital-resolved view of laser-dressed electron dynamics. In the next chapter, we use this approach to interpret the computational results of our trXAS modeling. The results of the chapter are published in Ref. [158].

4.1. Introduction

Coupling matter to an optical field can lead to significant changes in its electronic structure, opening the way for the optical manipulation of material properties. Laser dressing can modify the band structure of a material - the concept behind Floquet engineering [26–32, 46], - and can be used to control its topological properties [33–35]. In the context of Floquet engineering, it is interesting to observe quasi-equilibrium laser-dressed states that arise from dynamics averaged over many optical cycles [26–29] and, in the context of ultrafast optoelectronics, to study laser-driven electron dynamics in a time-resolved manner [9–14, 16, 17, 159–161].

These novel time-resolved experiments motivate theoretical developments and advances in *ab initio* computational tools to describe laser-dressed electron dynamics [67, 91, 109, 110, 150, 162–165]. One of the main theoretical tools to analyze properties of laser-dressed electronic systems is the laser-dressed density of states (DOS) [43, 166]. The laser-dressed DOS describes the changes of electronic population due to the interaction with light. Analysis of its changes depending on the properties of a driving pulse offers a way to tune optical, topological and transport properties of laser-driven materials [43, 45, 166–178]. In a field-free case, a PDOS is an extension of DOS, which provides its orbital decomposition. A PDOS is a valuable computational tool of characterizing the electronic structure of materials in a ground state that reveals the contribution of specific orbitals to the bond formation. For a nonequilibrium state, similar information is especially relevant in view of recent experiments that demonstrate optical control of structural dynamics and ultrafast, optically induced bond formation or breaking [179–184]. Here, we introduce a laser-dressed PDOS that describes laser-driven changes in the electronic population in a site- and orbital-resolved manner.

Analyzing a laser-dressed DOS, it is common to focus only on its time-averaged part. Here, we also go beyond this standard approach and analyze both the time-averaged and the

time-dependent part of the laser-dressed PDOS. We show that the time-dependent part of the PDOS reveals the contribution of specific orbitals to the time-dependent changes in the electron density. This information provides a structure of instantaneous bonds formed during the interaction with light. On the one hand, it provides new details about microscopic optical response of a material, and, on the other hand, it can be useful for the interpretation of subcycle-resolved measurements. We illustrate our approach with the calculations of the PDOS of a laser-dressed wurtzite ZnO crystal.

4.2. Derivation of observables of a laser-dressed electronic system

The strong coupling of an electronic system to a driving electromagnetic field leads to the emergence of laser-dressed electronic states. These states provide observable quantities of the driven system, such as the time-dependent electron density or the electron current density [67, 69, 133]. Here, we derive another observable of the laser-dressed system, namely the laser-dressed PDOS and electron density for a selected energy window. To obtain the laser-dressed states, we use as basis states the Bloch electronic states defined within the LAPW+lo method (see Section 2.4), since it provides a full-potential treatment of the electronic structure and allows for a convenient projection of the DOS on particular orbitals.

4.2.1. Partial density of states

Ground state

We first consider a momentum- and projection-resolved PDOS of a periodic material in the ground state. In the following, we refer to the momentum- and projection-resolved PDOS as simply PDOS for convenience. A PDOS within the LAPW+lo basis set can be defined via the localized part of a Kohn–Sham orbital inside an MT region; see Eq. (2.84). This part is given by

$$\varphi^{\mathrm{MT}}_{n\mathbf{k}}(\mathbf{r}_\alpha) = \sum_{lm} F^{n\mathbf{k}}_{lm\alpha}(r_\alpha) Y_{lm}(\hat{\mathbf{r}}_\alpha) \equiv \sum_{lm} \mathcal{F}^{n\mathbf{k}}_{lm\alpha}(r_\alpha) \mathcal{Y}_{lm}(\hat{\mathbf{r}}_\alpha), \tag{4.1}$$

where the radius vector $\mathbf{r}_\alpha$ is defined inside an MT sphere of radius R_α centered on atoms labeled α, n is a band and spin index, and $\mathbf{k}$ is the Bloch wave vector [185]. The function $F^{n\mathbf{k}}_{lm\alpha}(r_\alpha)$ depends on a material and is computed during electron-structure calculations. In the rightmost part of Eq. (4.1) we transform the basis of complex spherical harmonics $Y_{lm}(\hat{\mathbf{r}}_\alpha)$ to the basis of the real spherical harmonics, $\mathcal{Y}_{lm}(\hat{\mathbf{r}}_\alpha)$ [186], and express $F^{n\mathbf{k}}_{lm\alpha}(r_\alpha)$ in

the real harmonics basis via

$$\mathcal{F}^{n\mathbf{k}}_{lm\alpha}(r_\alpha) = \begin{cases} \frac{i}{\sqrt{2}}((-1)^m F^{n\mathbf{k}}_{lm\alpha}(r_\alpha) - F^{n\mathbf{k}}_{l,-m\alpha}(r_\alpha)), \text{if } \ m<0, \\ F^{n\mathbf{k}}_{lm\alpha}(r_\alpha), \text{if } \ m=0, \\ \frac{1}{\sqrt{2}}((-1)^m F^{n\mathbf{k}}_{lm\alpha}(r_\alpha) + F^{n\mathbf{k}}_{l,-m\alpha}(r_\alpha)), \text{if } \ m>0. \end{cases} \tag{4.2}$$

Analogously to the standard definition of the stationary DOS, we define an atomic-resolved DOS as the contribution to the total DOS from the electronic states localized within the corresponding atomic sphere of radius R_α, $\sum_{n,\mathbf{k}} \int d^3 r_\alpha |\varphi^{\mathrm{MT}}_{n\mathbf{k}}(\mathbf{r}_\alpha)|^2 \delta(\omega - E_{n\mathbf{k}})$. We then decompose it in terms of different l and m components to obtain a PDOS as follows:

$$D^\alpha_{lm}(\omega) = \sum_{n\mathbf{k}} \int_0^{R_\alpha} dr_\alpha \, r_\alpha^2 |\mathcal{F}^{n\mathbf{k}}_{lm\alpha}(r_\alpha)|^2 \delta(\omega - E_{n\mathbf{k}}), \tag{4.3}$$

where the sum is taken over all Kohn–Sham states $|\varphi_{n\mathbf{k}}\rangle$ with eigenenergies $E_{n\mathbf{k}}$. Here, indices l and m refer to specific angular characteristics rather than fixed quantum numbers l and m. For example, the component with $l = 1$ and $m = +1$ corresponds to the p_x-projected PDOS, $l = 1$ and $m = -1$ – to the p_y-projected PDOS, and $l = 1$ and $m = 0$ – to the p_z-projected PDOS.

Laser-dressed state

We now consider a crystal under a spatially uniform and temporally periodic electromagnetic field with the electric field $\mathbf{E}(t) = \mathbf{F}_0 \sin \Omega t$, where $\mathbf{F}_0$ is the amplitude. The Hamiltonian of the irradiated system is time-periodic and given by Eq. (2.61). We apply the Floquet–Bloch formalism [67, 120, 133–136] to describe the interaction of a material with the electromagnetic field beyond a perturbative regime as it was described in Section 2.3.2. According to the Floquet–Bloch theory, a solution of the corresponding time-dependent Schrödinger equation is a Floquet–Bloch state defined as follows:

$$\Psi_{i\mathbf{k}}(\mathbf{r}, t) = \frac{1}{\sqrt{V}} e^{-i\mathcal{E}_{i\mathbf{k}} t} \sum_\mu \sum_n C^i_{n\mathbf{k}\mu} e^{-i\mu\Omega t} \varphi_{n\mathbf{k}}(\mathbf{r}). \tag{4.4}$$

Here, $\mathcal{E}_{i\mathbf{k}}$ is the corresponding quasienergy of the Floquet–Bloch state, and the wavefunction is normalized to the system volume V. The coefficients $C^i_{n\mathbf{k}\mu}$ are determined by diagonalization of a Floquet–Bloch Hamiltonian.

DOS of the irradiated electronic system is given by

$$D(\omega, t) = \frac{1}{2\pi} \sum_{\mathbf{k}} \mathrm{Tr} \hat{A}_{\mathbf{k}}(\omega, t), \tag{4.5}$$

where $\hat{A}_{\mathbf{k}}(\omega, t)$ is a spectral function that has the form

$$\hat{A}_{\mathbf{k}}(\omega, t) = \int_{-\infty}^{\infty} d\tau e^{i\omega\tau} \sum_i |\Psi_{i\mathbf{k}}\left(t + \frac{\tau}{2}\right)\rangle \langle \Psi_{i\mathbf{k}}\left(t - \frac{\tau}{2}\right)| \tag{4.6}$$

in the non-interacting limit [166]. For the one-body Floquet–Bloch electronic states defined in Eq. (4.4), the spectral function in Eq. (4.6) takes the form

$$\hat{A}_{\mathbf{k}}(\omega, t) = \frac{2\pi}{V} \sum_{i,\mu} e^{i\mu\Omega t} \sum_{n_1, n_2, \mu'} C^{i*}_{n_2\mathbf{k}\mu'+\mu} C^{i}_{n_1\mathbf{k}\mu'} |\varphi_{n_1\mathbf{k}}\rangle \langle \varphi_{n_2\mathbf{k}}| \, \delta\Big(\omega - [\mathcal{E}_{i\mathbf{k}} + (\mu' + \mu/2)\Omega]\Big). \tag{4.7}$$

The PDOS can be obtained using the spectral function according to Eq. (4.5). Analogously to the definition of a PDOS in a field-free case, we find a laser-dressed PDOS by substituting $\varphi^{\mathrm{MT}}_{n\mathbf{k}}(\mathbf{r}_\alpha)$ instead of $\varphi_{n\mathbf{k}}(\mathbf{r})$ in the expression for a Floquet–Bloch state in Eq. (4.4). We substitute the resulting spatially localized part of $\Psi_{i\mathbf{k}}(\mathbf{r}, t)$ into Eqs. (4.5) and (4.7) to obtain a laser-dressed PDOS. The time-dependent PDOS for the specific (lm)-component in the real spherical harmonics basis takes the form

$$\mathcal{D}^{\alpha}_{lm}(\omega, t) = \sum_{\mu} e^{i\mu\Omega t} \tilde{D}^{\alpha(\mu)}_{lm}(\omega), \tag{4.8}$$

where the amplitudes are defined as follows:

$$\tilde{D}^{\alpha(\mu)}_{lm}(\omega) = \frac{1}{V} \sum_{i\mathbf{k}} \sum_{n,\mu'} C^{i*}_{n\mathbf{k}\mu'+\mu} C^{i}_{n\mathbf{k}\mu'} \int_0^{R_\alpha} dr_\alpha r_\alpha^2 |\mathcal{F}^{n\mathbf{k}}_{lm\alpha}(r_\alpha)|^2 \delta\Big(\omega - [\mathcal{E}_{i\mathbf{k}} + (\mu' + \mu/2)\Omega]\Big). \tag{4.9}$$

We can further simplify the expression using the symmetry under the transformation $\mu \to -\mu$, noting that $\tilde{\mathcal{D}}^{\alpha(-\mu)}_{lm}(\omega) = \left(\tilde{\mathcal{D}}^{\alpha(\mu)}_{lm}(\omega)\right)^*$. This leads to the time-dependent laser-dressed PDOS of the form

$$\mathcal{D}^{\alpha}_{lm}(\omega, t) = \langle \mathcal{D}^{\alpha}_{lm}(\omega)\rangle + 2 \sum_{\mu \geq 1} \mathrm{Re}\left[e^{i\mu\Omega t} \tilde{D}^{\alpha(\mu)}_{lm}(\omega)\right] \tag{4.10}$$

with the amplitudes

$$\tilde{D}^{\alpha(\mu)}_{lm}(\omega) = \sum_{i\mathbf{k}} \sum_{n,\mu'} C^{i*}_{n\mathbf{k}\mu'+\mu} C^{i}_{n\mathbf{k}\mu'} \int_0^{R_\alpha} dr_\alpha r_\alpha^2 |\mathcal{F}^{n\mathbf{k}}_{lm\alpha}(r_\alpha)|^2 \delta\Big(\omega - [\mathcal{E}_{i\mathbf{k}} + (\mu' + \mu/2)\Omega]\Big). \tag{4.11}$$

The first term in Eq. (4.10) is the zero-order amplitude $\langle \mathcal{D}^{\alpha}_{lm}(\omega, t)\rangle = \tilde{D}^{\alpha(\mu=0)}_{lm}(\omega)$ that gives a PDOS averaged over the period T of the driving electromagnetic field. It captures the steady-state behavior of a system under a continuous periodic excitation. The second term in Eq. (4.10) is the time-dependent part of a PDOS. This term represents the oscillating part of the response and comes from the interference between different modes of the one-body

Floquet–Bloch state.

Time-reversal symmetry can be used to further simplify the time-dependence of a PDOS. If an electronic system with time-reversal symmetry is driven by a linearly polarized pulse of the form $\mathbf{E}(t) = \mathbf{F}_0 \sin \Omega t$, a property of the Floquet–Bloch coefficients $c^i_{n\mathbf{k}\mu} = (-1)^\mu \left(c^i_{n-\mathbf{k}\mu}\right)^*$ derived in [69] applies, and for a system with time-reversal symmetry it is also true that $F^{n\mathbf{k}}_{lm\alpha}(r_\alpha) = (-1)^m \left[F^{n-\mathbf{k}}_{l-m\alpha}(r_\alpha)\right]^*$. This relates the terms at opposite $\mathbf{k}$ in the sum in Eq. (4.11) as complex conjugates multiplied by a factor $(-1)^\mu$. The amplitudes of a PDOS are then real for even orders and are imaginary for odd orders, which leads to

$$\mathcal{D}^\alpha_{lm}(\omega, t) = \langle \mathcal{D}^\alpha_{lm}(\omega) \rangle - \sum_{\mu_{\text{odd}} \geq 1} \mathcal{D}^{\alpha(\mu_{\text{odd}})}_{lm}(\omega) \sin(\mu_{\text{odd}} \Omega t) + \sum_{\mu_{\text{even}} \geq 2} \mathcal{D}^{\alpha(\mu_{\text{even}})}_{lm}(\omega) \cos(\mu_{\text{even}} \Omega t), \tag{4.12}$$

where $\mathcal{D}^{\alpha(\mu_{\text{odd}})}_{lm}(\omega) = 2 \operatorname{Im}\left(\tilde{D}^{\alpha(\mu_{\text{odd}})}_{lm}(\omega)\right)$ and $\mathcal{D}^{\alpha(\mu_{\text{even}})}_{lm}(\omega) = 2 \operatorname{Re}\left(\tilde{D}^{\alpha(\mu_{\text{even}})}_{lm}(\omega)\right)$ are real-valued amplitudes.

Eq. (4.12) introduces a generalized momentum and angular resolved partial density of states, $\mathcal{D}^\alpha_{lm}(\omega, t)$, which is time dependent due to the external electric field. Whether a measurement probes generalized PDOS or its weighted time average depends on the various time scales of the particular experiment; here we focus on the full time dependence because it contains the most information. Note that in the non-equilibrium case in general, the quantity $D(\omega, t)$ defined in Eq. (4.5) can turn out to be negative and can not be interpreted as the density of states. However, following from the properties of Floquet–Bloch coefficients [120], the absolute value of $\mathcal{D}^{\alpha(\mu)}_{lm}(\omega)$ decreases progressively with increasing order μ, leading to a positive semidefinite function $\mathcal{D}^\alpha_{lm}(\omega, t)$ defined by Eq. (4.12), which justifies the interpretation as a time-dependent partial density of states.

4.2.2. Electron density for a selected energy window

In the following we analyze the oscillations of the laser-dressed PDOS by comparing them to the laser-dressed electron density introduced by Eq. (2.80). We additionally introduce the electron density corresponding to a selected energy window defined in terms of the spectral function as

$$\rho(\mathbf{r}, \omega, t) = \frac{1}{2\pi} \sum_{\mathbf{k}} \langle \mathbf{r} | \, \hat{A}_{\mathbf{k}}(\omega, t) \, | \mathbf{r} \rangle \, . \tag{4.13}$$

The spectral function for the one-body Floquet–Bloch electronic states is given by Eq. (4.7). Substituting this expression into the definition of the electron density for a certain energy window in Eq. (4.13) gives:

$$\rho(\mathbf{r}, \omega, t) = \rho_0(\mathbf{r}, \omega) + \sum_{\mu \geq 1} 2 \operatorname{Re}\left[e^{i\mu\Omega t} \tilde{\rho}_\mu(\mathbf{r}, \omega)\right], \tag{4.14}$$

where the amplitudes $\tilde{\rho}_\mu(\mathbf{r},\omega)$ are defined as follows:

$$\tilde{\rho}_\mu(\mathbf{r},\omega) = \frac{1}{V}\sum_{i,\mathbf{k}}\sum_{n_1,n_2}\sum_{\mu'} C^{i*}_{n_2\mathbf{k},\mu'+\mu} C^{i}_{n_1\mathbf{k},\mu'} \varphi_{n_1\mathbf{k}}(\mathbf{r})\varphi^*_{n_2\mathbf{k}}(\mathbf{r})\delta\left(\omega - \left[\mathcal{E}_{i\mathbf{k}} + \left(\mu' + \frac{\mu}{2}\right)\Omega\right]\right). \tag{4.15}$$

Here, we use the symmetry property of the harmonics $\tilde{\rho}_{-\mu}(\mathbf{r},\omega) = \left(\tilde{\rho}_\mu(\mathbf{r},\omega)\right)^*$. Additionally, if an electronic system with time-reversal symmetry is driven by a linearly polarized pulse of the form $\mathbf{E}(t) = \mathbf{F}_0 \sin\Omega t$, a property $C^i_{n\mathbf{k}\mu} = (-1)^\mu (C^i_{n-\mathbf{k}\mu})^*$ derived in [69] applies. This relates the terms with a positive and negative $\mathbf{k}$ in the sum in Eq. (4.15) as complex conjugates multiplied by a factor $(-1)^\mu$. The amplitudes of the electron density for an energy window are then real for even orders and are imaginary for odd orders, which leads to

$$\begin{aligned}\rho(\mathbf{r},\omega,t) = \langle\rho(\mathbf{r},\omega,t)\rangle &- \sum_{\mu_{\text{odd}}\geq 1}\rho_{\mu_{\text{odd}}}(\mathbf{r},\omega)\sin(\mu_{\text{odd}}\Omega t) \\ &+ \sum_{\mu_{\text{even}}\geq 2}\rho_{\mu_{\text{even}}}(\mathbf{r},\omega)\cos(\mu_{\text{even}}\Omega t),\end{aligned} \tag{4.16}$$

where $\rho_{\mu_{\text{odd}}}(\mathbf{r},\omega) = 2\,\text{Im}\left(\tilde{\rho}_{\mu_{\text{odd}}}(\mathbf{r},\omega)\right)$ and $\rho_{\mu_{\text{even}}}(\mathbf{r},\omega) = 2\,\text{Re}\left(\tilde{\rho}_{\mu_{\text{even}}}(\mathbf{r},\omega)\right)$ are real-valued amplitudes. Later we use the introduced electron density for a selected energy window to interpret the bonding formation following from the laser-dressed PDOS.

4.3. Laser-dressed partial density of states of ZnO

We illustrate how a laser-dressed PDOS can be used to analyze the optical response of a laser-driven material with calculations for a wurtzite ZnO crystal. Wurtzite ZnO has served as a prototypical system for studying strong-field phenomena in solids, where distinctly non-perturbative nonlinear responses have been observed at driving laser intensities exceeding 1 TW/cm^2 [187]. Here, we consider the driving electromagnetic field with an intensity of 5 TW/cm^2, a photon energy of 1.55 eV, and the electric field polarization $\boldsymbol{\epsilon}$ aligned along the z axis.

We first discuss PDOS of a wurtzite ZnO in the ground state. Fig. 4.1(b) shows the calculated PDOS of the valence states, which is in good agreement with the calculations in Ref. [188]. The valence region is dominated by electronic states of strong O $2p$ and Zn $3d$ character. The d states splitting due to the tetrahedral environment around the Zn atom leads to the t_{2g} and e_g peaks at energies -4.75 eV and -5.7 eV below the Fermi level. The e_g states hybridize with the O $2p$ states to form bonding and antibonding states.

Assuming that the dynamics is launched by a pulse with a slowly changing envelop and with our conditions of the sub-gap-driving, the electron dynamics is launched adiabatically [189]. The Floquet–Bloch states that have a maximum overlap with the valence electronic state are occupied and determine the laser-driven dynamics. We analyze the corresponding

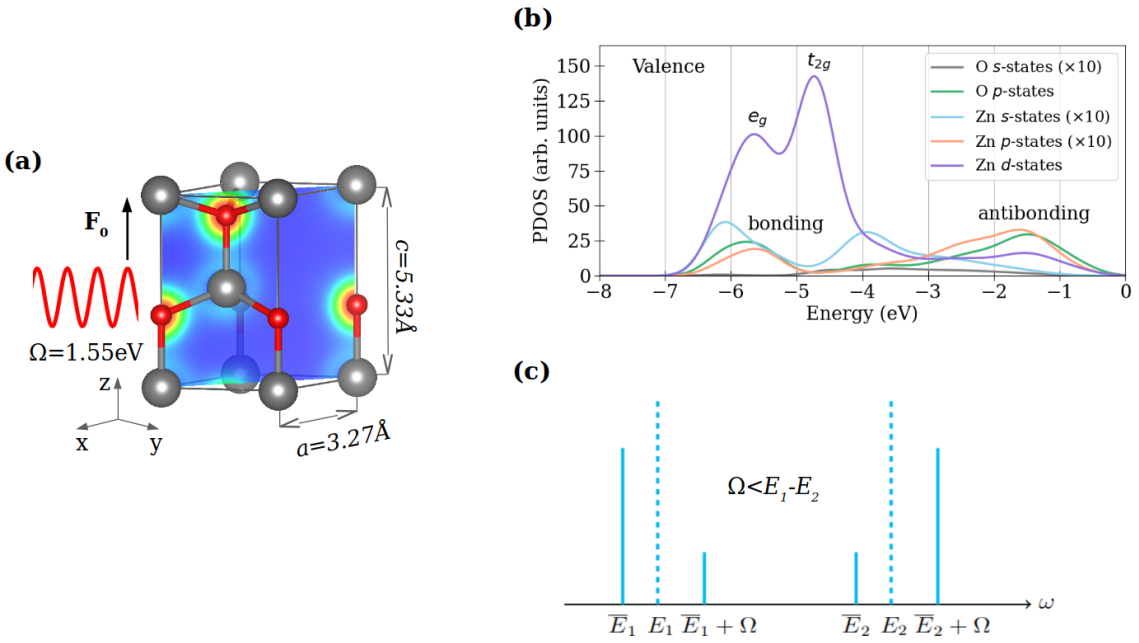

Figure 4.1.: (a) Unit cell of a wurtzite ZnO, where the red spheres represent O and the gray spheres represent Zn, and a cut through the electron density. This and the following densities are visualized using VESTA [156]. (b) PDOS of a wurtzite ZnO in the ground state. The Zn *s*-, *p*-, and O *s*-projected PDOS are magnified by a factor of ten. The Fermi energy, E_F, is set to 0 eV. (c) Illustration of the DOS of the two-level laser-driven system. The laser-dressed DOS is shown in solid lines next to the DOS in the absence of laser driving in dotted lines. Adapted from Ref. [158].

PDOS of these states. Fig. 4.2 shows the laser-dressed PDOS of the states that have emerged from the valence states shown in Fig. 4.1(b). Each pair of plots in Fig. 4.2 shows a time-averaged PDOS next to a corresponding field-free PDOS in the left panels and the time-dependent part of the PDOS in the right panels. We refer to $\mathcal{D}^{\alpha}_{lm}$ as the projection-resolved PDOS and to the sum of the corresponding orbital-projected PDOS, $\sum_m \mathcal{D}^{\alpha}_{lm}$, as the projection-unresolved PDOS. The total laser-dressed PDOS, which is the sum of the time-averaged and time-dependent parts, is positive for all energies. Since the driving electromagnetic field is polarized along the z axis, we consider separately the PDOS projected on the oxygen p_z orbitals aligned along the electric field and the oxygen p_x orbitals aligned perpendicular to the electric field. The O p_x-projected PDOS is identical to the PDOS projected on the oxygen p_y orbitals. We also consider separately the PDOS projected on the zinc d_{z^2} orbitals and the sum of the PDOS projected on the remaining zinc d orbitals, which we denote as $\mathrm{D}^{\mathrm{Zn}}_{d_{r^2-z^2}}$ for the field-free case and $\mathcal{D}^{\mathrm{Zn}}_{d_{r^2-z^2}}$ for the laser-dressed case. Note that our choice of axes is different from the conventional choice of axes in the crystal field theory that explains the $e_g - t_{2g}$ splitting [190]. With our choice of axes, the d_{z^2} orbital contributes to both the e_g and t_{2g} peaks.

First, we notice that all time-averaged PDOSs below the ground-state Fermi level shift

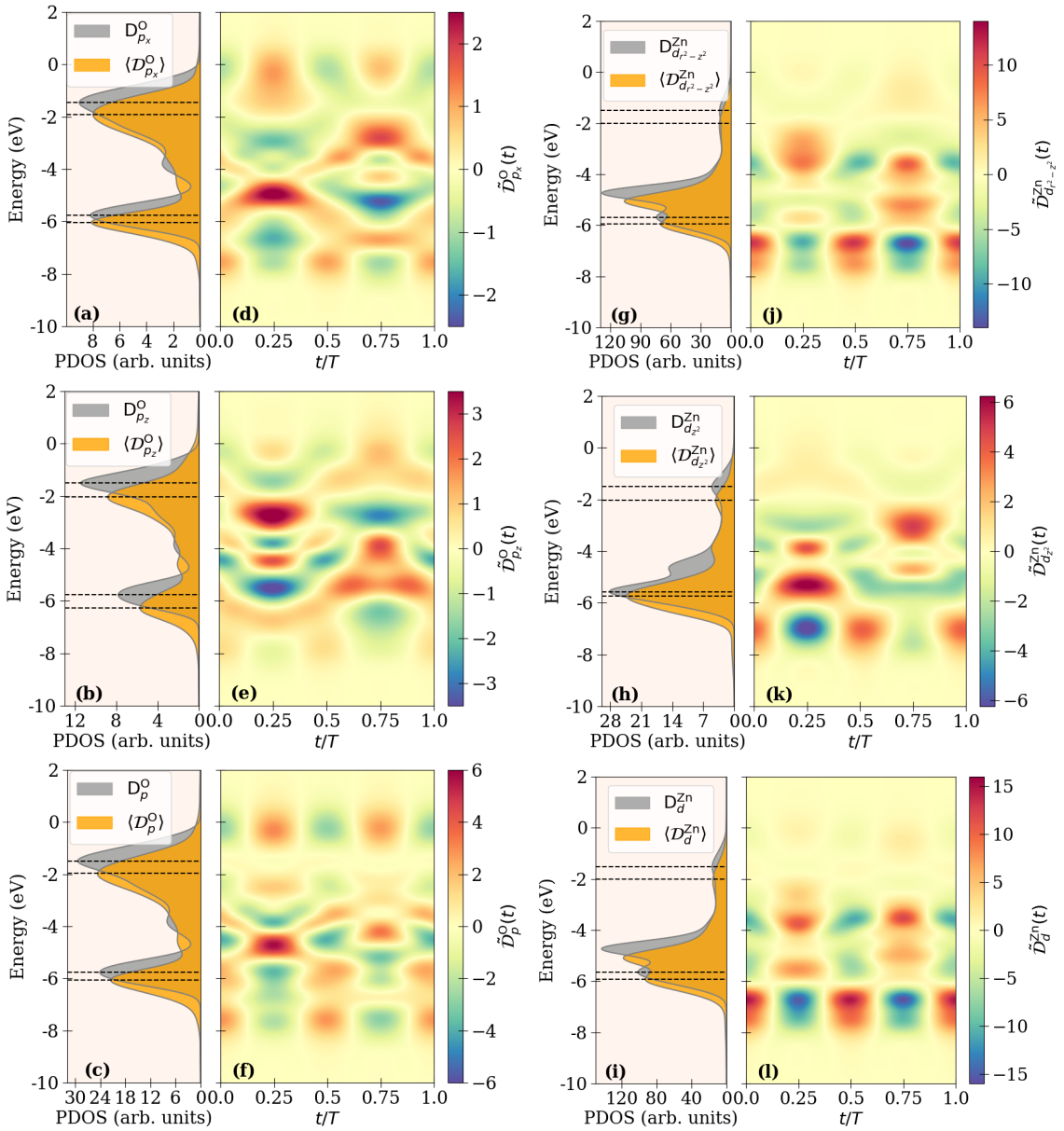

Figure 4.2.: Projection-resolved and -unresolved PDOS for oxygen p- and zinc d-orbitals. Field-free results are shown in gray, and time-averaged laser-dressed results are shown in orange. Panels (a)–(c) show the projections onto O p_x, O p_z, and total O p-states, respectively. Panels (d)–(f) display the corresponding time-dependent oscillatory components. Panels (g)–(i) repeat the same sequence for Zn d-orbitals: (g) shows all d-components except d_{z^2} referred to here as $d_{r^2-z^2}$; (h) is the d_{z^2} orbital; and (i) is the total Zn d-state contribution. Panels (j)–(l) present the time-dependent parts for the same orbitals shown in (g)–(i). Adapted from Ref. [158].

towards higher binding energies when compared with the field-free PDOS. The dashed lines in Fig. 4.2 go through the maxima of the laser-dressed and field-free PDOSs. This shows that the energy shift values vary depending on the binding energy and projection.

The variation in the values of the energy shifts can be understood with the help of a

two-level system. Let us consider a system with the energies E_1 and E_2 and corresponding wavefunctions $\phi_1(\mathbf{r})$ and $\phi_2(\mathbf{r})$ driven by a single-mode electromagnetic field with the frequency $\Omega < E_2 - E_1$. The system of the matter and the light has states with the energies that are different from E_1 and E_2. This phenomenon is the optical Stark effect [191]. The shifted energy levels $\overline{\mathcal{E}}_{1,2}$ obtained in the RWA and taking only one-photon absorption processes into account are given by [132]:

$$\begin{aligned}\overline{\mathcal{E}}_1 &= E_1 - \frac{\sqrt{\Delta^2 + \Omega_R^2} - \Delta}{2}, \\ \overline{\mathcal{E}}_2 &= E_2 + \frac{\sqrt{\Delta^2 + \Omega_R^2} - \Delta}{2} - \Omega.\end{aligned} \tag{4.17}$$

Here, $\Delta = E_2 - E_1 - \Omega$ is the detuning and Ω_R is the Rabi frequency. The corresponding eigenstates are given by [132]:

$$\begin{aligned}|\overline{\Psi}_1\rangle &= \cos\Theta\,|1, N\rangle - \sin\Theta\,|2, N-1\rangle\,, \\ |\overline{\Psi}_2\rangle &= \sin\Theta\,|1, N\rangle + \cos\Theta\,|2, N-1\rangle\,.\end{aligned} \tag{4.18}$$

The basis states $|i, N-\mu\rangle$ are product states formed by the electronic states $|i = 1, 2\rangle$, and Fock states of the field $|N-\mu\rangle$. Here, $N-\mu$ is the number of photons in the mode of the considered single-mode field and $N \gg \mu$ is the number of the photons before the interaction with the electronic system. The coefficients in front of the basis states depend on the ratio of the detuning to the Rabi frequency via $\Theta = \arctan\left(\Omega_R/\Delta\right)/2$.

The connection of a laser-dressed picture to the Floquet picture has been discussed in Ref. [120]. The corresponding Floquet states (see Eq. (4.4)) are

$$\begin{aligned}\Psi_1(\mathbf{r}, t) &= \frac{e^{-i\overline{\mathcal{E}}_1 t}}{\sqrt{V}}\left(\cos\Theta\phi_1(\mathbf{r}) - \sin\Theta e^{-i\Omega t}\phi_2(\mathbf{r})\right), \\ \Psi_2(\mathbf{r}, t) &= \frac{e^{-i\overline{\mathcal{E}}_2 t}}{\sqrt{V}}\left(\sin\Theta\phi_1(\mathbf{r}) + \cos\Theta e^{-i\Omega t}\phi_2(\mathbf{r})\right).\end{aligned} \tag{4.19}$$

The density of states according to Eq. (4.5) is

$$\begin{aligned}D(\omega) = &\cos^2\Theta\delta(\omega - \overline{\mathcal{E}}_1) + \sin^2\Theta\delta\left(\omega - \left[\overline{\mathcal{E}}_1 + \Omega\right]\right) \\ &+ \sin^2\Theta\delta\left(\omega - \overline{\mathcal{E}}_2\right) + \cos^2\Theta\delta\left(\omega - \left[\overline{\mathcal{E}}_2 + \Omega\right]\right)\end{aligned} \tag{4.20}$$

and it is shown in Fig. 4.1(c). For the case of a nonresonant field, the parameter Θ remains small, so $\cos\Theta$ is noticeably larger than $\sin\Theta$. In this case, we can consider the state $|\Psi_1\rangle$ as the state that has emerged from the the state $|1\rangle$, and the state $|\Psi_2\rangle$ as the state that has emerged from the state $|2\rangle$. The first two terms of the DOS in Eq. (4.20) are then due to the state that has emerged from the ground state, while the last two terms are due to the state that has emerged from the excited state.

The DOS of the field-free two level system consists of two delta peaks $\delta(\omega - E_1) + \delta(\omega - E_2)$. With Eq. (4.20), we obtain that these peaks are split into four peaks in the laser-dressed case, see Fig. 4.1(c). Two of these peaks are the main intense peaks weighted by $\cos^2\Theta$ centered at the new energies $\overline{\mathcal{E}}_1$ and $\overline{\mathcal{E}}_2 + \Omega$, and each main peak has a side peak weighted by $\sin^2\Theta$. The intensity of the peaks in the laser-dressed DOS in Eq. (4.20) gives the probability of occupation of a particular electronic state. For example, the first two peaks in Eq. (4.20) are due to the Floquet state $|\Psi_1\rangle$. In this state, the occupation probability of the electronic state $|1\rangle$ is equal to $\cos^2\Theta$, and the occupation probability of the electronic state $|2\rangle$ is $\sin^2\Theta$. The nature of the side peak shifted by Ω can then be intuitively understood as an indication that the state $|2\rangle$ can be excited due to absorption of a photon with an energy Ω.

4.3.1. Time-averaged PDOS of ZnO

The main intense peaks in the PDOS shown in Fig. 4.2 are shifted relative to their positions in the field-free distributions, and the intensity of the peaks is reduced. This behaviour is analogous to that of the ground state peak in the DOS of the two-level system. Fig. 4.1(c) shows that the peak centered at E_1 in the field-free DOS shifts to a new energy position centered at $\overline{\mathcal{E}}_1$ and its intensity decreases from 1 to $\cos^2\Theta$. We also observe that the distributions are broader than those in the field-free case. This is due to the appearance of the side peaks. The large number of states leading to the broadening of the distribution means that individual side peaks are indistinguishable.

We observe similar behaviour in all averaged PDOS data shown in Fig. 4.2 except for the oxygen p_z-projected PDOS. States closer to the Fermi level experience a larger shift than the states with higher binding energies. This is consistent with the simple two-level model described previously. In this model, the Rabi frequency determines the strength of the coupling between the system and the electromagnetic field. If the Rabi frequency is much smaller than the detuning, $\Omega_R \ll \Delta$, then the energies of the state $|\Psi_1\rangle$ of the two-level system are approximated by $\overline{\mathcal{E}}_1 = E_1 - \Omega_R^2/(4\Delta)$. Thus, the energy shift is inversely proportional to the detuning. The states closer to the Fermi level experience a larger shift than states with higher binding energies. This is because the difference between the energies of the valence states close to the Fermi level and the excited states is smaller than the difference between states with higher binding energies and excited states. The detuning for states with higher binding energies is larger, resulting in a smaller energy shift. However, the behavior of the O p_z-projected PDOS is different, because the assumption $\Omega_R \ll \Delta$ does not apply to the states with a significant contribution of p_z-type states due to their strong coupling to the driving field.

The O p-Zn d antibonding peaks at around -1.5 eV in all data for the ground-state PDOS shown in Fig. 4.2 are synchronously shifted by about 0.5 eV in the corresponding time-averaged laser-dressed PDOS. The bonding peaks at about -6 eV in the PDOS projected

into the orbitals not aligned with the electric field, namely O p_x and Zn $d_{r^2-z^2}$, are also synchronously shifted by the value of about 0.2 eV (see Fig. 4.2(a) and (g)). However, the shift of the bonding peak differs in the PDOS projected into the orbitals aligned with the electric field (see Fig. 4.2(b) and (h)). This misalignment of the bonding peaks between the O p_z and Zn d_{z^2} orbitals in the laser-dressed ZnO indicates that hybridization between the orbitals is destroyed. This should result in a weaker Zn–O bond along the z-axis.

We demonstrate the bonding and antibonding characteristics of solids by calculating the electron density corresponding to a selected energy window, as described in Section 4.2.2. In particular, we compare the ground-state electron density for the energy window around the bonding peak in Fig. 4.3(a) with the time-averaged laser-dressed electron density for the energy window around the new position of the corresponding peak in Fig. 4.3(b). This comparison confirms the weakening of the bond. The difference is most evident in the 2D cuts at the boundaries of the unit cell. Figure 4.4 show the ground-state electron density

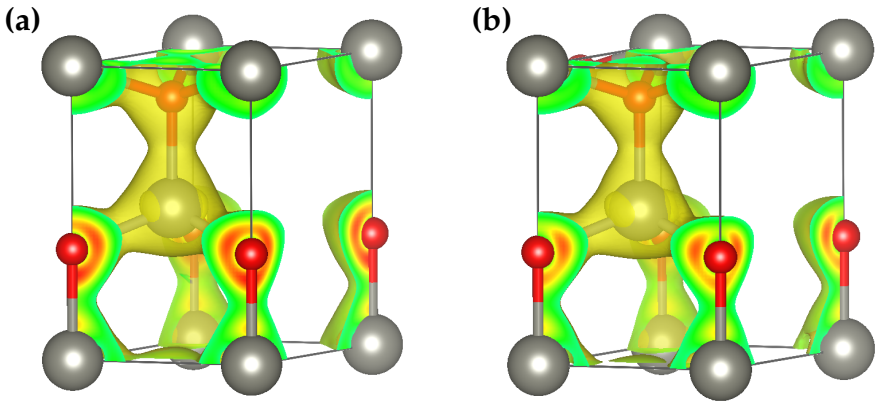

Figure 4.3.: (a) Ground-state and (b) time-averaged laser-dressed electron density corresponding to an energy window of bonding states. The same isosurface level is used for both panels. Adapted from Ref. [158].

for the energy window around the antibonding peak in Fig. 4.4(a) with the time-averaged laser-dressed electron density for the energy window around the new position of the corresponding peak in Fig. 4.4(b). The differences in the electron density is most evident in the 2D cuts at the boundaries of the unit cell. For consistency, the same isosurface level is used for all plots in both figures.

4.3.2. Time-dependent part of PDOS of ZnO

We use a simple two-level system to gain an understanding of the time-dependent part of the DOS. First, we observe that the DOS of the two-level system considered in Eq. (4.20) is time-independent. We then introduce a hypothetical Floquet state with an energy $\mathcal{E}_\mathrm{h}$ that

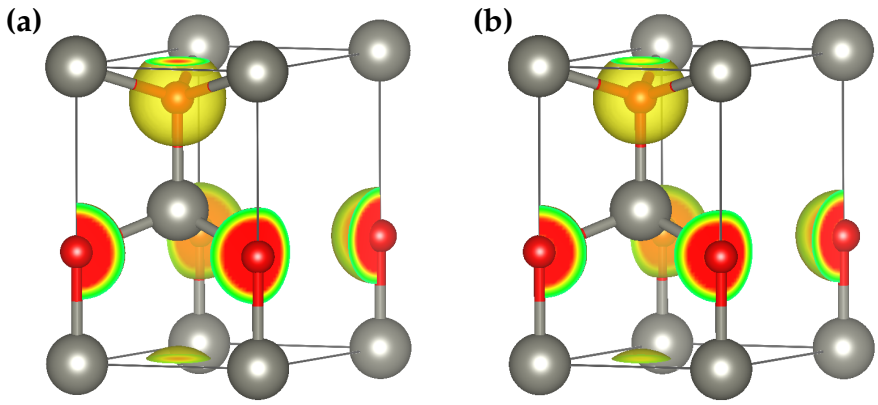

Figure 4.4.: (a) Ground-state and (b) time-averaged laser-dressed electron density corresponding to an energy window of antibonding states. The same isosurface value is used for both panels. Adapted from Ref. [158].

would result in a time-dependent DOS term

$$\Psi_\mathrm{h}(\mathbf{r},t) = \frac{e^{-i\mathcal{E}_\mathrm{h}t}}{\sqrt{V}}\left(C_{10}\phi_1(\mathbf{r}) + C_{11}\phi_1(\mathbf{r})e^{-i\Omega t} + C_{21}\phi_2(\mathbf{r})e^{-i\Omega t}\right). \tag{4.21}$$

The DOS that is due to only this Floquet state and its replicas is

$$\begin{aligned} D_\mathrm{h}(\omega,t) =& |C_{10}|^2\delta(\omega-\mathcal{E}_\mathrm{h}) + \left(|C_{11}|^2+|C_{21}|^2\right)\delta\left(\omega-[\mathcal{E}_\mathrm{h}+\Omega]\right) \\ &+ 2\,\mathrm{Re}\left(C_{11}^* C_{10} e^{i\Omega t}\right)\delta\left(\omega-[\mathcal{E}_\mathrm{h}+\Omega/2]\right). \end{aligned} \tag{4.22}$$

In Eq. (4.22), the occupation probability of the state $|1\rangle$ is equal to $|C_{10}|^2 + 2\,\mathrm{Re}\left(C_{11}^* C_{10} e^{i\Omega t}\right)$, where the time-dependent term has an intensity of $2\,\mathrm{Re}\left(C_{11}^* C_{10} e^{i\Omega t}\right)$. Thus, we can conclude that the time-dependent part of the DOS is related to the time-dependent part of the occupation probability of an electronic state. This conclusion can be generalized by considering the occupation probabilities of the electronic states $|n\mathbf{k}\rangle$ of a system occupying a Floquet state $|\Phi_{i\mathbf{k}}\rangle$. In this case, the time-dependent part of the DOS contains the interference terms of the occupation probabilities of the different electronic states $|n\mathbf{k}\rangle$.

The spectral position of the time-dependent term in the DOS in Eq. (4.22) is in the middle between the energy of the main peak at $\mathcal{E}_\mathrm{h}$ and its side peak at $\mathcal{E}_\mathrm{h}+\Omega$. In general, the interference terms are centred at $\mathcal{E}_{i\mathbf{k}} + (\mu' + \mu/2)\Omega$ for $\mu \neq 0$ according to Eq. (4.11), which is either in the middle between a main peak and its side peaks, or in the middle between side peaks. We observed the analogous behavior of a signal due to an optical dressing in our study of subcycle-resolved x-ray diffraction [150]. We showed that the time-dependent signal in this process consists of peaks with time-independent amplitudes and interference peaks with time-dependent amplitudes. The peaks with time-independent amplitudes are shifted by $n\Omega$ from a ground-state signal, where n is an integer. The interference peaks are centered right in the middle between the spectral positions of the time-independent peaks, *i.e.* are shifted by $n\Omega/2$. Thus, the behavior of the laser-dressed DOS is related to

the behavior of time-dependent, subcycle-resolved spectra of laser-driven systems.

Colormaps in Figs. 4.2(d)-(f) and 4.2(j)-(l) show the time-dependent part of the PDOS. The total PDOS is the sum of the time-dependent part and the time-averaged part shown on the corresponding panels to the left of the colormaps [Figs. 4.2(a)- (c) and 4.2(g)-(i)]. The total PDOS is positive at any given energy. We observe that the projection-resolved O p_x-, p_z-projected PDOS and Zn d_{z^2}-, $d_{r^2-z^2}$-projected PDOS shown in Figs. 4.2(d), (e), (j) and (k) have energy regions with oscillations at the frequency of both Ω and 2Ω. However, the projection-unresolved O p-projected PDOS shown in Fig. 4.2(f) and Zn d-projected PDOS shown in Fig. 4.2(l) predominantly oscillate at the frequency 2Ω. The absence of oscillations at frequency Ω in projection-unresolved distributions indicates that charge oscillations of frequency Ω around zinc and oxygen cancel out after angle averaging.

First-order optical response

We analyze the oscillations of the PDOS by comparing them to the oscillations of the laser-dressed electron density, as defined by Eqs. (2.80) and (2.81). For a material with time-reversal symmetry, driven by an electromagnetic field with an electric field of the form $\mathbf{E}(t) = \mathbf{F}_0 \sin \Omega t$, this takes the following form [69]:

$$\rho(\mathbf{r}, t) = \rho_0(\mathbf{r}) - \sum_{\mu_{\text{odd}} \geq 1} \rho_{\mu_{\text{odd}}}(\mathbf{r}) \sin(\mu_{\text{odd}} \Omega t) + \sum_{\mu_{\text{even}} \geq 2} \rho_{\mu_{\text{even}}}(\mathbf{r}) \cos(\mu_{\text{even}} \Omega t). \tag{4.23}$$

Here, $\rho_0(\mathbf{r})$ is the time-averaged electron density and $\rho_\mu(\mathbf{r})$ are the real-valued amplitudes of the oscillations. A μth-order amplitude of the electron density leads to a μth-order oscillation amplitude of polarization. For example, $-\rho_1(\mathbf{r}) \sin(\Omega t)$ leads to the oscillation of polarization as $\mathbf{P}^{(1)} \sin(\Omega t)$. The electron density and the PDOS have the analogous time dependence. The μth-order density amplitudes $\rho_\mu(\mathbf{r})$ are related to the μth-order amplitudes of PDOS $\mathcal{D}^{\alpha}_{lm,\mu}(\omega)$ and describe the μth-order microscopic optical response of a material.

Figure 4.5(a) shows a two-dimensional cut through the first-order amplitude $\rho_1(\mathbf{r})$ (see also Fig. 4.6). Charges rearrange around atoms to form regions that are either positively or negatively charged. The positively- and negatively-charged regions switch their signs after half a cycle. Their magnitudes are maximal at $1/4$ and $3/4$ of the optical period, which is also when the first-order oscillations of the projection-resolved PDOS have maxima and minima in Figs. 4.2(d), (e), (j) and (k). Due to their interaction with the electric field of light, dipoles are formed around oxygen and zinc, giving rise to polarization parallel to the electric field. The net charges around zinc and oxygen remains almost neutral, despite considerable charge density distributions. Hence, the oscillations at the frequency Ω are effectively averaged out in the projection-unresolved PDOS in in Figs. 4.2(f) and (l), but

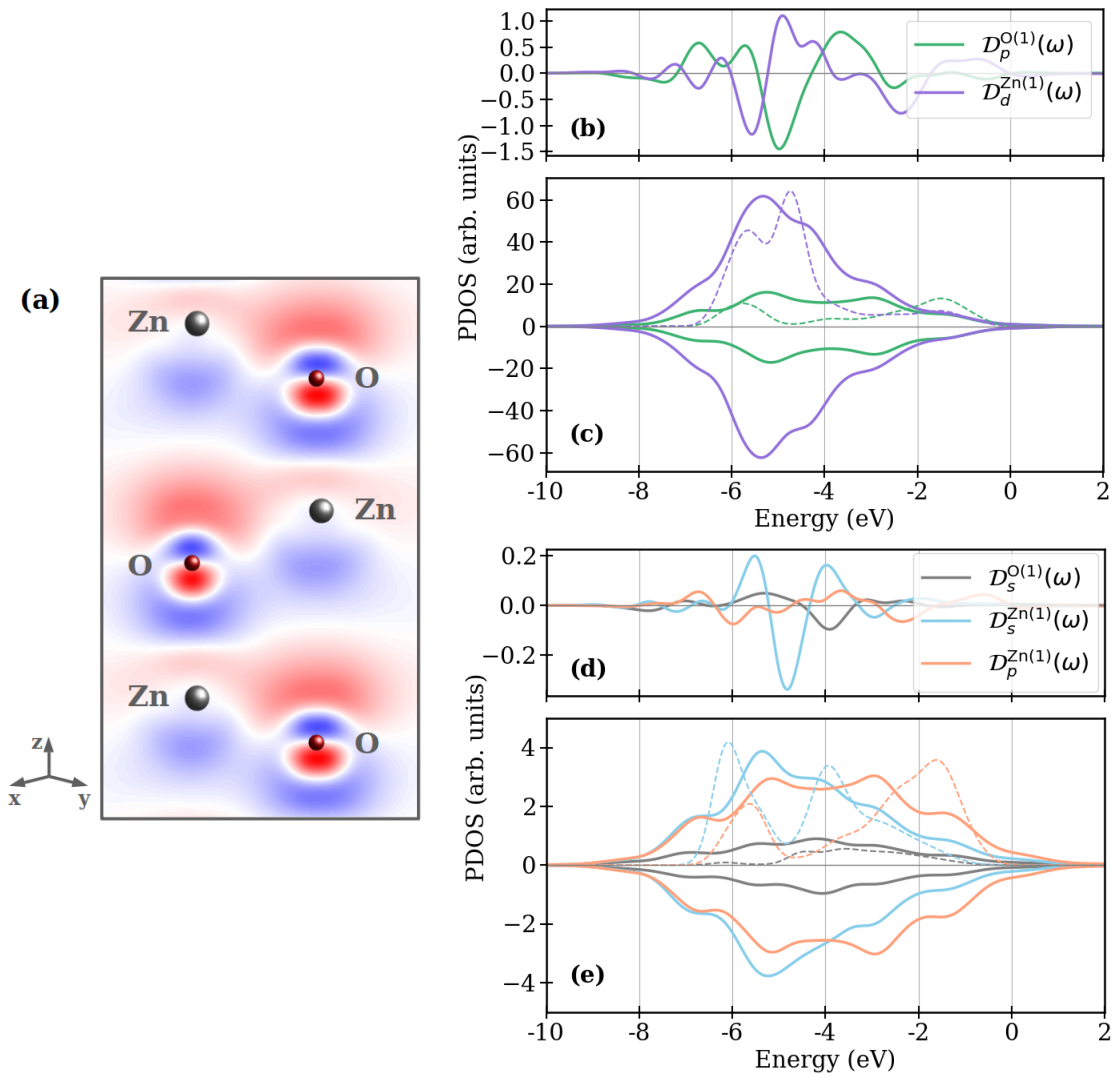

Figure 4.5.: First-order amplitudes of the electron density and the PDOS. (a) Two-dimensional cut through the first-order density amplitudes $\rho_1(\mathbf{r})$ in the plane shown in Fig. 4.1(a). The red and blue colors represent negative and positive charges, respectively. (b) First-order projection-unresolved amplitudes $\mathcal{D}_p^{\mathrm{O}(1)}(\omega)$ and $\mathcal{D}_d^{\mathrm{Zn}(1)}(\omega)$. (c) Positive and negative contributions to the projection-unresolved amplitudes in (b). (d) First-order amplitudes $\mathcal{D}_s^{\mathrm{O}(1)}(\omega)$, $\mathcal{D}_s^{\mathrm{Zn}(1)}(\omega)$, and $\mathcal{D}_p^{\mathrm{Zn}(1)}(\omega)$. (e) Positive and negative contributions to the amplitudes in (d). The dotted lines in (c) and (e) in a corresponding color show the ground-state PDOS with reduced amplitudes for ease of comparison. Adapted from Ref. [158].

are pronounced in the projection-resolved PDOS in Figs. 4.2(d), (e), (j) and (k).

We observe that bonds between positively-charged regions around zinc and oxygen as well as bonds between negatively-charged regions around zinc and oxygen are formed. We analyze the structure of the bonds using the first-order amplitudes of PDOS $\mathcal{D}_{lm}^{\alpha(1)}(\omega)$, *cf.* (4.12). Figure 4.5(b) shows projection-unresolved amplitudes $\mathcal{D}_p^{\mathrm{O}(1)}$ and $\mathcal{D}_d^{\mathrm{Zn}(1)}$. They

change sign several times over the energy range due to competing positive and negative contributions to the total distribution, which makes them difficult to analyze. To facilitate analysis, we disentangle the positive and negative contributions to the PDOS by summing the positive and negative terms separately in Eq. (4.11) during the calculations. The resulting contributions are shown in Fig. 4.5(c). The sum of the distributions in Fig. 4.5(c) gives the PDOS in Fig. 4.5(b). The positive contributions to the amplitudes of the PDOS correspond to a negative charge and the negative contributions correspond to a positive charge. Looking at the disentangled contributions to the PDOS, we can analyze how different orbitals contribute to the formation of optically-induced charge distributions due to the first-order optical response. The positive and negative distributions in Figs. 4.5(c) are almost identical, which reflects the similar shapes of the positive and negative regions in the first-order density amplitude.

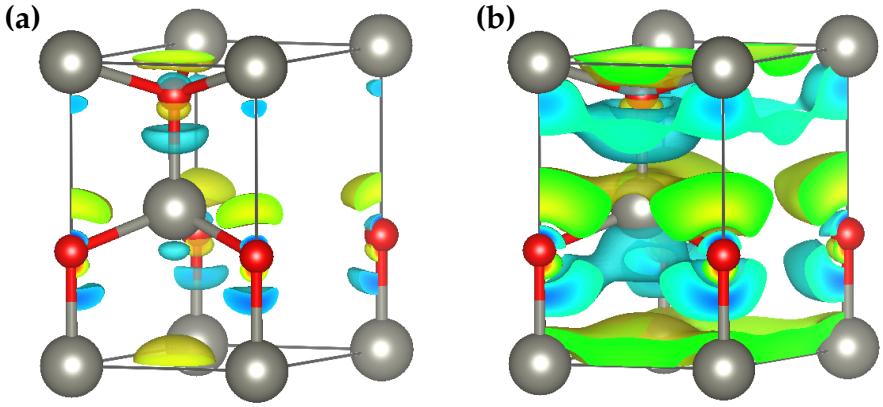

Figure 4.6.: **The first-order microscopic optical response of wurtzite ZnO.** The first-order optically-induced charge distribution $\rho_1(\mathbf{r})$ is shown for two different isosurface levels in panels (a) and (b). The electron densities are represented in terms of an isosurface using VESTA [156]. The yellow and blue colors represent negative and positive charges, respectively. Adapted from Ref. [158].

The laser-dressed first-order Zn *d*-projected PDOS in Fig. 4.5(c) consists of multiple peaks structure. The crystal field theory states that the *d* states splitting in ZnO is due to charges that are localized on oxygen atoms. In Fig. 4.5(a), there is still a small imbalance between the charges on zinc and oxygen, the net charge around zinc is positive and the net charge around oxygen is negative. This imbalance leads to a minor $e_g - t_{2g}$ splitting in the distribution. The electric field of the light polarized along the z axis breaks the symmetry of the tetrahedral field further. This leads to the additional splitting of the e_g and t_{2g} states, resulting in the five peaks of the *d*-projected PDOS. The positions of the peaks in the O *p*-projected PDOS and in the Zn *d*-projected PDOS in Fig. 4.5(c) continue to align. Thus, the O *p* - Zn *d* hybridized orbitals respond synchronously to the optical drive in the first-order optical response.

In the ground state, the O *s*-, Zn *s*-, and Zn *p*-projected PDOS are approximately one order of magnitude smaller than the O p- and Zn d-projected PDOS. Figure 4.5(d) shows the

first-order amplitude of the O s-, Zn s-, and Zn p-projected PDOS. Their weight relative to the Zn d- and O p-projected PDOS increases by about a factor of two in the first-order response. Dipole transitions from O p and Zn d states to O s and Zn p states explain the relative increase of the corresponding distributions. However, an analysis of dipole-allowed transitions alone is insufficient to explain transitions in a material with bonds. The relative increase of the Zn s-projected PDOS indicates that these states also contribute to the response via their contribution to hybridization.

Second-order optical response

Figure 4.7(a) shows the second-order density amplitude. The positively- and negatively-charged regions of this charge distribution have a completely different shape to those of the first order. A positive charge is formed on oxygen. This positive charge is surrounded by a negative charge that repeats the shape of the positive charge in the vicinity of the oxygen atom. Further away from oxygen, a strong bond with zinc along the z-axis is formed by a negative charge. Negative charges also form weak bonds with zinc atoms at other positions. Additionally, a delocalized positively charged region forms between the zinc and oxygen atoms (see Fig. 4.8(b)). The charge around the zinc atom is negative. Note that the second-order density amplitude corresponds to the oscillations at a frequency of 2Ω. After a quarter of the optical cycle, the positively and negatively charged regions switch signs.

As shown in Fig. 4.7(c), the shapes of the positive and negative contributions to the second-order PDOS are also quite different. As a result, their sum leads to a considerable total second-order O p- and Zn d-projected PDOS amplitudes, as shown in Fig. 4.7(b). This is much larger than the corresponding first-order projection-unresolved PDOS amplitude. For this reason, oscillations at the 2Ω frequency dominate the time evolution of the projection-unresolved PDOS in Figs. 4.2(f) and (l).

The positive contribution to the Zn d-projected PDOS amplitude, which corresponds to the negative charge, splits into two broad peaks. This is due to the nonuniform distribution of negative charges around Zn; see Fig. 4.7(a) and Fig. 4.8(b). Orbitals localized on zinc are more strongly repelled by the negative charge around oxygen in the z direction than by the charges around other oxygen atoms. In contrast, the negative contribution to the Zn d-projected PDOS amplitude contains only the higher-energy peak and has no strongly bound peak. This indicates that the positively charged region formed by Zn d orbitals is surrounded by a more homogeneous distribution of charges than the negatively charged regions. In Fig. 4.8, the positive delocalized charge between the zinc and oxygen atoms is surrounded by a nearly uniformly distributed negative charge. This likely explains why the splitting of the Zn d-projected PDOS is considerably smaller in the negative than in the positive contribution.

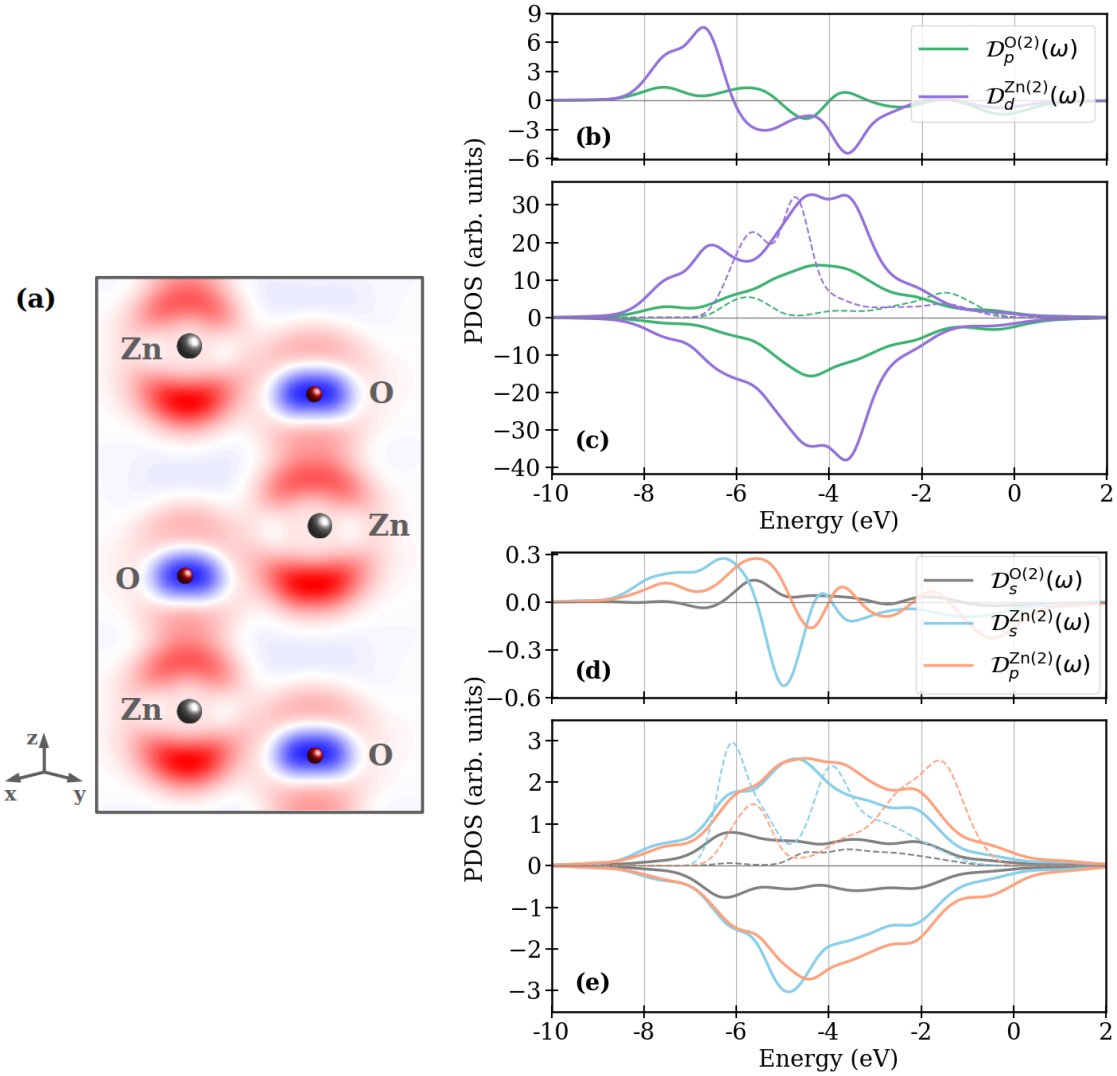

Figure 4.7.: Second-order amplitudes of the electron density and the PDOS. (a) Two-dimensional cut through the second-order density amplitudes $\rho_2(\mathbf{r})$ in the plane shown in Fig. 4.1(a). The red and blue colors represent negative and positive charges, respectively. (b) Second-order projection-unresolved amplitudes $\mathcal{D}_p^{\mathrm{O}(2)}(\omega)$ and $\mathcal{D}_d^{\mathrm{Zn}(2)}(\omega)$. (c) Positive and negative contributions to the projection-unresolved amplitudes in (b). (d) Second-order amplitudes $\mathcal{D}_s^{\mathrm{O}(2)}(\omega)$, $\mathcal{D}_s^{\mathrm{Zn}(2)}(\omega)$, and $\mathcal{D}_p^{\mathrm{Zn}(2)}(\omega)$. (e) Positive and negative contributions to the amplitudes in (d). The dotted lines in (c) and (e) in a corresponding color show the ground-state PDOS with reduced amplitudes for ease of comparison. Adapted from Ref. [158].

The second-order amplitude of the O p-projected PDOS has a broad, multi-peaked structure. These peaks coincide with those in the second-order amplitude of the Zn d-projected PDOS, indicating orbital interaction. The maximum of the peak is at a higher binding energy for positive charge than for negative charge. The positive charge is more localized around oxygen than the negative charge, which explains the difference in binding energies.

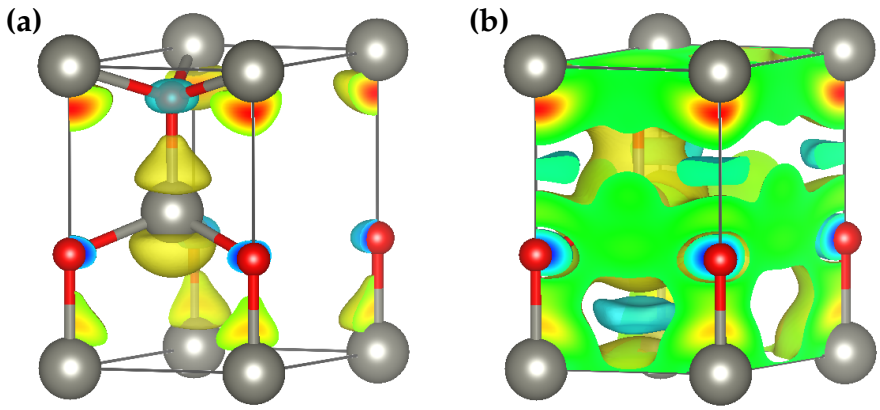

Figure 4.8.: **The second-order microscopic optical response of wurtzite ZnO.** The second-order optically-induced charge distribution $\rho_2(\mathbf{r})$ is shown for two different isosurface levels in panels (a) and (b). The electron densities are represented in terms of an isosurface using VESTA [156]. The yellow and blue colors represent negative and positive charges, respectively. Adapted from Ref. [158].

The weight of O s-, Zn s- and Zn p-projected PDOS relative to Zn d- and O p-projected PDOS increase again in the second-order response, see Fig. 4.7(e). The relative contributions of these states are about four times larger compared to the ground state. The increase of the role of Zn s-like states is due to two-photon transitions from Zn d states. The increase of the relative weights of O s- and Zn p-projected PDOS should be via bonds that involve these states. Additionally, it should be due to an increasing role of two-photon transitions from Zn $3p$-like states and O $2s$-like states to unoccupied states of Zn p-like and O s-like character, correspondingly.

4.4. *Ab initio* computational scheme

Figure 4.9 illustrates the computational workflow for the calculation of the laser-dressed PDOS.

Since the laser-dressed PDOS is calculated to support the interpretation of the transient x-ray absorption spectra, we adopted the same numerical parameters that were obtained from the convergence study of x-ray absorption in Section 5.5. Thus, the PDOS was calculated using 150 conduction states, $2\mu_{\max}+1 = 121$ Floquet blocks, and a $16 \times 16 \times 10$ $\mathbf{k}$-point grid. In this way, the description of the electronic structure entering the PDOS calculations is consistent with that used for the absorption spectra.

The workflow starts with ground-state calculations of wurtzite ZnO. The one-body wavefunctions $\varphi_{n\mathbf{k}}(\mathbf{r})$ and the corresponding eigenenergies $E_{n\mathbf{k}}$ of the field-free Hamiltonian $H^{(0)}$ are obtained using the LAPW+lo method as implemented in `exciting` [137]. We employ the GGA-PBE functional [151], and treat the Zn $3d^{10}4s^2$ and O $2s^22p^4$ electrons as valence states. In addition, the Zn $3p$ orbitals are included as semicore states in the basis

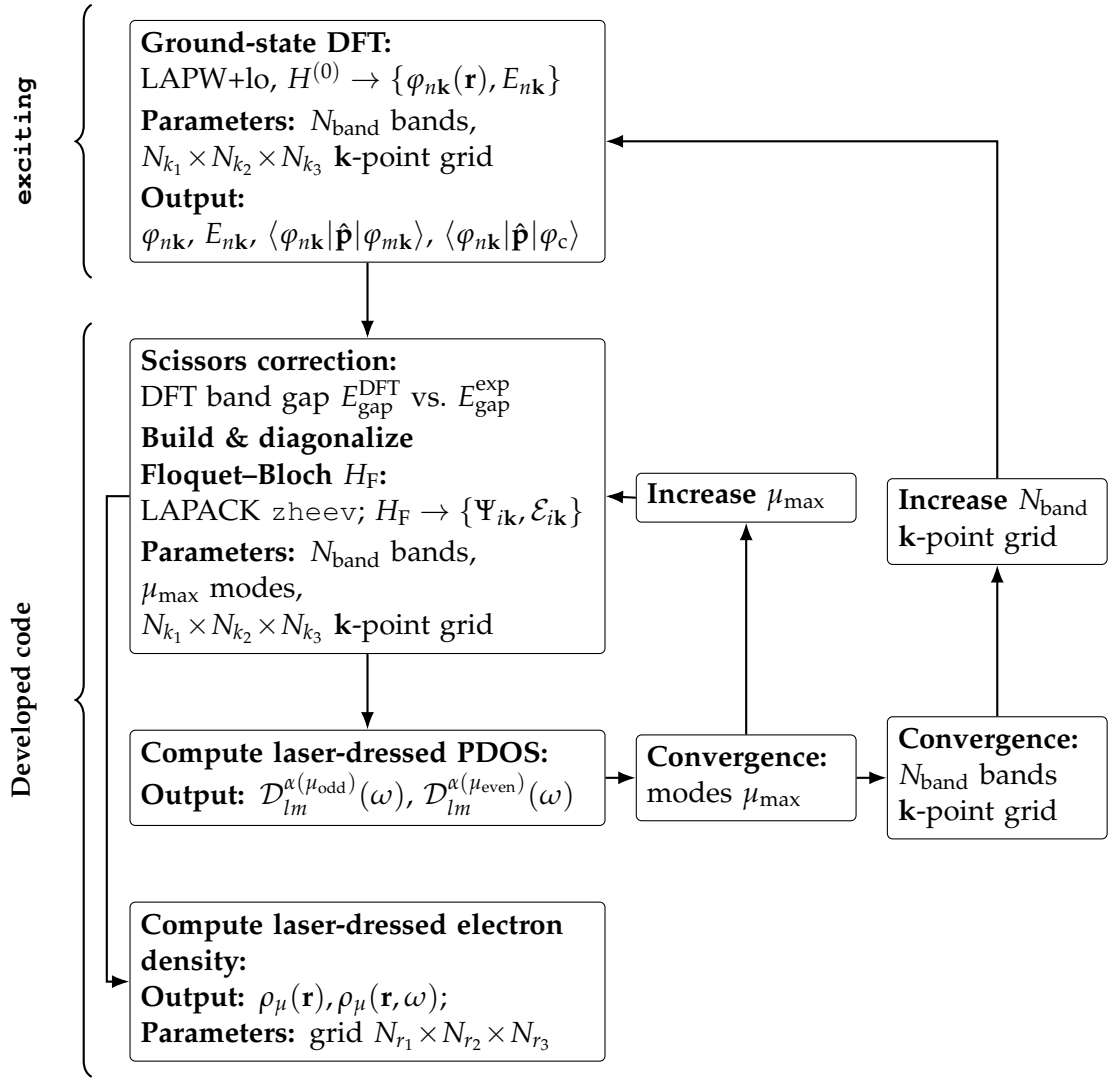

Figure 4.9.: *Ab initio* computational scheme for laser-dressed PDOS with left-side grouping braces indicating external (`exciting`) and developed code components.

within LAPW+lo method.

In the ground state output, a scissors correction [153] is applied to adjust the underestimated DFT band gap of 0.77 eV to the experimental value of 3.4 eV [192]. Previous GW calculations [188] have shown that the conduction-band DOS obtained within DFT GGA-PBE agrees well with GW results up to an overall energy shift, validating the use of the scissors operator for this purpose.

During the ground-state calculations we also calculate several quantities that are required in later steps of the workflow. These include the momentum matrix elements between different Kohn–Sham states, as well as radial atomic wavefunctions $u_{\ell\alpha}^{(j)}(r_\alpha)$, matching coefficients $A_{lm\alpha}^{\mathbf{G}+\mathbf{k}}$, and Kohn–Sham coefficients $C_{i\mathbf{G}}^{\mathbf{k}}$. From these, we can construct the radial wavefunctions $\mathcal{F}_{lm\alpha}^{n\mathbf{k}}(r_\alpha)$ and the plane-wave part of the Kohn–Sham wavefunctions.

The calculated Bloch wavefunctions, eigenenergies, and momentum matrix elements

are then used to construct and diagonalize the Floquet–Bloch Hamiltonian [133]. The diagonalization yields the Floquet–Bloch states together with their quasienergies. As mentioned above, the number of conduction states and Floquet blocks used here is taken from the x-ray absorption convergence study, ensuring consistency between the two types of calculations.

The eigenvalues and eigenvectors of the Floquet–Bloch matrix are used to evaluate the amplitudes of the laser-dressed PDOS. A Gaussian broadening with full width at half maximum (FWHM) of 0.6 eV is applied in the PDOS calculations. The number of **k**-points is increased in the computations until convergence of the amplitudes $\mathcal{D}_{lm}^{\alpha(\mu_{\mathrm{odd}})}(\omega)$ and $\mathcal{D}_{lm}^{\alpha(\mu_{\mathrm{even}})}(\omega)$ of the laser-dressed PDOS in Eq. (4.12) is reached. Figure 4.10 shows the results of the convergence study with respect to the number of **k**-points in the calculations. The laser-driven changes are found to be converged for a $16 \times 16 \times 10$ **k**-point grid. In

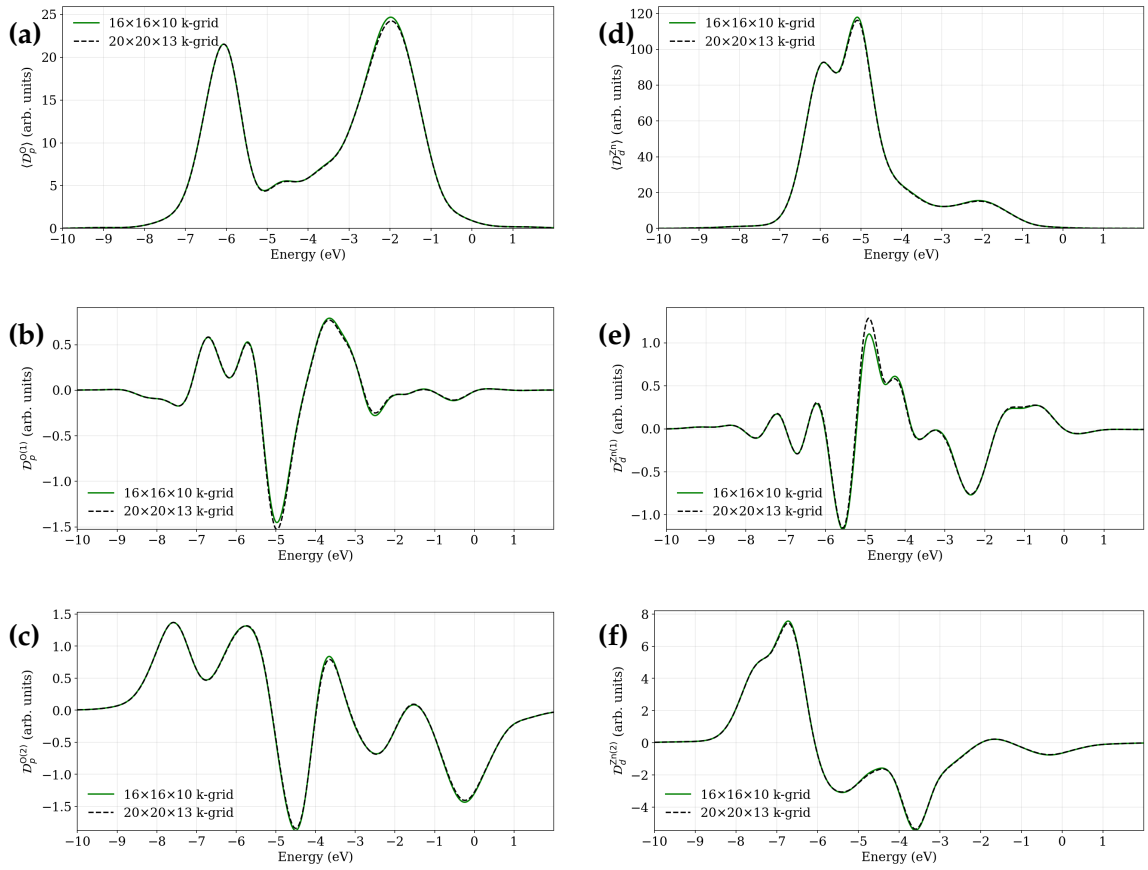

Figure 4.10.: Convergence with respect to the number of **k**-points for O p- and Zn d-projected PDOS: (a,d) zero order, (b,e) first order, (c,f) second order. The results were obtained using $20\times20\times13$ and $16\times16\times10$ **k**-point grids, with all spectra scaled by the number of **k**-points in each case.

addition, the laser-dressed electron density is evaluated using the formalism of Ref. [69]. The μth-order density amplitudes, $\rho_\mu(\mathbf{r})$, are computed by considering only the plane-wave part of the Kohn–Sham wavefunctions $\varphi_{n\mathbf{k}}(\mathbf{r})$. The calculations are performed on a spatial grid of $50 \times 50 \times 80$ points within single unit cell.

4.5. Summary

In this chapter, we introduce a computational framework for calculating the PDOS of a material subjected to a periodic driving field. Using a wurtzite ZnO crystal as an example, we demonstrate how laser-dressed PDOS can be used to analyse laser-driven electron dynamics. Our focus is on how initially occupied electronic states evolve into dressed states when the field is turned on adiabatically, since these states remain occupied and define electron dynamics.

Our results for laser-driven ZnO demonstrate a weakening of chemical bonds. By analyzing the laser-induced energy shifts resolved by site, orbital, and angular character, we find that under excitation the Zn d and O p states, which primarily form the bonding structure in the ground state, shift non-uniformly. In particular, the O p states have a larger blue-shift than the Zn d states at the energies corresponding to bonding states. This difference reduces orbital overlap and weakens the Zn–O bond. We further confirmed laser-driven bond weakening by calculating electron density for the energy window corresponding to the bonding state and observing a decrease in electron density along the Zn–O bond.

The time-dependent amplitudes of the PDOS provide a subcycle-resolved view of the electron dynamics, which is not accessible via a simple time-averaged DOS. We analyzed first- and second-order optical responses. This allowed us to track how the dynamics are defined by initially occupied states and how the relative weight of different orbital characters changes in the valence and conduction bands. We observed an increase in orbital characters that were not present in the ground state valence band, such as O s and Zn p. Under laser excitation, these states become partially occupied and appear in the laser-dressed valence band. We qualitatively explained these trends using dipole selection rules.

Within the presented framework, we can track changes to the material's electronic structure over time as it interacts with the laser. In the stationary case, the density of states shows which atomic orbitals are present at certain energies, providing insight into the material's electronic structure and bonding. Under a strong optical field, however, the electronic band structure becomes modulated. For example, Floquet sidebands appear and band energies oscillate over time. The laser-dressed PDOS offers a complementary real-space perspective on these effects, similar to that provided by a conventional PDOS for a stationary system.

5. X-ray absorption spectroscopy of the laser-driven materials

This chapter contains the developed theoretical framework and *ab initio* computational scheme to describe trXAS measurement from a material in the presence of a driving field. We introduce two approaches to calculate the absorption cross section, one based on the so-called projection treatment of x-ray absorption and the other based on the so-called time- and frequency-domain treatment of x-ray absorption. We compare the results of the two approaches with the corresponding laser-dressed PDOS to demonstrate how trXAS data can be used to extract information about laser-dressed electron dynamics. As a case study, we present calculations for laser-dressed wurtzite ZnO.

5.1. Introduction

The trXAS technique, which involves measuring the transient absorption spectrum in the x-ray range, has enabled the observation of electronic and structural dynamics on subfemtosecond timescale [79–82]. This technique has already been used to resolve electron, hole, and phonon dynamics in materials with subfemtosecond resolution, including during the time during the interaction with a driving pulse [7, 8, 86, 88, 89]. Here, we consider a pump-probe scheme in which pump pulse excites the electron dynamics. An attosecond XUV or x-ray probe pulse then captures these dynamics in the absorption spectrum [79, 83, 84]. By varying the time delay of the x-ray probe pulse, dynamic changes in the absorption edge can be tracked. This reveals, in the case of solids, the evolution of the carrier population and coupled electron-phonon dynamics during the action of the driving field [49, 85–87]. In the case of attosecond XAS [49], the high photon energy of the broadband XUV pulse, which typically lies above the energy range of interband transitions, offers an additional advantage. It enables simultaneous observation of laser-driven carrier dynamics in both the valence and conduction bands, thus avoiding the ambiguities often found in optical pump-probe spectroscopy due to overlapping spectral features. Additionally, broadband attosecond XUV or x-ray pulses allow measurements across several tens of eVs, potentially covering multiple absorption edges simultaneously. This provides a further advantage for probing non-equilibrium electron dynamics within the band structure of solid-state materials.

Interpreting XAS data can be challenging due to competing physical effects. These include core-hole decay and the associated Auger cascades, which significantly modify the absorption spectrum and need to be taken into account. Another complication is represented by

multiplet effects caused by multiple excitation pathways that an x-ray photon can induce in the system. In the case of solids, additional effects include low-energy electron-electron scattering and electron-phonon interactions. These challenges require advanced theoretical tools for the analysis. The theoretical description of x-ray absorption under stationary conditions is well established, with many powerful computational tools currently in use [193, 194]. However, the development of trXAS necessitates theoretical advancements in *ab initio* methods to accurately describe electron and lattice dynamics under non-equilibrium conditions, as well as the resulting XAS data.

RT-TDDFT is widely used to simulate electron dynamics in molecules and solids under external driving fields [90–94]. However, accurate treatment of core excitations within RT-TDDFT remains challenging. Additionally, capturing electronic correlation effects remains a significant challenge for DFT-based methods. Complementary approaches such as non-equilibrium Green's function methods, including the Bethe–Salpeter equation formalism, have been developed [98–106], though their application to trXAS in solids remains limited. In practice, most descriptions combine computational time propagation under the pump with a perturbative treatment of the probe pulse within linear-response theory [107–110].

In this chapter, we present a theoretical framework and an *ab initio* computational scheme to describe a process in which trXAS is applied to track laser-dressed electron dynamics in materials. Our computational scheme combines the Floquet–Bloch formalism with DFT using LAPW+lo method. The Floquet–Bloch formalism enables the study of non-perturbative electron dynamics in solids driven by intense laser fields without explicit time propagation of the electronic states [111, 112]. The LAPW+lo method provides a full-potential treatment of the crystal electronic structure, accurately capturing the effects of both valence and core electrons. As a case study, we consider a ZnO crystal interacting with a near-infrared pulse in the high-order harmonic generation regime, demonstrating how trXAS can be used to probe electron dynamics in a solid-state system under strong-field excitation. Although the primary focus is on laser-driven crystals, the derived formalism is general and applicable to any electronic system driven by a temporally periodic electromagnetic field.

5.2. Theory of x-ray absorption from a laser-driven material

When a resonant x-ray pulse interacts with an electronic system under the influence of a temporally periodic laser field that drives electron dynamics, the Hamiltonian takes on the following form:

$$\hat{H} = \hat{H}_{\mathrm{el-em}} + \hat{H}_{\mathrm{x}} + \hat{H}^{\mathrm{x}}_{\mathrm{int}}, \tag{5.1}$$

where $\hat{H}_{\mathrm{el-em}}$ describes the laser-driven electronic system, discussed in Chapter 2, and $\hat{H}_{\mathrm{x}}$ is the Hamiltonian of the x-ray field

$$\hat{H}_{\mathrm{x}} = \sum_{\boldsymbol{\kappa}_{\mathrm{x}}, s_{\mathrm{x}}} \omega_{\boldsymbol{\kappa}_{\mathrm{x}}} \hat{a}^{\dagger}_{\boldsymbol{\kappa}_{\mathrm{x}}, s_{\mathrm{x}}} \hat{a}_{\boldsymbol{\kappa}_{\mathrm{x}}, s_{\mathrm{x}}}, \tag{5.2}$$

operators $\hat{a}^{\dagger}_{\boldsymbol{\kappa}_{\mathrm{x}}, s_{\mathrm{x}}}$ and $\hat{a}_{\boldsymbol{\kappa}_{\mathrm{x}}, s_{\mathrm{x}}}$ are the creation and annihilation operators of the x-ray photon with wave vector $\boldsymbol{\kappa}_{\mathrm{x}}$ and polarization s_{x}. $\hat{H}^{\mathrm{x}}_{\mathrm{int}}$ denotes the interaction between the x-ray probe pulse and the laser-driven system within the minimal-coupling scheme. Omitting the $\hat{\mathbf{A}}^2_{\mathrm{x}}(\mathbf{r})$ term, it takes the form

$$\hat{H}^{\mathrm{x}}_{\mathrm{int}} = \frac{1}{c} \int d^3 r \hat{\psi}^{\dagger}(\mathbf{r}) \left(\hat{\mathbf{A}}_{\mathrm{x}}(\mathbf{r}) \cdot \hat{\mathbf{p}} \right) \hat{\psi}(\mathbf{r}), \tag{5.3}$$

where $\hat{\mathbf{A}}_{\mathrm{x}}(\mathbf{r})$ is the vector potential operator of the x-ray field. In the following, the x-ray field is treated as a quantized multimode field, represented by photons occupying different modes

$$\hat{\rho}^{\mathrm{x}}_{\mathrm{in}} = \sum_{\{n_{\mathrm{x}}\}, \{\bar{n}_{\mathrm{x}}\}} \rho^{\mathrm{x}}_{\{n_{\mathrm{x}}\}, \{\bar{n}_{\mathrm{x}}\}} \left| \{n_{\mathrm{x}}\} \right\rangle \left\langle \{\bar{n}_{\mathrm{x}}\} \right|. \tag{5.4}$$

Here, $\rho^{\mathrm{x}}_{\{n_{\mathrm{x}}\}, \{\bar{n}_{\mathrm{x}}\}}$ denotes the populations and coherence of all the occupied field modes associated with the incoming beam; $\{n_{\mathrm{x}}\}$ denotes a complete set of numbers that specify the number of photons in all field modes.

We assume that the full system, matter and light, is described as the tensor product of the laser-driven system and the state of the probe field. The time-dependent density operator for the full system is given by

$$\hat{\rho}^{\mathrm{s}}(t) = \sum_{\{n_{\mathrm{x}}\}, \{\bar{n}_{\mathrm{x}}\}} \rho^{\mathrm{x}}_{\{n_{\mathrm{x}}\}, \{\bar{n}_{\mathrm{x}}\}} \left| \Psi_{\{n_{\mathrm{x}}\}}(t) \right\rangle \left\langle \Psi_{\{\bar{n}_{\mathrm{x}}\}}(t) \right|, \tag{5.5}$$

where $|\Psi_{\{n_{\mathrm{x}}\}}(t)\rangle = |\Psi(t)\rangle \, |\{n_{\mathrm{x}}\}(t)\rangle$ is a product of the state of the dressed electron system and the x-ray field states. The density operator of the entire system evolves under the time-evolution operator for the whole system $\hat{U}_{\mathrm{total}}(t_{\mathrm{f}}, t_{\mathrm{i}})$ and it is given by

$$\hat{\rho}^{\mathrm{s}}(t) = \lim_{t_{\mathrm{i}} \to -\infty} \hat{U}_{\mathrm{total}}(t, t_{\mathrm{i}}) \hat{\rho}^{\mathrm{s}}_{\mathrm{in}} \hat{U}^{\dagger}_{\mathrm{total}}(t, t_{\mathrm{i}}), \tag{5.6}$$

where $\hat{\rho}^{\mathrm{s}}_{\mathrm{in}} = \hat{\rho}^{\mathrm{m}}_{\mathrm{in}} \otimes \hat{\rho}^{\mathrm{x}}_{\mathrm{in}}$ is defined as the tensor product of the initial density operators of the matter and x-ray field. Long before interaction with the x-ray pulse laser-driven electronic system evolved periodically in time and with the initial state described by a single family of Floquet states.

In the following, we assume that interaction between the probe x-ray field and the system can be treated perturbatively. Accordingly, we expand the full density matrix of the laser-driven electronic system in orders of the perturbation theory. Keeping only the first-order

term in the x-ray field, it leads to

$$\hat{\rho}^{(1)}(t) = \sum_{\{n_x\},\{\bar{n}_x\}} \rho^{x}_{\{n_x\},\{\bar{n}_x\}} \left|\Psi^{(0)}_{\{n_x\}}(t)\right\rangle \left\langle\Psi^{(1)}_{\{\bar{n}_x\}}(t)\right| + \sum_{\{n_x\},\{\bar{n}_x\}} \rho^{x}_{\{n_x\},\{\bar{n}_x\}} \left|\Psi^{(1)}_{\{n_x\}}(t)\right\rangle \left\langle\Psi^{(0)}_{\{\bar{n}_x\}}(t)\right| \tag{5.7}$$

and in the next leading order on the interaction Hamiltonian with the x-ray field

$$\hat{\rho}^{(1,1)}(t) = \sum_{\{n_x\},\{\bar{n}_x\}} \rho^{x}_{\{n_x\},\{\bar{n}_x\}} \left|\Psi^{(1)}_{\{n_x\}}(t)\right\rangle \left\langle\Psi^{(1)}_{\{\bar{n}_x\}}(t)\right| . \tag{5.8}$$

Here, the first correction to the full wavefunction in the Eqs. (5.7),(5.8) is given by

$$\left|\Psi^{(1)}_{\{n_x\}}(t)\right\rangle = -i \lim_{t_0\to-\infty} \int_{t_0}^{t} dt' \hat{U}(t,t') \hat{H}^{x}_{\text{int}} \hat{U}(t',t_0) \left|\Psi(t_0)\right\rangle \left|\{n_x\}(t_0)\right\rangle . \tag{5.9}$$

The expectation value of a physical observable as a function of time is given by the trace of the density matrix with the corresponding canonical operator

$$O(t) = \text{Tr}[\hat{\rho}^{s}(t)\hat{O}]. \tag{5.10}$$

5.3. Projection treatment of x-ray absorption

First, we introduce a method for calculating the x-ray absorption cross section based on the projection treatment of x-ray absorption. This method is an extension of the standard definition and is only suitable for quasi-monochromatic probe x-ray pulses. The next section introduces a method applicable to the general case of ultrashort probe x-ray pulses.

The standard definition of the x-ray absorption cross section σ_F includes the ratio of the transition rate Γ_{FI} to the constant x-ray photon flux J_x of a continuous wave x-ray light source:

$$\sigma_F = \frac{\Gamma_{FI}}{J_x}. \tag{5.11}$$

The transition rate is given by the transition probability per unit time and depends on the overlap between the final stationary state $|F\rangle$, which is an eigenstate of the system Hamiltonian, and the time-dependent state of a system $|\Psi(t)\rangle$.

In the context of time-resolved absorption measurement, as discussed in Ref. [195], this formalism is extended to probe pulses with finite pulse duration and a spectral bandwidth $\Delta\omega_x$. In the perturbative regime, the transition rate remains linearly proportional to the photon flux $\Gamma(t) = \sigma(\omega_x) J_x(\omega_x, t)$. It leads to the following relation between absorption

probability and cross section [195]

$$P_{\mathrm{FI}}(t_{\mathrm{f}} \to \infty) = \sigma(\omega_{\mathrm{x}}) \int_{-\infty}^{+\infty} J_{\mathrm{x}}(\omega_{\mathrm{x}}, t) dt. \tag{5.12}$$

The underlying assumption in Eq. (5.12) is that we can calculate the absorption cross section for a small range of frequencies $\Delta\omega_{\mathrm{x}}$ around ω_{x} by calculating the response of the atom to a pulse of bandwidth $\Delta\omega_{\mathrm{x}}$.

The absorption probability is given by

$$P = \sum_{F,\{n'_{\mathrm{x}}\}} \langle \Psi_F; \{n'_{\mathrm{x}}\} | \, \hat{\rho}_F \, | \Psi_F; \{n'_{\mathrm{x}}\} \rangle \,, \tag{5.13}$$

where $\hat{\rho}_{\mathrm{f}}$ is the density matrix after interaction with the probe x-ray pulse. In the final states $|\Psi_F; \{n'_{\mathrm{x}}\}\rangle$, the set of Fock states after the absorption process is defined by the relation $|\{n'_{\mathrm{x}}\}\rangle = \hat{a}_{\boldsymbol{\kappa}_{\mathrm{x_a}}, s_{\mathrm{x_a}}} |\{n_{\mathrm{x}}\}\rangle$. The summation includes all possible final states $|\Psi_F\rangle$, which are eigenstates of the Hamiltonian $\hat{H}_{\mathrm{el-em}}$.

In first-order time-dependent perturbation theory, the density matrix $\hat{\rho}_{\mathrm{f}}$ is obtained by substituting Eq. (5.9) into Eq. (5.8)

$$\hat{\rho}_{\mathrm{f}}^{(1,1)} = \lim_{\substack{t_{\mathrm{i}} \to -\infty \\ t_{\mathrm{f}} \to +\infty}} \sum_{\{n_{\mathrm{x}}\},\{\bar{n}_{\mathrm{x}}\}} \rho^{\mathrm{x}}_{\{n_{\mathrm{x}}\},\{\bar{n}_{\mathrm{x}}\}} \int_{t_{\mathrm{i}}}^{t_{\mathrm{f}}} \int_{t_{\mathrm{i}}}^{t_{\mathrm{f}}} dt_1 dt_2 \Bigg(\hat{U}(t_{\mathrm{f}}, t_1) \hat{H}_{\mathrm{int}} \hat{U}(t_1, t_{\mathrm{i}}) \, |\Psi^{(0)}_{\{n_{\mathrm{x}}\}}(t_{\mathrm{i}})\rangle \times \langle \Psi^{(0)}_{\{\bar{n}_{\mathrm{x}}\}}(t_{\mathrm{i}})| \, \hat{U}^{\dagger}(t_2, t_{\mathrm{i}}) \hat{H}^{\dagger}_{\mathrm{int}} \hat{U}^{\dagger}(t_{\mathrm{f}}, t_2) \Bigg). \tag{5.14}$$

Substituting the density matrix from Eq.(5.14) into Eq.(5.13), and simplifying the expression (see Appendix A.1.1), leads to the result given in Eq. (A.4) as follows:

$$\begin{aligned} P^{(1)} = \sum_F \int_{-\infty}^{\infty} \int_{-\infty}^{\infty} dt_1 dt_2 \int d^3 r_1 \int d^3 r_2 \, e^{i\mathcal{E}_F(t_1 - t_2)} \sum_{\boldsymbol{\kappa}_{\mathrm{x_1}}, s_{\mathrm{x_1}}} \sum_{\boldsymbol{\kappa}_{\mathrm{x_2}}, s_{\mathrm{x_2}}} \frac{2\pi}{V\sqrt{\omega_{\boldsymbol{\kappa}_{\mathrm{x_1}}} \omega_{\boldsymbol{\kappa}_{\mathrm{x_2}}}}} \\ \times e^{-i\omega_{\boldsymbol{\kappa}_{\mathrm{x_1}}} t_1} e^{i\omega_{\boldsymbol{\kappa}_{\mathrm{x_2}}} t_2} e^{i\boldsymbol{\kappa}_{\mathrm{x_1}} \cdot \mathbf{r}_1} e^{-i\boldsymbol{\kappa}_{\mathrm{x_2}} \cdot \mathbf{r}_2} \, \mathrm{Tr} \left[\hat{\rho}^{\mathrm{x}}_{\mathrm{in}} \hat{a}^{\dagger}_{\boldsymbol{\kappa}_{\mathrm{x_2}}, s_{\mathrm{x_2}}} \hat{a}_{\boldsymbol{\kappa}_{\mathrm{x_1}}, s_{\mathrm{x_1}}} \right] \\ \times \langle \Psi_F | \, \boldsymbol{\epsilon}_{\boldsymbol{\kappa}_{\mathrm{x_1}}, s_{\mathrm{x_1}}} \cdot \hat{\psi}^{\dagger}(\mathbf{r}_1) \nabla \hat{\psi}(\mathbf{r}_1) \, |\Psi(t_1)\rangle \, \langle \Psi(t_2)| \, \boldsymbol{\epsilon}^{*}_{\boldsymbol{\kappa}_{\mathrm{x_2}}, s_{\mathrm{x_2}}} \cdot \hat{\psi}^{\dagger}(\mathbf{r}_2) \nabla \hat{\psi}(\mathbf{r}_2) \, |\Psi_F\rangle \,. \end{aligned} \tag{5.15}$$

Equation (5.15) provides the absorption probability of an x-ray probe pulse with arbitrary coherence properties and pulse duration, applicable to both time-resolved and time-unresolved measurements. The absorption probability depends on the properties of the incoming x-ray pulse through its first-order correlation function, which is defined as follows:

$$G^{(1)}_{ab}(x, x') = \mathrm{Tr} \left[\hat{\rho} \hat{E}^{-}_{a}(x) \hat{E}^{+}_{b}(x') \right], \tag{5.16}$$

where $x = (\mathbf{r}, t)$ and

$$\hat{E}_a^-(x) = -i\sum_{\boldsymbol{\kappa},s}\sqrt{\frac{2\pi\omega_{\boldsymbol{\kappa}}}{V}}\hat{a}^\dagger_{\boldsymbol{\kappa},s}(\boldsymbol{\epsilon}^*_{\boldsymbol{\kappa},s})_a e^{-i(\boldsymbol{\kappa}\mathbf{r}-\omega_\kappa t)}, \tag{5.17}$$

$$\hat{E}_b^+(x') = i\sum_{\boldsymbol{\kappa},s}\sqrt{\frac{2\pi\omega_{\boldsymbol{\kappa}}}{V}}\hat{a}_{\boldsymbol{\kappa},s}(\boldsymbol{\epsilon}_{\boldsymbol{\kappa},s})_b e^{i(\boldsymbol{\kappa}\mathbf{r}'-\omega_\kappa t')}. \tag{5.18}$$

Here, the indices a, b, c run over the three spatial coordinates x, y, z.

Let us assume that the incident x-ray beam is characterized by a mean wave vector $\boldsymbol{\kappa}^{\text{in}}_{\text{x}}$ and a corresponding mean polarization vector $\boldsymbol{\epsilon}^{\text{in}}_{\boldsymbol{\kappa}_{\text{x}},s_{\text{x}}}$. If the pulse is quasi-monochromatic, meaning it has a narrow spectral bandwidth $\Delta\omega_{\text{x}}$ and a small angular divergence $\Delta\boldsymbol{\kappa}_{\text{x}}$, then the non-negligible components of the density matrix $\rho^{\text{x}}_{\{n_{\text{x}}\},\{\bar{n}_{\text{x}}\}}$ are concentrated within a limited range of mode indices $\boldsymbol{\kappa}_{\text{x}_i}, s_{\text{x}_i}$. Within this narrow range, we replace the polarization vectors $\boldsymbol{\epsilon}_{\boldsymbol{\kappa}_{\text{x}_1},s_{\text{x}_1}}$ and $\boldsymbol{\epsilon}_{\boldsymbol{\kappa}_{\text{x}_2},s_{\text{x}_2}}$ by the mean polarization vector $\boldsymbol{\epsilon}^{\text{in}}_{\boldsymbol{\kappa}_{\text{x}},s_{\text{x}}}$. Similarly, the frequency-dependent prefactor can be approximated as

$$\sqrt{\omega_{\boldsymbol{\kappa}_{\text{x}_1}}\omega_{\boldsymbol{\kappa}_{\text{x}_2}}} = \sqrt{(\omega^{\text{in}}_{\boldsymbol{\kappa}_{\text{x}}} + \Delta\omega_{\boldsymbol{\kappa}_{\text{x}_1}})(\omega^{\text{in}}_{\boldsymbol{\kappa}_{\text{x}}} + \Delta\omega_{\boldsymbol{\kappa}_{\text{x}_2}})} \approx \omega^{\text{in}}_{\boldsymbol{\kappa}_{\text{x}}}, \tag{5.19}$$

since the variations $\Delta\omega_{\boldsymbol{\kappa}_{\text{x}_i}}$ are small. For an incident beam with mean wave vector $\boldsymbol{\kappa}^{\text{in}}_{\text{x}}$ and mean polarization vector $\boldsymbol{\epsilon}^{\text{in}}_{\boldsymbol{\kappa}_{\text{x}},s_{\text{x}}}$, the probability is then given by

$$P = \frac{1}{(\omega^{\text{in}}_{\boldsymbol{\kappa}_{\text{x}}})^2}\sum_F \int_{-\infty}^{\infty}\int_{-\infty}^{\infty} dt_1 dt_2 \int d^3r_1 d^3r_2 G^{(1)}_{ab}(\mathbf{r}_2, t_2; \mathbf{r}_1, t_1) D^{F*}_a(\mathbf{r}_2, t_2) D^F_b(\mathbf{r}_1, t_1), \tag{5.20}$$

where

$$D^F_b(\mathbf{r}, t) = e^{i\mathcal{E}_F t}\left\langle\Psi_F\right| \hat{\psi}^\dagger(\mathbf{r})(\boldsymbol{\epsilon}^{\text{in}}_{\boldsymbol{\kappa}_{\text{x}},s_{\text{x}}})_b \partial_b \hat{\psi}(\mathbf{r}) \left|\Psi(t)\right\rangle. \tag{5.21}$$

Since in the Eq. (5.20) each final Floquet state belongs to a family of replica states $|\Psi_{F_{\Delta\mu}}\rangle = \sum_{n,\mu} C^{F_0}_{n\mu+\Delta\mu} |\Phi_n\rangle |N-\mu\rangle$ with the energies $\mathcal{E}_{F_{\Delta\mu}} = \mathcal{E}_{F_0} + \Delta\mu\Omega$, we transform the summation over all final states $|\Psi_F\rangle$ into the summation over reference states $|\Psi_{F_0}\rangle$, see Appendix A.1.2, in this case

$$P = \frac{1}{(\omega^{\text{in}}_{\boldsymbol{\kappa}_{\text{x}}})^2}\sum_{F_0} \int_{-\infty}^{\infty}\int_{-\infty}^{\infty} dt_1 dt_2 \int d^3r_1 d^3r_2 G^{(1)}_{ab}(\mathbf{r}_2, t_2; \mathbf{r}_1, t_1) D^{F_0*}_a(\mathbf{r}_2, t_2) D^{F_0}_b(\mathbf{r}_1, t_1), \tag{5.22}$$

where

$$D^{F_0}_b(\mathbf{r}, t) = e^{i(\mathcal{E}_{F_0}-\mathcal{E}_{I_0})t}\sum_{\Delta\mu} e^{i\Delta\mu\Omega t}\tilde{D}^{F_0}_b(\mathbf{r}, \Delta\mu) \tag{5.23}$$

with amplitudes

$$\tilde{D}^{F_0}_b(\mathbf{r}, \Delta\mu) = \sum_{n,k,\mu} C^{F_0*}_{n\mu+\Delta\mu} C^{I_0}_{k\mu} \left\langle\Phi_n\right| \hat{\psi}^\dagger(\mathbf{r})(\boldsymbol{\epsilon}^{\text{in}}_{\boldsymbol{\kappa}_{\text{x}},s_{\text{x}}})_b \partial_b \hat{\psi}(\mathbf{r}) \left|\Phi_k\right\rangle. \tag{5.24}$$

5.3.1. Coherent probe x-ray pulse

For a fully coherent x-ray pulse, the first-order correlation function in Eq. (5.16) factorizes into a product of two terms, represented as [196]

$$G^{(1)}_{ab}\left(\mathbf{r}_2,t_2;\mathbf{r}_1,t_1\right)=E^{\mathrm{x}*}_a\left(\mathbf{r}_2,t_2-t_{\mathrm{p}}\right)e^{i\omega^{\mathrm{in}}_{\boldsymbol{\kappa}_{\mathrm{x}}}t_2-i\boldsymbol{\kappa}^{\mathrm{in}}_{\mathrm{x}}\mathbf{r}_2}\times E^{\mathrm{x}}_b\left(\mathbf{r}_1,t_1-t_{\mathrm{p}}\right)e^{-i\omega^{\mathrm{in}}_{\boldsymbol{\kappa}_{\mathrm{x}}}t_1+i\boldsymbol{\kappa}^{\mathrm{in}}_{\mathrm{x}}\mathbf{r}_1}, \tag{5.25}$$

where $E^{\mathrm{x}}_{a(b)}$ are the components of the x-ray field in the a and b directions, respectively. In the following, we assume that the amplitude of the electric field does not vary significantly across the characteristic size of the system centered at $\mathbf{r}_0$ and the electric field amplitude can be approximated by its value at $\mathbf{r}_0$, yielding

$$P=\frac{1}{\left(\omega^{\mathrm{in}}_{\boldsymbol{\kappa}_{\mathrm{x}}}\right)^2}\sum_{F_0}\left|\sum_{\Delta\mu}\tilde{E}_{\mathrm{x}}\left(\Omega_{F_0I_0}+\Delta\mu\Omega,t_{\mathrm{p}}\right)D^{F_0}(\boldsymbol{\kappa}^{\mathrm{in}}_{\mathrm{x}},\Delta\mu)\right|^2. \tag{5.26}$$

Here, the spatial derivative is taken along the direction of the polarization vector $\boldsymbol{\epsilon}^{\mathrm{in}}_{\mathrm{x}}$ and the notation

$$D^{F_0}(\boldsymbol{\kappa}^{\mathrm{in}}_{\mathrm{x}},\Delta\mu)=\int d^3r\,\tilde{D}^{F_0}(\mathbf{r},\Delta\mu)e^{i\boldsymbol{\kappa}^{\mathrm{in}}_{\mathrm{x}}\mathbf{r}} \tag{5.27}$$

is used to define the integrated system response, and the function

$$\tilde{E}_{\mathrm{x}}\left(\Omega_{F_0I_0}+\Delta\mu\Omega,t_{\mathrm{p}}\right)=\int_{-\infty}^{\infty}dt\,e^{i\left(\Omega_{F_0I_0}+\Delta\mu\Omega\right)t}E_{\mathrm{x}}\left(\mathbf{r}_0,t-t_{\mathrm{p}}\right) \tag{5.28}$$

denotes the Fourier transform of the electric field at the probe time t_{p}, with $\Omega_{F_0I_0}=\mathcal{E}_{F_0}-\mathcal{E}_{I_0}-\omega^{\mathrm{in}}_{\boldsymbol{\kappa}_{\mathrm{x}}}$ representing the energy difference between the initial and final states, adjusted for the incident x-ray photon energy. For a Gaussian-shaped probe pulse with the amplitude of an electric field

$$E_{\mathrm{x}}\left(\mathbf{r}_0,t-t_{\mathrm{p}}\right)=\sqrt{(8\pi/c)I_0(\mathbf{r}_0)}e^{-\left(\frac{t-t_{\mathrm{p}}}{\tau_{\mathrm{p}}}\right)^2\times 2\ln 2}, \tag{5.29}$$

where $I_0(\mathbf{r}_0)=(c/8\pi)E^2_{\mathrm{x}}(\mathbf{r}_0,t=0)$ is the peak intensity, and τ_{p} is the pulse duration, the integral Eq. (5.28) turns into

$$\tilde{E}_{\mathrm{x}}\left(\Omega_{F_0I_0}+\Delta\mu\Omega,t_{\mathrm{p}}\right)=\sqrt{\frac{4\pi^2\tau^2_{\mathrm{p}}I_0(\mathbf{r}_0)}{c\ln 2}}e^{i\left(\Omega_{F_0I_0}+\Delta\mu\Omega\right)t_{\mathrm{p}}}e^{-\frac{\tau^2_{\mathrm{p}}}{8\ln 2}\left(\Omega_{F_0I_0}+\Delta\mu\Omega\right)^2}. \tag{5.30}$$

Therefore, the definition of the absorption probability for a coherent, narrow, Gaussian-shaped probe x-ray pulse is

$$P(\omega^{\mathrm{in}}_{\boldsymbol{\kappa}_{\mathrm{x}}},t_{\mathrm{p}})=P_0\sum_{F_0}\left|\sum_{\Delta\mu}e^{i\left(\Omega_{F_0I_0}+\Delta\mu\Omega\right)t_{\mathrm{p}}}e^{-\frac{\tau^2_{\mathrm{p}}}{8\ln 2}\left(\Omega_{F_0I_0}+\Delta\mu\Omega\right)^2}D^{F_0}(\boldsymbol{\kappa}^{\mathrm{in}}_{\mathrm{x}},\Delta\mu)\right|^2 \tag{5.31}$$

where

$$P_0 = \frac{(2\pi)^2 \tau_p^2 I_0(\mathbf{r}_0)}{c(\omega^{\text{in}}_{\boldsymbol{\kappa}_x})^2 \ln 2}. \tag{5.32}$$

The expression in Eq. (5.31) includes the $\Delta\mu$th spectral component of the Fourier transform of the x-ray pulse envelope, given by $\tilde{E}_x\left(\Omega_{F_0 I_0} + \Delta\mu\Omega\right) \propto e^{-\frac{\tau_p^2}{8\ln 2}\left(\Omega_{F_0 I_0}+\Delta\mu\Omega\right)^2}$. If the probe pulse duration τ_p is much longer than the optical cycle, the spectral components of the $\Delta\mu$th and $\Delta\mu'$th orders are narrow and well-separated. In this limit, the absorption probability becomes independent of the pulse arrival time t_p, and the signal reduces to a sum over sidebands with different $\Delta\mu$. As τ_p decreases, the spectral components broaden and begin to overlap. This leads to interference between components with different $\Delta\mu$, and the resulting signal depends on the arrival time t_p. The interference between overlapping sidebands gives rise to time-dependent modulations in the absorption probability.

5.3.2. Application to a spatially periodic electronic system

We now evaluate the functions in Eq. (5.27) for a system of non-interacting electrons. In this case, the many-body wavefunction can be represented as a Slater determinant constructed from single-particle states. Each one-electron state $\phi^{\text{el}}_{i\mathbf{k}}(\mathbf{r},t)$ takes the form

$$\phi^{\text{el}}_{i\mathbf{k}}(\mathbf{r},t) = e^{-i\varepsilon_{i\mathbf{k}}t} \sum_{m,\mu} c^{i_n}_{m\mathbf{k}\mu}\, e^{-i\mu\Omega t}\, \varphi_{m\mathbf{k}}(\mathbf{r}), \tag{5.33}$$

where $\varepsilon_{i\mathbf{k}}$ is the quasienergy of the one-body Floquet state and $\varphi_{m\mathbf{k}}(\mathbf{r})$ are the field-free Bloch states, see Eq. (2.79). Substituting Eq. (5.33) into Eq. (5.27) and simplifying the resulting expression (see Appendix A.1.3), we obtain the transition amplitude $D^{F_0}(\boldsymbol{\kappa}^{\text{in}}_x, \Delta\mu)$, given by

$$D^{F_0}(\boldsymbol{\kappa}^{\text{in}}_x, \Delta\mu) = \sum_{m,m',\mu} c^{f*}_{m'\mathbf{k}'\mu+\Delta\mu}\, c^{i}_{m\mathbf{k}\mu} \int d^3r\, e^{i\boldsymbol{\kappa}^{\text{in}}_x\cdot\mathbf{r}}\, \varphi^{\dagger}_{m'\mathbf{k}'}(\mathbf{r})(\boldsymbol{\epsilon}^{\text{in}}_{\boldsymbol{\kappa}_x,s_x}\cdot\boldsymbol{\nabla})\varphi_{m\mathbf{k}}(\mathbf{r}), \tag{5.34}$$

where the final Floquet state $|\Psi_{F_0}\rangle$ results from the transition of an electron from the state $|\phi^{\text{el}}_{i\mathbf{k}}\rangle$ to the state $|\phi^{\text{el}}_{f\mathbf{k}}\rangle$. We consider an initial state $|\phi^{\text{el}}_{i\mathbf{k}}\rangle$ corresponding to a core electron, which resides deep below the Fermi energy. Assuming that the driving field does not significantly alter this state, the initial one-body electronic Floquet–Bloch state can be expressed as

$$|\phi^{\text{el}}_{i\mathbf{k}}, t\rangle = e^{-i(\varepsilon_c+\mu_i\Omega)t}\,|\varphi^{c}_{\mathbf{k}}\rangle\,, \tag{5.35}$$

where the core electron Bloch state is represented by a flat band, $\varphi^{c}_{\mathbf{k}}(\mathbf{r}) = \sum_{\mathbf{R}} \varphi^{c}(\mathbf{r}-\mathbf{R})e^{i\mathbf{k}\mathbf{R}}$. Substituting Eq. (5.35) into Eq. (5.34) gives

$$D^{F_0}(\boldsymbol{\kappa}^{\text{in}}_x, \Delta\mu) = \sum_{m'} c^{f*}_{m'\mathbf{k}'\mu_i+\Delta\mu} \int d^3r e^{i\boldsymbol{\kappa}^{\text{in}}_x\mathbf{r}} \varphi^{\dagger}_{m'\mathbf{k}'}(\mathbf{r})(\boldsymbol{\epsilon}^{\text{in}}_{\boldsymbol{\kappa}_x,s_x}\cdot\boldsymbol{\nabla})\varphi^{c}_{\mathbf{k}}(\mathbf{r}), \tag{5.36}$$

where different modes μ_i correspond to the different initial one-body states of the core electron participating in the transition. The integral in Eq. (5.36) is evaluated in the Appendix A.1.1, see Eq. (A.10)

$$\int d^3r e^{i\boldsymbol{\kappa}_{\mathrm{x}}^{\mathrm{in}}\mathbf{r}}\varphi^{\dagger}_{m'\mathbf{k}'}(\mathbf{r})(\boldsymbol{\epsilon}^{\mathrm{in}}_{\boldsymbol{\kappa}_{\mathrm{x}},s_{\mathrm{x}}}\cdot\boldsymbol{\nabla})\varphi^{\mathrm{c}}_{\mathbf{k}}(\mathbf{r}) = N_{\mathrm{cell}}^2\sum_{\mathbf{G}}\delta^{(3)}(\mathbf{k}+\boldsymbol{\kappa}_{\mathrm{x}}^{\mathrm{in}}-\mathbf{k}'-\mathbf{G})\left\langle\varphi_{m'\mathbf{k}'}\right|\hat{p}_{\boldsymbol{\epsilon}}\left|\varphi^{\mathrm{c}_0}\right\rangle, \tag{5.37}$$

where we introduce the notation for the derivative along the field as $\boldsymbol{\epsilon}^{\mathrm{in}}_{\boldsymbol{\kappa}_{\mathrm{x}},s_{\mathrm{x}}}\cdot\boldsymbol{\nabla}=\hat{p}_{\boldsymbol{\epsilon}}$. The exponential term $e^{i\boldsymbol{\kappa}_{\mathrm{x}}^{\mathrm{in}}\cdot\mathbf{r}}$ in the momentum matrix element gives rise to a delta function that enforces momentum conservation during the absorption process. Since the final Floquet state $|\Psi_{F_0}\rangle$ results from the transition of an electron from the initial state $|\phi^{\mathrm{el}}_{i\mathbf{k}}\rangle$ to the final state $|\phi^{\mathrm{el}}_{f\mathbf{k}'}\rangle$, the absorption probability includes a sum over the momentum $\mathbf{k}$ of the core electron. However, the momentum dependence appears only through the matrix elements in Eq. (5.37), which involve the flat-band core state as follows:

$$\sum_{\mathbf{k}}\sum_{\mathbf{G}}\delta^{(3)}(\mathbf{k}+\boldsymbol{\kappa}_{\mathrm{x}}^{\mathrm{in}}-\mathbf{k}'-\mathbf{G})f(\mathbf{k}') = \sum_{\mathbf{G}}f(\mathbf{k}')\big|_{\mathbf{k}=\mathbf{k}'+\mathbf{G}-\boldsymbol{\kappa}_{\mathrm{x}}^{\mathrm{in}}} = N_{\mathbf{G}}f(\mathbf{k}'). \tag{5.38}$$

Here, we used the fact that, for each final quasimomentum $\mathbf{k}'$ there are $N_{\mathbf{G}}$ values of the quasimomentum $\mathbf{k}$ of the initial core electron state at the flat band. The result implies that, although the absorption process conserves momentum via the x-ray wave vector, the final expression becomes independent of $\boldsymbol{\kappa}_{\mathrm{x}}^{\mathrm{in}}$ due to the flat-band nature of the initial core electron state.

Equation (5.31) now leads to an absorption probability of the following form:

$$P(\omega^{\mathrm{in}}_{\boldsymbol{\kappa}_{\mathrm{x}}},t_{\mathrm{p}}) = \tilde{P}_0\sum_{f,\mathbf{k}'}\left|\sum_{\Delta\mu}e^{i\Delta\mu\Omega t_{\mathrm{p}}}e^{-\frac{\tau_{\mathrm{p}}^2}{8\ln 2}\left(\Omega_{fi}+\Delta\mu\Omega\right)^2}\sum_{m'}c^{f*}_{m'\mathbf{k}'\Delta\mu}\left\langle\varphi_{m'\mathbf{k}'}\right|\hat{p}_{\boldsymbol{\epsilon}}\left|\varphi^{\mathrm{c}_0}\right\rangle\right|^2. \tag{5.39}$$

Here, $\tilde{P}_0 = P_0 N_{\mathrm{cell}}^4 N_{\mathbf{G}}$, $\Omega_{fi}=\varepsilon_{f\mathbf{k}'}-\varepsilon_{\mathrm{c}}-\omega^{\mathrm{in}}_{\boldsymbol{\kappa}_{\mathrm{x}}}$, and $\mathbf{k}'-\boldsymbol{\kappa}_{\mathrm{x}}^{\mathrm{in}}+\mathbf{G}=\mathbf{k}$, corresponding to the conservation of energy and momentum, up to an integer multiple of the driving frequency $\Delta\mu\Omega$ and a reciprocal lattice vector $\mathbf{G}$, respectively.

In the form of Fourier series:

$$P(\omega^{\mathrm{in}}_{\boldsymbol{\kappa}_{\mathrm{x}}},t_{\mathrm{p}}) = \tilde{P}_0\sum_{\Delta\mu}e^{i\Delta\mu\Omega t_{\mathrm{p}}}\tilde{P}_{\Delta\mu}(\omega^{\mathrm{in}}_{\boldsymbol{\kappa}_{\mathrm{x}}}), \tag{5.40}$$

where the amplitudes $\tilde{P}_{\Delta\mu}(\omega^{\mathrm{in}}_{\boldsymbol{\kappa}_{\mathrm{x}}})$ are given by

$$\begin{aligned}\tilde{P}_{\Delta\mu}(\omega^{\mathrm{in}}_{\boldsymbol{\kappa}_{\mathrm{x}}}) = \sum_{f,\mathbf{k}}\sum_{\mu}e^{-\frac{\tau_{\mathrm{p}}^2}{8\ln 2}\left(\Omega_{fi}+(\mu+\Delta\mu)\Omega\right)^2}\sum_{m}c^{f*}_{m\mathbf{k}\mu+\Delta\mu}\int_{\mathrm{MT}_{\mathrm{c}_0}}d^3r\varphi^{\dagger}_{m\mathbf{k}}(\mathbf{r})(\boldsymbol{\epsilon}^{\mathrm{in}}_{\boldsymbol{\kappa}_{\mathrm{x}},s_{\mathrm{x}}}\cdot\boldsymbol{\nabla})\varphi^{\mathrm{c}_0}(\mathbf{r}) \\ \times e^{-\frac{\tau_{\mathrm{p}}^2}{8\ln 2}\left(\Omega_{fi}+\mu\Omega\right)^2}\sum_{m'}c^{f}_{m'\mathbf{k}\mu}\int_{\mathrm{MT}_{\mathrm{c}_0}}d^3r\varphi_{m'\mathbf{k}}(\mathbf{r})(\boldsymbol{\epsilon}^{\mathrm{in}*}_{\boldsymbol{\kappa}_{\mathrm{x}},s_{\mathrm{x}}}\cdot\boldsymbol{\nabla})\varphi^{\mathrm{c}_0\dagger}(\mathbf{r}).\end{aligned} \tag{5.41}$$

We can further simplify the expression using the symmetry under the transformation $\Delta\mu \to -\Delta\mu$, noting that $\tilde{P}_{-\Delta\mu}(\omega^{\text{in}}_{\boldsymbol{\kappa}_x}) = \left(\tilde{P}_{\Delta\mu}(\omega^{\text{in}}_{\boldsymbol{\kappa}_x})\right)^*$. We redefine the probability as follows: $P(\omega^{\text{in}}_{\boldsymbol{\kappa}_x}, t_p)/\tilde{P}_0 \to P(\omega^{\text{in}}_{\boldsymbol{\kappa}_x}, t_p)$. This leads to the time-dependent absorption probability of the form

$$P(\omega^{\text{in}}_{\boldsymbol{\kappa}_x}, t_p) = \tilde{P}_{\Delta\mu=0}(\omega^{\text{in}}_{\boldsymbol{\kappa}_x}) + \sum_{\Delta\mu\geq 1} 2\,\text{Re}\left[e^{i\Delta\mu\Omega t_p}\tilde{P}_{\Delta\mu}(\omega^{\text{in}}_{\boldsymbol{\kappa}_x})\right]. \tag{5.42}$$

The first term in Eq. (5.42) is the zero-order amplitude $\langle P(\omega^{\text{in}}_{\boldsymbol{\kappa}_x}, t_p)\rangle = \tilde{P}_{\Delta\mu=0}(\omega^{\text{in}}_{\boldsymbol{\kappa}_x})$ that gives the probability averaged over the period T of the driving electromagnetic field, similar to the Eq. (4.10). It captures the steady-state behavior of a system under a continuous periodic excitation. The second term in Eq. (5.42) is the time-dependent part of the probability. The spectral position of the time-dependent terms in the probability in Eq. (5.42) is at $\omega^{\text{in}}_{\boldsymbol{\kappa}_x} = \varepsilon_c - \varepsilon_{f\mathbf{k}'} + (\mu + \Delta\mu/2)\Omega$ for $\Delta\mu \neq 0$ according to Eq. (5.41), which is either in the middle between a main peak and its side peaks or in the middle between side peaks.

Similar to the PDOS, time-reversal symmetry can be used to further simplify the time-dependence of the probability. If an electronic system with time-reversal symmetry is driven by a linearly polarized pulse of the form $\mathbf{E}(t) = \mathbf{F}_0 \sin\Omega t$, a property of the Floquet–Bloch coefficients $c^i_{n\mathbf{k}\mu} = (-1)^\mu \left(c^i_{n-\mathbf{k}\mu}\right)^*$ derived in [69] applies. It is also true for a system with time-reversal symmetry that $\varphi_{n\mathbf{k}}(\mathbf{r}) = (\varphi_{n-\mathbf{k}}(\mathbf{r}))^*$. This relates the terms with positive $\mathbf{k}$ in the sum in Eq. (5.41) as complex conjugates multiplied by a factor $(-1)^{\Delta\mu}$. The amplitudes of the probability are then real for even orders and are imaginary for odd orders, which leads to

$$\begin{aligned} P(\omega^{\text{in}}_{\boldsymbol{\kappa}_x}, t_p) = \langle P(\omega^{\text{in}}_{\boldsymbol{\kappa}_x}, t_p)\rangle &- \sum_{\Delta\mu_{\text{odd}}\geq 1} P_{\Delta\mu_{\text{odd}}}(\omega^{\text{in}}_{\boldsymbol{\kappa}_x}) \sin(\mu_{\text{odd}}\Omega t) \\ &+ \sum_{\Delta\mu_{\text{even}}\geq 2} P_{\Delta\mu_{\text{even}}}(\omega^{\text{in}}_{\boldsymbol{\kappa}_x}) \cos(\mu_{\text{even}}\Omega t), \end{aligned} \tag{5.43}$$

where $P_{\Delta\mu_{\text{odd}}}(\omega^{\text{in}}_{\boldsymbol{\kappa}_x}) = 2\,\text{Im}\left(\tilde{P}_{\Delta\mu_{\text{odd}}}(\omega^{\text{in}}_{\boldsymbol{\kappa}_x})\right)$ and $P_{\Delta\mu_{\text{even}}}(\omega^{\text{in}}_{\boldsymbol{\kappa}_x}) = 2\,\text{Im}\left(\tilde{P}_{\Delta\mu_{\text{even}}}(\omega^{\text{in}}_{\boldsymbol{\kappa}_x})\right)$ are real-valued amplitudes.

The absorption cross section can be calculated using Eq. (5.12). Assuming a linear relationship between the photon flux and the intensity of the probe x-ray pulse, the integral in Eq. (5.12) can be evaluated analytically as follows: $\int J_x(\omega^{\text{in}}_{\boldsymbol{\kappa}_x}, t)dt = \frac{\sqrt{2\ln 2}}{\omega^{\text{in}}_{\boldsymbol{\kappa}_x}\tau_p} I_0(\mathbf{r}_0)$. Thus, in the case of trXAS using quasi-monochromatic pulses, the absorption cross section is proportional to the absorption probability given by Eq. (5.43). The latter has a time dependence analogous to that of the PDOS, as defined by Eq. (4.12). The amplitudes $P_{\Delta\mu_{\text{odd}}}(\omega^{\text{in}}_{\boldsymbol{\kappa}_x})$ correspond to the μth-order components of the PDOS, $\mathcal{D}^{\alpha(\mu)}_{lm}(\omega)$, which is shifted by the core electron binding energy. The amplitudes of the time-dependent absorption cross section provide direct information about the transient modifications to the electronic structure of the material induced by the driving field.

5.4. Time-frequency treatment of x-ray absorption

The time–frequency treatment of ultrafast x-ray absorption provides a general formalism to calculate the absorption cross section in time-dependent problems [197]. The method of calculation of the x-ray absorption cross section is based on the energy conservation principle between the quantum system and the electromagnetic field. The exchange of energy is defined as

$$\Delta\mathcal{E} = \int_{-\infty}^{+\infty} \Delta\dot{\mathcal{E}}(t)dt, \tag{5.44}$$

where $\Delta\dot{\mathcal{E}}(t)$ is the instantaneous power transferred to the quantum system due to its coupling with the field [197].

The equation of motion for the expectation value of the energy operator can be derived using Ehrenfest's theorem and is given by

$$\frac{d}{dt}\langle\Psi(t)|\,\hat{H}\,|\Psi(t)\rangle = \frac{q}{2}\langle\Psi(t)|\,\hat{\mathbf{v}}\cdot\mathbf{E}+\mathbf{E}\cdot\hat{\mathbf{v}}\,|\Psi(t)\rangle\,, \tag{5.45}$$

where the velocity operator is defined as $\hat{\mathbf{v}} = [\hat{\mathbf{p}} - \frac{q}{c}\mathbf{A}]$, and $\mathbf{E}(\mathbf{r},t)$ is the electric field. According to the correspondence principle, the Hamiltonian $\hat{H}$ can be associated with the instantaneous energy operator of the quantum system. As follows, the instantaneous power in ultrafast absorption theory is given by

$$\Delta\dot{\mathcal{E}}(t) = \frac{q}{2}\langle\hat{\mathbf{v}}\cdot\mathbf{E}+\mathbf{E}\cdot\hat{\mathbf{v}}\rangle, \tag{5.46}$$

with expectation values $\langle\cdots\rangle \equiv \langle\Psi(t)|\cdots|\Psi(t)\rangle$. The field can be represented as $\mathbf{E}(\mathbf{r},t) = \mathbf{E}(t)e^{i\boldsymbol{\kappa}_x\cdot\mathbf{r}} + \mathbf{E}^*(t)e^{-i\boldsymbol{\kappa}_x\cdot\mathbf{r}}$. Substituting this form of the field into Eq. (5.46) gives

$$\Delta\dot{\mathcal{E}}(t) = \frac{q}{2}\left(\mathbf{E}(t)\langle\{e^{i\boldsymbol{\kappa}_x\cdot\mathbf{r}},\hat{\mathbf{v}}\}\rangle + \mathbf{E}^*(t)\langle\{e^{-i\boldsymbol{\kappa}_x\cdot\mathbf{r}},\hat{\mathbf{v}}\}\rangle\right), \tag{5.47}$$

where brackets $\{...\}$ denote anti-commutators. We introduce the $\boldsymbol{\kappa}_x$-resolved velocity operator as $\hat{\mathbf{v}}_{\boldsymbol{\kappa}_x} = \{e^{-i\boldsymbol{\kappa}_x\cdot\mathbf{r}},\hat{\mathbf{v}}\}$ with the property $\hat{\mathbf{v}}^\dagger_{\boldsymbol{\kappa}_x} = \hat{\mathbf{v}}_{-\boldsymbol{\kappa}_x}$, when the instantaneous power in terms of expectation value becomes

$$\Delta\dot{\mathcal{E}}(t) = \frac{q}{2}\left(\mathbf{E}(t)\mathbf{v}^*_{\boldsymbol{\kappa}_x}(t) + \mathbf{E}^*(t)\mathbf{v}_{\boldsymbol{\kappa}_x}(t)\right), \tag{5.48}$$

where $\mathbf{v}_{\boldsymbol{\kappa}_x}(t) = \langle\hat{\mathbf{v}}_{\boldsymbol{\kappa}_x}\rangle$ is the expectation value of the $\boldsymbol{\kappa}_x$-resolved velocity operator. There-

fore, the total energy exchange, using Plancherel's theorem, is given by

$$\Delta\mathcal{E}_z = q\int_{-\infty}^{\infty}\mathrm{Re}\left(E^*(t')v^z_{\boldsymbol{\kappa}_x}(t')\right)dt' = q\int_{-\infty}^{\infty}\mathrm{Re}\left(\tilde{E}^*(\omega)\tilde{v}^z_{\boldsymbol{\kappa}_x}(\omega)\right)d\omega \equiv 2q\int_0^{\infty}\mathrm{Re}\left[\tilde{E}^*(\omega)\tilde{v}^z_{\boldsymbol{\kappa}_x}(\omega)\right]d\omega,\quad \omega\geq 0. \tag{5.49}$$

We assumed $\mathbf{E} = E\mathbf{e}_z$. This implies that the energy-resolved gain by the system is given by

$$\Delta\mathcal{E}_z(\omega) = 2q\,\mathrm{Re}\left[\tilde{E}^*(\omega)\tilde{v}^z_{\boldsymbol{\kappa}_x}(\omega)\right],\quad \omega\geq 0. \tag{5.50}$$

Writing $E(t) = -\frac{1}{c}\partial_t A(t)$ or in Fourier transforms $\tilde{E}(\omega) = i\omega/c\tilde{A}(\omega)$ and using the definition of velocity operator $\tilde{v}_z(\omega) = [\tilde{p}_z(\omega) - \frac{q}{c}\tilde{A}(\omega)]$, we can express the absorbed energy in terms of $\tilde{p}_z(\omega)$. For the Fourier transform of the $\boldsymbol{\kappa}_x$-resolved velocity we have

$$\tilde{v}^z_{\boldsymbol{\kappa}_x}(\omega) = \left[\tilde{p}^z_{\boldsymbol{\kappa}_x}(\omega) - \frac{q}{c}\tilde{C}_{\boldsymbol{\kappa}_x}(\omega)\right], \tag{5.51}$$

where

$$\tilde{p}^z_{\boldsymbol{\kappa}_x}(\omega) \equiv \mathcal{F}_t\langle\{e^{-i\boldsymbol{\kappa}_x\cdot\mathbf{r}},\hat{p}_z\}\rangle \;\text{ and }\; \tilde{C}_{\boldsymbol{\kappa}_x}(\omega) \equiv \mathcal{F}_t\langle\{e^{-i\boldsymbol{\kappa}_x\cdot\mathbf{r}},A\}\rangle. \tag{5.52}$$

Keeping only the linear term in $\tilde{A}(\omega)$, we find

$$\Delta\mathcal{E}_z(\omega) = -\frac{2q\omega}{c}\,\mathrm{Re}\left[i\tilde{A}^*(\omega)\tilde{v}^z_{\boldsymbol{\kappa}_x}(\omega)\right] = \frac{2q\omega}{c}\,\mathrm{Im}\left[\tilde{A}^*(\omega)\tilde{p}^z_{\boldsymbol{\kappa}_x}(\omega)\right]. \tag{5.53}$$

For a quasi-monochromatic component at frequency ω, one identifies the absorbed energy $\Delta\mathcal{E}(\omega)$ with the incident spectral intensity times the cross section. Therefore, comparing $\Delta\mathcal{E}(\omega)$ to the incident energy flux $I(\omega) = (\omega^2/4\pi c)|\tilde{A}(\omega)|^2$ of a plane wave, one obtains ($q = -1$ in atomic units)

$$\sigma(\omega) = \frac{\Delta\mathcal{E}_z(\omega)}{I(\omega)} = -\frac{8\pi}{\omega}\,\mathrm{Im}\Big[\frac{\tilde{A}^*(\omega)\tilde{p}^z_{\boldsymbol{\kappa}_x}(\omega)}{|\tilde{A}(\omega)|^2}\Big] = -\frac{8\pi}{\omega}\,\mathrm{Im}\Big[\frac{\tilde{p}^z_{\boldsymbol{\kappa}_x}(\omega)}{\tilde{A}(\omega)}\Big]. \tag{5.54}$$

In Eq. (5.54) we use the $\boldsymbol{\kappa}_x$–resolved momentum $\hat{p}^z_{\boldsymbol{\kappa}_x} \equiv \{e^{-i\boldsymbol{\kappa}_x\cdot\hat{\mathbf{r}}},\hat{p}_z\}$, using the canonical commutation relation

$$\left[\hat{p}_z,\, e^{-i\boldsymbol{\kappa}_x\cdot\hat{\mathbf{r}}}\right] = -\,\kappa^z_x\, e^{-i\boldsymbol{\kappa}_x\cdot\hat{\mathbf{r}}}, \tag{5.55}$$

one finds the exact identity

$$\hat{p}^z_{\boldsymbol{\kappa}_x} = 2e^{-i\boldsymbol{\kappa}_x\cdot\hat{\mathbf{r}}}\,\hat{p}_z - \kappa^z_x\, e^{-i\boldsymbol{\kappa}_x\cdot\hat{\mathbf{r}}}. \tag{5.56}$$

Hence the expectation value in Eq. (5.54) splits into two terms

$$\tilde{p}^z_{\boldsymbol{\kappa}_x}(\omega) = \mathcal{F}_t\langle 2e^{-i\boldsymbol{\kappa}_x\cdot\hat{\mathbf{r}}}\hat{p}_z\rangle - \kappa^z_x\mathcal{F}_t\langle e^{-i\boldsymbol{\kappa}_x\cdot\hat{\mathbf{r}}}\rangle. \tag{5.57}$$

In Coulomb gauge the field is transverse and $\boldsymbol{\kappa}_x\cdot\boldsymbol{\epsilon}_x = 0$. If the z–axis is chosen along the probe polarization ($\hat{\mathbf{z}} \parallel \boldsymbol{\epsilon}$), then $\kappa^z_x = \boldsymbol{\kappa}_x\cdot\boldsymbol{\epsilon}_x = 0$ and the second term vanishes, thus

$$\tilde{p}^z_{\boldsymbol{\kappa}_x}(\omega) \equiv \mathcal{F}_t\langle 2e^{-i\boldsymbol{\kappa}_x\cdot\hat{\mathbf{r}}}\hat{p}_z\rangle. \tag{5.58}$$

In the first order of perturbation theory on the interaction Hamiltonian, using Eq. (5.7) and Eq. (5.10), the expectation value of the $\boldsymbol{\kappa}_x$-resolved momentum operator is given by

$$p^{z(1)}_{\boldsymbol{\kappa}_x}(\mathbf{r},t) \propto -i\sum_{\{n_x\},\{\bar{n}_x\}}\rho^x_{\{n_x\},\{\bar{n}_x\}}\lim_{t_0\to-\infty}\int_{t_0}^{t}dt'\langle\Psi(t)|\langle\{\bar{n}_x\}(t)|\hat{p}^z_{\boldsymbol{\kappa}_x}\hat{U}(t,t') \times \hat{H}^x_{\text{int}}\hat{U}(t',t_0)\,|\Psi(t_0)\rangle\,|\{n_x\}(t_0)\rangle + \text{c.c.} \tag{5.59}$$

We use the form of the evolution operator in the interaction picture as $\hat{U}(t',t_0) = e^{-i\left(\hat{H}_{\text{el-em}}+\hat{H}_x\right)(t'-t_0)}$ to propagate the states in Eq. (5.59) then

$$p^{z(1)}_{\boldsymbol{\kappa}_x}(\mathbf{r},t) \propto -i\sum_{\{n_x\},\{\bar{n}_x\}}\rho^x_{\{n_x\},\{\bar{n}_x\}}\int_{-\infty}^{t}dt'\langle\Psi(t)|\langle\{\bar{n}_x\}|e^{iE_{\{\bar{n}_x\}}t'}\hat{p}^z_{\boldsymbol{\kappa}_x}e^{-i\hat{H}_{\text{el-em}}(t-t')} \times \hat{H}^x_{\text{int}}\,|\Psi(t')\rangle\,e^{-iE_{\{n_x\}}t'}\,|\{n_x\}\rangle + \text{c.c.} \tag{5.60}$$

We can insert the unity operator as $\hat{1} = \sum_F |\Psi_F\rangle\langle\Psi_F|$ and simplify the expression further

$$p^{z(1)}_{\boldsymbol{\kappa}_x}(\mathbf{r},t) = -i\sum_F\sum_{\{n_x\},\{\bar{n}_x\}}\rho^x_{\{n_x\},\{\bar{n}_x\}}\int_{-\infty}^{t}dt'e^{-i\mathcal{E}_F(t-t')}\langle\Psi(t)|\hat{p}^z_{\boldsymbol{\kappa}_x}\,|\Psi_F\rangle \times e^{i\left(E_{\{\bar{n}_x\}}-E_{\{n_x\}}\right)t'}\langle\{\bar{n}_x\}|\,\langle\Psi_F|\,\hat{H}^x_{\text{int}}\,|\Psi(t')\rangle\,|\{n_x\}\rangle + \text{c.c.} \tag{5.61}$$

In the Eq. (5.61), the minimal coupling interaction Hamiltonian with the probe x-ray pulse has the form

$$\hat{H}^x_{\text{int}} = \frac{1}{c}\hat{A}_x(\mathbf{r})\cdot\hat{p}_z, \tag{5.62}$$

where the vector potential operator in the second quantization includes multiple modes

$$\hat{\mathbf{A}}_x(\mathbf{r}) = \sum_{\boldsymbol{\kappa}_x,s_x}\sqrt{\frac{2\pi c^2}{V\omega_{\boldsymbol{\kappa}_x}}}\left(\hat{a}_{\boldsymbol{\kappa}_x,s_x}\boldsymbol{\epsilon}_{\boldsymbol{\kappa}_x,s_x}e^{i\boldsymbol{\kappa}_x\mathbf{r}} + \hat{a}^\dagger_{\boldsymbol{\kappa}_x,s_x}\boldsymbol{\epsilon}^*_{\boldsymbol{\kappa}_x,s_x}e^{-i\boldsymbol{\kappa}_x\mathbf{r}}\right) \equiv \hat{\mathbf{A}}^{(+)}(\mathbf{r}) + \hat{\mathbf{A}}^{(-)}(\mathbf{r}). \tag{5.63}$$

We use the form of the vector potential operator in Eq. (5.61) as follows:

$$p^{z(1)}_{\boldsymbol{\kappa}_x}(\mathbf{r},t) = -\frac{i}{c}\sum_F \sum_{\{n_x\},\{\bar{n}_x\}} \rho^x_{\{n_x\},\{\bar{n}_x\}} \int_{-\infty}^{t} dt' e^{-i\mathcal{E}_F(t-t')} \langle \Psi(t)|\hat{p}^z_{\boldsymbol{\kappa}_x}|\Psi_F\rangle \tag{5.64}$$
$$\times \sum_{\boldsymbol{\kappa}_x,s_x} \sqrt{\frac{2\pi c^2}{V\omega_{\boldsymbol{\kappa}_x}}} e^{i\left(E_{\{\bar{n}_x\}}-E_{\{n_x\}}\right)t'} \Big(\langle \Psi_F| \langle \{\bar{n}_x\}|\hat{a}_{\boldsymbol{\kappa}_x,s_x}\boldsymbol{\epsilon}_{\boldsymbol{\kappa}_x,s_x} e^{i\boldsymbol{\kappa}_x\mathbf{r}} |\{n_x\}\rangle \cdot \hat{\mathbf{p}} |\Psi(t')\rangle$$
$$+ \langle \Psi_F| \langle \{\bar{n}_x\}|\hat{a}^\dagger_{\boldsymbol{\kappa}_x,s_x}\boldsymbol{\epsilon}^*_{\boldsymbol{\kappa}_x,s_x} e^{-i\boldsymbol{\kappa}_x\mathbf{r}} |\{n_x\}\rangle \cdot \hat{\mathbf{p}} |\Psi(t')\rangle \Big) + \text{c.c.}$$

In the assumption that energies of the sets $\{n_x\}$ and $\{\bar{n}_x\}$ are different by some x-ray photon energy $\omega_{\boldsymbol{\kappa}_x}$, meaning $E_{\{n_x\}} - E_{\{\bar{n}_x\}} = \omega_{\boldsymbol{\kappa}_x}$, only the part $\hat{\mathbf{A}}^{(+)}(\mathbf{r})$ of the vector potential gives a nonzero matrix element in Eq. (5.64) and

$$p^{z(1)}_{\boldsymbol{\kappa}_x}(\mathbf{r},t) = -\frac{i}{c}\sum_F \sum_{\{n_x\},\{\bar{n}_x\}} \rho^x_{\{n_x\},\{\bar{n}_x\}} \int_{-\infty}^{t} dt' e^{-i\mathcal{E}_F(t-t')} \langle \Psi(t)|\hat{p}^z_{\boldsymbol{\kappa}_x}|\Psi_F\rangle \tag{5.65}$$
$$\times \sum_{\boldsymbol{\kappa}_x,s_x} \sqrt{\frac{2\pi c^2}{V\omega_{\boldsymbol{\kappa}_x}}} e^{i\left(E_{\{\bar{n}_x\}}-E_{\{n_x\}}\right)t'} \langle \Psi_F| \langle \{\bar{n}_x\}|\hat{a}_{\boldsymbol{\kappa}_x,s_x}\boldsymbol{\epsilon}_{\boldsymbol{\kappa}_x,s_x} e^{i\boldsymbol{\kappa}_x\mathbf{r}} |\{n_x\}\rangle \cdot \hat{\mathbf{p}} |\Psi(t')\rangle + \text{c.c.}$$

Eq. (5.65) can be simplified by introducing the assumptions about the state of the probe x-ray pulse, which define the expectation value of the $\hat{\mathbf{A}}^{(+)}(\mathbf{r})$

$$f(\mathbf{r},t') = \sum_{\{n_x\},\{\bar{n}_x\}} \rho^x_{\{n_x\},\{\bar{n}_x\}} \langle \{\bar{n}_x\}| \sum_{\boldsymbol{\kappa}_x,s_x} \sqrt{\frac{2\pi c^2}{V\omega_{\boldsymbol{\kappa}_x}}} \hat{a}_{\boldsymbol{\kappa}_x,s_x}\boldsymbol{\epsilon}_{\boldsymbol{\kappa}_x,s_x} e^{i\boldsymbol{\kappa}_x\mathbf{r}-i\omega_{\boldsymbol{\kappa}_x}t'} |\{n_x\}\rangle . \tag{5.66}$$

We assume that the probe x-ray pulse is described by a multimode coherent field. We also assume that absorption does not influence the coherent state. In this case,

$$f(\mathbf{r}_0,t') = \langle \{\alpha\}|\hat{\mathbf{A}}^{(+)}(\mathbf{r},t')|\{\alpha\}\rangle = \mathbf{A}^{(+)}(\mathbf{r},t'), \tag{5.67}$$

where the multimode coherent state is $|\{\widetilde{\alpha}\}\rangle = \prod_{\boldsymbol{\kappa}_x,s_x} |\alpha_{\boldsymbol{\kappa}_x,s_x}\rangle$, $|\alpha_{\boldsymbol{\kappa}_x,s_x}\rangle$ is the coherent state and the eigenvector of $\hat{a}_{\boldsymbol{\kappa}s}$. $|\{\widetilde{\alpha}\}\rangle$ is the eigenvector of $\hat{\mathbf{A}}^{(+)}(\mathbf{r},t)$ with the eigenvalue $\mathbf{A}^{(+)}(\mathbf{r},t)$. In the case if the probe x-ray field is described by the multimode coherent state, the expectation value of the canonical momentum is proportional to the $\mathbf{A}^{(+)}(\mathbf{r},t')$. Applying the same procedure to the $\mathbf{A}^{(-)}(\mathbf{r},t)$ part yields a similar result. Collecting both terms together gives

$$p^{z(1)}_{\boldsymbol{\kappa}_x}(\mathbf{r},t) = -\frac{i}{c}\sum_F \int_{-\infty}^{t} dt' e^{-i\mathcal{E}_F(t-t')} \langle \Psi(t)|\hat{p}^z_{\boldsymbol{\kappa}_x}|\Psi_F\rangle \tag{5.68}$$
$$\times \Big(\mathbf{A}(t') \langle \Psi_F| e^{i\boldsymbol{\kappa}_x\cdot\mathbf{r}} \cdot \hat{\mathbf{p}} |\Psi(t')\rangle + \mathbf{A}^*(t') \langle \Psi_F| e^{-i\boldsymbol{\kappa}_x\cdot\mathbf{r}} \cdot \hat{\mathbf{p}} |\Psi(t')\rangle \Big) + \text{c.c.}$$

For the classical field we have vector potential of the form

$$\mathbf{A}(\mathbf{r},t) = \mathbf{A}(t)e^{i\boldsymbol{\kappa}_\mathrm{x}\cdot\mathbf{r}} + \mathbf{A}^*(t)e^{-i\boldsymbol{\kappa}_\mathrm{x}\cdot\mathbf{r}} \equiv \mathbf{A}^{(+)}(\mathbf{r},t) + \mathbf{A}^{(-)}(\mathbf{r},t) \tag{5.69}$$

In Eq. (5.68) each Floquet state $|\Psi_F\rangle$ belongs to a family of replica states $|\Psi_{F_{\Delta\mu}}\rangle$. Similarly to Eq. (5.20), the summation over Floquet states $|\Psi_F\rangle$ can be written as a sum over reference states $|\Psi_{F_0}\rangle$ and Floquet bands $\Delta\mu$. Additionally, taking into account the form of time-dependent electronic state $|\Psi_\mathrm{el}(t)\rangle$ given by Eq. (2.35) and (2.36), we get

$$\begin{aligned}
&\sum_F e^{-i\mathcal{E}_F(t-t')}\langle\Psi(t)|\hat{p}^z_{\boldsymbol{\kappa}_\mathrm{x}}|\Psi_F\rangle\langle\Psi_F|\mathbf{A}(\mathbf{r},t')\cdot\hat{\mathbf{p}}|\Psi(t')\rangle \\
&= \sum_{F_0} e^{-i(\mathcal{E}_{F_0}-\mathcal{E}_{I_0})(t-t')} \sum_{n,k,\mu,\Delta\mu} e^{-i\Delta\mu\Omega t} C^{F_0}_{n\mu+\Delta\mu} C^{I_0*}_{k\mu} \langle\Phi_k|\hat{p}^z_{\boldsymbol{\kappa}_\mathrm{x}}|\Phi_n\rangle \\
&\quad\times \sum_{n',k',\mu',\Delta\mu'} e^{i\Delta\mu'\Omega t'} C^{F_0*}_{n'\mu'+\Delta\mu'} C^{I_0}_{k'\mu'} \langle\Phi_{n'}|\mathbf{A}(\mathbf{r},t')\cdot\hat{\mathbf{p}}|\Phi_{k'}\rangle .
\end{aligned} \tag{5.70}$$

In Eq. (5.70) the matrix elements are defined via many-body electronic states $|\Phi_k\rangle$. The goal is to represent it via the matrix elements between one-body Kohn–Sham wavefunctions, since we do not consider electronic correlations. The many-body wavefunction can be expanded in terms of the many-body eigenstates of the electronic Hamiltonian $\hat{H}_\mathrm{el}$ as $|\Psi^{I_0}_\mathrm{el}(t)\rangle = e^{-i\mathcal{E}_{I_0}t}\sum_{k,\nu} C^{I_0}_{k\nu} e^{-i\nu\Omega t}|\Phi_k\rangle$. Using this expansion, the matrix element of the operator $\hat{\mathbf{O}}$ is given by:

$$\langle\Psi^{F_0}_\mathrm{el}(t)|\hat{\mathbf{O}}|\Psi^{I_0}_\mathrm{el}(t)\rangle = e^{i(\mathcal{E}_{F_0}-\mathcal{E}_{I_0})t}\sum_{\Delta\mu} e^{i\Delta\mu\Omega t}\sum_{n,k,\mu} C^{F_0*}_{n\mu+\Delta\mu} C^{I_0}_{k\mu}\langle\Phi_n|\hat{\mathbf{O}}|\Phi_k\rangle . \tag{5.71}$$

On the other hand, using the Slater–Condon rules

$$\langle\Psi^{F_0}_\mathrm{el}(t)|\hat{\mathbf{O}}|\Psi^{I_0}_\mathrm{el}(t)\rangle = e^{i(\varepsilon_{f\mathbf{k}'}-\varepsilon_{i\mathbf{k}})t}\sum_{\Delta\mu} e^{i\Delta\mu\Omega t}\sum_{m,m',\mu} c^{f*}_{m'\mathbf{k}'\mu+\Delta\mu} c^{i}_{m\mathbf{k}\mu}\langle\varphi_{m'\mathbf{k}'}|\hat{\mathbf{O}}|\varphi_{m\mathbf{k}}\rangle . \tag{5.72}$$

Using Eq. (5.71) and Eq. (5.72), Eq. (5.70) can be rewritten as

$$\begin{aligned}
&\sum_F e^{-i\mathcal{E}_F(t-t')}\langle\Psi(t)|\hat{p}^z_{\boldsymbol{\kappa}_\mathrm{x}}|\Psi_F\rangle\langle\Psi_F|\mathbf{A}(\mathbf{r},t')\cdot\hat{\mathbf{p}}|\Psi(t')\rangle \\
&= \sum_{i,f,\mathbf{k},\mathbf{k}'} e^{i(\varepsilon_{f\mathbf{k}'}-\varepsilon_{i\mathbf{k}})t'}\sum_{\Delta\mu} e^{i\Delta\mu\Omega t'}\sum_{m,m',\mu} c^{f*}_{m'\mathbf{k}'\mu+\Delta\mu} c^{i}_{m\mathbf{k}\mu}\langle\varphi_{m'\mathbf{k}'}|\mathbf{A}(\mathbf{r},t')\cdot\hat{\mathbf{p}}|\varphi_{m\mathbf{k}}\rangle \\
&\quad\times e^{-i(\varepsilon_{f\mathbf{k}'}-\varepsilon_{i\mathbf{k}})t}\sum_{\Delta\nu} e^{-i\Delta\nu\Omega t}\sum_{n,n',\nu} c^{f}_{n'\mathbf{k}'\nu+\Delta\nu} c^{i*}_{n\mathbf{k}\nu}\langle\varphi_{n\mathbf{k}}|\hat{p}^z_{\boldsymbol{\kappa}_\mathrm{x}}|\varphi_{n'\mathbf{k}'}\rangle .
\end{aligned} \tag{5.73}$$

As previously, we consider an initial state corresponding to a core electron residing deep below the Fermi energy. Then, we can express the initial one-body electronic Floquet–Bloch

state as given in Eq. (5.35). Equation (5.73) can now be written as follows:

$$\sum_F e^{-i\mathcal{E}_F(t-t')}\langle\Psi(t)|\hat{p}^z_{\boldsymbol{\kappa}_x}|\Psi_F\rangle\langle\Psi_F|\,\mathbf{A}(\mathbf{r},t')\cdot\hat{\mathbf{p}}\,|\Psi(t')\rangle \tag{5.74}$$
$$= \sum_{f,\mathbf{k},\mathbf{k}'} e^{i(\varepsilon_{f\mathbf{k}'}-\varepsilon_c)t'}\sum_{\Delta\mu} e^{i\Delta\mu\Omega t'}\sum_{m'} c^{f*}_{m'\mathbf{k}'\Delta\mu}\langle\varphi_{m'\mathbf{k}'}|\,\mathbf{A}(\mathbf{r},t')\cdot\hat{\mathbf{p}}\,|\varphi^c_{\mathbf{k}}\rangle$$
$$\times e^{-i(\varepsilon_{f\mathbf{k}'}-\varepsilon_c)t}\sum_{\Delta\nu} e^{-i\Delta\nu\Omega t}\sum_{n'} c^{f}_{n'\mathbf{k}'\Delta\nu}\langle\varphi^c_{\mathbf{k}}|\,\hat{p}^z_{\boldsymbol{\kappa}_x}|\varphi_{n'\mathbf{k}'}\rangle\,.$$

Substituting the Eq. (5.74) into the expectation value in Eq. (5.68) gives

$$p^{z(1)}_{\boldsymbol{\kappa}_x}(\mathbf{r},t) = -\frac{i}{c}\int_{-\infty}^{t} dt' \sum_{f,\mathbf{k},\mathbf{k}'} e^{i(\varepsilon_{f\mathbf{k}'}-\varepsilon_c)t'}\sum_{\Delta\mu} e^{i\Delta\mu\Omega t'}\sum_{m'} c^{f*}_{m'\mathbf{k}'\Delta\mu}\langle\varphi_{m'\mathbf{k}'}|\,\mathbf{A}(\mathbf{r},t')\cdot\hat{\mathbf{p}}\,|\varphi^c_{\mathbf{k}}\rangle \tag{5.75}$$
$$\times e^{-i(\varepsilon_{f\mathbf{k}'}-\varepsilon_c)t}\sum_{\Delta\nu} e^{-i\Delta\nu\Omega t}\sum_{n'} c^{f}_{n'\mathbf{k}'\Delta\nu}\langle\varphi^c_{\mathbf{k}}|\,\hat{p}^z_{\boldsymbol{\kappa}_x}|\varphi_{n'\mathbf{k}'}\rangle + \text{c.c.}$$

The momentum matrix elements $\langle\varphi_{m'\mathbf{k}'}|\,e^{\pm i\boldsymbol{\kappa}_x\mathbf{r}}\hat{\mathbf{p}}\,|\varphi^c_{\mathbf{k}}\rangle$ can be evaluated using the procedure described in Section 5.3.2 and in the Appendix A.1.4, see Eq. (A.10)

$$\int d^3r e^{\pm i\boldsymbol{\kappa}_x\mathbf{r}}\varphi^\dagger_{m'\mathbf{k}'}(\mathbf{r})(\boldsymbol{\epsilon}_{\boldsymbol{\kappa}_x}\cdot\boldsymbol{\nabla})\varphi^c_{\mathbf{k}}(\mathbf{r}) = N^2_{\text{cell}}\sum_{\mathbf{G}}\delta^{(3)}(\mathbf{k}\pm\boldsymbol{\kappa}_x-\mathbf{k}'-\mathbf{G})\langle\varphi_{m'\mathbf{k}'}|\,\hat{p}_{\boldsymbol{\epsilon}}\,|\varphi^{c_0}\rangle\,, \tag{5.76}$$

where we introduce the notation for the derivative along the field as $\boldsymbol{\epsilon}_{\boldsymbol{\kappa}_x}\cdot\boldsymbol{\nabla} = \hat{p}_{\boldsymbol{\epsilon}}$. We substitute Eq. (5.76) into Eq. (5.75) and use the fact that, for each final quasimomentum $\mathbf{k}'$, there are $N_{\mathbf{G}}$ values of the quasimomentum $\mathbf{k}$ of the initial core electron state at the flat band

$$\sum_{\mathbf{k}}\sum_{\mathbf{G}}\delta^{(3)}(\mathbf{k}\pm\boldsymbol{\kappa}_x-\mathbf{k}'-\mathbf{G})f(\mathbf{k}') = \sum_{\mathbf{G}} f(\mathbf{k}')\big|_{\mathbf{k}=\mathbf{k}'+\mathbf{G}\mp\boldsymbol{\kappa}_x} = N_{\mathbf{G}}f(\mathbf{k}'). \tag{5.77}$$

The result implies that, although the absorption process conserves momentum via the x-ray wave vector, the final expression becomes independent of $\boldsymbol{\kappa}_x$ due to the flat-band nature of the initial core electron state. Collecting all together

$$p^{z(1)}_{\mathbf{k}}(t) = -i\int_{-\infty}^{t} dt'\,\left[A(t')+A^*(t')\right]\sum_{f,\mathbf{k}'}\sum_{\nu,\Delta\nu} e^{i(\varepsilon_{f\mathbf{k}'}-\varepsilon_c+\nu\Omega)(t'-t)}e^{i\Delta\nu\Omega t'}\mathcal{D}^{f\mathbf{k}'}_{\nu,\Delta\nu} + \text{c.c.}, \tag{5.78}$$

where we introduce notation

$$\mathcal{D}^{f\mathbf{k}'}_{\nu,\Delta\nu} = \frac{1}{c}N^4_{\text{cell}}N_{\mathbf{G}}\sum_{m',n'} c^{f*}_{m'\mathbf{k}'\nu+\Delta\nu}c^{f}_{n'\mathbf{k}'\nu}\langle\varphi_{m'\mathbf{k}'}|\,\hat{p}_{\boldsymbol{\epsilon}}\,|\varphi^{c_0}\rangle\langle\varphi^{c_0}|\,\hat{p}_{\boldsymbol{\epsilon}}\,|\varphi_{n'\mathbf{k}'}\rangle\,. \tag{5.79}$$

The momentum expectation value in the frequency domain $\tilde{p}(\omega)$ is calculated in Ap-

pendix A.1.6 and given by

$$\tilde{p}(\omega) = \sum_{f,\mathbf{k}'} \sum_{\nu,\Delta\nu} \tilde{A}(\omega + \Delta\nu\Omega) \frac{\omega - (\varepsilon_{f\mathbf{k}'} - \varepsilon_c + \nu\Omega) - i\eta}{(\omega - (\varepsilon_{f\mathbf{k}'} - \varepsilon_c + \nu\Omega))^2 + \eta^2} \mathcal{D}^{f\mathbf{k}'}_{\nu,\Delta\nu} \\ -\tilde{A}^*(-\omega + \Delta\nu\Omega) \frac{\omega + (\varepsilon_{f\mathbf{k}'} - \varepsilon_c + \nu\Omega) - i\eta}{(\omega + (\varepsilon_{f\mathbf{k}'} - \varepsilon_c + \nu\Omega))^2 + \eta^2} \left(\mathcal{D}^{f\mathbf{k}'}_{\nu,\Delta\nu}\right)^* \tag{5.80}$$

In the calculations, the ultrashot probe x-ray pulse is described by a vector potential with a Gaussian-shaped envelope, defined as

$$A^x(t) = A^x_0 \cos(\omega_0(t - t_p) + \phi) e^{-a(t-t_p)^2}, \tag{5.81}$$

where $a = 2\ln 2/\tau_p^2$. A_0, ω_0, ϕ, and τ_p are the amplitude, central frequency, carrier-envelope phase, and pulse duration, respectively.

The frequency-dependent vector potential is obtained through the Fourier transform as

$$\tilde{A}^{\pm}(\omega) = \frac{A_0}{2\sqrt{2a}} \exp\left(\pm i\phi - \frac{(\omega \pm \omega_0)^2}{4a} - i\omega t_p\right), \tag{5.82}$$

where $\tilde{A}^{\pm}$ denotes $A = A^+ + A^-$. Note that in this expression the component A^+ is negligible for positive frequencies. In the following, we keep only the component A^-. In the RWA and considering only the resonant contribution

$$\tilde{p}(\omega) = \sum_{f,\mathbf{k}'} \sum_{\nu,\Delta\nu} \tilde{A}(\omega + \Delta\nu\Omega) \frac{\omega - (\varepsilon_{f\mathbf{k}'} - \varepsilon_c + \nu\Omega) - i\eta}{(\omega - (\varepsilon_{f\mathbf{k}'} - \varepsilon_c + \nu\Omega))^2 + \eta^2} \mathcal{D}^{f\mathbf{k}'}_{\nu,\Delta\nu}, \tag{5.83}$$

where

$$\tilde{A}(\omega + \Delta\nu\Omega) \approx \frac{A_0 e^{-i(\omega+\Delta\nu\Omega)t_p}}{2\sqrt{2a}} \exp\left(-i\phi - \frac{(\omega - \omega_0 + \Delta\nu\Omega)^2}{4a}\right). \tag{5.84}$$

The absorption cross section in the velocity gauge can be calculated according to Eq. (5.54):

$$\sigma(\omega) = -\frac{8\pi}{\omega} \operatorname{Im}\left(\sum_{f,\mathbf{k}'} \sum_{\nu,\Delta\nu} \frac{\tilde{A}(\omega + \Delta\nu\Omega)}{\tilde{A}(\omega)} \frac{\omega - \overline{\omega}_{f\mathbf{k}'\nu} - i\eta}{(\omega - \overline{\omega}_{f\mathbf{k}'\nu})^2 + \eta^2} \mathcal{D}^{f\mathbf{k}'}_{\nu,\Delta\nu}\right), \tag{5.85}$$

where $\overline{\omega}_{f\mathbf{k}'\nu} = \varepsilon_{f\mathbf{k}'} - \varepsilon_c + \nu\Omega$ and the ratio

$$\frac{\tilde{A}(\omega + \Delta\nu\Omega)}{\tilde{A}(\omega)} \approx e^{-i\Delta\nu\Omega t_p} e^{-\frac{(\omega-\omega_0+\Delta\nu\Omega)^2}{4a}} e^{\frac{(\omega-\omega_0)^2}{4a}}. \tag{5.86}$$

We use the time-reversal symmetry property of the Floquet–Bloch coefficients for linearly polarized driving field of the form $\mathbf{E}(t) = \mathbf{F}_0 \sin\Omega t$, namely $c^i_{n\mathbf{k}\mu} = (-1)^\mu c^{i*}_{n-\mathbf{k}\mu}$. We then obtain the following symmetry relation for the transition moment amplitudes $\mathcal{D}^{f\mathbf{k}'}_{\nu,\Delta\nu}$:

$$\mathcal{D}^{f\mathbf{k}'}_{\nu,\Delta\nu} = (-1)^{\Delta\nu} \left(\mathcal{D}^{f-\mathbf{k}'}_{\nu,\Delta\nu}\right)^*. \tag{5.87}$$

This relation leads to the absorption cross section with the amplitudes of the odd order $\Delta\nu_{\text{odd}}$ proportional to the imaginary part $\text{Im}\,\mathcal{D}^{f\mathbf{k}'}_{\nu,\Delta\nu}$ and the even order amplitudes $\Delta\nu_{\text{even}}$ proportional to the real part $\text{Re}\,\mathcal{D}^{f\mathbf{k}'}_{\nu,\Delta\nu}$ of the transition moment amplitudes. Thus, in general, the time-dependent absorption cross section can be written in terms of the amplitudes as follows:

$$\begin{aligned}\sigma(\omega,t_{\text{p}}) = \tilde{\sigma}_{\cos}(\omega,\Delta\nu=0) + \sum_{\Delta\nu\geq 1}\left(\tilde{\sigma}_{\sin}(\omega,\Delta\nu) - \tilde{\sigma}_{\sin}(\omega,-\Delta\nu)\right)\sin(\Delta\nu\Omega t_{\text{p}}) \\ + \sum_{\Delta\nu\geq 1}(-1)^{\Delta\nu}\left(\tilde{\sigma}_{\cos}(\omega,\Delta\nu) + \tilde{\sigma}_{\cos}(\omega,-\Delta\nu)\right)\cos(\Delta\nu\Omega t_{\text{p}}),\end{aligned} \tag{5.88}$$

where the amplitudes are defined as follows for even orders:

$$\begin{aligned}\tilde{\sigma}_{\sin}(\omega,\Delta\nu_{\text{even}}) &= \frac{8\pi}{\omega}e^{-\frac{\Delta\nu\Omega}{2a}(\omega-\omega_0+\Delta\nu_{\text{even}}\Omega/2)}\sum_{f,\mathbf{k}',\nu}F(\omega;\overline{\omega}_{f\mathbf{k}'\nu},\eta)\,\text{Re}\left(\mathcal{D}^{f\mathbf{k}'}_{\nu,\Delta\nu_{\text{even}}}\right), \\ \tilde{\sigma}_{\cos}(\omega,\Delta\nu_{\text{even}}) &= \frac{8\pi}{\omega}e^{-\frac{\Delta\nu\Omega}{2a}(\omega-\omega_0+\Delta\nu_{\text{even}}\Omega/2)}\sum_{f,\mathbf{k}',\nu}L(\omega;\overline{\omega}_{f\mathbf{k}'\nu},\eta)\,\text{Re}\left(\mathcal{D}^{f\mathbf{k}'}_{\nu,\Delta\nu_{\text{even}}}\right)\end{aligned} \tag{5.89}$$

and for the odd orders:

$$\begin{aligned}\tilde{\sigma}_{\sin}(\omega,\Delta\nu_{\text{odd}}) &= \frac{8\pi}{\omega}e^{-\frac{\Delta\nu\Omega}{2a}(\omega-\omega_0+\Delta\nu_{\text{odd}}\Omega/2)}\sum_{f,\mathbf{k}',\nu}L(\omega;\overline{\omega}_{f\mathbf{k}'\nu},\eta)\,\text{Im}\left(\mathcal{D}^{f\mathbf{k}'}_{\nu,\Delta\nu_{\text{odd}}}\right), \\ \tilde{\sigma}_{\cos}(\omega,\Delta\nu_{\text{odd}}) &= -\frac{8\pi}{\omega}e^{-\frac{\Delta\nu\Omega}{2a}(\omega-\omega_0+\Delta\nu_{\text{odd}}\Omega/2)}\sum_{f,\mathbf{k}',\nu}F(\omega;\overline{\omega}_{f\mathbf{k}'\nu},\eta)\,\text{Im}\left(\mathcal{D}^{f\mathbf{k}'}_{\nu,\Delta\nu_{\text{odd}}}\right).\end{aligned} \tag{5.90}$$

In Eqs. (5.89) and (5.90), we introduce the following notation for line shape functions:

$$L(\omega;\overline{\omega}_{f\mathbf{k}'\nu},\eta) = \frac{\eta}{(\omega-\overline{\omega}_{f\mathbf{k}'\nu})^2+\eta^2}, \quad F(\omega;\overline{\omega}_{f\mathbf{k}'\nu},\eta) = \frac{\omega-\overline{\omega}_{f\mathbf{k}'\nu}}{(\omega-\overline{\omega}_{f\mathbf{k}'\nu})^2+\eta^2}, \tag{5.91}$$

where $L(\omega;\overline{\omega}_{f\mathbf{k}'\nu},\eta)$ corresponds to the symmetric Lorentzian profile, and $F(\omega;\overline{\omega}_{f\mathbf{k}'\nu},\eta)$ represents the asymmetric Fano-like profile. Since Eq. (5.85) lacks symmetry under the transformation $\Delta\nu \to -\Delta\nu$, the amplitudes corresponding to the $\Delta\nu$ and $-\Delta\nu$ orders are not complex conjugates of each other. Plotting the extracted amplitudes reveals that the $\Delta\nu$ and $-\Delta\nu$ components differ in absolute magnitude and are shifted in energy by $\Delta\nu\Omega$.

We will show that the symmetric component is directly related to the density of available final states at a given energy, while the asymmetric contribution arises due to the finite spectral bandwidth of the probe pulse. In ultrafast XAS, the observed line shape depends not only on the number of final states accessible for the transition but also on the intensity distribution of spectral components within the probe pulse. The interplay between these symmetric and asymmetric contributions gives rise to the characteristic "fishbone" resonance structures, which has been both explained theoretically [198] and observed experimentally [8, 86, 87].

5.5. *Ab initio* computational scheme

Figure 5.1 illustrates the computational workflow used in this work.

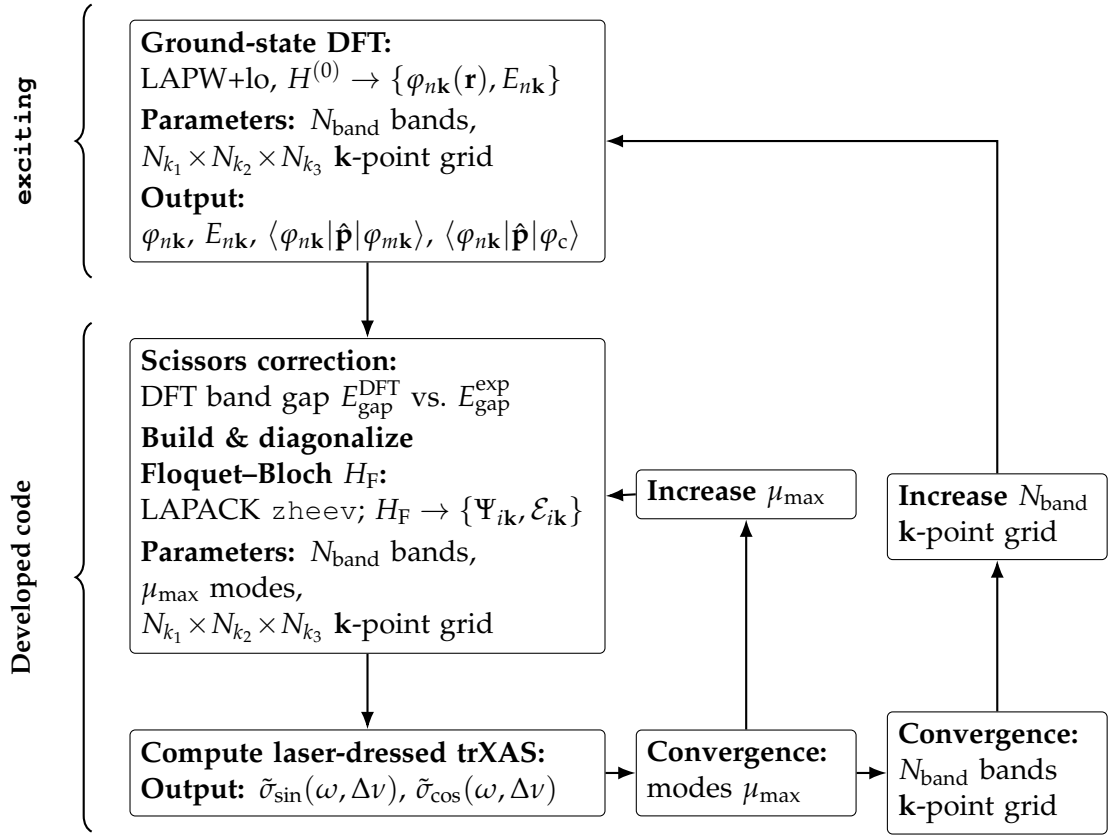

Figure 5.1.: *Ab initio* computational scheme for laser-dressed XAS with left-side grouping braces indicating external (`exciting`) and developed code components.

The aim is to obtain a converged transient x-ray absorption signal for given driving-field intensity and polarization. For the convergence analysis, we focused on the Zn L_3-edge because it has both pronounced pre-edge and near-edge XAS features. We chose a probe x-ray pulse with a polarization of $\boldsymbol{\epsilon}_{\text{x}} = (001)$ and a duration of 125 as.

Before starting the convergence study, we first performed a full lattice relaxation to determine the equilibrium structural parameters of wurtzite ZnO. The convergence analysis was then carried out with respect to the number of conduction states, the number of Floquet modes, and the **k**-point sampling. We assumed that **k**-point convergence is independent from the convergence with respect to the number of conduction states and Floquet modes. The convergence study started from a $4 \times 4 \times 3$ **k**-point grid and 50 conduction bands, and for each new set of parameters the first step was always a ground-state DFT calculation.

We calculate the Bloch electron wavefunctions $\varphi_{n\mathbf{k}}(\mathbf{r})$ and the corresponding eigenenergies $E_{n\mathbf{k}}(\mathbf{r})$ of the field-free Hamiltonian $H^{(0)}$, which describe the ground state of wurtzite ZnO, using the LAPW+lo method implemented in `exciting` [137]. We use the GGA-PBE

functional [151] and consider the $3d^{10}4s^2$ electrons of Zn and the $2s^22p^4$ electrons of O as valence electrons. In addition, the Zn $3p$ orbitals are included as semicore states in the basis within LAPW+lo method. Next, the matrix elements of the momentum between the different Kohn–Sham states are calculated. The matrix elements are used later in the workflow. In addition, we extracted the momentum matrix elements between the entire set of Kohn–Sham wavefunctions and the core electron wavefunction of the selected initial state, which are required to describe the x-ray-induced transitions.

For a fixed number of conduction states, the Floquet–Bloch Hamiltonian is constructed and diagonalized [133]. We apply a scissors correction [153] to compensate for the underestimated DFT band gap compared to the experimental 3.4 eV [192]. The diagonalization of the Floquet–Bloch Hamiltonian matrix gives the set of Floquet–Bloch states and quasienergies. The number of Floquet modes is then increased in workflow until the convergence of absorption profile is archived.

We use the calculated eigenvalues and eigenvectors of the Floquet–Bloch matrix to evaluate the transition amplitudes into the different reference Floquet–Bloch states, as well as the resulting absorption cross section. The number of conduction bands is then increased in workflow until the convergence of absorption profile is archived. Figure 5.2 shows the results of the convergence study with respect to the number of conduction bands included in the calculations.

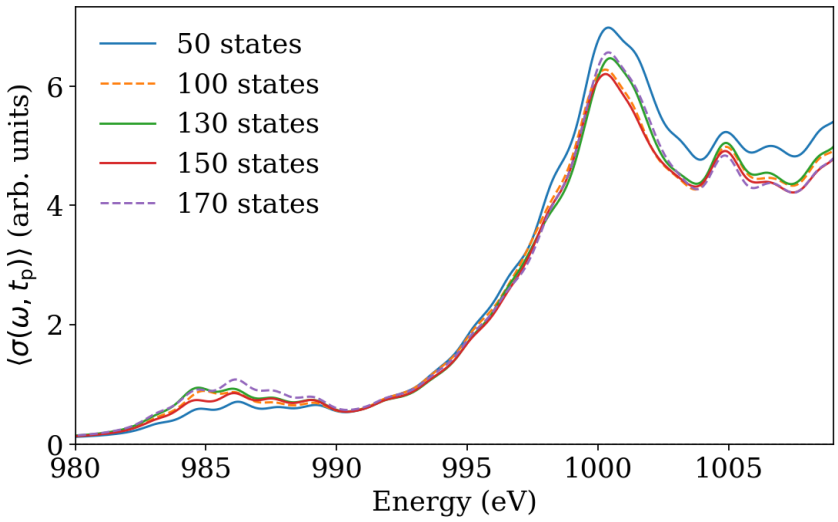

Figure 5.2.: A convergence study of the x-ray absorption cross section $\langle\sigma(\omega, t_p)\rangle$ at the Zn L_3-edge with respect to the number of conduction states included in the calculation. The polarization of the probe x-ray pulse was chosen to be $\epsilon_x = (001)$.

Finally, with the number of conduction states and Floquet modes fixed, the **k**-point mesh was refined step by step until the transient x-ray absorption signal converged. Figure 5.3 shows the results of the convergence study with respect to the number of **k**-points in the calculations. According to a convergence study, the laser-induced changes in the signals

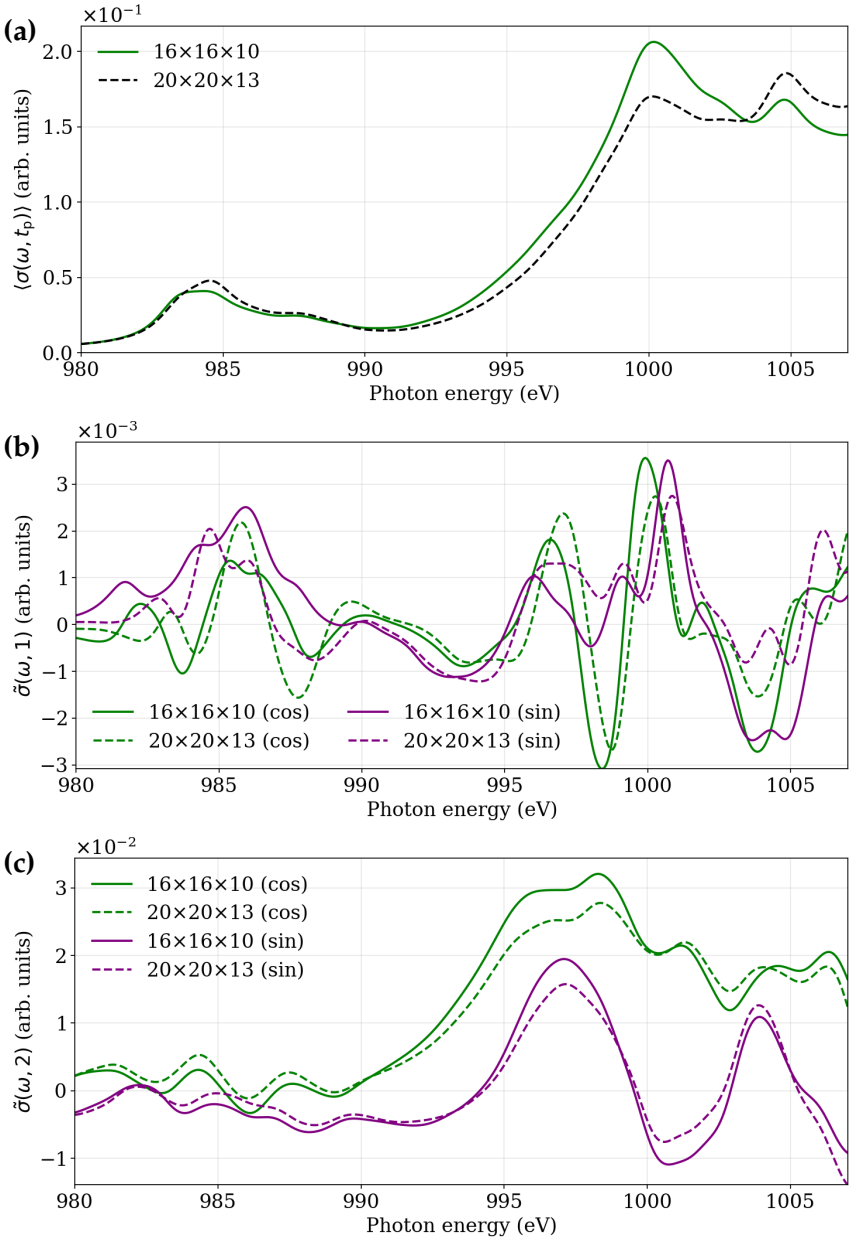

Figure 5.3.: A convergence study with respect to the number of **k**-points. The amplitudes of the x-ray absorption cross section at the Zn L_3-edge for (a) the zero-order, (b) the first-order, and (c) the second-order components. The results were obtained using 20×20×13 and 16×16×10 **k**-point grids, with all spectra scaled by the number of **k**-points in each case.

are found to be converged for a $16 \times 16 \times 10$ **k**-point grid, 150 conduction states, and $2\mu_{\max} + 1 = 121$ blocks of the Floquet Hamiltonian.

The trXAS data are calculated for the converged parameters and a probe x-ray pulse with a duration of 125 as. In the calculations, the values of the linewidth η are taken to be proportional to the corresponding natural widths of atomic K and L levels [199]. The value η used for the calculations of the O K-edge is 0.5 eV, and the value η used to calculate the

Zn L_3-edge is 0.8 eV.

5.6. Results

We calculate the ultrafast x-ray absorption spectra of a wurtzite ZnO crystal in the presence of a strong driving field. The field has an intensity of 5 TW/cm^2, a photon energy of 1.55 eV, and an electric field polarization aligned along the z-axis. As the crystal's band gap is approximately 3.4 eV, the driving field is non-resonant. We calculate the laser-dressed x-ray absorption spectra at the O K and Zn L_3 absorption edges over an energy range covering both the valence and conduction bands. The x-ray absorption spectra are calculated for a probe x-ray pulse with a duration of 125 as. In the calculations, the linewidth parameter η is taken to be proportional to the natural widths of the chosen atomic levels [199].

In XAS, a core electron is excited from a localized core level into an unoccupied valence or conduction state by absorbing an x-ray photon. According to Fermi's golden rule, the transition rate is proportional to the product of the squared transition matrix element and the unoccupied density of final states available for the transition. Because the core level is highly localized, XAS probes the density of unoccupied states associated with the absorbing atom. In most cases, the dominant contributions come from dipole-allowed transitions, while higher-order multipole contributions provide smaller corrections at higher x-ray photon energies. The resulting absorption spectrum therefore carries detailed information about the density and character of the unoccupied electronic states. Thus, the ability to extract information about the electronic structure of a system through the x-ray absorption spectrum depends on the unique connection between the x-ray absorption profile and the unoccupied PDOS.

We begin by analyzing the unoccupied PDOS of wurtzite ZnO crystal in its ground state, as this provides a reference for identifying the relevant energy range and supports the interpretation of our XAS modeling results. Figure 5.4 shows the calculated PDOS of the conduction band in the ground state of a wurtzite ZnO crystal, which agrees well with the results presented in Ref. [188]. Ref. [188] has shown that the DOS of the conduction states, as calculated in the GW approximation, agrees well with that obtained in the DFT calculation using the GGA-PBE potential, except for an energy shift. This validates the application of the scissor operator.

The lowest-energy part of the conduction band is formed primarily by states with strong O p and Zn s characters. At around 5 eV, an additional contribution from Zn $4p$ states increases. At 11.7 eV, the conduction-band PDOS displays a sharp peak formed by O $2p$–Zn $4s$ antibonding states. Above 13.3 eV, the contribution of the states with strong Zn p character is predominant, although these states are still hybridized with the Zn s states.

In the presence of the driving field, an attosecond XAS measurement provides access

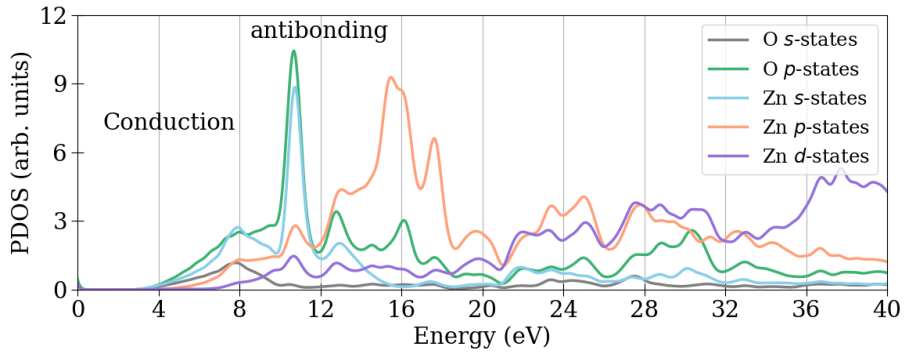

Figure 5.4.: PDOS of wurtzite ZnO in the conduction band in the ground state. The gray, green, blue, orange and purple lines correspond to the O s-, O p-, Zn s-, Zn p- and Zn d-projected PDOS, respectively. The Fermi energy, E_F, is set to 0 eV.

to the laser-driven changes in the electronic populations. Analysis of these changes allows for the study of excited-carrier dynamics and electron transfer from valence- to conduction-band states. In such measurements, an x-ray probe pulse with a bandwidth spanning several tens of electronvolts enables the simultaneous observation of laser-driven electron dynamics within the valence and conduction bands through the measured x-ray absorption spectrum. At the O K-edge, the dipole-allowed transitions correspond to excitations from the 1s core level to unoccupied states with strong np-character. At the Zn L_3-edge, the dipole-allowed transitions involve excitations from the $2p_{3/2}$ core level to unoccupied states with strong ns- and nd-character. Thus, attosecond XAS measurements at the O K- and Zn L_3-edges are expected to provide an orbital- and site-selective view of laser-dressed electron dynamics.

In Chapter 4, we illustrated that, in the presence of a strong driving field, the PDOS distribution changes relative to the corresponding field-free distributions. Due to the optical Stark effect, the energy positions of the main peaks in the PDOS shift relative to the corresponding positions in the field-free distributions and its intensity changes. The distributions also become broader due to the appearance of side peaks. In this regime, using the ground-state PDOS as a reference when interpreting the x-ray absorption signal can be misleading. We calculate the laser-dressed PDOS of the unoccupied states using the approach developed in Chapter 4 to support the interpretation of our trXAS modeling. The results are shown in Fig. 5.5. Each pair of plots in Fig. 5.5 shows the time-averaged PDOS together with the corresponding field-free PDOS in the left panels and the time-dependent part of the PDOS in the right panels. The total laser-dressed PDOS, obtained as the sum of the time-averaged and time-dependent parts, is positive for all energies. We group the PDOS projections according to the orientation of the corresponding orbitals relative to the z axis. This is due to the wurtzite crystal structure with the hexagonal c-axis oriented along the z direction and the polarization of the driving field parallel to the z-axis. The PDOS projected onto orbitals lying in the xy plane includes component $\mathcal{D}^{\mathrm{O}}_{p_x}$ and components $\mathcal{D}^{\mathrm{Zn}}_{d_{xy}}$, $\mathcal{D}^{\mathrm{Zn}}_{d_{x^2-y^2}}$, which are denoted together as $\mathcal{D}^{\mathrm{Zn}}_{d_x}$. The PDOS projected onto orbitals with

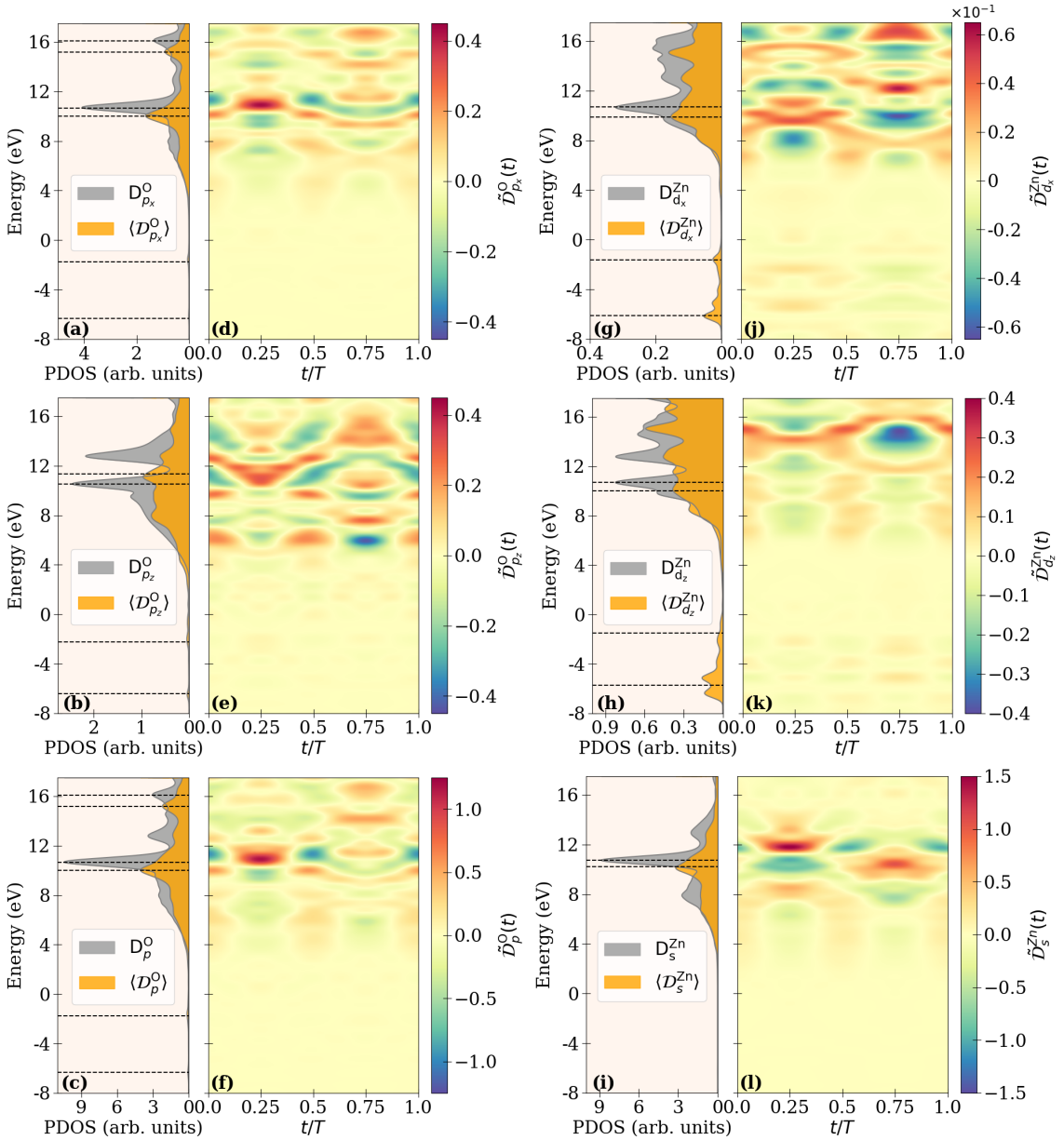

Figure 5.5.: Laser-dressed unoccupied partial density of states (PDOS) of a wurtzite ZnO crystal: The field-free PDOS is shown in gray, and the time-averaged laser-dressed PDOS is shown in orange for the (a) O p_x-projected, (b) O p_z-projected, and (c) O p-projected PDOS. The time-dependent part of the laser-dressed PDOS for the (d) O p_x-projected, (e) O p_z-projected, and (f) O p-projected PDOS. (g)-(i) The same as (a)-(c), but for the (g) Zn d_x-projected PDOS, which is the PDOS projected on the Zn d_{xy} and $d_{x^2-y^2}$ orbitals; (h) Zn d_z-projected PDOS, which is the PDOS projected on the Zn d_{xz}, d_{yz}, and d_{z^2} orbitals; and (i) Zn s-projected PDOS. (j)-(l) The same as (d)-(f), but for the (j) Zn d_x-projected PDOS; (k) Zn d_z-projected PDOS; (l) Zn s-projected PDOS.

components along the z direction includes the $\mathcal{D}^{\mathrm{O}}_{p_z}$ component and the $\mathcal{D}^{\mathrm{Zn}}_{d_{xz}}$, $\mathcal{D}^{\mathrm{Zn}}_{d_{yz}}$, and $\mathcal{D}^{\mathrm{Zn}}_{d_{z^2}}$ components, which are denoted together as $\mathcal{D}^{\mathrm{Zn}}_{d_z}$.

We use the calculated laser-dressed unoccupied PDOS to draw connection between the

XAS signal and underlying laser-dressed electron dynamics. We study the dynamics of electrons excited from the valence to the conduction band, as well as the evolution of valence-band vacancies that form unoccupied states accessible as final states in the x-ray–induced transitions. The full x-ray absorption signal is time-dependent, we analyze separately its time-averaged and time-dependent parts. The sum of both is positive for any given energy.

In the energy domain, the x-ray absorption spectrum can be divided into two parts: the near-edge structure, which overlaps with the field-free absorption spectrum, and the pre-edge structure, which emerges due to laser dressing. Near-edge structure corresponds to the transition to the laser-dressed unoccupied state within the conduction band. Pre-edge structure corresponds to the transition in the new available state formed by vacancies left behind after electron transfer to the conduction band.

5.6.1. Time-averaged signal

Near-edge structure

Under a driving field, the electronic states become dressed, as the field transiently mixes the valence and conduction band states of the ground-state electronic structure. In this section, we analyze the part of the laser-dressed x-ray absorption spectrum that overlaps with the ground-state spectrum. This region of the spectrum reflects changes in electronic populations within the conduction band following carrier excitation. Figure 5.6 shows the corresponding parts of the x-ray absorption spectra at the O K-edge and Zn L_3-edge. Each pair of plots in Fig. 5.6 shows the time-averaged signal together with the corresponding field-free signal in the left panels and the time-dependent part of the signal in the right panels. The total laser-dressed signal, obtained as the sum of the time-averaged and time-dependent parts, is positive for all energies. In the time-dependent data shown in Fig. 5.6, a characteristic "fishbone" resonance structure can be observed, which has been explained theoretically [198] and confirmed experimentally [8, 86, 87]. This structure arises from the interplay between the symmetric Lorentzian and asymmetric Fano contributions to the absorption cross section in Eq. (5.88).

The absorption edges are separated in energy due to the different binding energies of the O $1s$ and Zn $2p_{3/2}$ core levels, which are around 502 eV and 986 eV, respectively, in ground state calculations. The O K-edge corresponds predominantly to the $1s \rightarrow np$ x-ray-induced transitions and, therefore, the associated spectrum reflects the O p-projected unoccupied PDOS. Similarly, the Zn L_3-edge corresponds to the $2p_{3/2} \rightarrow ns, nd$ transitions and reflects the Zn s- and d-projected unoccupied PDOS. Taken together, they provide a complementary, site- and orbital-resolved view of the laser-driven electron dynamics. The spectra were calculated for two distinct polarizations of the probe x-ray pulse: one aligned along the x-axis and the other along the z-axis. In our coordinate system, the hexagonal

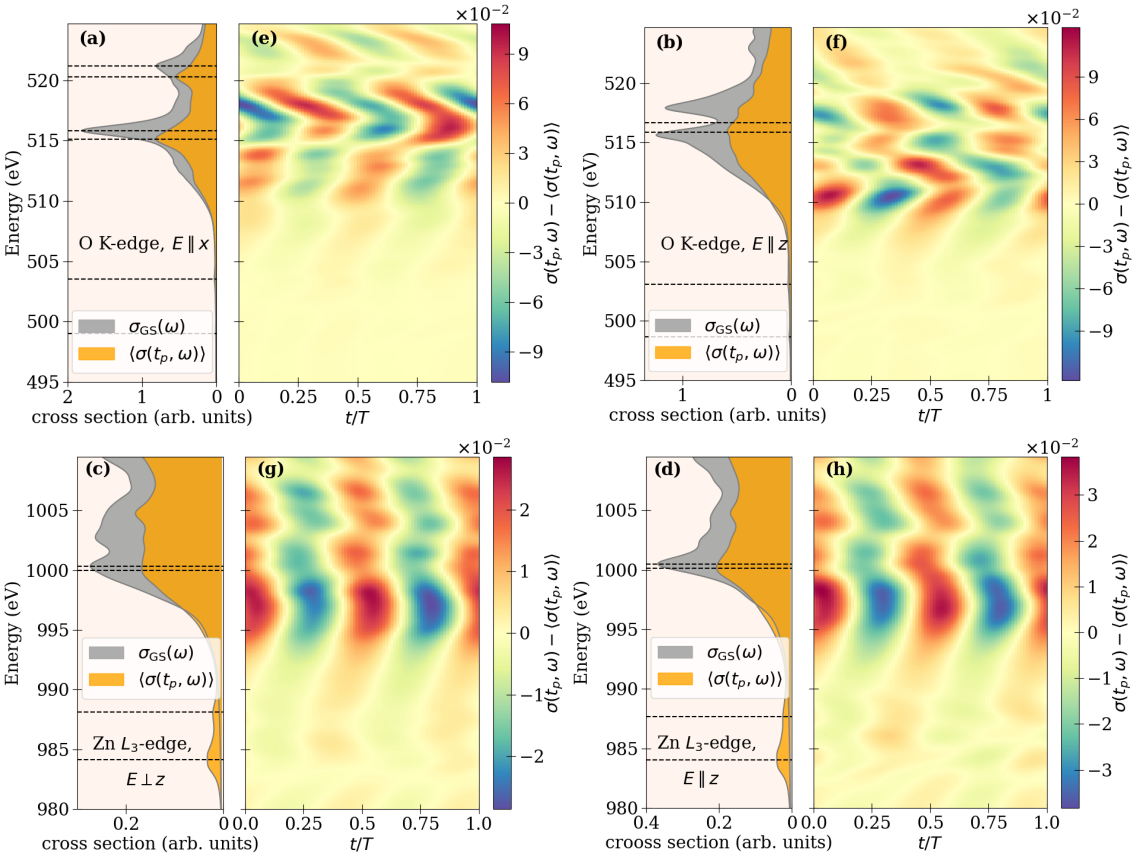

Figure 5.6.: Polarization-dependent x-ray absorption spectra at the O K-edge and Zn L_3-edge. The field-free spectra are shown in gray, and the time-averaged laser-dressed spectra are shown in orange. Panels (a) and (b) show the O K-edge XAS for $\boldsymbol{\epsilon}_x = (100)$ and $\boldsymbol{\epsilon}_x = (001)$, respectively. Panels (c) and (d) display the Zn L_3-edge XAS, with (c) showing the averaged data for $\boldsymbol{\epsilon}_x = (100)$ and (010), and (d) for $\boldsymbol{\epsilon}_x = (001)$. Panels (e)–(h) present the time-dependent component of the laser-dressed spectra: (e) and (f) for the O K-edge with $\boldsymbol{\epsilon}_x = (100)$ and (001), respectively; (g) and (h) for the Zn L_3-edge with averaged data for $\boldsymbol{\epsilon}_x = (100)$ and (010), and for (001), respectively.

c-axis is oriented along z, as shown in Fig. 4.1(a). This configuration enables the study of the crystal's anisotropy.

The O p-projected unoccupied PDOS exhibits pronounced anisotropy due to the wurtzite crystal structure, as seen from the ground-state distributions, as well as from the laser-dressed distributions in Figs. 5.5(a) and (b). The obtained polarization-dependent spectra at the O K-edge for the ground state are in good agreement with existing experimental data [200, 201]. Within the first 20 eV of the conduction band, the p_x contribution dominates over the p_z contribution, leading to a higher absorption intensity for $E \perp c$ in Fig. 5.6(a) compared to $E \parallel c$ in Fig. 5.6(b). This polarization dependence of the absorption spectrum reflects the angular character of the O p orbitals that contribute to the formation of the conduction-band states.

At the Zn L_3-edge, the x-ray absorption spectrum reflects the Zn s- and d-projected

unoccupied PDOS. Due to dipole selection rules, the low-energy region of the spectrum is primarily dominated by the $2p \rightarrow 5s$ transition when the x-ray pulse is polarized along the z-axis. The $2p \rightarrow 5s$ transition is favored over the $2p \rightarrow 4d$ transition, despite both being dipole-allowed. As a result, the x-ray absorption spectrum at the Zn L_3-edge shows anisotropy depending on the probe polarization, as illustrated by the larger time-averaged signal for $E \parallel c$ in Fig. 5.6 (d) compared to $E \perp c$ in Fig. 5.6 (c). The obtained polarization-dependent spectra at the Zn L_3-edge for the ground state are in good agreement with existing experimental data [202] and theoretical works [203, 204].

The application of the driving field leads to a reduction in the net x-ray absorption signal due to the filling of previously unoccupied states following electron transfer from valence- to conduction-band states. This effect is due to Pauli blocking and evident from the time-averaged data in Fig. 5.6 and from the laser-dressed unoccupied PDOS distributions in Fig. 5.5. The suppression of x-ray absorption, or equivalently the increase in transmission, in the presence of a strong driving field is often referred to as electromagnetically induced transparency for x-rays. The electromagnetically induced transparency has been demonstrated experimentally in both atomic gases [205] and solids [206, 207]. In particular, the authors of Ref. [206] experimentally observed a $\sim$40% increase in above-bandgap transmission in GaAs driven by mid-infrared pulses with intensities of $\sim$1 GW/cm^2, attributed to the dynamic Franz–Keldysh effect and ponderomotive band renormalization.

By comparing the laser-dressed spectra with the ground-state data at the O K-edge for $E \parallel c$ in Fig. 5.6(b), we observe that the driving field introduces additional broadening due to the appearance of side peaks. This results in the smearing of the main two-peak structure around 517 eV in the x-ray absorption spectrum [Fig. 5.6(b)] and around 12 eV in the O p_z-projected unoccupied PDOS [Fig. 5.5(b)].

We also observe that the main peaks in the laser-dressed PDOS distributions in Fig. 5.5 and in the x-ray absorption spectra in Fig. 5.6 are shifted toward lower excitation energies relative to the corresponding ground-state distributions. The dashed lines in Fig. 5.5 and Fig. 5.6 go through the maxima of the laser-dressed and ground-state distributions. This shows that the values of the energy shifts vary depending on the energy position and projection. According to the two-level model discussed in Chapter 4, the position of the DOS peak corresponding to the excited state shifts approximately as $\overline{\omega}_2 = \omega_2 + \frac{\Omega_R^2}{4\Delta}$, resulting in an effective level repulsion. Thus, the observed redshifts of the main peaks in the laser-dressed PDOS distributions and in the x-ray absorption spectra cannot be explained by the simplified two-level model. Under a strong driving field, electronic states within the conduction band can couple to states with both lower and higher energies. We can assume that coupling to higher-lying states within the conduction band results in a redshift of the main peaks in the laser-dressed distributions in Fig. 5.5 and Fig. 5.6. A detailed analysis requires a three-level model to be considered.

The consistent redshifts observed across all XAS features and laser-dressed PDOS distri-

butions indicate that the energy shift scales inversely with the detuning. The redshift is larger for higher-energy conduction states than for those closer to the conduction band minimum. The described trend in energy shifts can be followed in the laser-dressed PDOS distributions and in the polarization-dependent x-ray absorption spectra at the oxygen *K*-edge shown in Figs. 5.6(a) and (b). The redshift increases from approximately 0.65 eV for the low-energy peak in Fig. 5.6(a) to about 0.8 eV for the main peak in Fig. 5.6(b) and to 0.9 eV for the high-energy peak in Fig. 5.6(a).

Pre-edge structure

In the presence of the driving field, new features emerge in the pre-edge energy range of the x-ray absorption spectrum. In this section, we analyze this part of the laser-dressed x-ray absorption spectra. This region of the spectra reflects changes in electronic populations within the valence band following carrier excitation. Under a strong driving field, electron transfer from valence- to conduction-band states results in vacancies below the Fermi level. This leads to increased absorption in the pre-edge region and gives rise to a pre-edge feature in the x-ray absorption spectrum, as it opens new final states available for the core electron.

Figure 5.7 shows a zoom-in of the pre-edge region from the corresponding spectra in Fig. 5.6. The spectra shown in Figs. 5.6 and 5.7 indicate that, as electrons are promoted into the conduction band, the corresponding holes enable a new low-energy x-ray-induced transition. In addition to carrier excitation, the driving field can induce coherent superpositions of valence-band states with overlapping spatial wavefunctions. This coherence leads to a net displacement of charge density, giving rise to quantum beats in the transient absorption signal.

The electronic states within the valence band of a wurtzite ZnO crystal have strong O 2p and Zn 3d character. The main valence-band PDOS peaks are formed by bonding and antibonding combinations of these orbitals, as shown in Fig. 4.1(b). Hole dynamics within the valence band arise from carrier excitation involving these hybridized states. As a result, the bonding–antibonding energy splitting can be clearly seen in the pre-edge x-ray absorption spectra shown in Fig. 5.7.

The dotted lines in Fig. 5.7 indicate the energies of the peaks associated with x-ray-induced transitions of core electrons into the bonding and antibonding states of the laser-dressed electronic structure. The XAS signal intensity across the bonding and antibonding energy ranges qualitatively follows the laser-dressed PDOS in the Figs. 4.2 and 5.5. The x-ray-induced transitions into deep-lying Zn 3d states produce intense peaks at lower x-ray photon energies, seen clearly in Figs. 5.7(c) and (d). In contrast, transitions into states with predominantly O 2p character produce intense peaks at higher x-ray photon energies in Figs. 5.7(a) and (b). This suggests that O 2p-projected states near the Fermi level dominate

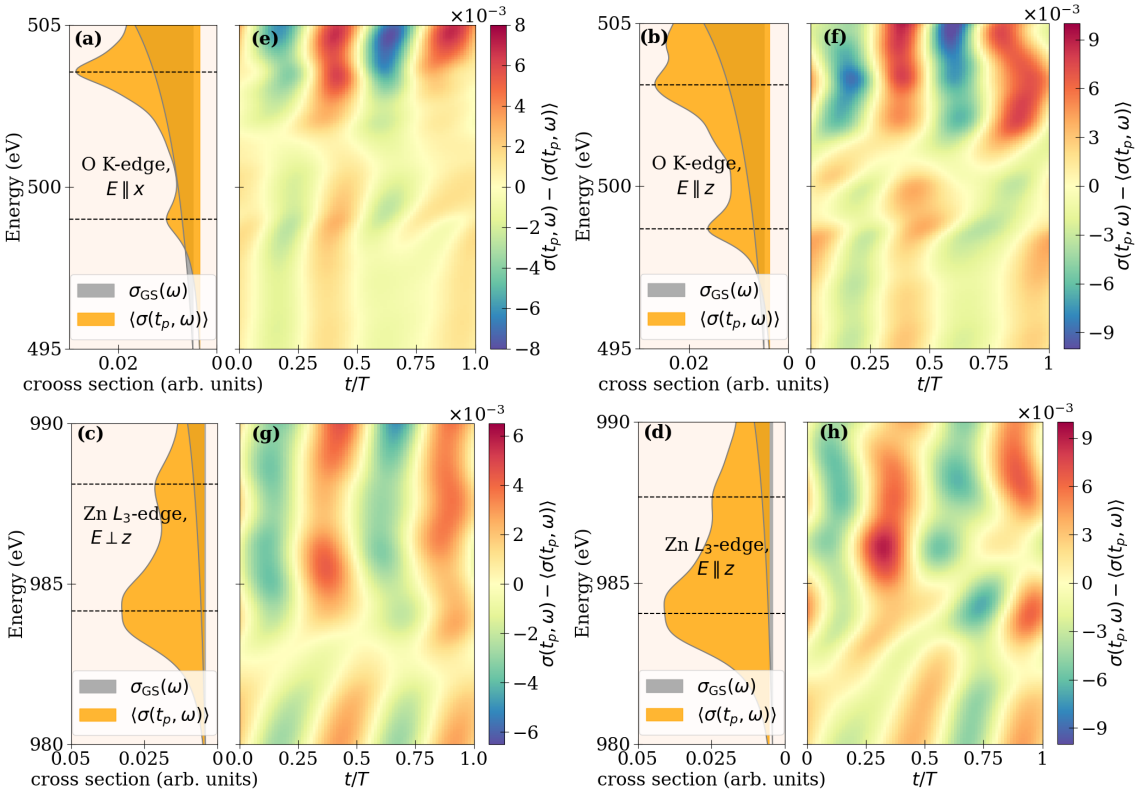

Figure 5.7.: Polarization-dependent pre-edge x-ray absorption spectra at the O K- and Zn L_3-edges. The field-free spectra are shown in gray, and the time-averaged laser-dressed spectra are shown in orange. Panels (a) and (b) show the pre-edge spectra at the O K-edge for $\boldsymbol{\epsilon}_x = (100)$ and $\boldsymbol{\epsilon}_x = (001)$, respectively. Panels (c) and (d) display the pre-edge spectra at the Zn L_3-edge, with (c) showing the averaged data for $\boldsymbol{\epsilon}_x = (100)$ and (010), and (d) for $\boldsymbol{\epsilon}_x = (001)$. Panels (e)–(h) show the time-dependent part of the laser-dressed spectra: (e) and (f) correspond to the O K-edge with $\boldsymbol{\epsilon}_x = (100)$ and (001), respectively, while (g) and (h) correspond to the Zn L_3-edge with averaged data for $\boldsymbol{\epsilon}_x = (100)$ and (010), and for (001), respectively.

the laser-dressed electron dynamics within the valence band. The corresponding energy window also shows the most pronounced time-dependent changes in the pre-edge XAS signal, as seen in Figs. 5.7(e) and (f).

The XAS signal exhibits pronounced anisotropy with respect to the polarization of the probe x-ray pulse. This is due to the intrinsic anisotropy of the wurtzite ZnO crystal structure and the presence of the driving optical field. Aligning the driving field with the z-axis leads to stronger coupling with electronic states that have the same angular orbital character. When the probe pulse is also polarized along the z-axis with $E \parallel c$, it couples more strongly to these field-driven states. This results in a stronger absorption signal at the energy corresponding to the main peak positions in Figs. 5.7(b) and (d), compared to the x-ray absorption spectra for $E \perp c$ shown in Figs. 5.7(a) and (c).

5.6.2. Time-dependent part of a signal

As mentioned, the unoccupied PDOS is the main tool for interpreting XAS data, as the unique correspondence between the absorption profile and the unoccupied PDOS helps to extract information about a system's electronic structure from its x-ray absorption spectrum. We analyze the oscillations of the x-ray absorption spectra by comparing them to the laser-dressed PDOS oscillations. Previously, we demonstrated that the time-dependent PDOS of a crystal evolves over time according to Eq. (4.12). We assume that the PDOS corresponding to the (ℓm) component on site α is taken and rewrite Eq. (4.12) in a simplified form as follows:

$$\mathcal{D}(\omega,t) = \langle \mathcal{D}(\omega,t) \rangle - \mathcal{D}_1(\omega)\sin(\Omega t) + \mathcal{D}_2(\omega)\cos(2\Omega t) + ... \tag{5.92}$$

Here, the first-order amplitudes are defined via the imaginary part of the complex-valued amplitudes as $\mathcal{D}_1(\omega) = 2\,\mathrm{Im}\left(\tilde{D}_1(\omega)\right)$ and the second-order amplitudes are defined via the real part of the complex-valued amplitudes as $\mathcal{D}_2(\omega) = 2\,\mathrm{Re}\left(\tilde{D}_2(\omega)\right)$. The complex-valued amplitudes $\tilde{D}_\mu(\omega)$ are defined as follows:

$$\tilde{D}_\mu(\omega) = \sum_{i,\mathbf{k},\nu} d^{\mu}_{i\mathbf{k}\nu}\,\delta\left(\omega - [\mathcal{E}_{i\mathbf{k}} + (\nu + \mu/2)\Omega]\right), \tag{5.93}$$

with the coefficients $d^{\mu}_{i\mathbf{k}\nu}$ given by Eq. (4.11).

The time-dependent absorption cross section, given by Eq. (5.88), is used here in a simplified form expanded up to second order, as follows:

$$\begin{aligned}\sigma(\omega,t) = \langle \sigma(\omega,t) \rangle + \overline{\sigma}_1^{\sin}(\omega)\sin(\Omega t) - \overline{\sigma}_1^{\cos}(\omega)\cos(\Omega t) \\ + \overline{\sigma}_2^{\sin}(\omega)\sin(\Omega t) + \overline{\sigma}_2^{\cos}(\omega)\cos(\Omega t) + ...\end{aligned} \tag{5.94}$$

Here, the first-order amplitude $\overline{\sigma}_1^{\sin}(\omega)$ is defined via the imaginary part of the complex-valued amplitudes as $\overline{\sigma}_1^{\sin}(\omega) = \mathrm{Im}\left(\tilde{\sigma}_1(\omega) - \tilde{\sigma}_{-1}(\omega)\right)$ and the second-order amplitude $\overline{\sigma}_2^{\cos}(\omega)$ is defined via the real part of the complex-valued amplitudes as $\overline{\sigma}_2^{\cos}(\omega) = \mathrm{Re}\left(\tilde{\sigma}_2(\omega) + \tilde{\sigma}_{-2}(\omega)\right)$. The complex-valued amplitudes $\tilde{\sigma}_\mu(\omega)$ have the form

$$\tilde{\sigma}_\mu(\omega) = \frac{8\pi}{\omega} e^{-\frac{\mu\Omega}{2a}(\omega-\omega_0+\mu\Omega/2)} \sum_{i,\mathbf{k},\nu} \left[\frac{\eta D^{i\mathbf{k}}_{\nu,\mu}}{(\omega - \overline{\omega}_{i\mathbf{k}\nu})^2 + \eta^2} \right], \tag{5.95}$$

where the coefficients $D^{f\mathbf{k}}_{\nu,\mu}$ given by Eq. (5.79).

In comparison to the PDOS defined in Eq. (5.92), the absorption cross section in Eq. (5.94) contains both sine and cosine terms for each frequency component. This is because the absorption cross section includes dispersive effects. In the following, we compare the amplitudes of the sine component for the first order, $\mathcal{D}_1(\omega)$ and $\overline{\sigma}_1^{\sin}(\omega)$, and the amplitudes of the cosine component for the second order, $\mathcal{D}_2(\omega)$ and $\overline{\sigma}_2^{\cos}(\omega)$. The amplitudes

$\overline{\sigma}_1^{\cos}(\omega)$ and $\overline{\sigma}_2^{\sin}(\omega)$ contain a different spectral line shape, namely a Fano profile, as given by Eqs. (5.88)–(5.91).

In order to qualitatively compare the form of the energy dependence, we introduce Gaussian broadening to the PDOS amplitudes. The introduced broadening is defined by the linewidth η of the chosen atomic level. At the same time, we replace the Lorentzian profile in the absorption cross section amplitudes with a Gaussian function having the same FWHM

$$\begin{aligned}\tilde{D}_\mu(\omega) &\approx \sum_{i,\mathbf{k},\nu} d^\mu_{i\mathbf{k}\nu} e^{-\frac{\ln 2}{\eta^2}(\omega-[\mathcal{E}_{i\mathbf{k}}+(\nu+\mu/2)\Omega])^2}, \\ \tilde{\sigma}_\mu(\omega) &\approx \frac{4\pi}{\omega} e^{-\frac{\mu\Omega}{2a}(\omega-\omega_0+\mu\Omega/2)} \sum_{i,\mathbf{k},\nu} D^{i\mathbf{k}}_{\nu,\mu} e^{-\frac{\ln 2}{\eta^2}(\omega-\overline{\omega}_{i\mathbf{k}\nu})^2}.\end{aligned} \tag{5.96}$$

In the case of the PDOS, only a single parameter defines the energy dependence—the linewidth η. In contrast, the absorption cross section depends on two parameters: the linewidth η and the duration of the probe x-ray pulse τ_p through the parameter $a = 2\ln 2/\tau_\mathrm{p}^2$. To proceed, we now expand the square of the sum in the PDOS amplitudes

$$e^{-\frac{\ln 2}{\eta^2}(\omega-[\mathcal{E}_{i\mathbf{k}}+(\nu+\mu/2)\Omega])^2} = e^{-\frac{\ln 2}{\eta^2}(\omega-\mathcal{E}_{i\mathbf{k}}-\nu\Omega)^2} e^{\frac{\mu\Omega\ln 2}{\eta^2}(\omega-\mathcal{E}_{i\mathbf{k}}-\nu\Omega)} e^{-\frac{\ln 2(\mu\Omega)^2}{4\eta^2}}. \tag{5.97}$$

For the amplitudes of the absorption cross section, we take into account that $\overline{\omega}_{i\mathbf{k}\nu} = \mathcal{E}_{i\mathbf{k}} - E_\mathrm{c} + \nu\Omega$, then

$$e^{-\frac{\mu\Omega}{2a}(\omega-\omega_0+\mu\Omega/2)} e^{-\frac{\ln 2}{\eta^2}(\omega-\mathcal{E}_{i\mathbf{k}}+E_\mathrm{c}-\nu\Omega)^2} = e^{-\frac{\ln 2}{\eta^2}((\omega+E_\mathrm{c})-\mathcal{E}_{i\mathbf{k}}-\nu\Omega)^2} e^{-\frac{\mu\Omega}{2a}(\omega-\omega_0)} e^{-\frac{(\mu\Omega)^2}{4a}}. \tag{5.98}$$

The main difference between Eq. (5.97) and Eq. (5.98) lies in the term associated with the exponential decay as the μth order increases, namely: $e^{\frac{\mu\Omega\ln 2}{\eta^2}(\omega-\mathcal{E}_{i\mathbf{k}}-\nu\Omega)}$ and $e^{-\frac{\mu\Omega}{2a}(\omega-\omega_0)}$. Let's substitute the frequency value, ω, in the second term for the resonance condition for the x-ray absorption, in this case $e^{-\frac{\mu\Omega}{2a}(\omega-\omega_0)} = e^{\frac{\mu\Omega}{2a}((E_\mathrm{c}+\omega_0)-\mathcal{E}_{i\mathbf{k}}-\nu\Omega)}$.

We can now rewrite the PDOS and absorption cross section amplitudes in a form that makes their differences immediately apparent

$$\begin{aligned}\tilde{D}_\mu(\omega) &\propto e^{-\frac{\ln 2(\mu\Omega)^2}{4\eta^2}} \sum_{i,\mathbf{k}} e^{\frac{\mu\Omega\ln 2}{\eta^2}(\omega-\mathcal{E}_{i\mathbf{k}})} \sum_\nu d^\mu_{i\mathbf{k}\nu} e^{-\frac{\ln 2}{\eta^2}(\omega-\mathcal{E}_{i\mathbf{k}}-\nu\Omega)^2} e^{-\frac{\mu\nu\Omega^2\ln 2}{\eta^2}}, \\ \tilde{\sigma}_\mu(\omega) &\propto e^{-\frac{(\mu\Omega)^2}{4a}} \sum_{i,\mathbf{k}} e^{\frac{\mu\Omega}{2a}((E_\mathrm{c}+\omega_0)-\mathcal{E}_{i\mathbf{k}})} \sum_\nu D^{i\mathbf{k}}_{\nu,\mu} e^{-\frac{\ln 2}{\eta^2}((\omega+E_\mathrm{c})-\mathcal{E}_{i\mathbf{k}}-\nu\Omega)^2} e^{-\frac{\mu\nu\Omega^2}{2a}}.\end{aligned} \tag{5.99}$$

The PDOS and x-ray absorption cross-section amplitudes are defined in different energy ranges due to the binding energy of the core electron. To compare them, the absorption cross-section amplitudes must be shifted by the core-electron binding energy E_c. Because of the exponential terms $e^{\frac{\mu\Omega\ln 2}{\eta^2}(\omega-\mathcal{E}_{i\mathbf{k}})}$ and $e^{\frac{\mu\Omega}{2a}((E_\mathrm{c}+\omega_0)-\mathcal{E}_{i\mathbf{k}})}$ in the expression for the amplitudes, some differences remain after this shift. These differences are related to the deviation of the

incoming photon frequency ω from the central frequency ω_0. As a result, the absorption cross-section amplitudes, shifted by the core-electron binding energy, agree well with the PDOS amplitudes around the central frequency ω_0 or the shifted central frequency $\omega_0 + E_c$. The largest discrepancies are expected for ω values near the edges of the x-ray pulse bandwidth.

The conclusion that the discrepancies between the amplitudes $\tilde{D}_\mu(\omega)$ and $\tilde{\sigma}_\mu(\omega)$ increase as the x-ray photon energy deviates from the central frequency ω_0 also holds for the linear combinations $\tilde{D}_\mu(\omega) \pm \tilde{D}_{-\mu}(\omega)$ and $\tilde{\sigma}_\mu(\omega) \pm \tilde{\sigma}_{-\mu}(\omega)$. These combinations must be compared because, in the calculations, the PDOS is defined in terms of real-valued amplitudes. The PDOS amplitudes of the μth and $-\mu$th orders are related to each other by complex conjugation. In contrast, the corresponding absorption cross-section amplitudes are related by complex conjugation and an additional energy shift of $\mu\Omega$. This means that if the μth PDOS amplitude has a peak at energy ω_p, the corresponding combination of the μth- and $-\mu$th-order amplitudes in the absorption cross section will have a peak at $\omega_p + \mu\Omega/2$. Thus, the μth-order absorption cross-section amplitudes $\tilde{\sigma}_\mu(\omega)$ must be additionally shifted by $\mu\Omega/2$.

Figures 5.8 and 5.9 show the first- and second-order amplitudes of the absorption cross section, alongside the corresponding unoccupied PDOS broadened and normalized arbitrary for better comparison. The second-order amplitudes shown in Fig. 5.9 are generally larger than the corresponding first-order amplitudes in Fig. 5.8. Thus, the time-dependent PDOS and XAS signals predominantly oscillate at the frequency 2Ω in Figs. 5.5, 5.6, and 5.7. This effect can be explained by the spatial symmetry of the first-order laser-dressed electron density distribution in Fig. 4.6. Upon integration over the unit cell, the first-order response is largely averaged out in a symmetric crystal. In contrast, the nonlinear response in Fig. 4.8 involves charge distributions that are not symmetric with respect to an atomic site position. In such a distribution, positive and negative charge displacements do not cancel each other out when averaged, so the overall contribution remains significant. A similar effect was previously observed experimentally in centrosymmetric crystals, where the x-ray absorption [5, 7, 8, 86] or reflection signal [208, 209] was found to oscillate at twice the frequency of the driving field during the temporal overlap of the pump and probe pulses.

At the O K-edge, the absorption cross section amplitudes follow the unoccupied O $2p$-projected PDOS in their spectral shape. In Figs. 5.8(a) and (c), the first-order PDOS amplitudes, which correspond to the O p_x projection for the probe x-ray pulse polarization $\boldsymbol{\epsilon}_x \parallel x$ and to the O p_z projection for $\boldsymbol{\epsilon}_x \parallel z$, show good agreement with the corresponding absorption cross section amplitudes. The largest discrepancies occur at higher energies and arise from the difference in the energy dependence of the amplitudes described by Eq. (5.99). The second-order absorption cross section amplitudes in Figs. 5.9(a) and (c) also follow the corresponding PDOS amplitudes in their spectral shape.

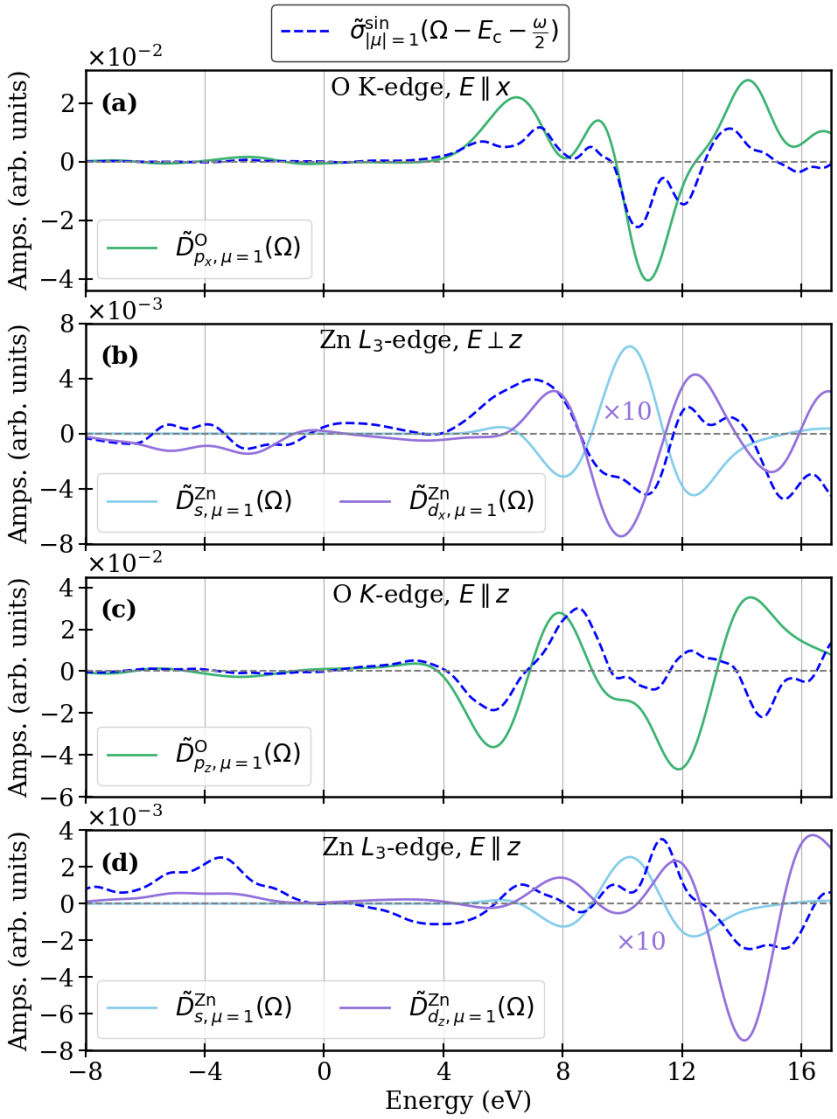

Figure 5.8.: First-order amplitudes of the absorption cross section (dashed blue lines), compared with the corresponding PDOS amplitudes. The green, blue, and purple solid lines correspond to the O p-, Zn s and Zn d-projected PDOS, respectively. Panels (a) and (b) display first-order amplitudes of the x-ray absorption spectra at the O K-edge and Zn L_3-edge, respectively, for polarization $\boldsymbol{\epsilon}_{\mathrm{x}} = (100)$ and the averaged data for $\boldsymbol{\epsilon}_{\mathrm{x}} = (100)$ and (010); panels (c) and (d) show the same for $\boldsymbol{\epsilon}_{\mathrm{x}} = (001)$.

At the Zn L_3-edge, we analyze the averaged data for the polarizations $\boldsymbol{\epsilon}_{\mathrm{x}} = (100)$ and $\boldsymbol{\epsilon}_{\mathrm{x}} = (010)$, as well as the data for the polarization $\boldsymbol{\epsilon}_{\mathrm{x}} = (001)$. In the following, these cases are referred to as $\boldsymbol{\epsilon}_{\mathrm{x}} \perp z$ and $\boldsymbol{\epsilon}_{\mathrm{x}} \parallel z$, respectively. For $\boldsymbol{\epsilon}_{\mathrm{x}} \perp z$, the main contribution to the signal is expected to come from core electron transitions into Zn s states and into Zn d_{xy} and $d_{x^2-y^2}$ states. The sum of the PDOS amplitudes projected onto these d orbitals is denoted as $\mathcal{D}^{\mathrm{Zn}}_{d_x}$ in Fig. 5.8 and Fig. 5.9. For $\boldsymbol{\epsilon}_{\mathrm{x}} \parallel z$, the dominant contribution is expected to come from transitions into Zn s states and into Zn d_{xz}, d_{yz}, and d_{z^2} states. The sum of the PDOS amplitudes projected onto these three d orbitals is denoted as $\mathcal{D}^{\mathrm{Zn}}_{d_z}$ in Figs. 5.8

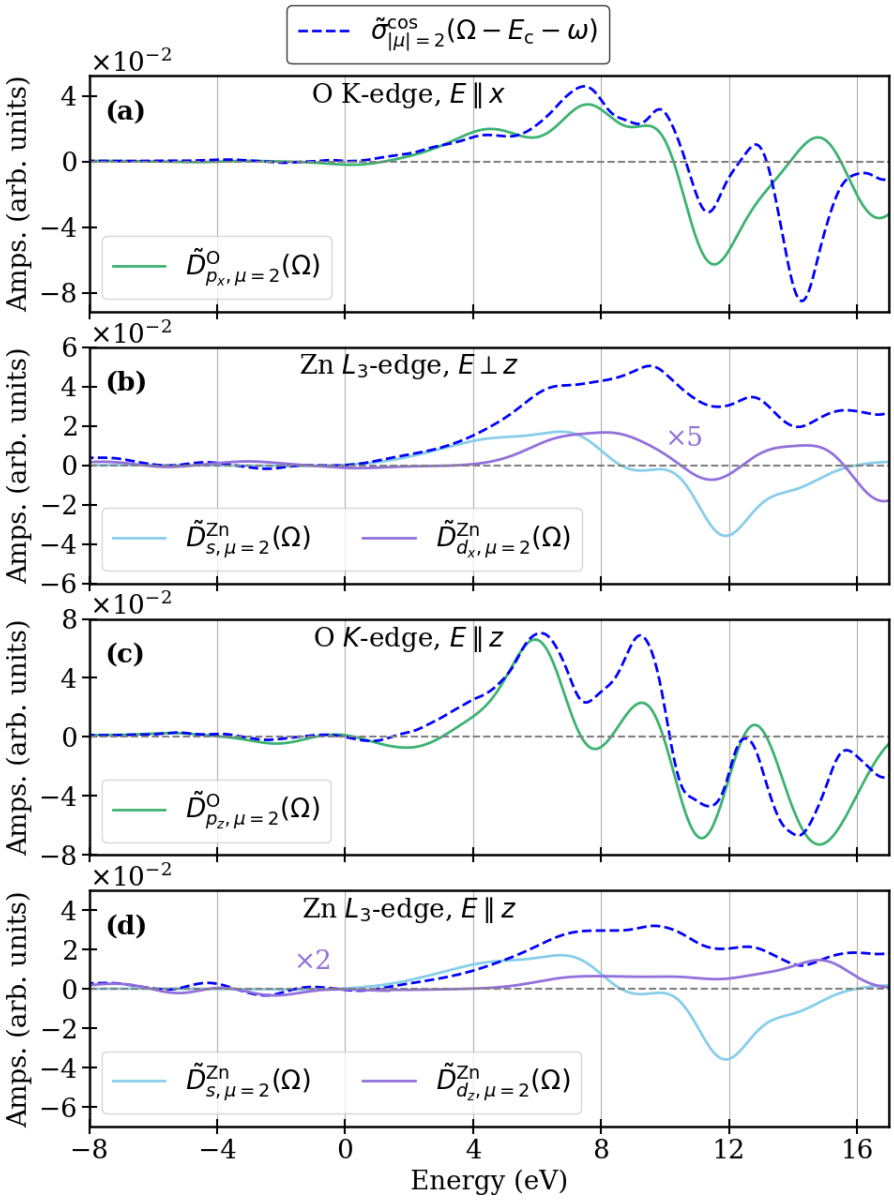

Figure 5.9.: Second-order amplitudes of the absorption cross section (dashed blue lines), compared with the corresponding PDOS amplitudes. The green, blue, and purple solid lines correspond to the O p-, Zn s and Zn d-projected PDOS, respectively. Panels (a) and (b) display second-order components at the O K-edge and Zn L_3-edge respectively for polarization $\boldsymbol{\epsilon}_x = (100)$ and the averaged data for $\boldsymbol{\epsilon}_x = (100)$ and (010); panels (c) and (d) show the same for $\boldsymbol{\epsilon}_x = (001)$.

and 5.9.

For the first-order response at the Zn L_3-edge in the case of $\boldsymbol{\epsilon}_x \perp z$ shown in Fig. 5.8(b), the amplitudes of the absorption cross section follow the Zn d_x-projected PDOS amplitude, whereas the corresponding Zn s-projected PDOS amplitude has the opposite sign. For $\boldsymbol{\epsilon}_x \parallel z$, shown in Fig. 5.8(d), the spectral shape of the absorption cross section amplitude aligns with the Zn s-projected PDOS amplitude. In the energy region below the Fermi

level, however, the absorption cross section amplitude instead follows the Zn d_z-projected PDOS. Notably, the amplitudes corresponding to the Zn s- and d_z-projected PDOS have opposite signs. This inversion likely indicates state hybridization, where the Zn s and d states represent two complementary transition channels for the Zn $2p$ core electron.

For the second-order response at the Zn L_3-edge shown in Figs. 5.9(b) and (d), the absorption cross section amplitudes follow the Zn s-projected PDOS amplitudes in the low-energy region of the conduction band, while at higher energies they align with the Zn d-projected PDOS amplitudes. This observation is consistent with the energy positions of states with strong Zn s- and d-character in the laser-dressed PDOS, as shown in Fig. 5.5.

5.7. Summary

In this chapter, we developed a theoretical framework and an *ab initio* computational scheme for modeling trXAS measurement of the materials in the presence of a strong driving field. In Section 5.3, we developed an approach for calculating an ultrafast x-ray absorption cross section based on the projection treatment of x-ray absorption. This method can be considered a generalization of the stationary absorption cross section to the time-dependent case involving quasi-monochromatic pulses. In the following Section 5.4, we developed an approach based on time-frequency treatment of x-ray absorption, applicable to ultrashort probe pulses. We analyzed a general expression for the time-dependent absorption cross section, which is valid for both time-resolved and time-unresolved measurements. This expression accounts for arbitrary pulse durations and coherence properties.

We found that, in the case of a quasi-monochromatic probe pulse, there is a direct correspondence between the amplitudes of the unoccupied laser-dressed PDOS and the amplitudes of the time-dependent absorption cross section. However, for ultrashort pulses with an inherently large bandwidth, the absorption of a certain spectral component additionally depends on its initial intensity. This effect, which we refer to as dispersion, introduces an asymmetric Fano profile and leads to the "fishbone" resonance structures observed experimentally and predicted theoretically.

As a case study, we used the developed framework to calculate the ultrafast x-ray absorption spectra of a wurtzite ZnO crystal under a non-resonant driving field. We calculated the spectra at the O K- and Zn L_3-edges over an energy range covering both valence and conduction bands. In the conduction-band region, we observed a reduction in signal intensity due to carrier excitation. Around the valence band, a pre-edge feature emerges due to the vacancy left behind after carrier excitation in the conduction band. We compared the results with the corresponding laser-dressed PDOS to illustrate how the signal is connected to the laser-dressed electron dynamics. This information could be particularly useful for developing strategies to manipulate the optical properties of materials for

application in future optoelectronic devices, such as ultrafast switches and modulators.

6. Conclusion

In this thesis, we developed the theoretical framework and *ab initio* computational scheme to describe a process in which trXAS is applied to study laser-dressed electron dynamics in materials. Our computational scheme is based on Floquet–Bloch formalism combined with DFT using the LAPW+lo method. The Floquet–Bloch formalism enables the study of non-perturbative electron dynamics in laser-dressed solids and makes the scheme computationally feasible. The LAPW+lo method provides a full-potential treatment of the crystal electronic structure, accurately capturing the effects of both valence and core electrons. The developed framework represents an analytical tool for the interpretation of experiments involving ultrafast x-ray probe techniques and for the development of strategies for optical manipulation of material properties.

In Chapter 3, we described the x-ray diffraction measurement of a laser-dressed material with the focus on the angular dependence of the side peaks to the elastic Bragg peak. We perform the simulation of x-ray diffraction from a laser-dressed silicon crystal using a previously developed *ab initio* computational scheme. The results show excellent agreement with recent experimental measurement. In particular, the angular dependence of the first-order side peak is consistent with the driven current following the field direction. The second-order side peak exhibits a distinctly different angular dependence. We have found that the second-order microscopic optical response originates from charge displacements at specific sites that locally break inversion symmetry. This leads to non-zero second-order response in centrosymmetric crystals, such as silicon. The results show that measuring higher-order diffraction side peaks provides atomic-scale information on the local symmetry of the laser-dressed electron density.

This led us to look into another technique for probing laser-dressed electron dynamics, namely ultrafast XAS. To interpret the results of our ultrafast XAS modeling we developed a framework for calculating the PDOS of laser-dressed materials in Chapter 4. We also showed that laser-dressed PDOS provides a valuable computational tool on its own as it captures laser-driven changes in the electronic population in a site- and orbital-resolved way. The developed computational framework combines Floquet–Bloch formalism with DFT using the LAPW+lo method. The approach, illustrated using wurtzite zinc oxide, reveals how the driving field dynamically alters the electronic structure and chemical bonding. We connected the evolution of the laser-dressed PDOS with the corresponding laser-dressed electron density. We showed that the laser-dressed PDOS provides information about the structure of the bonds that form the laser-dressed electron density, analogous to the field-free case. By analyzing the laser-driven energy shifts, we found that under excitation the Zn d and O p states shift non-uniformly. This non-uniform shift

reduces orbital overlap and weakens the bond. We further confirmed laser-driven bond weakening by calculating electron density for the energy window corresponding to the bonding state in the ground and laser-dressed states. By analyzing first- and second-order optical responses, we followed how the relative weight of different orbital characters changes in the valence and conduction bands. We observed an increase in orbital characters absent in the ground-state valence band, such as O s and Zn p. Under laser excitation, these states become partially occupied and appear in the laser-dressed valence band. We next used the developed approach to interpret the computational results of our modeling of trXAS.

In Chapter 5, we presented the theoretical framework and *ab initio* computational scheme for describing the application of ultrafast XAS to study laser-dressed electron dynamics in materials. We demonstrated two approaches for calculating the absorption cross section: the projection treatment of x-ray absorption, suitable only for a quasi-monochromatic probe pulse, and the time- and frequency-domain treatment of x-ray absorption, suitable for the general case of ultrashort pulses. We calculated the ultrafast x-ray absorption spectra at the O K- and Zn L_3-edges over an energy range covering both valence and conduction bands. In the conduction-band region, we observed a reduction in signal intensity due to carrier excitation. Around the valence band, a pre-edge feature emerges due to the vacancy left behind after carrier excitation in the conduction band. To interpret the trXAS, we used the laser-dressed PDOS and compared the results of both approaches with the corresponding laser-dressed PDOS. In the projection treatment, we found that the amplitudes of the time-dependent absorption cross section correspond directly to the unoccupied laser-dressed PDOS. In the time- and frequency-domain treatment, we found that the absorption of a spectral component depends additionally on its initial intensity within the probe pulse. This dispersion effect introduces an asymmetric Fano profile, giving rise to the experimentally observed "fishbone" resonance structures. By comparing the symmetric Lorentzian contribution with the corresponding PDOS amplitudes, we found good overall agreement in the spectral shape, with the largest discrepancies appearing at the edges of the probe pulse bandwidth.

The developed framework provides a tool for interpretation of the ultrafast x-ray experiments on laser-driven solids and for developing strategies of optical manipulations of material properties. As an outlook, it is important to go beyond the one-electron approximation and incorporate electronic correlation effects into our *ab initio* computational scheme. This includes excitonic effects and dynamical electron screening, that can play an important role in electron dynamics and potentially shift or broaden spectral features. This step requires going beyond the DFT output as the basis for diagonalizing the Floquet–Bloch Hamiltonian within our *ab initio* computational scheme. Another way to develop our work would be to apply the approach to a wider range of materials. In this thesis, we have only demonstrated the developed approach on conventional semiconductors. A similar study of complex materials, such as heterostructures or two-dimensional

quantum materials, could reveal novel ultrafast phenomena.

A. Derivations

A.1. X-ray absorption cross section

A.1.1. Absorption probability

In the first order time-dependent perturbation theory the state $|\Psi^{(1)}_{\{n_x\}}(t_f)\rangle$, in the Schrödinger picture, for a particular Fock state of the radiation field is evaluated as

$$|\Psi^{(1)}_{\{n_x\}}(t_f)\rangle = \lim_{t_i\to-\infty}(-i)\int_{t_i}^{t_f} dt'\hat{U}(t_f,t')\hat{H}_{int}\hat{U}(t',t_i)\,|\Psi^{(0)}_{\{n_x\}}(t_i)\rangle\,. \tag{A.1}$$

The term in the perturbative expansion of $\hat{\rho}_f$ that determines the scattering probability in this approximation is

$$\hat{\rho}^{(1)}_f = \lim_{t_i\to-\infty}\lim_{t_f\to+\infty}\sum_{\{n_x\},\{\bar{n}_x\}}\rho^x_{\{n_x\},\{\bar{n}_x\}}\int_{t_i}^{t_f}\int_{t_i}^{t_f} dt_1dt_2\Bigg(\hat{U}(t_f,t_1)\hat{H}_{int}\hat{U}(t_1,t_i)\,|\Psi^{(0)}_{\{n_x\}}(t_i)\rangle$$
$$\times\langle\Psi^{(0)}_{\{\bar{n}_x\}}(t_i)|\,\hat{U}^\dagger(t_2,t_i)\hat{H}^\dagger_{int}\hat{U}^\dagger(t_f,t_2)\Bigg). \tag{A.2}$$

Therefore, after substituting the expression for density matrix of entire system in the form Eq. (A.2) into the expression for absorption probability Eq. (5.13) can be written as

$$P^{(1)} = \sum_{F,\{n'_x\}}\sum_{\{n_x\},\{\bar{n}_x\}}\rho^x_{\{n_x\},\{\bar{n}_x\}}\int_{-\infty}^{\infty}\int_{-\infty}^{\infty} dt_1dt_2\int\int d^3r_1d^3r_2\,e^{i\mathcal{E}_F(t_1-t_2)}\sum_{\boldsymbol{\kappa}_{x_1},s_{x_1}}\sum_{\boldsymbol{\kappa}_{x_2},s_{x_2}}\frac{2\pi}{V\sqrt{\omega_{\boldsymbol{\kappa}_{x_1}}\omega_{\boldsymbol{\kappa}_{x_2}}}}e^{-i\omega_{\kappa_{x_1}}t_1}e^{i\omega_{\kappa_{x_2}}t_2}$$
$$\times\Bigg(\langle\{n'_x\}|\,\hat{a}_{\boldsymbol{\kappa}_{x_1},s_{x_1}}\,|\{n_x\}\rangle\,\langle\Psi_F|\,\boldsymbol{\epsilon}_{\boldsymbol{\kappa}_{x_1},s_{x_1}}\cdot\hat{\psi}^\dagger(\mathbf{r}_1)\nabla\hat{\psi}(\mathbf{r}_1)e^{i\boldsymbol{\kappa}_{x_1}\cdot\mathbf{r}_1}\,|\Psi(t_1)\rangle$$
$$+\langle\{n'_x\}|\,\hat{a}^\dagger_{\boldsymbol{\kappa}_{x_1},s_{x_1}}\,|\{n_x\}\rangle\,\langle\Psi_F|\,\boldsymbol{\epsilon}^*_{\boldsymbol{\kappa}_{x_1},s_{x_1}}\cdot\hat{\psi}^\dagger(\mathbf{r}_1)\nabla\hat{\psi}(\mathbf{r}_1)e^{-i\boldsymbol{\kappa}_{x_1}\cdot\mathbf{r}_1}\,|\Psi(t_1)\rangle\Bigg)$$
$$\times\Bigg(\langle\{\bar{n}_x\}|\,\hat{a}_{\boldsymbol{\kappa}_{x_2},s_{x_2}}\,|\{n'_x\}\rangle\,\langle\Psi(t_2)|\,\boldsymbol{\epsilon}_{\boldsymbol{\kappa}_{x_2},s_{x_2}}\cdot\hat{\psi}^\dagger(\mathbf{r}_2)\nabla\hat{\psi}(\mathbf{r}_2)e^{i\boldsymbol{\kappa}_{x_2}\cdot\mathbf{r}_2}\,|\Psi_F\rangle$$
$$+\langle\{\bar{n}_x\}|\,\hat{a}^\dagger_{\boldsymbol{\kappa}_{x_2},s_{x_2}}\,|\{n'_x\}\rangle\,\langle\Psi(t_2)|\,\boldsymbol{\epsilon}^*_{\boldsymbol{\kappa}_{x_2},s_{x_2}}\cdot\hat{\psi}^\dagger(\mathbf{r}_2)\nabla\hat{\psi}(\mathbf{r}_2)e^{-i\boldsymbol{\kappa}_{x_2}\cdot\mathbf{r}_2}\,|\Psi_F\rangle\Bigg) \tag{A.3}$$

The energies $E_{\{n'_x\}}$ and $E_{\{n_x\}}$ corresponds to the Fock states $|\{n'_x\}\rangle$ and $|\{n'_x\}\rangle$, accordingly, differ from each other by the energy of absorbed photons - $\omega_{\boldsymbol{\kappa}_{x_a}}$, $E_{\{n'_x\}} = E_{\{n_x\}} - \omega_{\boldsymbol{\kappa}_{x_a}}$, coinciding with one frequency from the range $\{\omega_{\boldsymbol{\kappa}_x}\}$ as follows $E_{\{n_x\}} = \sum_{\boldsymbol{\kappa}_x,s_x}\omega_{\boldsymbol{\kappa}_x}N_{\boldsymbol{\kappa}_x,s_x}$.

The creation (annihilation) operators $\hat{a}^\dagger_{\boldsymbol{\kappa}_{x_{1,2}},s_{x_{1,2}}}$ ($\hat{a}_{\boldsymbol{\kappa}_{x_{1,2}},s_{x_{1,2}}}$) corresponding to x-ray photons

in the state $(\boldsymbol{\kappa}_{x_{1,2}}, s_{x_{1,2}})$ act only on the Fock state sets $|\{n_x\}\rangle$, $|\{\bar{n}_x\}\rangle$, and $|\{n'_x\}\rangle$, which are characterized by energy differences given by $E_{\{n_x\},\{\bar{n}_x\}} - E_{\{n'_x\}} = \omega_{\boldsymbol{\kappa}_{x_{1,2}}}$. Considering this, and using the definition of the trace of a matrix Eq. (A.3) can be further simplified as follows

$$P^{(1)} = \sum_F \int_{-\infty}^{\infty}\int_{-\infty}^{\infty} dt_1 dt_2 \int\int d^3r_1 d^3r_2 e^{i\mathcal{E}_F(t_1-t_2)} \sum_{\boldsymbol{\kappa}_{x_1}, s_{x_1}} \sum_{\boldsymbol{\kappa}_{x_2}, s_{x_2}} \frac{2\pi}{V\sqrt{\omega_{\boldsymbol{\kappa}_{x_1}}\omega_{\boldsymbol{\kappa}_{x_2}}}} e^{-i\omega_{\boldsymbol{\kappa}_{x_1}}t_1} e^{i\omega_{\boldsymbol{\kappa}_{x_2}}t_2} e^{i\boldsymbol{\kappa}_{x_1}\mathbf{r}_1} e^{-i\boldsymbol{\kappa}_{x_2}\mathbf{r}_2}$$
$$\times \mathrm{Tr}\left[\hat{\rho}^{X}_{\mathrm{in}} \hat{a}^\dagger_{\boldsymbol{\kappa}_{x_2}, s_{x_2}} \hat{a}_{\boldsymbol{\kappa}_{x_1}, s_{x_1}}\right] \langle\Psi_F| \boldsymbol{\epsilon}_{\boldsymbol{\kappa}_{x_1}, s_{x_1}} \cdot \hat{\psi}^\dagger(\mathbf{r}_1)\nabla\hat{\psi}(\mathbf{r}_1) |\Psi(t_1)\rangle \langle\Psi(t_2)| \boldsymbol{\epsilon}^*_{\boldsymbol{\kappa}_{x_2}, s_{x_2}} \cdot \hat{\psi}^\dagger(\mathbf{r}_2)\nabla\hat{\psi}(\mathbf{r}_2) |\Psi_F\rangle . \tag{A.4}$$

A.1.2. Final-to-reference state summation transformation

The summation over all final states $|\Psi_F\rangle$ has been transformed into the summation over reference eigenstates $|\Psi_{F_0}\rangle$:

$$\sum_F D^{F*}_a(\mathbf{r}_2, t_2) D^F_b(\mathbf{r}_1, t_1) = \sum_{F_0, \Delta\mu} e^{-i(\mathcal{E}_{F_0}+\Delta\mu\Omega)(t_2-t_1)} \sum_{n,\mu} C^{F_0}_{n\mu+\Delta\mu} \langle\Psi_{\mathrm{el}}(t_2)| \langle\alpha(t_2)| \hat{\psi}^\dagger(\mathbf{r}_2)\partial_a\hat{\psi}(\mathbf{r}_2) |\Phi_n\rangle |N-\mu\rangle$$
$$\times \sum_{n',\mu'} C^{F_0*}_{n'\mu'+\Delta\mu} \langle\Phi_{n'}| \langle N-\mu'| \hat{\psi}^\dagger(\mathbf{r}_1)\partial_b\hat{\psi}(\mathbf{r}_1) |\Psi_{\mathrm{el}}(t_1)\rangle |\alpha(t_1)\rangle . \tag{A.5}$$

Due to the fact that $\langle\alpha(t_2)|N-\mu\rangle \langle N-\mu'|\alpha(t_1)\rangle = A^*_{N-\mu}A_{N-\mu'}e^{i(N-\mu)\Omega t_2 - i(N-\mu')\Omega t_1}$ and by using that $\sum_\mu A^*_{N-\mu}A_{N-\mu+\Delta\mu} \approx 1$ independently of $\Delta\mu$ for a large N, we get

$$\sum_F D^{F*}_a(\mathbf{r}_2, t_2) D^F_b(\mathbf{r}_1, t_1) = \sum_{F_0} e^{i(\mathcal{E}_{F_0}-\mathcal{E}_{I_0})(t_1-t_2)} \sum_{\Delta\mu,\Delta\mu'} e^{i\Delta\mu\Omega t_1 - i\Delta\mu'\Omega t_2} \sum_{n,k,\mu} C^{F_0*}_{n\mu+\Delta\mu} C^{I_0}_{k\mu} \langle\Phi_n| \hat{\psi}^\dagger(\mathbf{r}_1)\partial_b\hat{\psi}(\mathbf{r}_1) |\Phi_k\rangle$$
$$\times \sum_{n',k',\mu'} C^{F_0}_{n'\mu'+\Delta\mu'} C^{I_0*}_{k'\mu'} \langle\Phi_{k'}| \hat{\psi}^\dagger(\mathbf{r}_2)\partial_a\hat{\psi}(\mathbf{r}_2) |\Phi_{n'}\rangle . \tag{A.6}$$

A.1.3. The dipole moment via one-body Floquet states

We now evaluate the functions $D^{F_0}(\boldsymbol{\kappa}^{\mathrm{in}}_x, \Delta\mu)$ for a system of non-interacting electrons. In this case, the many-body wavefunction $|\Theta^{\mathrm{el}}_{I_0}(t)\rangle$, which solves the time-dependent Schrödinger equation for an electronic system, can be expressed as the Slater determinant of the corresponding one-body solutions as $|\Theta^{\mathrm{el}}_{I_0}(t)\rangle = |\phi^{\mathrm{el}}_{i_1\mathbf{k}_1}, \phi^{\mathrm{el}}_{i_2\mathbf{k}_2}, \ldots, \phi^{\mathrm{el}}_{i_n\mathbf{k}_n}, \ldots\rangle$, where each one-body state $\phi^{\mathrm{el}}_{i_n\mathbf{k}_n}(\mathbf{r}, t)$ is given by $\phi^{\mathrm{el}}_{i_n\mathbf{k}_n}(\mathbf{r}, t) = e^{-i\varepsilon_{i_n\mathbf{k}_n}t} \sum_{m,\mu} c^{i_n}_{m\mathbf{k}_n\mu} e^{-i\mu\omega t} \varphi_{m\mathbf{k}_n}(\mathbf{r})$.

The many-body wavefunction can be expanded in terms of the many-body eigenstates of the electronic Hamiltonian $\hat{H}_{\mathrm{el}}$ as $|\Theta^{\mathrm{el}}_{I_0}(t)\rangle = \sum_{n,\mu} C^{I_0}_{n\mu} e^{-i\mu\omega t} |\Phi_n\rangle$, using this expansion, the matrix element of the operator $\left[\hat{\psi}^\dagger(\mathbf{r})\nabla\hat{\psi}(\mathbf{r})\right]$ is given by:

$$\langle\Theta^{\mathrm{el}}_{F_0}(t)| \hat{\psi}^\dagger(\mathbf{r})\nabla\hat{\psi}(\mathbf{r}) |\Theta^{\mathrm{el}}_{I_0}(t)\rangle = e^{i(\mathcal{E}_{F_0}-\mathcal{E}_{I_0})t} \sum_{\Delta\mu} e^{i\Delta\mu\omega t} \sum_{n,k,\mu} C^{F_0*}_{n\mu+\Delta\mu} C^{I_0}_{k\mu} \langle\Phi_n| \hat{\psi}^\dagger(\mathbf{r})\nabla\hat{\psi}(\mathbf{r}) |\Phi_k\rangle . \tag{A.7}$$

On the other hand, using the relation:

$$\langle \Theta^{\mathrm{el}}_{F_0}(t)|\, \hat{\psi}^\dagger(\mathbf{r})\nabla\hat{\psi}(\mathbf{r})\, |\Theta^{\mathrm{el}}_{I_0}(t)\rangle = e^{i(\mathcal{E}_{F_0}-\mathcal{E}_{I_0})t}\sum_{\Delta\mu} e^{i\Delta\mu\omega t}\sum_{m,m',\mu} c^{f*}_{m'\mathbf{k}'\mu+\Delta\mu}c^{i}_{m\mathbf{k}\mu}\varphi^\dagger_{m'\mathbf{k}'}(\mathbf{r})\nabla\varphi_{m\mathbf{k}}(\mathbf{r}), \tag{A.8}$$

we obtain the expression for the amplitude $D^{F_0}(\boldsymbol{\kappa}^{\mathrm{in}}_{\mathrm{x}},\Delta\mu)$, which can be represented in terms of one-body Floquet states as:

$$\begin{aligned} D^{F_0}(\boldsymbol{\kappa}^{\mathrm{in}}_{\mathrm{x}},\Delta\mu) &= \sum_{n,k,\mu} C^{F_0*}_{n\mu+\Delta\mu}C^{I_0}_{k\mu}\int d^3r\, e^{i\boldsymbol{\kappa}^{\mathrm{in}}_{\mathrm{x}}\mathbf{r}}\,\langle\Phi_n|\,\hat{\psi}^\dagger(\mathbf{r})(\boldsymbol{\epsilon}^{\mathrm{in}}_{\boldsymbol{\kappa}_{\mathrm{x}},s_{\mathrm{x}}}\cdot\boldsymbol{\nabla})\hat{\psi}(\mathbf{r})\,|\Phi_k\rangle \\ &= \delta(F_0;(i\mathbf{k},f\mathbf{k}'))\sum_{m,m',\mu} c^{f*}_{m'\mathbf{k}'\mu+\Delta\mu}c^{i}_{m\mathbf{k}\mu}\int d^3r\, e^{i\boldsymbol{\kappa}^{\mathrm{in}}_{\mathrm{x}}\mathbf{r}}\varphi^\dagger_{m'\mathbf{k}'}(\mathbf{r})(\boldsymbol{\epsilon}^{\mathrm{in}}_{\boldsymbol{\kappa}_{\mathrm{x}},s_{\mathrm{x}}}\cdot\boldsymbol{\nabla})\varphi_{m\mathbf{k}}(\mathbf{r}). \end{aligned} \tag{A.9}$$

A.1.4. Core-valence momentum matrix elements

We evaluate the following integral

$$\begin{aligned} &\int d^3r e^{i\boldsymbol{\kappa}^{\mathrm{in}}_{\mathrm{x}}\mathbf{r}}\varphi^\dagger_{m',\mathbf{k}'}(\mathbf{r})(\boldsymbol{\epsilon}^{\mathrm{in}}_{\boldsymbol{\kappa}_{\mathrm{x}},s_{\mathrm{x}}}\cdot\boldsymbol{\nabla})\varphi^{\mathrm{c}}_{\mathbf{k}}(\mathbf{r}) \\ &= \sum_{\mathbf{R}} e^{i\mathbf{k}\mathbf{R}}\int d^3r e^{i(\boldsymbol{\kappa}^{\mathrm{in}}_{\mathrm{x}}-\mathbf{k}')\mathbf{r}}u^\dagger_{m'\mathbf{k}'}(\mathbf{r})(\boldsymbol{\epsilon}^{\mathrm{in}}_{\boldsymbol{\kappa}_{\mathrm{x}},s_{\mathrm{x}}}\cdot\boldsymbol{\nabla})\varphi^{\mathrm{c}}(\mathbf{r}-\mathbf{R}) \\ &= \sum_{\mathbf{R}} e^{i\mathbf{k}\mathbf{R}}\int d^3r' e^{i(\boldsymbol{\kappa}^{\mathrm{in}}_{\mathrm{x}}-\mathbf{k}')(\mathbf{r}'+\mathbf{R})}u^\dagger_{m'\mathbf{k}'}(\mathbf{r}')(\boldsymbol{\epsilon}^{\mathrm{in}}_{\boldsymbol{\kappa}_{\mathrm{x}},s_{\mathrm{x}}}\cdot\boldsymbol{\nabla})\varphi^{\mathrm{c}}(\mathbf{r}') \\ &\approx \sum_{\mathbf{R}} e^{i(\mathbf{k}+\boldsymbol{\kappa}^{\mathrm{in}}_{\mathrm{x}}-\mathbf{k}')\mathbf{R}}\times N_{\mathrm{cell}}\int_{MT_{\mathrm{c}_0}} d^3r'\varphi^\dagger_{m'\mathbf{k}'}(\mathbf{r}')(\boldsymbol{\epsilon}^{\mathrm{in}}_{\boldsymbol{\kappa}_{\mathrm{x}},s_{\mathrm{x}}}\cdot\boldsymbol{\nabla})\varphi^{\mathrm{c}_0}(\mathbf{r}') \\ &= N^2_{\mathrm{cell}}\sum_{\mathbf{G}}\delta^{(3)}(\mathbf{k}+\boldsymbol{\kappa}^{\mathrm{in}}_{\mathrm{x}}-\mathbf{k}'-\mathbf{G})\int_{MT_{\mathrm{c}_0}} d^3r'\varphi^\dagger_{m'\mathbf{k}'}(\mathbf{r}')(\boldsymbol{\epsilon}^{\mathrm{in}}_{\boldsymbol{\kappa}_{\mathrm{x}},s_{\mathrm{x}}}\cdot\boldsymbol{\nabla})\varphi^{\mathrm{c}_0}(\mathbf{r}') \\ &= N^2_{\mathrm{cell}}\sum_{\mathbf{G}}\delta^{(3)}(\mathbf{k}+\boldsymbol{\kappa}^{\mathrm{in}}_{\mathrm{x}}-\mathbf{k}'-\mathbf{G})\,\langle\varphi_{m',\mathbf{k}'}|\,\hat{p}_{\boldsymbol{\epsilon}}\,|\varphi^{\mathrm{c}_0}\rangle\,. \end{aligned} \tag{A.10}$$

A.1.5. Decay of the core hole state

In this section, we revisit the expression for a coherent x-ray pulse given in Eq. (5.26) and incorporate the effect of core hole decay. The core hole state's decay results in a broadening of the x-ray absorption signal, which we model by introducing a small imaginary component to the final state energy, such that $\mathcal{E}_{F_0}\to\mathcal{E}_{F_0}+i\delta$. For a Gaussian-shaped probe pulse, we express the amplitude of the electric field as

$$E_{\mathrm{x}}(\mathbf{r}_0,t-t_{\mathrm{p}}) = \sqrt{\frac{8\pi}{c}}I_0(\mathbf{r}_0)e^{-\left(\frac{t-t_{\mathrm{p}}}{\tau_{\mathrm{p}}}\right)^2\times 2\ln 2}, \tag{A.11}$$

where $I_0(\mathbf{r}_0)=\frac{c}{8\pi}E^2_{\mathrm{x}}(\mathbf{r}_0,t=0)$ denotes the peak intensity, and τ_{p} is the duration of the pulse. Accounting for the decay of the core hole state results in the following expression

for the Fourier transform of the probe x-ray pulse:

$$\tilde{E}_{\mathrm{x}}(\Omega_{F_0 I_0} + \Delta\mu\Omega) = E_{\mathrm{x}}^0 e^{i(\Omega_{F_0 I_0}+\Delta\mu\Omega)t_{\mathrm{P}}} \frac{\sqrt{\pi}\tau_p}{2\sqrt{2\ln 2}} w(z_+) + E_{\mathrm{x}}^0 e^{i(\Omega_{F_0 I_0}+\Delta\mu\Omega)t_{\mathrm{P}}} \frac{\sqrt{\pi}\tau_p}{2\sqrt{2\ln 2}} w(z_-), \tag{A.12}$$

where $w(z)$ is defined as the Faddeeva function:

$$w(z) := e^{-z^2}\,\mathrm{erf}(-iz), \tag{A.13}$$

with the following arguments:

$$z_\pm = i\tau_p \frac{\delta \pm i(\Omega_{F_0 I_0} + \Delta\mu\Omega)}{2\sqrt{2\ln 2}}. \tag{A.14}$$

A.1.6. The frequency-domain momentum expectation value

We consider the integral

$$I = \int_{-\infty}^{\infty} dt e^{i\omega t} e^{-iE_2 t} \int_{-\infty}^{t} dt' f(t') e^{iE_1 t'}. \tag{A.15}$$

We change the order of integration. Note that $t' \leq t$, $t \in (-\infty, \infty) \Rightarrow t' \in (-\infty, \infty)$, $t \in (t', \infty)$, so we rewrite the integral as:

$$I = \int_{-\infty}^{\infty} dt'\, f(t') e^{iE_1 t'} \int_{t'}^{\infty} dt\, e^{i\omega t} e^{-iE_2 t}. \tag{A.16}$$

We evaluate the inner integral under the assumption that $\mathrm{Im}(\omega - E_2) = \eta > 0$, in this case

$$\int_{t'}^{\infty} dt\, e^{i(\omega - E_2)t - \eta t} = i e^{i(\omega - E_2 + i\eta)t'} \frac{\omega - E_2 - i\eta}{(\omega - E_2)^2 + \eta^2}. \tag{A.17}$$

The same can be achieved by introducing small imaginary correction to the core state energy $\varepsilon_c \to \varepsilon_c + i\eta$. In this case both energies $E_{1,2}$ will be shifted into the complex plain, then $E_{1,2} \to E_{1,2} - i\eta$. Now we plug back into the outer integral, which gives

$$I = i\frac{\omega - E_2 - i\eta}{(\omega - E_2)^2 + \eta^2} \int_{-\infty}^{\infty} dt'\, f(t') e^{i(E_1 - i\eta)t'} e^{i(\omega - E_2 + i\eta)t'} = i\frac{\omega - E_2 - i\eta}{(\omega - E_2)^2 + \eta^2} \tilde{f}(\omega + E_1 - E_2), \tag{A.18}$$

where $\tilde{f}(\omega) = \int_{-\infty}^{\infty} dt\, f(t) e^{i\omega t}$ is the Fourier transform of $f(t)$.

Bibliography

[1] P. M. Paul, E. S. Toma, P. Breger, et al. Observation of a Train of Attosecond Pulses from High Harmonic Generation. *Science*, 292 (5522), 2001, pp. 1689–1692, URL: https://www.science.org/doi/abs/10.1126/science.1059413, https://www.science.org/doi/pdf/10.1126/science.1059413.

[2] M. Hentschel, R. Kienberger, Ch. Spielmann, et al. Attosecond metrology. *Nature*, 414 (6863), 2001, pp. 509–513, URL: https://doi.org/10.1038/35107000.

[3] A. Baltuška, Th. Udem, M. Uiberacker, et al. Attosecond control of electronic processes by intense light fields. *Nature*, 421 (6923), 2003, pp. 611–615, URL: https://doi.org/10.1038/nature01414.

[4] P. B. Corkum and Ferenc Krausz. Attosecond science. *Nature Physics*, 3 (6), 2007, pp. 381–387, URL: https://doi.org/10.1038/nphys620.

[5] Martin Schultze, Elisabeth M. Bothschafter, Annkatrin Sommer, et al. Controlling dielectrics with the electric field of light. *Nature*, 493 (7430), 2013, pp. 75–78, URL: https://doi.org/10.1038/nature11720.

[6] O. Schubert, M. Hohenleutner, F. Langer, et al. Sub-cycle control of terahertz high-harmonic generation by dynamical Bloch oscillations. *Nature Photonics*, 8 (2), 2014, pp. 119–123, URL: https://doi.org/10.1038/nphoton.2013.349.

[7] Martin Schultze, Krupa Ramasesha, C.D. Pemmaraju, et al. Attosecond band-gap dynamics in silicon. *Science*, 346 (6215), 2014, pp. 1348–1352, URL: https://www.science.org/doi/abs/10.1126/science.1260311, https://www.science.org/doi/pdf/10.1126/science.1260311.

[8] M. Lucchini, S. A. Sato, A. Ludwig, et al. Attosecond dynamical Franz-Keldysh effect in polycrystalline diamond. *Science*, 353 (6302), 2016, pp. 916–919, URL: https://www.science.org/doi/abs/10.1126/science.aag1268, https://www.science.org/doi/pdf/10.1126/science.aag1268.

[9] Fabian Langer, Yen-Po Liu, Zhe Ren, et al. Few-cycle lightwave-driven currents in a semiconductor at high repetition rate. *Optica*, 7 (4), 2020, pp. 276–279, URL: https://opg.optica.org/optica/abstract.cfm?URI=optica-7-4-276.

[10] Tim Paasch-Colberg, Stanislav Yu. Kruchinin, Özge Sağlam, et al. Sub-cycle optical control of current in a semiconductor: from the multiphoton to the tunneling regime. *Optica*, 3 (12), 2016, pp. 1358–1361, URL: https://opg.optica.org/optica/abstract.cfm?URI=optica-3-12-1358.

[11] Václav Hanus, Viktória Csajbók, Zsuzsanna Pápa, et al. Light-field-driven current control in solids with pJ-level laser pulses at 80 MHz repetition rate. *Optica*, 8 (4), 2021, pp. 570–576, URL: https://opg.optica.org/optica/abstract.cfm?URI=optica-8-4-570.

[12] Ojoon Kwon, Tim Paasch-Colberg, Vadym Apalkov, et al. Semimetallization of dielectrics in strong optical fields. *Scientific Reports*, 6 (1), 2016, p. 21272, URL: https://doi.org/10.1038/srep21272.

[13] Ojoon Kwon and D. Kim. PHz current switching in calcium fluoride single crystal. *Applied Physics Letters*, 108 (19), 2016, p. 191112, URL: https://doi.org/10.1063/1.4949487.

[14] M. Garg, M. Zhan, T. T. Luu, et al. Multi-petahertz electronic metrology. *Nature*, 538 (7625), 2016, pp. 359–363, URL: https://doi.org/10.1038/nature19821.

[15] J. Schoetz, Z. Wang, E. Pisanty, M. Lewenstein, M. F. Kling, and M. F. Ciappina. Perspective on Petahertz Electronics and Attosecond Nanoscopy. *ACS Photonics*, 6 (12), 2019, pp. 3057–3069, URL: https://doi.org/10.1021/acsphotonics.9b01188.

[16] M. Ossiander, K. Golyari, K. Scharl, et al. The speed limit of optoelectronics. *Nature Communications*, 13 (1), 2022, p. 1620, URL: https://doi.org/10.1038/s41467-022-29252-1.

[17] Christian Heide, Phillip D. Keathley, and Matthias F. Kling. Petahertz electronics. *Nature Reviews Physics*, 6 (11), 2024, pp. 648–662, URL: https://doi.org/10.1038/s42254-024-00764-7.

[18] E. Goulielmakis, V. S. Yakovlev, A. L. Cavalieri, et al. Attosecond Control and Measurement: Lightwave Electronics. *Science*, 317 (5839), 2007, pp. 769–775, URL: https://www.science.org/doi/abs/10.1126/science.1142855, https://www.science.org/doi/pdf/10.1126/science.1142855.

[19] Ferenc Krausz and Mark I. Stockman. Attosecond metrology: from electron capture to future signal processing. *Nature Photonics*, 8 (3), 2014, pp. 205–213, URL: https://doi.org/10.1038/nphoton.2014.28.

[20] Christian Heide, Tobias Boolakee, Takuya Higuchi, and Peter Hommelhoff. Adiabaticity parameters for the categorization of light-matter interaction: From weak to strong driving. *Phys. Rev. A*, 104, 2021, p. 023103, URL: https://link.aps.org/doi/10.1103/PhysRevA.104.023103.

[21] Leonid V. Keldysh. Ionization in the field of a strong electromagnetic wave. *Soviet Physics JETP*, 20, 1965, pp. 1307–1314, URL: https://www.slac.stanford.edu/grp/arb/tn/arbvol5/AARD451.pdf.

[22] Stanislav Yu. Kruchinin, Ferenc Krausz, and Vladislav S. Yakovlev. Colloquium: Strong-field phenomena in periodic systems. *Rev. Mod. Phys.*, 90, 2018, p. 021002, URL: https://link.aps.org/doi/10.1103/RevModPhys.90.021002.

[23] Ferenc Krausz and Misha Ivanov. Attosecond physics. *Rev. Mod. Phys.*, 81, 2009, pp. 163–234, URL: https://link.aps.org/doi/10.1103/RevModPhys.81.163.

[24] Shambhu Ghimire, Georges Ndabashimiye, Anthony D DiChiara, et al. Strong-field and attosecond physics in solids. *Journal of Physics B: Atomic, Molecular and Optical Physics*, 47 (20), 2014, p. 204030, URL: https://dx.doi.org/10.1088/0953-4075/47/20/204030.

[25] Stefano M. Cavaletto, Katarzyna M. Kowalczyk, Francisco O. Navarrete, and Javier Rivera-Dean. The attoscience of strong-field-driven solids. *Nature Reviews Physics*, 7 (1), 2025, pp. 38–49, URL: https://doi.org/10.1038/s42254-024-00784-3.

[26] D. N. Basov, R. D. Averitt, and D. Hsieh. Towards properties on demand in quantum materials. *Nature Materials*, 16 (11), 2017, pp. 1077–1088, URL: https://doi.org/10.1038/nmat5017.

[27] Takashi Oka and Sota Kitamura. Floquet engineering of quantum materials. *Annual Review of Condensed Matter Physics*, 10 (1), 2019, pp. 387–408, URL: https://www.annualreviews.org/content/journals/10.1146/annurev-conmatphys-031218-013423.

[28] Mark S. Rudner and Netanel H. Lindner. Band structure engineering and non-equilibrium dynamics in Floquet topological insulators. *Nature Reviews Physics*, 2 (5), 2020, pp. 229–244, URL: https://doi.org/10.1038/s42254-020-0170-z.

[29] Alberto de la Torre, Dante M. Kennes, Martin Claassen, Simon Gerber, James W. McIver, and Michael A. Sentef. Colloquium: Nonthermal pathways to ultrafast control in quantum materials. *Rev. Mod. Phys.*, 93, 2021, p. 041002, URL: https://link.aps.org/doi/10.1103/RevModPhys.93.041002.

[30] Y. H. Wang, H. Steinberg, P. Jarillo-Herrero, and N. Gedik. Observation of Floquet-Bloch States on the Surface of a Topological Insulator. *Science*, 342 (6157), 2013, pp. 453–457, URL: https://www.science.org/doi/abs/10.1126/science.1239834, https://www.science.org/doi/pdf/10.1126/science.1239834.

[31] Fahad Mahmood, Ching-Kit Chan, Zhanybek Alpichshev, et al. Selective scattering between Floquet–Bloch and Volkov states in a topological insulator. *Nature Physics*, 12 (4), 2016, pp. 306–310, URL: https://doi.org/10.1038/nphys3609.

[32] S. Ito, M. Schüler, M. Meierhofer, et al. Build-up and dephasing of Floquet–Bloch bands on subcycle timescales. *Nature*, 616 (7958), 2023, pp. 696–701, URL: https://doi.org/10.1038/s41586-023-05850-x.

[33] Edbert J. Sie, Clara M. Nyby, C. D. Pemmaraju, et al. An ultrafast symmetry switch in a Weyl semimetal. *Nature*, 565 (7737), 2019, pp. 61–66, URL: https://doi.org/10.1038/s41586-018-0809-4.

[34] J. W. McIver, B. Schulte, F.-U. Stein, et al. Light-induced anomalous Hall effect in graphene. *Nature Physics*, 16 (1), 2020, pp. 38–41, URL: https://doi.org/10.1038/s41567-019-0698-y.

[35] Shaohua Zhou, Changhua Bao, Benshu Fan, et al. Pseudospin-selective Floquet band engineering in black phosphorus. *Nature*, 614 (7946), 2023, pp. 75–80, URL: https://doi.org/10.1038/s41586-022-05610-3.

[36] L. Stojchevska, I. Vaskivskyi, T. Mertelj, et al. Ultrafast Switching to a Stable Hidden Quantum State in an Electronic Crystal. *Science*, 344 (6180), 2014, pp. 177–180, URL: https://www.science.org/doi/abs/10.1126/science.1241591, https://www.science.org/doi/pdf/10.1126/science.1241591.

[37] M Naseska, P Sutar, Y Vaskivskyi, et al. First-order kinetics bottleneck during photoinduced ultrafast insulator–metal transition in 3D orbitally-driven Peierls insulator CuIr2S4. *New Journal of Physics*, 23 (5), 2021, p. 053023, URL: https://dx.doi.org/10.1088/1367-2630/abf86d.

[38] Allan S. Johnson, Daniel Perez-Salinas, Khalid M. Siddiqui, et al. Ultrafast X-ray imaging of the light-induced phase transition in VO2. *Nature Physics*, 19 (2), 2023, pp. 215–220, URL: https://doi.org/10.1038/s41567-022-01848-w.

[39] D. Fausti, R. I. Tobey, N. Dean, et al. Light-Induced Superconductivity in a Stripe-Ordered Cuprate. *Science*, 331 (6014), 2011, pp. 189–191, URL: https://www.science.org/doi/abs/10.1126/science.1197294, https://www.science.org/doi/pdf/10.1126/science.1197294.

[40] M. Mitrano, A. Cantaluppi, D. Nicoletti, et al. Possible light-induced superconductivity in K3C60 at high temperature. *Nature*, 530 (7591), 2016, pp. 461–464, URL: https://doi.org/10.1038/nature16522.

[41] A. Cantaluppi, M. Buzzi, G. Jotzu, et al. Pressure tuning of light-induced superconductivity in K3C60. *Nature Physics*, 14 (8), 2018, pp. 837–841, URL: https://doi.org/10.1038/s41567-018-0134-8.

[42] M. Budden, T. Gebert, M. Buzzi, et al. Evidence for metastable photo-induced superconductivity in K3C60. *Nature Physics*, 17 (5), 2021, pp. 611–618, URL: https://doi.org/10.1038/s41567-020-01148-1.

[43] Takashi Oka and Hideo Aoki. Photovoltaic Hall effect in graphene. *Phys. Rev. B*, 79, 2009, p. 081406, URL: https://link.aps.org/doi/10.1103/PhysRevB.79.081406.

[44] Sven Aeschlimann, Shunsuke A. Sato, Razvan Krause, et al. Survival of Floquet–Bloch States in the Presence of Scattering. *Nano Letters*, 21 (12), 2021, pp. 5028–5035, URL: https://doi.org/10.1021/acs.nanolett.1c00801.

[45] Sein Park, Wonjun Lee, Seong Jang, et al. Steady Floquet–Andreev states in graphene Josephson junctions. *Nature*, 603 (7901), 2022, pp. 421–426, URL: https://doi.org/10.1038/s41586-021-04364-8.

[46] Dongsung Choi, Masataka Mogi, Umberto De Giovannini, et al. Observation of Floquet–Bloch states in monolayer graphene. *Nature Physics*, 21 (7), 2025, pp. 1100–1105, URL: https://doi.org/10.1038/s41567-025-02888-8.

[47] Kong-Thon Tsen, ed. *Ultrafast Phenomena in Semiconductors*. Springer, 2012.

[48] Joseph Orenstein. Ultrafast spectroscopy of quantum materials. *Physics Today*, 65 (9), 2012, pp. 44–50, URL: https://doi.org/10.1063/PT.3.1717.

[49] Bárbara Buades, Antonio Picón, Emma Berger, et al. Attosecond state-resolved carrier motion in quantum materials probed by soft x-ray XANES. *Applied Physics Reviews*, 8 (1), 2021, p. 011408, URL: https://doi.org/10.1063/5.0020649.

[50] J Fink, E Schierle, E Weschke, and J Geck. Resonant elastic soft x-ray scattering. *Reports on Progress in Physics*, 76 (5), 2013, p. 056502, URL: https://dx.doi.org/10.1088/0034-4885/76/5/056502.

[51] Krupa Ramasesha, Stephen R. Leone, and Daniel M. Neumark. Real-Time Probing of Electron Dynamics Using Attosecond Time-Resolved Spectroscopy. *Annual Review of Physical Chemistry*, 67, 2016, pp. 41–63, URL: https://www.annualreviews.org/content/journals/10.1146/annurev-physchem-040215-112025.

[52] Martina Fracchia, Paolo Ghigna, Alberto Vertova, Sandra Rondinini, and Alessandro Minguzzi. Time-Resolved X-ray Absorption Spectroscopy in (Photo)Electrochemistry. *Surfaces*, 1 (1), 2018, pp. 138–150, URL: https://www.mdpi.com/2571-9637/1/1/11.

[53] Nanshun Huang, Haixiao Deng, Bo Liu, Dong Wang, and Zhentang Zhao. Features and futures of X-ray free-electron lasers. *The Innovation*, 2 (2), 2021, p. 100097.

[54] Douglas Garratt, Mary Matthews, and Jon Marangos. Toward ultrafast soft x-ray spectroscopy of organic photovoltaic devices. *Structural Dynamics*, 11 (1), 2024, p. 010901, URL: https://doi.org/10.1063/4.0000214.

[55] R. Mankowsky, A. Subedi, M. Först, et al. Nonlinear lattice dynamics as a basis for enhanced superconductivity in YBa2Cu3O6.5. *Nature*, 516 (7529), 2014, pp. 71–73, URL: https://doi.org/10.1038/nature13875.

[56] S. Gerber, K. W. Kim, Y. Zhang, et al. Direct characterization of photoinduced lattice dynamics in BaFe2As2. *Nature Communications*, 6 (1), 2015, p. 7377, URL: https://doi.org/10.1038/ncomms8377.

[57] L. Rettig, S. O. Mariager, A. Ferrer, et al. Ultrafast Structural Dynamics of the Fe-Pnictide Parent Compound $BaFe_2As_2$. *Phys. Rev. Lett.*, 114, 2015, p. 067402, URL: https://link.aps.org/doi/10.1103/PhysRevLett.114.067402.

[58] S. Gerber, S.-L. Yang, D. Zhu, et al. Femtosecond electron-phonon lock-in by photoemission and x-ray free-electron laser. *Science*, 357 (6346), 2017, pp. 71–75, URL: https://www.science.org/doi/abs/10.1126/science.aak9946, https://www.science.org/doi/pdf/10.1126/science.aak9946.

[59] M. Först, R. I. Tobey, S. Wall, et al. Driving magnetic order in a manganite by ultrafast lattice excitation. *Phys. Rev. B*, 84, 2011, p. 241104, URL: https://link.aps.org/doi/10.1103/PhysRevB.84.241104.

[60] W. S. Lee, Y. D. Chuang, R. G. Moore, et al. Phase fluctuations and the absence of topological defects in a photo-excited charge-ordered nickelate. *Nature Communications*, 3 (1), 2012, p. 838, URL: https://doi.org/10.1038/ncomms1837.

[61] P. Beaud, A. Caviezel, S. O. Mariager, et al. A time-dependent order parameter for ultrafast photoinduced phase transitions. *Nature Materials*, 13 (10), 2014, pp. 923–927, URL: https://doi.org/10.1038/nmat4046.

[62] T. Kubacka, J. A. Johnson, M. C. Hoffmann, et al. Large-Amplitude Spin Dynamics Driven by a THz Pulse in Resonance with an Electromagnon. *Science*, 343 (6177), 2014, pp. 1333–1336, URL: https://www.science.org/doi/abs/10.1126/science.1242862, https://www.science.org/doi/pdf/10.1126/science.1242862.

[63] M. P. M. Dean, Y. Cao, X. Liu, et al. Ultrafast energy- and momentum-resolved dynamics of magnetic correlations in the photo-doped Mott insulator Sr2IrO4. *Nature Materials*, 15 (6), 2016, pp. 601–605, URL: https://doi.org/10.1038/nmat4641.

[64] Matteo Mitrano, Sangjun Lee, Ali A. Husain, et al. Ultrafast time-resolved x-ray scattering reveals diffusive charge order dynamics in La2–xBaxCuO4. *Science Advances*, 5 (8), 2019, URL: https://www.science.org/doi/abs/10.1126/sciadv.aax3346, https://www.science.org/doi/pdf/10.1126/sciadv.aax3346.

[65] P. M. Eisenberger and S. L. McCall. Mixing of X-Ray and Optical Photons. *Phys. Rev. A*, 3, 1971, pp. 1145–1151, URL: https://link.aps.org/doi/10.1103/PhysRevA.3.1145.

[66] T. E. Glover, D. M. Fritz, M. Cammarata, et al. X-ray and optical wave mixing. *Nature*, 488 (7413), 2012, pp. 603–608, URL: https://doi.org/10.1038/nature11340.

[67] Daria Popova-Gorelova, David A. Reis, and Robin Santra. Theory of x-ray scattering from laser-driven electronic systems. *Phys. Rev. B*, 98, 2018, p. 224302, URL: https://link.aps.org/doi/10.1103/PhysRevB.98.224302.

[68] C. Ornelas-Skarin, T. Bezriadina, M. Fuchs, et al. "Nonlinear x-ray optical wave-mixing in silicon". In: *Proceedings of the 2023 Optica Nonlinear Optics Topical Meeting (NLO 2023)*. Optica Publishing Group, 2023. DOI: 10.1364/NLO.2023.Th2A.3.

[69] Daria Popova-Gorelova and Robin Santra. Microscopic nonlinear optical response: Analysis and calculations with the Floquet–Bloch formalism. *Structural Dynamics*, 11 (1), 2024, p. 014102, URL: https://doi.org/10.1063/4.0000220.

[70] Frank de Groot. High-Resolution X-ray Emission and X-ray Absorption Spectroscopy. *Chemical Reviews*, 101 (6), 2001, pp. 1779–1808, URL: https://doi.org/10.1021/cr9900681.

[71] C. R. Natoli, M. Benfatto, S. Della Longa, and K. Hatada. X-ray absorption spectroscopy: state-of-the-art analysis. *Journal of Synchrotron Radiation*, 10, 2003, pp. 26–42.

[72] Junko Yano and Vittal K. Yachandra. X-ray absorption spectroscopy. *Photosynthesis Research*, 102 (2), 2009, pp. 241–254, URL: https://doi.org/10.1007/s11120-009-9473-8.

[73] Grant Bunker. *Introduction to XAFS: A Practical Guide to X-ray Absorption Fine Structure Spectroscopy*. Cambridge University Press, 2010.

[74] Bipin K. Agarwal. *X-ray Spectroscopy: An Introduction*. Vol. 15. Springer, 2013.

[75] D. C. Koningsberger and R. Prins, eds. *X-ray Absorption: Principles, Applications, Techniques of EXAFS, SEXAFS and XANES*. Vol. 92. John Wiley and Sons Inc., 1988.

[76] Joachim Stöhr. *NEXAFS Spectroscopy*. Springer, 2013.

[77] Boon-Keng Teo. "Extended X-Ray Absorption Fine Structure (EXAFS) Spectroscopy: Techniques and Applications". In: Springer, 1981, pp. 13–58. URL: https://doi.org/10.1007/978-1-4757-1238-4_3.

[78] James E. Penner-Hahn. X-ray absorption spectroscopy in coordination chemistry. *Coordination Chemistry Reviews*, 190-192, 1999, pp. 1101–1123, URL: https://www.sciencedirect.com/science/article/pii/S0010854599001605.

[79] Romain Geneaux, Hugo J. B. Marroux, Alexander Guggenmos, Daniel M. Neumark, and Stephen R. Leone. Transient absorption spectroscopy using high harmonic generation: a review of ultrafast X-ray dynamics in molecules and solids. *Philosophical Transactions of the Royal Society A: Mathematical, Physical and Engineering Sciences*, 377 (2145), 2019, p. 20170463, URL: https://royalsocietypublishing.org/doi/abs/10.1098/rsta.2017.0463, https://royalsocietypublishing.org/doi/pdf/10.1098/rsta.2017.0463.

[80] Adam M. Summers, Stefano Severino, Maurizio Reduzzi, et al. Realizing Attosecond Core-Level X-ray Spectroscopy for the Investigation of Condensed Matter Systems. *Ultrafast Science*, 3, 2023, p. 0004, URL: https://spj.science.org/doi/abs/10.34133/ultrafastscience.0004, https://spj.science.org/doi/pdf/10.34133/ultrafastscience.0004.

[81] Peter M. Kraus, Michael Zürch, Scott K. Cushing, Daniel M. Neumark, and Stephen R. Leone. The ultrafast X-ray spectroscopic revolution in chemical dynamics. *Nature Reviews Chemistry*, 2 (6), 2018, pp. 82–94, URL: https://doi.org/10.1038/s41570-018-0008-8.

[82] Yuki Kobayashi and Stephen R. Leone. Characterizing coherences in chemical dynamics with attosecond time-resolved x-ray absorption spectroscopy. *The Journal of Chemical Physics*, 157 (18), 2022, p. 180901, URL: https://doi.org/10.1063/5.0119942.

[83] Christian Bressler and Majed Chergui. Ultrafast X-ray Absorption Spectroscopy. *Chemical Reviews*, 104 (4), 2004, pp. 1781–1812, URL: https://doi.org/10.1021/cr0206667.

[84] Eleftherios Goulielmakis, Zhi-Heng Loh, Adrian Wirth, et al. Real-time observation of valence electron motion. *Nature*, 466 (7307), 2010, pp. 739–743, URL: https://doi.org/10.1038/nature09212.

[85] Michael Zürch, Hung-Tzu Chang, Lauren J. Borja, et al. Direct and simultaneous observation of ultrafast electron and hole dynamics in germanium. *Nature Communications*, 8 (1), 2017, p. 15734, URL: https://doi.org/10.1038/ncomms15734.

[86] F. Schlaepfer, M. Lucchini, S. A. Sato, et al. Attosecond optical-field-enhanced carrier injection into the GaAs conduction band. *Nature Physics*, 14 (6), 2018, pp. 560–564, URL: https://doi.org/10.1038/s41567-018-0069-0.

[87] Giacomo Inzani, Lyudmyla Adamska, Amir Eskandari-asl, et al. Field-driven attosecond charge dynamics in germanium. *Nature Photonics*, 17 (12), 2023, pp. 1059–1065, URL: https://doi.org/10.1038/s41566-023-01274-1.

[88] T. P. H. Sidiropoulos, N. Di Palo, D. E. Rivas, et al. Probing the Energy Conversion Pathways between Light, Carriers, and Lattice in Real Time with Attosecond Core-Level Spectroscopy. *Phys. Rev. X*, 11, 2021, p. 041060, URL: https://link.aps.org/doi/10.1103/PhysRevX.11.041060.

[89] T. P. H. Sidiropoulos, N. Di Palo, D. E. Rivas, et al. Enhanced optical conductivity and many-body effects in strongly-driven photo-excited semi-metallic graphite. *Nature Communications*, 14 (1), 2023, p. 7407, URL: https://doi.org/10.1038/s41467-023-43191-5.

[90] K. Yabana and G. F. Bertsch. Time-dependent local-density approximation in real time. *Phys. Rev. B*, 54, 1996, pp. 4484–4487, URL: https://link.aps.org/doi/10.1103/PhysRevB.54.4484.

[91] Shunsuke A. Sato, Hannes Hübener, Umberto De Giovannini, and Angel Rubio. Technical review: Time-dependent density functional theory for attosecond physics ranging from gas-phase to solids. *npj Computational Materials*, 11 (1), 2025, p. 233, URL: https://doi.org/10.1038/s41524-025-01715-1.

[92] Mengqi Yang, Adonay Sissay, Min Chen, and Kenneth Lopata. Intruder Peak-Free Transient Inner-Shell Spectra Using Real-Time Simulations. *Journal of Chemical Theory and Computation*, 18 (2), 2022, pp. 992–1002, URL: https://doi.org/10.1021/acs.jctc.1c00079.

[93] Torsha Moitra, Lukas Konecny, Marius Kadek, Angel Rubio, and Michal Repisky. Accurate Relativistic Real-Time Time-Dependent Density Functional Theory for Valence and Core Attosecond Transient Absorption Spectroscopy. *The Journal of Physical Chemistry Letters*, 14 (7), 2023, pp. 1714–1724, URL: https://doi.org/10.1021/acs.jpclett.2c03599.

[94] Lucas Kurkowski, Adonay Sissay, Mengqi Yang, Alexander Meyer, and Kenneth Lopata. Simulations of Attosecond Metallization in Quartz and Diamond Probed with Inner-Shell Transient Absorption Spectroscopy. *The Journal of Physical Chemistry A*, 129 (3), 2025, pp. 650–660, URL: https://doi.org/10.1021/acs.jpca.4c05137.

[95] Ronaldo Rodrigues Pela and Claudia Draxl. All-electron full-potential implementation of real-time TDDFT in exciting. *Electronic Structure*, 3 (3), 2021, p. 037001, URL: https://dx.doi.org/10.1088/2516-1075/ac0c26.

[96] D. R. Hamann, M. Schlüter, and C. Chiang. Norm-Conserving Pseudopotentials. *Phys. Rev. Lett.*, 43, 1979, pp. 1494–1497, URL: https://link.aps.org/doi/10.1103/PhysRevLett.43.1494.

[97] W. Matthew C. Foulkes and Roger Haydock. Tight-binding models and density-functional theory. *Phys. Rev. B*, 39, 1989, pp. 12520–12536, URL: https://link.aps.org/doi/10.1103/PhysRevB.39.12520.

[98] Hartmut Haug and Antti-Pekka Jauho. *Quantum Kinetics in Transport and Optics of Semiconductors*. 2nd ed. Vol. 123. Springer Series in Solid-State Sciences. Springer, 2008.

[99] Gianluca Stefanucci and Robert van Leeuwen. *Nonequilibrium Many-Body Theory of Quantum Systems: A Modern Introduction*. Cambridge University Press, 2013.

[100] J. Vinson, J. J. Rehr, J. J. Kas, and E. L. Shirley. Bethe-Salpeter equation calculations of core excitation spectra. *Phys. Rev. B*, 83, 2011, p. 115106, URL: https://link.aps.org/doi/10.1103/PhysRevB.83.115106.

[101] Christian Vorwerk, Caterina Cocchi, and Claudia Draxl. Addressing electron-hole correlation in core excitations of solids: An all-electron many-body approach from first principles. *Phys. Rev. B*, 95, 2017, p. 155121, URL: https://link.aps.org/doi/10.1103/PhysRevB.95.155121.

[102] Martin Unzog, Alexey Tal, and Georg Kresse. X-ray absorption using the projector augmented-wave method and the Bethe-Salpeter equation. *Phys. Rev. B*, 106, 2022, p. 155133, URL: https://link.aps.org/doi/10.1103/PhysRevB.106.155133.

[103] C. Attaccalite, M. Grüning, and A. Marini. Real-time approach to the optical properties of solids and nanostructures: Time-dependent Bethe-Salpeter equation. *Phys. Rev. B*, 84, 2011, p. 245110, URL: https://link.aps.org/doi/10.1103/PhysRevB.84.245110.

[104] E. Perfetto, D. Sangalli, A. Marini, and G. Stefanucci. Nonequilibrium Bethe-Salpeter equation for transient photoabsorption spectroscopy. *Phys. Rev. B*, 92, 2015, p. 205304, URL: https://link.aps.org/doi/10.1103/PhysRevB.92.205304.

[105] Emilia Ridolfi, Paolo E. Trevisanutto, and Vitor M. Pereira. Expeditious computation of nonlinear optical properties of arbitrary order with native electronic interactions in the time domain. *Phys. Rev. B*, 102, 2020, p. 245110, URL: https://link.aps.org/doi/10.1103/PhysRevB.102.245110.

[106] D. Sangalli. Excitons and carriers in transient absorption and time-resolved ARPES spectroscopy: An ab initio approach. *Phys. Rev. Mater.*, 5, 2021, p. 083803, URL: https://link.aps.org/doi/10.1103/PhysRevMaterials.5.083803.

[107] Fulong Dong and Jie Liu. Fishbone resonance structure in the attosecond transient absorption spectrum of graphene. *Phys. Rev. A*, 106, 2022, p. 063107, URL: https://link.aps.org/doi/10.1103/PhysRevA.106.063107.

[108] Meiwen Du, Candong Liu, Yinghui Zheng, Zhinan Zeng, and Ruxin Li. Attosecond transient-absorption spectroscopy in one-dimensional periodic crystals. *Phys. Rev. A*, 100, 2019, p. 043840, URL: https://link.aps.org/doi/10.1103/PhysRevA.100.043840.

[109] Antonio Picón, L Plaja, and J Biegert. Attosecond x-ray transient absorption in condensed-matter: a core-state-resolved Bloch model. *New Journal of Physics*, 21 (4), 2019, p. 043029.

[110] Giovanni Cistaro, Mikhail Malakhov, Juan José Esteve-Paredes, et al. Theoretical Approach for Electron Dynamics and Ultrafast Spectroscopy (EDUS). *Journal of Chemical Theory and Computation*, 19 (1), 2023, pp. 333–348, URL: https://doi.org/10.1021/acs.jctc.2c00674.

[111] Darko Dimitrovski, Thomas Garm Pedersen, and Lars Bojer Madsen. Floquet-Bloch shifts in two-band semiconductors interacting with light. *Phys. Rev. A*, 95, 2017, p. 063420, URL: https://link.aps.org/doi/10.1103/PhysRevA.95.063420.

[112] Bing Gu and Ignacio Franco. Optical absorption properties of laser-driven matter. *Phys. Rev. A*, 98, 2018, p. 063412, URL: https://link.aps.org/doi/10.1103/PhysRevA.98.063412.

[113] Michael Schüler, Denis Golež, Yuta Murakami, et al. NESSi: The Non-Equilibrium Systems Simulation package. *Computer Physics Communications*, 257, 2020, p. 107484, URL: https://www.sciencedirect.com/science/article/pii/S0010465520302277.

[114] T. Otobe, Y. Shinohara, S. A. Sato, and K. Yabana. Femtosecond time-resolved dynamical Franz-Keldysh effect. *Phys. Rev. B*, 93, 2016, p. 045124, URL: https://link.aps.org/doi/10.1103/PhysRevB.93.045124.

[115] Nicolas Tancogne-Dejean, Michael A. Sentef, and Angel Rubio. Ultrafast transient absorption spectroscopy of the charge-transfer insulator NiO: Beyond the dynamical Franz-Keldysh effect. *Phys. Rev. B*, 102, 2020, p. 115106, URL: https://link.aps.org/doi/10.1103/PhysRevB.102.115106.

[116] S. K. Earl, M. A. Conway, J. B. Muir, et al. Coherent dynamics of Floquet-Bloch states in monolayer WS_2 reveals fast adiabatic switching. *Phys. Rev. B*, 104, 2021, p. L060303, URL: https://link.aps.org/doi/10.1103/PhysRevB.104.L060303.

[117] Matteo Lucchini, Fabio Medeghini, Yingxuan Wu, et al. Controlling Floquet states on ultrashort time scales. *Nature Communications*, 13 (1), 2022, p. 7103, URL: https://doi.org/10.1038/s41467-022-34973-4.

[118] Martin Holthaus. Floquet engineering with quasienergy bands of periodically driven optical lattices. *Journal of Physics B: Atomic, Molecular and Optical Physics*, 49 (1), 2015, p. 013001, URL: https://dx.doi.org/10.1088/0953-4075/49/1/013001.

[119] André Eckardt. Colloquium: Atomic quantum gases in periodically driven optical lattices. *Rev. Mod. Phys.*, 89, 2017, p. 011004, URL: https://link.aps.org/doi/10.1103/RevModPhys.89.011004.

[120] Jon H. Shirley. Solution of the Schrödinger Equation with a Hamiltonian Periodic in Time. *Phys. Rev.*, 138, 1965, B979–B987, URL: https://link.aps.org/doi/10.1103/PhysRev.138.B979.

[121] Hideo Sambe. Steady States and Quasienergies of a Quantum-Mechanical System in an Oscillating Field. *Phys. Rev. A*, 7, 1973, pp. 2203–2213, URL: https://link.aps.org/doi/10.1103/PhysRevA.7.2203.

[122] I. I. Rabi, N. F. Ramsey, and J. Schwinger. Use of Rotating Coordinates in Magnetic Resonance Problems. *Rev. Mod. Phys.*, 26, 1954, pp. 167–171, URL: https://link.aps.org/doi/10.1103/RevModPhys.26.167.

[123] Marin Bukov, Luca D'Alessio, and Anatoli Polkovnikov and. Universal high-frequency behavior of periodically driven systems: from dynamical stabilization to Floquet engineering. *Advances in Physics*, 64 (2), 2015, pp. 139–226, URL: https://doi.org/10.1080/00018732.2015.1055918.

[124] Michael Vogl, Martin Rodriguez-Vega, and Gregory A. Fiete. Effective Floquet Hamiltonian in the low-frequency regime. *Phys. Rev. B*, 101, 2020, p. 024303, URL: https://link.aps.org/doi/10.1103/PhysRevB.101.024303.

[125] Felix Bloch. Über die Quantenmechanik der Elektronen in Kristallgittern. *Zeitschrift für Physik*, 52 (7), 1929, pp. 555–600, URL: https://doi.org/10.1007/BF01339455.

[126] Werner Vogel and Dirk-Gunnar Welsch. *Quantum Optics*. 3rd ed. Wiley-VCH / John Wiley & Sons, 2006.

[127] T. P. Grozdanov and M. J. Raković. Quantum system driven by rapidly varying periodic perturbation. *Phys. Rev. A*, 38, 1988, pp. 1739–1746, URL: https://link.aps.org/doi/10.1103/PhysRevA.38.1739.

[128] Saar Rahav, Ido Gilary, and Shmuel Fishman. Effective Hamiltonians for periodically driven systems. *Phys. Rev. A*, 68, 2003, p. 013820, URL: https://link.aps.org/doi/10.1103/PhysRevA.68.013820.

[129] M Rodriguez-Vega, M Lentz, and B Seradjeh. Floquet perturbation theory: formalism and application to low-frequency limit. *New Journal of Physics*, 20 (9), 2018, p. 093022, URL: https://dx.doi.org/10.1088/1367-2630/aade37.

[130] Umberto De Giovannini and Hannes Hübener. Floquet analysis of excitations in materials. *Journal of Physics: Materials*, 3 (1), 2019, p. 012001, URL: https://dx.doi.org/10.1088/2515-7639/ab387b.

[131] Viktor Novičenko, Egidijus Anisimovas, and Gediminas Juzeliūnas. Floquet analysis of a quantum system with modulated periodic driving. *Phys. Rev. A*, 95, 2017, p. 023615, URL: https://link.aps.org/doi/10.1103/PhysRevA.95.023615.

[132] E.T. Jaynes and F.W. Cummings. Comparison of quantum and semiclassical radiation theories with application to the beam maser. *Proceedings of the IEEE*, 51 (1), 1963, pp. 89–109.

[133] Han Hsu and L. E. Reichl. Floquet-Bloch states, quasienergy bands, and high-order harmonic generation for single-walled carbon nanotubes under intense laser fields. *Phys. Rev. B*, 74, 2006, p. 115406, URL: https://link.aps.org/doi/10.1103/PhysRevB.74.115406.

[134] F. H. M. Faisal and J. Z. Kamiński. Floquet-Bloch theory of high-harmonic generation in periodic structures. *Phys. Rev. A*, 56, 1997, pp. 748–762, URL: https://link.aps.org/doi/10.1103/PhysRevA.56.748.

[135] N. Tzoar and J. I. Gersten. Theory of electronic band structure in intense laser fields. *Phys. Rev. B*, 12, 1975, pp. 1132–1139, URL: https://link.aps.org/doi/10.1103/PhysRevB.12.1132.

[136] Robin Santra and Chris H. Greene. Multiphoton ionization of xenon in the vuv regime. *Phys. Rev. A*, 70, 2004, p. 053401, URL: https://link.aps.org/doi/10.1103/PhysRevA.70.053401.

[137] Andris Gulans, Stefan Kontur, Christian Meisenbichler, et al. exciting: a full-potential all-electron package implementing density-functional theory and many-body perturbation theory. *Journal of Physics: Condensed Matter*, 26 (36), 2014, p. 363202, URL: https://dx.doi.org/10.1088/0953-8984/26/36/363202.

[138] David Vanderbilt. Soft self-consistent pseudopotentials in a generalized eigenvalue formalism. *Phys. Rev. B*, 41, 1990, pp. 7892–7895, URL: https://link.aps.org/doi/10.1103/PhysRevB.41.7892.

[139] X. Gonze, B. Amadon, P.-M. Anglade, et al. ABINIT: First-principles approach to material and nanosystem properties. *Computer Physics Communications*, 180 (12), 2009, pp. 2582–2615, URL: https://www.sciencedirect.com/science/article/pii/S0010465509002276.

[140] X. Gonze, F. Jollet, F. Abreu Araujo, et al. Recent developments in the ABINIT software package. *Computer Physics Communications*, 205, 2016, pp. 106–131, URL: https://www.sciencedirect.com/science/article/pii/S0010465516300923.

[141] Xavier Gonze, Bernard Amadon, Gabriel Antonius, et al. The Abinitproject: Impact, environment and recent developments. *Computer Physics Communications*, 248, 2020, p. 107042, URL: https://www.sciencedirect.com/science/article/pii/S0010465519303741.

[142] Aldo H. Romero, Douglas C. Allan, Bernard Amadon, et al. ABINIT: Overview and focus on selected capabilities. *The Journal of Chemical Physics*, 152 (12), 2020, p. 124102, URL: https://doi.org/10.1063/1.5144261.

[143] J. C. Slater. An Augmented Plane Wave Method for the Periodic Potential Problem. *Phys. Rev.*, 92, 1953, pp. 603–608, URL: https://link.aps.org/doi/10.1103/PhysRev.92.603.

[144] O. Krogh Andersen. Linear methods in band theory. *Phys. Rev. B*, 12, 1975, pp. 3060–3083, URL: https://link.aps.org/doi/10.1103/PhysRevB.12.3060.

[145] D D Koelling and G O Arbman. Use of energy derivative of the radial solution in an augmented plane wave method: application to copper. *Journal of Physics F: Metal Physics*, 5 (11), 1975, p. 2041, URL: https://dx.doi.org/10.1088/0305-4608/5/11/016.

[146] David Singh. Ground-state properties of lanthanum: Treatment of extended-core states. *Phys. Rev. B*, 43, 1991, pp. 6388–6392, URL: https://link.aps.org/doi/10.1103/PhysRevB.43.6388.

[147] E Sjöstedt, L Nordström, and D.J Singh. An alternative way of linearizing the augmented plane-wave method. *Solid State Communications*, 114 (1), 2000, pp. 15–20, URL: https://www.sciencedirect.com/science/article/pii/S0038109899005773.

[148] Chance Ornelas-Skarin, Tatiana Bezriadina, Matthias Fuchs, et al. Second-Order Microscopic Nonlinear Optical Susceptibility in a Centrosymmetric Material: Application to Imaging Valence Electron Motion. *Phys. Rev. X*, 16, 2026, p. 011006, URL: https://link.aps.org/doi/10.1103/7vqw-jbs7.

[149] Isaac Freund and B. F. Levine. Optically Modulated X-Ray Diffraction. *Phys. Rev. Lett.*, 25, 1970, pp. 1241–1245, URL: https://link.aps.org/doi/10.1103/PhysRevLett.25.1241.

[150] Daria Popova-Gorelova and Robin Santra. Atomic-scale imaging of laser-driven electron dynamics in solids. *Communications Physics*, 7 (1), 2024, p. 317, URL: https://doi.org/10.1038/s42005-024-01810-7.

[151] John P. Perdew, Kieron Burke, and Matthias Ernzerhof. Generalized Gradient Approximation Made Simple. *Phys. Rev. Lett.*, 77, 1996, pp. 3865–3868, URL: https://link.aps.org/doi/10.1103/PhysRevLett.77.3865.

[152] D. R. Hamann. Optimized norm-conserving Vanderbilt pseudopotentials. *Phys. Rev. B*, 88, 2013, p. 085117, URL: https://link.aps.org/doi/10.1103/PhysRevB.88.085117.

[153] Zachary H. Levine and Douglas C. Allan. Linear optical response in silicon and germanium including self-energy effects. *Phys. Rev. Lett.*, 63, 1989, pp. 1719–1722, URL: https://link.aps.org/doi/10.1103/PhysRevLett.63.1719.

[154] J. C. Phillips. Band Structure of Silicon, Germanium, and Related Semiconductors. *Phys. Rev.*, 125, 1962, pp. 1931–1936, URL: https://link.aps.org/doi/10.1103/PhysRev.125.1931.

[155] Mark S. Hybertsen and Steven G. Louie. First-Principles Theory of Quasiparticles: Calculation of Band Gaps in Semiconductors and Insulators. *Phys. Rev. Lett.*, 55, 1985, pp. 1418–1421, URL: https://link.aps.org/doi/10.1103/PhysRevLett.55.1418.

[156] Koichi Momma and Fujio Izumi. VESTA 3 for three-dimensional visualization of crystal, volumetric and morphology data. *Journal of Applied Crystallography*, 44 (6), 2011, pp. 1272–1276, URL: https://onlinelibrary.wiley.com/doi/abs/10.1107/S0021889811038970, https://onlinelibrary.wiley.com/doi/pdf/10.1107/S0021889811038970.

[157] Matthieu Chollet, Roberto Alonso-Mori, Marco Cammarata, et al. The X-ray Pump–Probe Instrument at the Linac Coherent Light Source. *Journal of Synchrotron Radiation*, 22 (3), 2015, pp. 503–507.

[158] Tatiana Bezriadina and Daria Popova-Gorelova. Laser-dressed partial density of states. *arXiv preprint arXiv:2505.19894*, 2025, URL: https://arxiv.org/abs/2505.19894, https://arxiv.org/pdf/2505.19894.

[159] A. Sommer, E. M. Bothschafter, S. A. Sato, et al. Attosecond nonlinear polarization and light–matter energy transfer in solids. *Nature*, 534 (7605), 2016, pp. 86–90, URL: https://doi.org/10.1038/nature17650.

[160] Takuya Higuchi, Christian Heide, Konrad Ullmann, Heiko B. Weber, and Peter Hommelhoff. Light-field-driven currents in graphene. *Nature*, 550 (7675), 2017, pp. 224–228, URL: https://doi.org/10.1038/nature23900.

[161] Florian Siegrist, Julia A. Gessner, Marcus Ossiander, et al. Light-wave dynamic control of magnetism. *Nature*, 571 (7764), 2019, pp. 240–244, URL: https://doi.org/10.1038/s41586-019-1333-x.

[162] T. Otobe, Y. Shinohara, S. A. Sato, and K. Yabana. Femtosecond time-resolved dynamical Franz-Keldysh effect. *Phys. Rev. B*, 93, 2016, p. 045124, URL: https://link.aps.org/doi/10.1103/PhysRevB.93.045124.

[163] Mingrui Yuan and Nikolay V. Golubev. Attosecond diffraction imaging of electron dynamics in solids. *Phys. Rev. Res.*, 7, 2025, p. L022042, URL: https://link.aps.org/doi/10.1103/PhysRevResearch.7.L022042.

[164] Nicolas Tancogne-Dejean, Michael A. Sentef, and Angel Rubio. Ultrafast transient absorption spectroscopy of the charge-transfer insulator NiO: Beyond the dynamical Franz-Keldysh effect. *Phys. Rev. B*, 102, 2020, p. 115106, URL: https://link.aps.org/doi/10.1103/PhysRevB.102.115106.

[165] Philipp Wopperer, Umberto De Giovannini, and Angel Rubio. Efficient and accurate modeling of electron photoemission in nanostructures with TDDFT. *The European Physical Journal B*, 90 (3), 2017, p. 51, URL: https://doi.org/10.1140/epjb/e2017-70548-3.

[166] Y. Zhou and M. W. Wu. Optical response of graphene under intense terahertz fields. *Phys. Rev. B*, 83, 2011, p. 245436, URL: https://link.aps.org/doi/10.1103/PhysRevB.83.245436.

[167] A. P. Jauho and K. Johnsen. Dynamical Franz-Keldysh Effect. *Phys. Rev. Lett.*, 76, 1996, pp. 4576–4579, URL: https://link.aps.org/doi/10.1103/PhysRevLett.76.4576.

[168] B. G. Enders, F. M. S. Lima, O. A. C. Nunes, et al. Electronic properties of a quasi-two-dimensional electron gas in semiconductor quantum wells under intense laser fields. *Phys. Rev. B*, 70, 2004, p. 035307, URL: https://link.aps.org/doi/10.1103/PhysRevB.70.035307.

[169] F M S Lima, O A C Nunes, A L A Fonseca, M A Amato, and E F da Silva. Effect of a terahertz laser field on the electron-DOS in a GaAs/AlGaAs cylindrical quantum wire: finite well model. *Semiconductor Science and Technology*, 23 (12), 2008, p. 125038, URL: https://dx.doi.org/10.1088/0268-1242/23/12/125038.

[170] F.M.S. Lima, O.A.C. Nunes, A.L.A. Fonseca, M.A. Amato, C.P. Lima, and E.F. da Silva. Terahertz laser-induced 1D–0D crossover in the density of states for electrons in a cylindrical semiconductor quantum wire. *Solid State Communications*, 149 (17), 2009, pp. 678–681, URL: https://www.sciencedirect.com/science/article/pii/S0038109809000945.

[171] Eric Suárez Morell and Luis E. F. Foa Torres. Radiation effects on the electronic properties of bilayer graphene. *Phys. Rev. B*, 86, 2012, p. 125449, URL: https://link.aps.org/doi/10.1103/PhysRevB.86.125449.

[172] Hernán L. Calvo, Pablo M. Perez-Piskunow, Stephan Roche, and Luis E. F. Foa Torres. Laser-induced effects on the electronic features of graphene nanoribbons. *Applied Physics Letters*, 101 (25), 2012, p. 253506, URL: https://doi.org/10.1063/1.4772496.

[173] Hamed Koochaki Kelardeh, Vadym Apalkov, and Mark I. Stockman. Graphene in ultrafast and superstrong laser fields. *Phys. Rev. B*, 91, 2015, p. 045439, URL: https://link.aps.org/doi/10.1103/PhysRevB.91.045439.

[174] V. N. Valmispild, C. Dutreix, M. Eckstein, M. I. Katsnelson, A. I. Lichtenstein, and E. A. Stepanov. Dynamically induced doublon repulsion in the Fermi-Hubbard model probed by a single-particle density of states. *Phys. Rev. B*, 102, 2020, p. 220301, URL: https://link.aps.org/doi/10.1103/PhysRevB.102.220301.

[175] P. Stadler, T. Löfwander, and M. Fogelström. Transport through vertical graphene contacts under intense laser fields. *Phys. Rev. Res.*, 2, 2020, p. 023274, URL: https://link.aps.org/doi/10.1103/PhysRevResearch.2.023274.

[176] Xue Li, Yongmei Li, Hao Yang, et al. Electrical gate assisted optical multisubband spin-orbit control in GaInAs/AlInAs quantum wells with tilted nonresonant laser fields. *Phys. Rev. B*, 108, 2023, p. 235429, URL: https://link.aps.org/doi/10.1103/PhysRevB.108.235429.

[177] Wen Liu, Xue Li, and Jiyong Fu. Laser-field-mediated Rashba and Dresselhaus spin–orbit control in GaInAs/AlInAs quantum wells. *Physica B: Condensed Matter*, 679, 2024, p. 415798, URL: https://www.sciencedirect.com/science/article/pii/S092145262400139X.

[178] Fangyang Zhan, Rui Chen, Zhen Ning, et al. Perspective: Floquet engineering topological states from effective models towards realistic materials. *Quantum Frontiers*, 3 (1), 2024, p. 21, URL: https://doi.org/10.1007/s44214-024-00067-z.

[179] Zhejun Jiang, Hao Huang, Chenxu Lu, et al. Ultrafast photoinduced C-H bond formation from two small inorganic molecules. *Nature Communications*, 15 (1), 2024, p. 2854, URL: https://doi.org/10.1038/s41467-024-47137-3.

[180] Christopher D. M. Hutchison, James M. Baxter, Ann Fitzpatrick, et al. Optical control of ultrafast structural dynamics in a fluorescent protein. *Nature Chemistry*, 15 (11), 2023, pp. 1607–1615, URL: https://doi.org/10.1038/s41557-023-01275-1.

[181] Shin-ichiro Ideta, Dongfang Zhang, Arend G. Dijkstra, et al. Ultrafast dissolution and creation of bonds in IrTe2 induced by photodoping. *Science Advances*, 4 (7), 2018, eaar3867, URL: https://www.science.org/doi/abs/10.1126/sciadv.aar3867, https://www.science.org/doi/pdf/10.1126/sciadv.aar3867.

[182] T. Frigge, B. Hafke, T. Witte, et al. Optically excited structural transition in atomic wires on surfaces at the quantum limit. *Nature*, 544 (7649), 2017, pp. 207–211, URL: https://doi.org/10.1038/nature21432.

[183] A. V. Kolobov, M. Krbal, P. Fons, J. Tominaga, and T. Uruga. Distortion-triggered loss of long-range order in solids with bonding energy hierarchy. *Nature Chemistry*, 3 (4), 2011, pp. 311–316, URL: https://doi.org/10.1038/nchem.1007.

[184] Jan Gerrit Horstmann, Hannes Böckmann, Bareld Wit, Felix Kurtz, Gero Storeck, and Claus Ropers. Coherent control of a surface structural phase transition. *Nature*, 583 (7815), 2020, pp. 232–236, URL: https://doi.org/10.1038/s41586-020-2440-4.

[185] E Sjöstedt, L Nordström, and D.J Singh. An alternative way of linearizing the augmented plane-wave method. *Solid State Communications*, 114 (1), 2000, pp. 15–20, URL: https://www.sciencedirect.com/science/article/pii/S0038109899005773.

[186] Milton Orchin, Roger S. Macomber, Allan R. Pinhas, and R. Marshall Wilson. *The Vocabulary and Concepts of Organic Chemistry*. 2nd ed. Wiley-Interscience, 2005, p. 912.

[187] Shambhu Ghimire, Anthony D. DiChiara, Emily Sistrunk, Pierre Agostini, Louis F. DiMauro, and David A. Reis. Observation of high-order harmonic generation in a bulk crystal. *Nature Physics*, 7 (2), 2011, pp. 138–141, URL: https://doi.org/10.1038/nphys1847.

[188] Lorenzo Sponza, Jacek Goniakowski, and Claudine Noguera. Structural, electronic, and spectral properties of six ZnO bulk polymorphs. *Phys. Rev. B*, 91, 2015, p. 075126, URL: https://link.aps.org/doi/10.1103/PhysRevB.91.075126.

[189] Tatsuhiko N. Ikeda, Satoshi Tanaka, and Yosuke Kayanuma. Floquet-Landau-Zener interferometry: Usefulness of the Floquet theory in pulse-laser-driven systems. *Phys. Rev. Res.*, 4, 2022, p. 033075, URL: https://link.aps.org/doi/10.1103/PhysRevResearch.4.033075.

[190] Roger G. Burns. *Mineralogical Applications of Crystal Field Theory*. 2nd ed. Vol. 5. Cambridge University Press, 1993.

[191] Gordon W. F. Drake, ed. *Springer Handbook of Atomic, Molecular, and Optical Physics*. 1st ed. Springer, 2006.

[192] Ü. Özgür, Ya. I. Alivov, C. Liu, et al. A comprehensive review of ZnO materials and devices. *Journal of Applied Physics*, 98 (4), 2005, p. 041301, URL: https://doi.org/10.1063/1.1992666.

[193] J.J. Rehr, A. Ankudinov, and S.I. Zabinsky. New developments in NEXAFS/EXAFS theory. *Catalysis Today*, 39 (4), 1998, pp. 263–269, URL: https://www.sciencedirect.com/science/article/pii/S0920586197001090.

[194] J. J. Rehr and R. C. Albers. Theoretical approaches to x-ray absorption fine structure. *Rev. Mod. Phys.*, 72, 2000, pp. 621–654, URL: https://link.aps.org/doi/10.1103/RevModPhys.72.621.

[195] Mette B. Gaarde, Christian Buth, Jennifer L. Tate, and Kenneth J. Schafer. Transient absorption and reshaping of ultrafast XUV light by laser-dressed helium. *Phys. Rev. A*, 83, 2011, p. 013419, URL: https://link.aps.org/doi/10.1103/PhysRevA.83.013419.

[196] Roy J. Glauber. The Quantum Theory of Optical Coherence. *Phys. Rev.*, 130, 1963, pp. 2529–2539, URL: https://link.aps.org/doi/10.1103/PhysRev.130.2529.

[197] Axel Stenquist, Felipe Zapata, and Jan Marcus Dahlström. Gauge-invariant absorption of light from a coherent superposition of states. *Phys. Rev. A*, 107, 2023, p. 053106, URL: https://link.aps.org/doi/10.1103/PhysRevA.107.053106.

[198] Fulong Dong and Jie Liu. Fishbone resonance structure in the attosecond transient absorption spectrum of graphene. *Phys. Rev. A*, 106, 2022, p. 063107, URL: https://link.aps.org/doi/10.1103/PhysRevA.106.063107.

[199] M. O. Krause and J. H. Oliver. Natural widths of atomic K and L levels, Kα X-ray lines and several KLL Auger lines. *Journal of Physical and Chemical Reference Data*, 8 (2), 1979, pp. 329–338, URL: https://doi.org/10.1063/1.555595.

[200] J-H Guo, L Vayssieres, C Persson, R Ahuja, B Johansson, and J Nordgren. Polarization-dependent soft-x-ray absorption of highly oriented ZnO microrod arrays. *Journal of Physics: Condensed Matter*, 14 (28), 2002, p. 6969, URL: https://doi.org/10.1088/0953-8984/14/28/308.

[201] C. Persson, C.L. Dong, L. Vayssieres, et al. X-ray absorption and emission spectroscopy of ZnO nanoparticle and highly oriented ZnO microrod arrays. *Microelectronics Journal*, 37 (8), 2006, pp. 686–689, URL: https://www.sciencedirect.com/science/article/pii/S0026269205004179.

[202] J. W. Chiou, J. C. Jan, H. M. Tsai, et al. Electronic structure of ZnO nanorods studied by angle-dependent x-ray absorption spectroscopy and scanning photoelectron microscopy. *Applied Physics Letters*, 84 (18), 2004, pp. 3462–3464, URL: https://doi.org/10.1063/1.1737075, https://pubs.aip.org/aip/apl/article-pdf/84/18/3462/18588730/3462_1_online.pdf.

[203] Teruyasu Mizoguchi, Isao Tanaka, Satoru Yoshioka, Masahiro Kunisu, Tomoyuki Yamamoto, and W. Y. Ching. First-principles calculations of ELNES and XANES of selected wide-gap materials: Dependence on crystal structure and orientation. *Phys. Rev. B*, 70, 2004, p. 045103, URL: https://link.aps.org/doi/10.1103/PhysRevB.70.045103.

[204] Isao Tanaka and Teruyasu Mizoguchi. First-principles calculations of x-ray absorption near edge structure and energy loss near edge structure: present and future. *Journal of Physics: Condensed Matter*, 21 (10), 2009, p. 104201, URL: https://doi.org/10.1088/0953-8984/21/10/104201.

[205] T. E. Glover, M. P. Hertlein, S. H. Southworth, et al. Controlling X-rays with light. *Nature Physics*, 6 (1), 2010, pp. 69–74, URL: https://doi.org/10.1038/nphys1430.

[206] Ajit Srivastava, Rahul Srivastava, Jigang Wang, and Junichiro Kono. Laser-Induced Above-Band-Gap Transparency in GaAs. *Phys. Rev. Lett.*, 93, 2004, p. 157401, URL: https://link.aps.org/doi/10.1103/PhysRevLett.93.157401.

[207] Mark C. Phillips, Hailin Wang, I. Rumyantsev, N. H. Kwong, R. Takayama, and R. Binder. Electromagnetically Induced Transparency in Semiconductors via Biexciton Coherence. *Phys. Rev. Lett.*, 91, 2003, p. 183602, URL: https://link.aps.org/doi/10.1103/PhysRevLett.91.183602.

[208] Giacomo Inzani, Lyudmyla Adamska, Amir Eskandari-asl, et al. Field-driven attosecond charge dynamics in germanium. *Nature Photonics*, 17 (12), 2023, pp. 1059–1065, URL: https://doi.org/10.1038/s41566-023-01274-1.

[209] Gian Luca Dolso, Shunsuke A. Sato, Giacomo Inzani, et al. Attosecond virtual charge dynamics in dielectrics. *Nature Photonics*, 19 (9), 2025, pp. 999–1005, URL: https://doi.org/10.1038/s41566-025-01700-6.